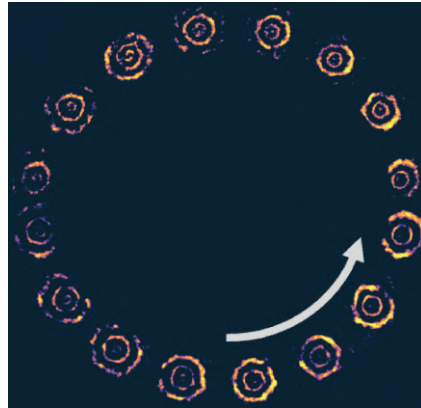




DEPARTMENT OF AEROSPACE ENGINEERING  
INDIAN INSTITUTE OF TECHNOLOGY MADRAS  
CHENNAI – 600036

# Thermoacoustic transitions and their control in turbulent combustors



*A Thesis*

*Submitted by*

**SAMARJEET SINGH**

*For the award of the degree*

*Of*

**DOCTOR OF PHILOSOPHY**

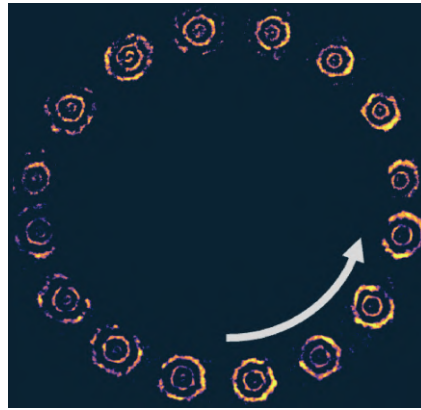
January 2024





DEPARTMENT OF AEROSPACE ENGINEERING  
INDIAN INSTITUTE OF TECHNOLOGY MADRAS  
CHENNAI – 600036

# Thermoacoustic transitions and their control in turbulent combustors



*A Thesis*

*Submitted by*

**SAMARJEET SINGH**

*For the award of the degree*

*Of*

**DOCTOR OF PHILOSOPHY**

January 2024



*Three golden rules of life:*

**ਕਿਰਤ ਕਰੋ**

***Kirat Karo***

*Work hard and honestly*

**ਵੰਡ ਛੱਕੋ**

***Vand chhako***

*Share with the needy*

**ਨਾਮ ਜਪੋ**

***Naam Jappo***

*Meditate God's name*

*– Guru Nanak Dev Ji*



*To my beloved parents, whose blessings are a constant source of  
enrichment in my life.*



# THESIS CERTIFICATE

This is to undertake that the Thesis titled **THERMOACOUSTIC TRANSITIONS AND THEIR CONTROL IN TURBULENT COMBUSTORS**, submitted by me to the Indian Institute of Technology Madras, for the award of **Doctor of Philosophy**, is a bona fide record of the research work done by me under the supervision of **Dr. R. I. Sujith**. The contents of this Thesis, in full or in parts, have not been submitted to any other Institute or University for the award of any degree or diploma.

To effectively convey the idea presented in this Thesis, the following work of other authors was reprinted with their permission:

1. Figure 1.1 : Image from [Zhao \(2023\)](#). Reproduced with permission from Elsevier.
2. Figure 1.2 : Image reproduced from [Lieuwen and Yang \(2005\)](#). Reproduced with permission from AIAA.
3. Figure 1.4 : Image from [Ananthkrishnan \*et al.\* \(1998\)](#). Reproduced with permission from Elsevier.
4. Figure 1.5 : Image reproduced from [George \*et al.\* \(2018\)](#). Reproduced with permission from Cambridge University Press.
5. Figure 1.6 : Image reproduced from [Kasthuri \*et al.\* \(2019\)](#). Reproduced with permission from American Institute of Physics.
6. Figure 1.7 : Image reproduced from [Mondal \*et al.\* \(2017b\)](#). Reproduced with permission from Cambridge University Press.
7. Figures 1.8(a) and (b) : Images reproduced from [Worth and Dawson \(2013a,b\)](#) and [Bourgoin \*et al.\* \(2013\)](#). Reproduced with permission from Elsevier and ASME.

**Chennai 600036**

**Samarjeet Singh**

**Date: January 2024**

**Dr. R. I. Sujith**  
Research advisor  
D. Srinivasan Institute Chair Professor  
Department of Aerospace Engineering, IIT Madras



# LIST OF PUBLICATIONS

## I. REFEREED JOURNALS BASED ON THESIS

1. **Singh, S.**, Roy, A., Reeja, K. V., Nair, A., Chaudhuri, S., and Sujith, R. I. (2021). Intermittency, Secondary Bifurcation and Mixed-Mode Oscillations in a Swirl-Stabilized Annular Combustor: Experiments and Modeling. *J. Eng. Gas Turbines Power*, **143** (5), 051028.
2. Roy, A., **Singh, S.**, Nair, A., Chaudhuri, S., and Sujith, R. I. (2022). Flame dynamics during intermittency and secondary bifurcation to longitudinal thermoacoustic instability in a swirl-stabilized annular combustor. *Proc. Combust. Inst.*, **38** (4), 6221-6230.
3. **Singh, S.**, Kumar D., A., Dhadphale, J. M., Roy, A., Sujith, R. I., and Chaudhuri, S. (2023). Mean-field model of synchronization for open-loop, swirl controlled thermoacoustic system. *Chaos*, **33** (4).
4. **Singh, S.**, Roy, A., Dhadphale, J. M., Chaudhuri, S., and Sujith, R. I. (2024). Continuous and explosive synchronization transition in turbulent combustors. *AIP Advances*, **14**, 065106.
5. **Singh, S.**, Bhavi R., Midhun P. R., Bhaskaran A., Mishra P., Chaudhuri S., and Sujith R. I. (2024). Intermittency transition to azimuthal instability in a turbulent annular combustor. *Int. J. Spray Combust. Dyn.*, **16** (3), 119-136.

## II. PRESENTATIONS IN CONFERENCES

1. **Singh, S.**, Roy A., K. V. Reeja, Nair A., Chaudhuri S., and Sujith R. I., Intermittency, Secondary Bifurcation and Mixed-Mode Oscillations in a Swirl-Stabilized Annular Combustor: Experiments and Modeling. *Proceedings of the ASME Turbo Expo 2020: Turbomachinery Technical Conference and Exposition. Volume 4B: Combustion, Fuels, and Emission*, (2020).
2. Roy, A., **Singh S.**, Nair A., Chaudhuri S., and Sujith R.I., Flame dynamics during intermittency and secondary bifurcation to longitudinal thermoacoustic instability in a swirl-stabilized annular combustor. *38<sup>th</sup> International Symposium on Combustion, Adelaide, Australia*, (2021).
3. **Singh, S.**, Roy A., Chaudhuri S., and Sujith R. I., Change of criticality in a turbulent annular combustor. *Dynamics Days Europe*, (2021).
4. **Singh, S.**, Bae J., Naderzadeh Y., Roy A., Dhadphale J., Chaudhuri S., and Sujith R. I., Phase-synchronization properties of a turbulent flame

in thermoacoustic system. *Combustion Institute Canadian Section 2023 Technical Meeting, University of Alberta campus, (2023).*

5. **Singh, S.**, Dutta A. K., Pawar S., Dhadphale J., Roy A., Sujith R. I., and Chaudhuri S., Phase-oscillator model for open-loop control of thermoacoustic instability in swirl-stabilized combustor. *Combustion Institute Canadian Section 2023 Technical Meeting, University of Alberta campus, (2023).*
6. **Singh, S.**, Roy A., Dhadphale J., Chaudhuri S., and Sujith R.I., Modeling turbulent thermoacoustic transitions using a mean-field synchronization approach. *Proceedings of the Third International Nonlinear Dynamics Conference, (2023).*
7. **Singh, S.**, Bhavi R., P. R. Midhun, Bhaskaran A., Mishra P., Chaudhuri S., and Sujith R.I., Intermittency transition to azimuthal instability in a turbulent annular combustor. *Symposium on Thermoacoustics in Combustion: Industry meets Academia, ETH Zurich, Switzerland, (2023).*



# ACKNOWLEDGEMENTS

This thesis is an outcome of extensive hard work, advice, and support from numerous individuals over the last five years, without whom this work would not have come to fruition. First and foremost, my deepest appreciation goes to Prof. R. I. Sujith for graciously accepting the role of my thesis advisor. His exceptional planning, relentless dedication to execution, and unwavering perseverance, even in challenging circumstances, have been invaluable. Prof. Sujith's consistent guidance and generous assistance at every stage of my research, whether it was in the development of an annular combustor, struggling for azimuthal thermoacoustic instability, or formulating a theoretical model, have been pivotal throughout my doctoral journey. He not only provided me with the freedom to explore but also patiently corrected my mistakes on numerous occasions. The knowledge and wisdom I have gained from him are immeasurable, and I will forever admire and seek inspiration from his mentorship.

I hold a deep sense of gratitude towards Prof. P. Sriram and Prof. H.S.N. Murthy for their encouragement and support in their roles as the Head of the Department. Their guidance has been invaluable. My heartfelt thanks extend to Prof. Nandan Kumar Sinha, Prof. Sunetra Sarkar, and Prof. S. Lakshmi Bala for their motivation and meticulous reviews of my research work as integral members of my Doctoral Committee. Additionally, I express my gratitude to Prof. K. Srinivasan for introducing me to the Jet flow and acoustics course, and to Prof. Srikrishna Sahu for his invaluable teachings in the Combustion course. Each of them has played an important role in shaping my academic journey, for which I am immensely thankful.

I am honored to have collaborated with Prof. Swetaprovo Chaudhuri. I extend my sincere thanks to him for his frequent visits to our laboratory during the development of the annular combustor rig. His invaluable suggestions significantly improved our annular combustor, leading to the successful excitation of thermoacoustic instabilities. I am also

deeply appreciative of Prof. Chaudhuri for graciously hosting my research visit to the University of Toronto. His commitment and passion for research are truly inspiring, and I feel incredibly fortunate to have had the opportunity to collaborate with him at the Propulsion and Energy Conversion, University of Toronto. I am extremely grateful for his support, and the wealth of knowledge I have gained during my time in his laboratory is immeasurable.

Being part of Prof. Sujith's group has been an absolute delight. Every achievement detailed in this thesis was accomplished with the help and support of fellow labmates and collaborators. I am deeply indebted to my senior, Dr. Amitesh Roy, for providing invaluable guidance and support during my first research work. I am immensely thankful to Dr. Samadhan Pawar, Dr. Abin Krishnan, Dr. Praveen Kasthuri, Dr. Induja Pavithran, and Dr. Manikandan Raghunathan for consistently inspiring me with their passion for research. Their eagerness to address my queries has been invaluable and truly motivating. Additionally, I extend my gratitude to Abhishek and Jayesh, whose presence has made both my professional and personal moments at work truly memorable. I would like to express my heartfelt gratitude to Ankit for being an unwavering source of support since 2018, through the highs and lows of my life.

I consider myself incredibly fortunate to have the constant support of the "Annular team." The team, initially included Dr. Amitesh Roy, Mr. Midhun P. R., Mrs. Reeja K. V., Ms. Asalatha Nair, Mr. Thilagaraj S., and Mr. Anand S., was later joined by Mr. Ramesh Bhavi, Ms. Anaswara Bhaskaran, and Mr. Pruthiraj Mishra. Experiments form an essential part of my work, and I could not have done any of the experiments without their help. I want to express my heartfelt gratitude to Mr. Mari from S.M. Engineering and Mr. Gokul from M.V. Engineering for their essential assistance in promptly fabricating the parts of the annular combustor. Additionally, Mr. John George sir, the Chief Engineer, was consistently available to offer his expertise and suggestions regarding the safety of combustors in the lab. Their contributions were truly indispensable. I also extend

my heartfelt gratitude to Mrs. Jegatha, Ms. Shanmugapriya, and Mrs. Jabasteena for their assistance with administrative tasks. Additionally, I express thanks to the Aerospace Department staff for their commitment to organizing timely meetings and efficient handling of administrative responsibilities.

I would also like to acknowledge the support my work has received from the Institute of Eminence (IoE) initiative of IIT Madras (SB/2021/0845/AE/MHRD/002696), the Office of Naval Research Global (Grant No. N62909-18-1-2061; Funder ID: 10.13039/100007297), Ontario Research Fund and the Natural Sciences and Engineering Research Council of Canada Discovery Grant (RGPIN-2021-02676). Additionally, I would like to express my sincere acknowledgment to the Ministry of Human Resource Development (MHRD) for providing Ph.D. funding through the Half-Time Research Assistantship (HTRA), as well as for the International Immersion Experience travel award from IIT Madras and the support received from the Mitacs Globalink Research Award, enabling me to conduct research as a Visiting student at the University of Toronto.

I am eternally indebted to my dearest parents for their constant and unconditional love and support throughout my life. Their steadfast belief in me and their continuous encouragement to learn and evolve have been constant pillars of strength. Despite my chaotic schedules and unforeseen plans, they embraced everything with joy, consistently inspiring and motivating me, not just through this Ph.D. journey but at every step of my life.



# ABSTRACT

**KEYWORDS** Combustion; Premixed flames; Thermoacoustic instabilities; Continuous and abrupt transitions; Intermittency and mixed-mode oscillations; Explosive synchronization; Open-loop control

Thermoacoustic instabilities observed in turbulent combustion systems have disastrous consequences and are notoriously challenging to model, predict, and control. Such instabilities are characterized by self-excited periodic oscillations, resulting from the constructive coupling between the acoustic pressure fluctuations and the unsteady heat release rate from the flame(s). In this thesis, we discuss the transitions to thermoacoustic instabilities in three disparate laboratory-scale combustors and their control by actuating the swirler.

In our initial study, we show the changes in the nature of bifurcation leading to longitudinal thermoacoustic instability when equivalence ratio and bulk velocity are systematically varied in the annular combustor. Depending upon the bulk velocity, we observe different states of combustor operation when the equivalence ratio is varied. These states include combustion noise, intermittency, low-amplitude thermoacoustic instability, mixed-mode oscillations, and high-amplitude thermoacoustic instability. A close inspection of the global and local flame dynamics reveals significant differences in the flame-flame interactions and structures across the periodic part of intermittency, low and high amplitude thermoacoustic instability, and mixed-mode oscillations. We further quantify the degree of temporal and spatiotemporal synchronization between different flames, and flames and pressure fluctuations using the Kuramoto order parameter and phase-locking value. To understand the underlying principle behind the criticalities of bifurcation, we present two distinct modeling approaches. The first approach is based on modeling the heat release rate fluctuations as nonlinear functions of the acoustic pressure, while the second approach is based on considering the flame response as an ensemble of phase

oscillators. The first approach successfully explains the temporal dynamics, while the second approach can reproduce both temporal and spatiotemporal dynamics observed in the experiments.

In our subsequent study, we alter the annular combustor geometry to excite azimuthal thermoacoustic instability. Our focus lies in investigating the transition to azimuthal thermoacoustic instability in the modified setup. We report that the transition from combustion noise to azimuthal instability occurs through a mode-switching phenomenon where the combustor switches from longitudinal mode to azimuthal mode as the equivalence ratio is decreased. Throughout this progression, the combustor exhibits various dynamical behaviors, including intermittency, dual-mode instability, standing azimuthal instability, and beating azimuthal instability. These dynamical states are determined from eight pressure transducers by decomposing the acoustic pressure fluctuations into clockwise and counterclockwise waves, enabling a reconstruction of the amplitude of acoustic pressure fluctuations, nature angle, nodal line location, and spin ratio. The global heat release response is also assessed during different dynamical states to contrast their behavior at different non-dimensional time steps by computing the phase-averaged fluctuations of the heat release rate over the acoustic pressure cycle. A number of differences were observed in the flame behavior depending on the direction of pressure wave propagation, demonstrating characteristic counterclockwise (CCW) spinning, standing, and clockwise (CW) spinning heat release patterns. Additionally, we quantify the flame-flame interaction during the various dynamical states.

In our final study, we present experimental observations and a synchronization model for the suppression of thermoacoustic instability achieved by rotating the otherwise static swirler in a lab-scale turbulent combustor. Starting with the state of thermoacoustic instability in the combustor, we find that a progressive increase in the swirler rotation rate leads to a transition from the state of limit cycle oscillations to low-amplitude aperiodic oscillations through a state of intermittency. To model such a transition while

also quantifying the underlying synchronization characteristics, we introduce feedback between the ensemble of phase oscillators and the acoustic field. The coupling strength in the model is carefully determined, taking into account the influence of both acoustic and actuating swirl frequencies. The link between the model and experimental results is quantitatively established by implementing an optimization algorithm for model parameter estimation. Remarkably, our model is capable of capturing the bifurcation characteristics, nonlinear features of the time series, the probability density function, and the amplitude spectrum of acoustic pressure and heat release rate fluctuations at various dynamical states observed during the transition to the state of suppression. Most importantly, we discuss the flame dynamics and demonstrate that the model without any spatial inputs qualitatively captures the characteristics of the spatiotemporal synchronization between the local heat release rate fluctuations and the acoustic pressure that underpins a transition to the state of suppression.



# CONTENTS

	<b>Page</b>
<b>ACKNOWLEDGEMENTS</b>	<b>i</b>
<b>ABSTRACT</b>	<b>v</b>
<b>LIST OF TABLES</b>	<b>xiii</b>
<b>LIST OF FIGURES</b>	<b>xv</b>
<b>GLOSSARY</b>	<b>xxv</b>
<b>ABBREVIATIONS</b>	<b>xxvii</b>
<b>NOTATION</b>	<b>xxix</b>
<b>CHAPTER 1 INTRODUCTION</b>	<b>1</b>
1.1 Combustion technologies in modern gas turbines . . . . .	1
1.2 Thermoacoustic instability phenomenon . . . . .	3
1.2.1 Thermoacoustic instability and its consequences . . . . .	3
1.2.2 Mechanism of thermoacoustic instability . . . . .	5
1.2.3 Origin of nonlinearities in thermoacoustics . . . . .	8
1.3 Longitudinal instability in thermoacoustic systems . . . . .	9
1.3.1 Bifurcations and transition to thermoacoustic instability . . . . .	9
1.3.2 Spatiotemporal dynamics of thermoacoustic systems . . . . .	15
1.4 Azimuthal and longitudinal instabilities in annular combustor . . . . .	17
1.4.1 Self-excited thermoacoustic modes in annular combustor . . . . .	17
1.4.2 Transition to azimuthal instabilities . . . . .	22
1.5 Suppression of thermoacoustic instabilities . . . . .	23
1.5.1 Active and passive control of thermoacoustic instabilities . . . . .	23
1.5.2 Recent strategies for mitigating thermoacoustic instabilities . . . . .	24
1.6 Theoretical analysis of thermoacoustic instabilities . . . . .	25
1.6.1 Time delay model . . . . .	26
1.6.2 FTF/FDF approach . . . . .	26
1.6.3 Kicked oscillator model . . . . .	27
1.6.4 Van der Pol type model with nonlinear terms . . . . .	28
1.7 Objective of the current work . . . . .	29
1.8 Overview of the thesis . . . . .	31
<b>CHAPTER 2 EXPERIMENTAL SETUPS AND DIAGNOSTICS</b>	<b>33</b>
2.1 Annular combustor facility . . . . .	33
2.1.1 Longitudinal thermoacoustic instability in annular combustor . . . . .	35
2.1.2 Azimuthal thermoacoustic instability in annular combustor . . . . .	37

2.2	Turbulent dump combustor . . . . .	38
2.2.1	Bluff-body stabilized configuration . . . . .	39
2.2.2	Swirl-stabilized configuration . . . . .	40
2.3	Rotating swirler combustor . . . . .	41
<b>CHAPTER 3 CRITICALITY OF BIFURCATION IN ANNULAR COMBUSTOR</b>		<b>45</b>
3.1	Routes to longitudinal thermoacoustic instability . . . . .	45
3.1.1	Transition to thermoacoustic instability through continuous bifurcation	46
3.1.2	Transition to thermoacoustic instability through abrupt bifurcation . . .	47
3.1.3	Transition to thermoacoustic instability through mixed-mode oscillations	49
3.2	The crossover of bifurcation . . . . .	51
3.2.1	Change of criticality across two-parameter family . . . . .	51
3.2.2	Stability map of the combustor . . . . .	53
3.3	Flame dynamics during the thermoacoustic transitions . . . . .	54
3.4	Quantification of flame-flame and flame-acoustic interactions . . . . .	64
3.5	Interim summary . . . . .	67
<b>CHAPTER 4 MODELING CRITICALITY OF BIFURCATION IN THERMOACOUSTIC SYSTEMS</b>		<b>69</b>
4.1	Governing equation for the acoustic field . . . . .	70
4.2	Modeling heat release rate using nonlinear functions . . . . .	71
4.3	Mean-field synchronization model for thermoacoustic transitions . . . . .	75
4.3.1	Phase-oscillator based heat release rate model . . . . .	75
4.3.2	Flame-acoustic coupling . . . . .	77
4.3.3	Slow flow amplitude and phase representation of the mean-field model .	77
4.3.4	Limit cycle solution . . . . .	80
4.4	Numerical simulation for the mean-field model . . . . .	81
4.4.1	Initialization and bifurcation analysis . . . . .	82
4.4.2	Parametric identification . . . . .	82
4.5	Model prediction of transitions to thermoacoustic instability . . . . .	85
4.5.1	Continuous transition to thermoacoustic instability . . . . .	85
4.5.2	Secondary bifurcation to high-amplitude thermoacoustic instability . . .	88
4.5.3	Relation between the control parameters in experiments and model . . . .	91
4.6	Continuous and explosive synchronization transition to thermoacoustic instability . . . . .	93
4.7	Interim summary . . . . .	103
<b>CHAPTER 5 INTERMITTENCY TRANSITION TO AZIMUTHAL INSTABILITIES IN ANNULAR COMBUSTOR</b>		<b>105</b>
5.1	Characterization of azimuthal modes . . . . .	105
5.2	Determination of azimuthal mode from our experiments . . . . .	107
5.3	Route to azimuthal thermoacoustic instability . . . . .	109
5.4	Azimuthal modal dynamics during the thermoacoustic transition . . . . .	113

5.5	Characterizing dynamical states during the transition to azimuthal thermoacoustic instability . . . . .	114
5.6	Flame dynamics during the transition to azimuthal thermoacoustic instability . . . . .	121
5.7	Quantify flame-flame interactions during different dynamical states . . .	127
5.8	Interim summary . . . . .	130
<b>CHAPTER 6</b>	<b>SUPPRESSING THERMOACOUSTIC INSTABILITY BY ACTUATING SWIRLER</b>	<b>133</b>
6.1	Characterizing the rotating swirler combustor . . . . .	133
6.2	Flame dynamics during the transition to suppression state . . . . .	135
6.3	Spatiotemporal behavior during the transition to suppression state . . .	137
6.4	Theoretical model for suppression of thermoacoustic instability . . . .	139
6.5	Model prediction of transition to suppression state . . . . .	140
6.5.1	Bifurcation diagram during the transition to suppression . . . . .	141
6.5.2	Characterizing various dynamical states . . . . .	142
6.5.3	Relation between the coupling strength and swirler rotation rate . . . .	145
6.6	Synchronization transition to suppression state . . . . .	146
6.7	Characterization of the nonlinear time series . . . . .	149
6.8	Interim summary . . . . .	153
<b>CHAPTER 7</b>	<b>CONCLUSION AND OUTLOOK</b>	<b>155</b>
7.0.1	Future directions . . . . .	157
<b>APPENDIX A</b>	<b>VERIFYING LONGITUDINAL INSTABILITY IN THE ANNULAR COMBUSTOR</b>	<b>161</b>
<b>APPENDIX B</b>	<b>NUMERICAL PROCEDURE FOR SAMPLING OSCILLATOR FREQUENCY DISTRIBUTION FROM EXPERIMENTAL DATA</b>	<b>163</b>
<b>APPENDIX C</b>	<b>CHOOSING OPTIMAL NUMBER OF PHASE OSCILLATORS</b>	<b>165</b>
<b>APPENDIX D</b>	<b>PARAMETER OPTIMISATION WITH RANDOM INITIAL CONDITIONS</b>	<b>167</b>
<b>APPENDIX E</b>	<b>SENSITIVITY ANALYSIS OF PARAMETER ESTIMATION</b>	<b>171</b>
E.1	Parameter sensitivity during the transition to thermoacoustic instability	171
E.2	Parameter sensitivity during the transition to suppression state . . . . .	172
<b>APPENDIX F</b>	<b>IDENTIFYING THE TYPE OF INTERMITTENCY IN OUR COMBUSTORS</b>	<b>175</b>
<b>APPENDIX G</b>	<b>MEAN-FIELD SYNCHRONIZATION MODEL WITH STOCHASTIC FORCING</b>	<b>179</b>

<b>APPENDIX H</b>	<b>EXTRACTING ORDER PARAMETER FROM SPATIOTEMPORAL EXPERIMENTAL DATA</b>	<b>181</b>
<b>APPENDIX I</b>	<b>ESTIMATED MODEL PARAMETERS FROM EXPERIMENTS</b>	<b>183</b>
I.1	Estimated parameter values during thermoacoustic transition . . . . .	183
I.2	Estimated parameter values during the transition to suppression state . .	184
	<b>REFERENCES</b>	<b>185</b>
	<b>CURRICULUM VITAE</b>	<b>203</b>
	<b>DOCTORAL COMMITTEE</b>	<b>205</b>

# LIST OF TABLES

<b>Table</b>	<b>Caption</b>	<b>Page</b>
2.1	Relevant properties of an annular combustor considered in this study for self-excited azimuthal instability. . . . .	38
2.2	Relevant properties of the turbulent combustors considered in this study for self-excited longitudinal instability. . . . .	40
2.3	Relevant properties of the turbulent combustor considered in this study for suppressing thermoacoustic instability. . . . .	42
I.1	Parameter estimated for states observed in the bluff-body combustor and marked as b-d in figure 4.3. . . . .	183
I.2	Parameter estimated for states observed in the swirl-stabilized combustor. . . . .	183
I.3	Parameter estimated for different states observed in the annular combustor and marked as a-d in figure 4.5. . . . .	184
I.4	Estimated parameter values in the rotating swirler combustor for different states marked as a-c in figure 6.5. . . . .	184



# LIST OF FIGURES

Figure	Caption	Page
1.1	Effect of equivalence ratio on NOx production and susceptibility to thermoacoustic instability. Adapted from Zhao (2023) with permission from Elsevier. . . . .	2
1.2	Combustion chamber assembly of the gas turbine engine (a) damaged by large amplitude thermoacoustic instability and (b) a new burner assembly. Adapted from Lieuwen and Yang (2005) with permission from AIAA. . . . .	4
1.3	Schematic of the positive feedback loop formed between the unsteady flame and the acoustic field within the combustor responsible for driving self-excited thermoacoustic instabilities. . . . .	6
1.4	Normal form of (a) supercritical Hopf, (b) subcritical Hopf, and (c) secondary bifurcation for a Van der Pol oscillators with nonlinear terms depicting the change in the nature of a bifurcation as a function of control parameter $\mu_0$ . Adapted from Ananthkrishnan <i>et al.</i> (1998) with permission from Elsevier. . . . .	10
1.5	Typical bifurcation diagram showing amplitude of acoustic pressure fluctuations ( $p'_{rms}$ ) as a function of the equivalence ratio ( $\phi$ ). State (i) corresponds to the state of combustion noise, (ii-v) intermittency, and (vi) thermoacoustic instability. The bifurcation and associated dynamical states are observed in a bluff-body stabilized combustor. Figure is adapted from George <i>et al.</i> (2018) with permission from Cambridge University Press. . . . .	12
1.6	Time series of acoustic pressure oscillations $p'$ inside the matrix burner during the state of (a) stable operation, (b) bursting oscillations, (c-e) mixed-mode oscillations, and (f) thermoacoustic instability. Figure is adapted from Kasthuri <i>et al.</i> (2019) with permission from the American Institute of Physics. . . . .	14
1.7	Illustration of the emergence of global phase synchronization during the transition from (a) combustion noise, followed by (b) intermittency to (c) thermoacoustic instability in a bluff-body turbulent combustor. Spatial view of the combustor showing the instantaneous phase difference ( $\psi$ ) between the acoustic pressure ( $\Phi$ ) and heat release rate ( $\theta_i$ ) oscillations. Adapted with permission from Mondal <i>et al.</i> (2017b), courtesy of Cambridge University Press. . . . .	15
1.8	First lab-scale atmospheric annular combustors to exhibit self-sustained azimuthal instabilities at (a) Cambridge University (Worth and Dawson, 2013a,b) and (b) EM2C laboratory. Reproduced from (a) Worth and Dawson (2013a) and (b) Bourgouin <i>et al.</i> (2013) with permission from Elsevier and ASME, respectively. . . . .	18

2.1	(a) Photograph of the annular combustor rig at IIT Madras, Chennai. Schematic of the (b) cross-section of the combustor, (c) the burner tube, and (d) the dump plane. The location of the eight pressure transducers is named as PC1, PC2, ..., PC8. The non-premixed pilot flame is used to ignite the sixteen flames in the combustion chamber. Eight flames are acquired during the longitudinal instability, while sixteen flames are acquired during the azimuthal instability. . . . .	34
2.2	(a) Schematic of the dump combustor. (b) Schematic of the combustor cross-section indicating the chemiluminescence field of view. We use two different flame-holding mechanisms, (c) a bluff-body and (d) swirl, attached to the burner by a central shaft. The shaded area in (b) is captured using CH* imaging. The box in (b) is the region chosen for synchronization analysis. The experiments on a bluff-body configuration were conducted by Dr. Manikandan Raghunathan and a swirl-stabilized configuration by Dr. Induja Pavithran under the guidance of Prof. R. I. Sujith at IIT Madras, Chennai. . . . .	39
2.3	A schematic of the experimental setup used for suppressing thermoacoustic instability along with the diagnostic tools. The swirler is actuated using the stepper motor for mitigation of thermoacoustic instability. The experiments were performed in the Turbulent Combustion and Spray Research Lab at IISC, Bangalore. . . . .	41
3.1	Transition from combustion noise (CN) to thermoacoustic instability (TAI) when $\phi$ is increased ( $\square$ ) for $v_z \approx 6.09$ m/s. Region I to III corresponds to the states of CN, intermittency, TAI. . . . .	46
3.2	Observed transition from combustion noise (CN) to thermoacoustic instability (TAI) when $\phi$ is increased ( $\square$ ) and back to CN when $\phi$ is decreased ( $\blacktriangledown$ ) for $v_z \approx 8.51$ m/s. Region I to V correspond to the states of CN, intermittency, low-amplitude TAI, high-amplitude TAI and bistable region (hatched region). . . . .	47
3.3	Time series and the power spectrum of pressure fluctuations observed during the states of (a,b) combustion noise (CN), (c,d) intermittency (INT), (e,f) low-amplitude TAI, and (g,h) high-amplitude TAI for $v_z \approx 8.51$ m/s. Experimental conditions: (a, b) $\phi = 0.44$ , (c, d) $\phi = 0.48$ , (e, f) $\phi = 0.49$ , and (g, h) $\phi = 0.5$ . . . . .	48
3.4	Transition from CN to high-amplitude TAI when $\phi$ is varied for $v_z \approx 7.3$ m/s. The transition from low-amplitude TAI to high-amplitude TAI takes place through MMO. Region I to V corresponds to CN, intermittency, low-amplitude TAI, MMO, and high-amplitude TAI. . . . .	49
3.5	(a,b) Time series of $p'$ (orange) and $\dot{q}'$ (blue), and the corresponding amplitude spectrum during MMO at $\phi = 0.54$ . . . . .	50
3.6	(a) Change in criticalities of bifurcations to the state of TAI when $v_z$ and $\phi$ are sequentially varied. The forward path is indicated by $\square$ and the backward path by $\blacktriangledown$ . (b) Interpolated stability map of the system. $\triangle$ Hopf point, $\times$ intermittent dynamics, $\square$ secondary bifurcation point, $\nabla$ fold point. A dashed line indicates an extrapolated boundary. The frequency of the oscillations was in the range of 215 – 230 Hz. . . . .	52

3.7	(a) Time series of acoustic pressure oscillations obtained during intermittency observed at $\phi = 0.47$ . (b) Aperiodic and (c) periodic part of intermittency. (d-g) Mean-subtracted instantaneous chemiluminescence images corresponding to the indicated points in the aperiodic region in (b). (h,i) Phase-averaged chemiluminescence image at the pressure maxima ( $90^\circ$ ) and minima ( $270^\circ$ ) measured from the points indicated in (c). . . . .	54
3.8	(a) Periodic part of intermittency observed at $\phi = 0.47$ . Temporal variation of (b) normalized amplitude and (c) phase difference (in deg) of HRR between burners and burner pairs. . . . .	57
3.9	(a) Time series of $p'$ during low-amplitude TAI at $\phi = 0.49$ . Phase-averaged CH* images at pressure (b) maxima ( $90^\circ$ ), (c) mean ( $0^\circ$ ) and (d) minima ( $270^\circ$ ) value. (e) Variation in the normalized amplitude of $\dot{q}'$ for each burner measured from each of the flames. (f) Relative phase (in degrees) evolution between $\dot{q}'$ measured from the indicated pair of burners. . . . .	58
3.10	(a) Time series of $p'$ during high-amplitude TAI at $\phi = 0.52$ . Phase-averaged CH* images at pressure (b) maxima ( $90^\circ$ ), (c) mean ( $0^\circ$ ), and (d) minima ( $270^\circ$ ) value. (e) Variation in the normalized amplitude of $\dot{q}'$ for each burner measured from each of the flames. (f) Relative phase (in degrees) evolution between $\dot{q}'$ measured from the indicated pair of burners. . . . .	60
3.11	Phase-averaged CH* chemiluminescence images at (a) pressure maxima ( $90^\circ$ ) and (b) pressure minima ( $270^\circ$ ) during epochs of high-amplitude oscillations in MMO, and (c) pressure maxima ( $90^\circ$ ) and (d) pressure minima ( $270^\circ$ ) during epochs of low-amplitude oscillations in MMO. This experimental investigation was conducted under the condition of $\phi = 0.54$ . . . . .	61
3.12	(a) Enlarged portion of $p'$ during MMO at $\phi = 0.54$ . (b) Temporal variation in the normalized amplitude of heat release rate ( $\sin \theta_k$ ) measured from all the burners. (c) Temporal variation in the relative phase (in degrees) from the indicated pair of burners. . . . .	62
3.13	(a) Low-amplitude pressure oscillations over one cycle during the state of MMO. (b-f) Portion of CH* images depicting the flame-flame interaction between burner pairs 2-3 and 6-7 corresponding to the points marked in (a). (g) High-amplitude pressure oscillations over one cycle during the state of MMO and (h-l) the corresponding CH* images. . . . .	64
3.14	Phase-locking value (PLV) between (a) $\dot{q}'$ measured from individual burners, and between (b) $\dot{q}'$ from each burner and $p'$ during combustion noise (CN), intermittency (INT) at $\phi = 0.47$ , low amplitude TAI at $\phi = 0.49$ , and high-amplitude TAI at $\phi = 0.52$ , respectively. (c) Kuramoto order parameter ( $R$ ) determined from the eight burners during different states of combustor operation. . . . .	66
3.15	Temporal variation in the Kuramoto order parameter ( $R$ ) measured from the eight flames during mixed-mode oscillations (MMO) at $\phi = 0.54$ . . . . .	67
4.1	(a) Change of criticalities of bifurcations observed from the model in Eq. (4.7) and the corresponding (b) stability diagram. . . . .	74

4.2	Frequency distribution $g(\omega)$ of $N = 2 \times 10^3$ phase oscillators obtained from the amplitude spectrum of heat release rate during the state of combustion noise for the (a) bluff-body stabilized dump combustor, (b) swirl-stabilized dump combustor and (c) annular combustor. Here, $\omega$ is distributed relative to the acoustic frequency $\tilde{\Omega}_0$ and also normalized by $\tilde{\Omega}_0$ . . . . .	83
4.3	Continuous transition to thermoacoustic instability through the state of intermittency observed in the bluff-body stabilized combustor. (a) Comparison of the normalized amplitude $p'_{\text{rms}}$ obtained from the experiments ( $\square$ ) and model ( $-$ ) as a function of the equivalence ratio ( $\phi$ ) and the model parameter ( $K$ ). The time series ( $p'$ , $\dot{q}'$ ), probability distribution function [ $\mathcal{P}(p')$ , $\mathcal{P}(\dot{q}')$ ] and amplitude spectrum [ $ \hat{p}(f) $ , $ \hat{q}(f) $ ] are shown during the states of (b) combustion noise ( $\phi = 0.86$ , $K = 0.23$ ), (c) intermittency ( $\phi = 0.72$ , $K = 0.75$ ) and (d) thermoacoustic instability ( $\phi = 0.56$ , $K = 2$ ). In panels (b-d) the experimental data are shown using a lighter shade, while the model result is shown using a darker shade. Only the envelope of the time series from the model is shown for clarity. . . . .	87
4.4	Abrupt secondary bifurcation to limit cycle oscillations in (a) swirl-stabilized dump combustor and (b) annular combustor. The bifurcation plots illustrate the comparison of the normalized amplitude $p'_{\text{rms}}$ obtained from the experiments ( $\square$ ) and the model ( $-$ ) as a function of equivalence ratio ( $\phi$ ) and the model parameter ( $K$ ). The forward and reverse transitions in the experiments are indicated as ( $\square$ ) and ( $\blacksquare$ ), while in the model are indicated as ( $-$ ) and ( $-$ ), respectively. In panel (b), heat release rate data is available only at the four points indicated by ( $\square$ ). For the remaining points (depicted by $\blacksquare$ ) only pressure data is available, we interpolated these points from the optimisation at the four points shown in figure 4.6. . . . .	88
4.5	Representative states observed during secondary bifurcation in the annular combustor. The time series ( $p'$ , $\dot{q}'$ ), probability distribution function [ $\mathcal{P}(p')$ , $\mathcal{P}(\dot{q}')$ ] and amplitude spectrum [ $ \hat{p}(f) $ , $ \hat{q}(f) $ ] are shown during the states of (a) combustion noise ( $\phi = 0.44$ , $K = 1.09$ ), (b) intermittency ( $\phi = 0.47$ , $K = 1.37$ ), (c) low-amplitude thermoacoustic instability ( $\phi = 0.49$ , $K = 1.55$ ) and (d) high-amplitude thermoacoustic instability ( $\phi = 0.52$ , $K = 1.71$ ). The experimental data are shown using a lighter shade, while the model result is shown using darker shade. . . . .	90

4.6	Correspondence between the control parameter in the model ( $K$ ) and experiments ( $\phi$ ) obtained using gradient descent optimisation for the (a) bluff-body stabilized dump combustor, (b) swirl-stabilized dump combustor, and (c) annular combustor. For all the cases, we obtain a linear relation between $\phi$ and $K$ where the fits are: (a) $K = -5.35\phi + 4.68$ , (b) $K = -4.85\phi + 4.28$ and (c) $K = 8.59\phi - 2.66$ . The goodness-of-fit corresponding to different combustors is 0.95, 0.94, and 0.96, respectively. The arrows in each panel indicate the direction in which $\phi$ was varied in experiments. In panel (c), heat release rate data were obtained only at four points. The remaining points were interpolated. Error bars correspond to the standard deviation in the estimation of $K$ by sliding the window used during optimisation (Appendix E.1). . . . .	91
4.7	Emergence of global phase synchronization during the transition to thermoacoustic instability in a bluff-body combustor (a-c) and annular combustor (d-f). Spatial view of the combustor showing the instantaneous (phasors, $\psi_l$ ) and time-averaged (colormap, $\langle\psi_l\rangle$ ) phase difference between the acoustic pressure ( $\Phi$ ) and heat release rate ( $\theta_l$ ) oscillations. Phasors have been colored as blue if $ \psi  < \pi/2$ (Rayleigh criteria) and red otherwise to delineate local acoustic power sources from sinks. The phase of pressure oscillations remains spatially uniform as the cases correspond to the longitudinal instability. The probability distribution of the relative phase $\mathcal{P}(\psi_l)$ for each state has also been shown to highlight the appearance of global phase synchronization during thermoacoustic instability. The experimental conditions for the bluff-body and annular combustor correspond to the states shown in figure 4.3 and figure 4.5, respectively. . . . .	94
4.8	The variation of time-averaged Kuramoto order parameter $\bar{r}$ in Eq. (4.38) as a function of coupling strength $K$ shows (a) a continuous <i>second-order</i> synchronization transition for the bluff-body stabilized combustor and (b) abrupt <i>first-order</i> explosive synchronization transition for the annular combustor. Panels (c-j) depict the instantaneous oscillator distribution in the $\dot{\theta}_l - \psi_l$ phase space along with the distribution $\mathcal{P}(\dot{\theta}_l)$ representative of various dynamical states indicated in panels (a) and (b). Here, $\dot{\theta}_l$ is the normalized frequency of the $l^{\text{th}}$ oscillator, and $\psi_l$ is the relative phase of the oscillator obtained by subtracting the phase of the heat release rate oscillator by phase of the acoustic pressure. In panels (c-f), the distribution of oscillators obtained from spatiotemporal imaging of the combustors is depicted using a pink shade, while the oscillators from the mean-field model using a blue shade. . . . .	97

4.9	Polar plot in the co-rotating frame showing the variation in the instantaneous distribution of relative phases ( $\psi_l$ ) between the phase of the oscillators ( $\theta_l$ ) and acoustic pressure ( $\Phi$ ) obtained from the experiments (dark shade) and model (light shade) during (g) combustion noise, (h) intermittency, (i) low-amplitude and (j) high-amplitude thermoacoustic instability. The representative states correspond to the points indicated in figure 4.8b observed during the abrupt <i>first-order</i> explosive synchronization in the annular combustor. Averaged relative phase from the experiments and the model are indicated using $\langle\psi_e\rangle$ and $\langle\psi_m\rangle$ along with the Kuramoto order parameter ( $r$ ) showing the level of synchrony among the oscillators, respectively. The dashed line indicates the reference phase of the acoustic pressure oscillations ( $\Phi$ ). . . . .	100
5.1	Poincaré-Bloch sphere representation of the azimuthal mode in the quaternion formalism. The amplitude $A$ corresponds to the radius, $2\chi$ the latitude and $\theta$ the longitude. Thermoacoustic states at the poles correspond to spinning modes, standing modes are located near the equator and mixed modes at intermediate latitudes. . . . .	108
5.2	Observed transition from a state of combustion noise to azimuthal thermoacoustic instability in a turbulent annular combustor. (a) The variation of $A$ and (b) the frequency of $p'$ from position PC2 as a function of equivalence ratio ( $\phi$ ). Time traces and the sound pressure level of the acoustic pressure fluctuations ( $p'$ ) from eight equispaced pressure sensors during (c) combustion noise, (d) intermittency, (e) dual-mode instability, (f) standing azimuthal instability, and (g) beating azimuthal instability. The transition involves a frequency shift – from a low frequency associated with the longitudinal mode to a higher frequency associated with the azimuthal mode. Experimental conditions: (c) $\phi = 1.38$ , (d) $\phi = 1.32$ , (e) $\phi = 1.28$ , (f) $\phi = 1.20$ , and (g) $\phi = 1.14$ . . . . .	110
5.3	The variation in the distribution of spin ratio ( $SR$ ) as a function of equivalence ratio ( $\phi$ ) indicates the change in the azimuthal mode dynamics during the thermoacoustic transition. . . . .	113
5.4	(a,b) Evolution of time series and scalogram of the acoustic pressure oscillations during the dual-mode instability at $\phi = 1.28$ . (c) and (d) Selected windows in the pressure time series are bandpass filtered in the range [250, 350] Hz and [734, 834] Hz, respectively. (e) and (f) Probability density function of the phase difference ( $\mathcal{P}(\Delta\Psi)$ ) of all pressure signals with respect to the signal in PC2. . . . .	115
5.5	Evolution of (a) amplitude ( $A$ ), (b) nature angle ( $\chi$ ), (c) orientation angle ( $\theta$ ), and (d) spin ratio ( $SR$ ) exacted using time series of $p'$ during the azimuthal mode of dual-mode instability. . . . .	116
5.6	(a) Time series of the acoustic pressure along with the slowly varying amplitude ( $A$ ) and (b) corresponding scalogram during the pure standing azimuthal instability at $\phi = 1.20$ . (c-e) Evolution of nature angle ( $\chi$ ), orientation angle ( $\theta$ ), and spin ratio ( $SR$ ) defining the dynamical state of the azimuthal thermoacoustic mode. . . . .	118

5.7	(a) Time series of the acoustic pressure along with the slowly varying amplitude ( $A$ ) and (b) corresponding scalogram during the beating azimuthal instability at $\phi = 1.14$ . (c-e) Evolution of nature angle ( $\chi$ ), orientation angle ( $\theta$ ), and spin ratio ( $SR$ ) defining the dynamical state of the azimuthal thermoacoustic mode. . . . .	120
5.8	Phase-averaged global heat release rate viewed from above the annulus in two distinct scenarios: (a-b) during the pressure maxima and minima associated with the longitudinal mode of the dual-mode instability, and (c-d) $\psi = 1/6$ and $\psi = 2/3$ in the acoustic cycle associated with the azimuthal mode of the dual-mode instability. The white line represents the nodal line. This experimental investigation was conducted under the condition of $\phi = 1.28$ . . . . .	121
5.9	Phase-averaged chemiluminescence images at six normalized time steps ( $\psi$ ) in the acoustic cycle during the pure standing azimuthal instability. Phase averaging is conducted across the time trace of acoustic pressure fluctuations in the interval from 1.05 s to 1.15 s. The white line represents the nodal line. This experimental investigation was conducted under the condition of $\phi = 1.20$ . . . . .	123
5.10	Time traces of acoustic pressure oscillations and associated phase-averaged chemiluminescence images at six normalized positions in the acoustic pressure cycle ( $\psi$ ) during the epochs of (I) counterclockwise spinning mode ( $SR = 1$ ), (II) standing azimuthal mode ( $SR = 0$ ), and (III) clockwise spinning mode ( $SR = -1$ ) in the beating azimuthal instability. This experimental investigation was conducted with $\phi = 1.14$ . . . . .	126
5.11	Distribution of the normalized phase difference of heat release rate fluctuations from flames is examined as a function of burner number during the (a) longitudinal and (b) azimuthal modes of the dual-mode instability. . . . .	127
5.12	Distribution of the normalized phase difference of heat release rate fluctuations from all the flames in the annular combustor is examined across burners during the pure standing azimuthal instability. . . . .	128
5.13	Distribution of the normalized phase difference of heat release rate fluctuations from all the flames is examined across burners during the epochs of (a) CCW spinning wave, (b) standing wave, and (c) CW spinning wave. . . . .	130
6.1	(a) Variation of the acoustic pressure amplitude of the first dominant mode as a function of the swirler rotation rate, depicting the suppression of thermoacoustic instability. (b) The frequency corresponding to the acoustic mode as a function of the swirler rotation rate. The error bar in (a) is associated with the variation of the amplitudes across three experimental runs. . . . .	134

6.2	Mean-subtracted phase-averaged flame images at pressure maxima (left) and minima (right) during the dynamical states: (a-b) thermoacoustic instability, (c-d) periodic epochs of intermittency, and (e-f) suppression state. The flame image depicting a well-defined circular shape with very high intensity during thermoacoustic instability transitions to non-uniform flame structures with low intensity during the state of suppression.	136
6.3	Disruption of order on varying the swirler rotation rate ( $\tilde{\Omega}_r$ ) from 0 to 2100 rpm in the turbulent combustor. A typical snapshot of the spatially distributed phasors ( $\psi_l$ ) is obtained by taking the phase difference between the local heat release rate ( $\theta_l$ ) and acoustic oscillations ( $\Phi$ ) during the state of (a) thermoacoustic instability, (b) intermittency, and (c) suppression. To delineate regions of acoustic power sources and sinks, phasors have been colored blue if $ \psi_l  < \pi/2$ and red otherwise.	138
6.4	Oscillator frequency distribution $g(\omega)$ as a function of $\omega$ obtained from the heat release rate spectrum during a state of suppression. $\omega$ is the normalized frequency centered around the acoustic frequency.	140
6.5	Comparison of the bifurcation diagrams obtained from the model (—) and experiments ( $\square$ ). The plot depicts the variation of the normalized $p'_{\text{rms}}$ as a function of the non-dimensional swirler rotation rate ( $\Omega_r$ ).	141
6.6	Comparison of the time trace, probability density function and amplitude spectrum of $p'$ obtained from experiments (lighter shade) and that obtained from our model (darker shade) during the states of (a) thermoacoustic instability, (b) intermittency, and (c) suppression. (a-c) corresponds to the markers shown in figure 6.5. The envelope of the time series from the model is shown in the first column for clarity.	143
6.7	Comparison of the time trace, probability density function and amplitude spectrum of $\dot{q}'$ obtained from experiments (lighter shade) and that obtained from our model (darker shade) during the states of (a) thermoacoustic instability, (b) intermittency, and (c) suppression. (a-c) corresponds to the markers shown in figure 6.5. Only the envelope of the time series from the model is shown.	144
6.8	Mapping between the swirler rotation rate ( $\Omega_r$ ) and coupling strength ( $K$ ) during a transition to the state of suppression. The relation between $\Omega_r$ and $K$ is: $K = 4.1(0.71 - \Omega_r)$ with the goodness-of-fit as 0.99. The error bars represent the standard deviation in estimating $K$ by sliding the window of the time series used during optimization (Appendix E.2).	145
6.9	The synchronization bifurcation diagram depicts the variation of time-averaged order parameter ( $\bar{r}$ ) as a function of non-dimensional swirler rotation rate ( $\Omega_r$ )	147
6.10	The typical instantaneous oscillator distribution in the $\hat{\theta}_l - \psi_l$ plane, as well as the distribution of $\mathcal{P}(\hat{\theta}_l)$ and $\mathcal{P}(\psi_l)$ during the state of (a) thermoacoustic instability, (b) intermittency, and (c) suppression for experimental (lighter marker) and modeling (darker marker) dataset. The Kuramoto order parameter ( $r$ ) from the experiments and model (—) is shown in the last column.	148

6.11	Comparison of the (a) permutation entropy ( $H_p$ ) and (b) recurrence rate ( $RR$ ) of dynamics as a function of swirler rotation rate ( $\Omega_r$ ) obtained from the model (–) and experiments ( $\square$ ) during the transition to suppression state in the rotating swirler combustor. . . . .	151
A.1	Observed dominant frequency in the annular combustor as a function of the equivalence ratio and correspond to the condition reported in figure 4.4(b). Comparison of (b, c) time series, (d, e) phase difference obtained from three pressure transducers on the combustor backplane during low-amplitude and high-amplitude TAI. . . . .	161
C.1	Test for convergence of dynamics when the number of phase oscillators is varied. The standard deviation $\nu$ is obtained from 20 simulations for each $N$ . . . . .	165
D.1	Comparison of time series, probability density function, amplitude spectrum of $p'$ obtained from model (b-d) with the experimental observations (a) during the state of intermittency in the bluff-body stabilized combustor. In the model, (b) is obtained by optimising the parameter vector ( $\mathbb{P}$ ), and (c-d) are obtained for randomly chosen initial conditions, with the optimised value of $K$ and $\zeta$ as 0.75 and 0.6, respectively. In (c), the initial conditions are $\eta(0) = 0.22$ , $\dot{\eta}(0) = 0.09$ and $\theta_l(0) = 0.5 + \mathcal{N}(0, 0.1)$ and in (d) the initial conditions are $\eta(0) = 0.1$ , $\dot{\eta}(0) = 0.12$ and $\theta_l(0) = 0.5 + \mathcal{N}(0, 0.1)$ . . . . .	167
D.2	The bifurcation plot illustrates the comparison of the amplitude of acoustic pressure obtained from the model and experiments as a function of the control parameter ( $K, \phi$ ). For each $K$ , 10 iterations are performed with different sets of initial conditions. The evaluation indicates the initial conditions do not exert any influence on the dynamical states. . . . .	168
D.3	Comparison of the $K - \phi$ relationship obtained through the optimisation of only the coupling strength ( $K$ ) with the optimisation of both $K$ and initial conditions ( $\eta(0), \dot{\eta}(0), \theta_l(0)$ ). . . . .	169
E.1	Convergence of parameter optimisation algorithm. Panel (a) shows the variation in the estimated coupling strength ( $K$ ) as a function of the size of the time window ( $t_w$ ) used for optimising the loss function $\mathcal{L}(\mathbb{P})$ for a fixed number of 1000 iterations. (b) Realisation of the minimisation scheme showing a change in the difference $\mathcal{L}_{i+1} - \mathcal{L}_i$ when the optimisation is performed with an initial value of $K = 0.25$ over 1000 iterations during the state of combustion noise in bluff-body stabilized combustor. . . . .	171

E.2	Panel (a) depicts the convergence of the coupling strength ( $K$ ) as a function of the time window width ( $t_{\text{win}}$ ) of the time series of $\mathbf{Y}_{\text{model}}$ and $\mathbf{Y}_{\text{exp}}$ over 500 iterations using the parameter optimization algorithm. The initial value of $K$ used is 1.2 and $t_{\text{win}}$ is varied from 0.05 to 1 s. Panel (b) shows optimization of $K$ by minimizing the loss function ( $\mathcal{L}_i$ ) over 500 iterations by taking difference between $\mathcal{L}_{i+1}$ and $\mathcal{L}_i$ . The sensitivity analysis on parameter estimation shown here is carried out during the state of suppression. . . . .	172
F.1	Illustration of the acoustic pressure signal during the state of intermittency consisting of low-amplitude aperiodic fluctuations (turbulent phases) interspersed between high-amplitude periodic oscillations (laminar phases). A threshold marks the delineation between the two phases, distinguishing high-amplitude periodic oscillations from low-amplitude aperiodic fluctuations. . . . .	176
F.2	Probability distribution of the length of turbulent phases observed in (a) Pawar <i>et al.</i> (2016), (b) experiments and mean-field model corresponding to the bluff-body stabilized combustor, and (c) experiments and mean-field model corresponding to the annular combustor. The distributions exhibit an exponential tail characteristic of type-II intermittency. . . . .	177
F.3	A log–log plot of the average length of turbulent phases ( $\langle T \rangle$ ) plotted against the control parameter, demonstrating the scaling law behavior characteristic of type-II intermittency in (a) Pawar <i>et al.</i> (2016), and (b) experimental data (bluff-body stabilized combustor) and (c) model simulations. . . . .	178
G.1	Comparison of time series, probability distribution function and amplitude spectrum of $p'$ and $q'$ obtained from model with stochastic noise term with the experimental observations. The comparison is shown during the states of (a) combustion noise ( $K \approx 0.21$ ), (b) intermittency ( $K \approx 0.73$ ), and (c) thermoacoustic instability ( $K \approx 1.94$ ). The value of damping coefficient ( $\zeta$ ) is 0.6 obtained using parameter optimisation during combustion noise and the initial conditions ( $\eta(0), \dot{\eta}(0), \theta_l(0)$ ) are chosen randomly and noise intensity as 0.1. . . . .	179

# GLOSSARY

<b>Intermittency</b>	Dynamical state consisting of a random switching between periodic and aperiodic fluctuations.
<b>Lean combustion</b>	Combustion of fuel in the presence of excess amount of air/oxidizer.
<b>Limit Cycle Oscillations</b>	Oscillations corresponding to a closed trajectory in phase space with the characteristic that at least one other trajectory spirals into it as time approaches infinity or negative infinity.
<b>Mixed-mode oscillations</b>	Periodic alternation between the epochs of high-amplitude and low-amplitude limit cycle oscillations.
<b>Premixed combustion</b>	Combustion of a mixture of fuel and oxidizer after undergoing thorough mixing.
<b>Thermoacoustic instability</b>	Self-sustaining periodic oscillations in acoustic pressure and velocity occur due to the interplay between the sound waves in confinement with the unsteady heat release rate caused by combustion.



# ABBREVIATIONS

<b>CN</b>	Combustion Noise.
<b>FDF</b>	Flame Describing Function.
<b>FTF</b>	Flame Transfer Function.
<b>HRR</b>	Heat Release Rate.
<b>INT</b>	Intermittency.
<b>LCO</b>	Limit Cycle Oscillations.
<b>LPG</b>	Liquefied Petroleum Gas.
<b>MFC</b>	Mass Flow Controllers.
<b>MMO</b>	Mixed-mode Oscillations.
<b>NO<sub>x</sub></b>	NO <sub>x</sub> Oxides of NO and NO <sub>2</sub> .
<b>PDF</b>	Probability Density Function.
<b>PLV</b>	Phase Locking Value.
<b>PM</b>	Particulate Matter.
<b>RMS</b>	Root Mean Square.
<b>RQL</b>	Rich-burn Quick-quench Lean-burn.
<b>TAI</b>	Thermoacoustic Instability.
<b>UHC</b>	Unburned Hydrocarbons.



## NOTATION

$\Delta\phi_{ij}$	Phase difference between heat release rate fluctuations from two burners labeled as $i$ and $j$
$\dot{\theta}_l$	Normalized frequency of $l^{\text{th}}$ oscillator
$\dot{m}_a$	Air flow rate
$\dot{m}_f$	Fuel flow rate
$\dot{q}'(t)$	Temporal variation of global heat release rate fluctuations
$\dot{q}'(x, y, t)$	Spatiotemporal variation of heat release rate fluctuations
$\eta$	Acoustic variable
$\gamma$	Specific heat ratio
$\Omega_0$	Frequency of the thermoacoustic oscillations
$\omega_l$	Frequency of the $l^{\text{th}}$ phase oscillator
$\Phi$	Phase of the acoustic pressure oscillations
$\phi$	Equivalence ratio
$\psi_l$	Relative phase between the phase of heat release rate and acoustic pressure fluctuations
$\rho_0$	Density at mean flow condition
$\theta_l$	Phase of heat release rate from $l^{\text{th}}$ oscillator
$\tilde{\zeta}$	Damping coefficient
$\tilde{L}$	Length of the duct
$v_z$	Bulk flow velocity

$c_0$	Average speed of sound
$f$	Natural frequency
$g(\omega)$	Frequency distribution
$K$	Coupling strength among phase oscillators
$N$	Number of oscillators
$p'$	Acoustic pressure fluctuations
$p'_{\text{rms}}$	Root mean square value of acoustic pressure fluctuations
$p_0$	Pressure at mean flow condition
$R$	Amplitude of the acoustic pressure oscillations
$r$	Kuramoto order parameter
$Re$	Reynolds number
$T$	Time period of an acoustic periodic cycle
$t$	Time
$z_f$	Position of flame in the duct

# CHAPTER 1

## INTRODUCTION

### 1.1 COMBUSTION TECHNOLOGIES IN MODERN GAS TURBINES

Climate change due to emissions from human activity is one of the paramount challenges in the twenty-first century. To tackle this urgent problem, stringent emission laws have been implemented, including restrictions on the emission of both carbon dioxide (CO<sub>2</sub>) and nitrogen oxides (NO<sub>x</sub>). Gas turbines primarily rely on the combustion of fuels such as methane or natural gas, ethane, ethylene, propane, and butane (Lieuwen and Yang, 2005). Unfortunately, the combustion of these fuels leads to the emission of carbon monoxide (CO), carbon dioxide (CO<sub>2</sub>), oxides of nitrogen (NO<sub>x</sub>), unburned hydrocarbons (UHC) and particulate matter (PM). The emission levels of these pollutants from gas turbines are directly linked to their diverse applications. For instance, aircraft gas turbines face the challenge of maintaining combustion at varying power levels throughout different stages of flight, necessitating the capability for re-ignition in the event of a flame blow-out. Similarly, ground-based gas turbines deployed in power plants must adeptly adjust power output based on energy demand, thereby restricting the choice of operating parameters such as the air-fuel ratio, pressure, and temperature. These operational demands inevitably lead to increased emissions of various pollutants at different stages of gas turbine operation. Therefore, it is of great importance to reduce the emissions from those sources as much as possible.

One promising strategy to curtail harmful gas emissions that has gained significant attention in recent years is the rich-quench-lean (RQL) combustion chamber. The RQL combustor is a type of low-emission combustor that has been shown to avoid favorable combustion conditions for the formation of thermal NO<sub>x</sub> (Samuelsen, 2006). This is achieved by controlling the fuel-air mixture in three distinct zones: a fuel-rich primary

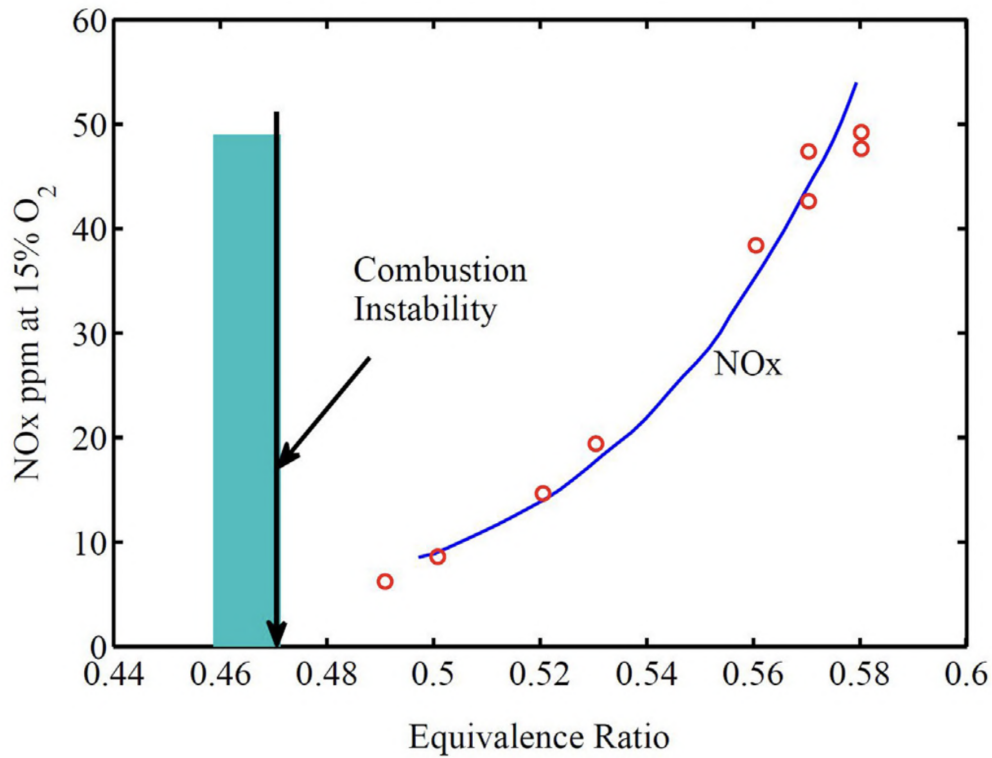


Figure 1.1: Effect of equivalence ratio on NO<sub>x</sub> production and susceptibility to thermoacoustic instability. Adapted from Zhao (2023) with permission from Elsevier.

zone, a quenching zone, and a lean-burn secondary zone (Lefebvre and Ballal, 2010; Lieuwen and Yang, 2013). However, for aero-engines where weight and space are crucial, RQL combustors must deliver high power densities. This necessity increases the risk of combustion or thermoacoustic instabilities, adversely affecting the operational flexibility (Eckstein *et al.*, 2006; Cai *et al.*, 2010; Renner *et al.*, 2022; March *et al.*, 2023). Additionally, limitations arise from the ability of the quenching process to rapidly and uniformly dilute the fuel-rich mixture followed by transport it to the lean zone.

Another highly effective strategy for significantly reducing the production of NO<sub>x</sub> involves lowering the temperature of the combustion process (Docquier and Candel, 2002). This reduction can be achieved by operating in a lean regime, where there is more air than required for the complete combustion process of the given amount of fuel. To ensure that the emissions are kept at a minimum, it is crucial to achieve a thorough mixing of

fuel and air before entering the combustion chamber, thereby reducing the chance of having zones with rich mixtures where  $\text{NO}_x$  can be more easily produced. Consequently, there is a preference for operating the combustor in the lean-premixed regime, signifying a transition from RQL combustion to lean-premixed systems. However, the major challenge in implementing lean, premixed combustion lies in ensuring the stability of the combustor operation.

Fully premixed flames are challenging to stabilize and are frequently susceptible to lift-off at the flame holder, as well as flashbacks upstream of the combustion chamber along the air-fuel lines. This challenge is exacerbated by the increased risk of autoignition of the air-fuel mixture before reaching the combustion zone (Lieuwen *et al.*, 2008). Additionally, premixed flames are prone to extinction and blow-out, posing a threat of complete power outage in the combustor (Shanbhogue *et al.*, 2009a). Furthermore, the compact flames and enhanced power density in lean premixed combustors make them more vulnerable to thermoacoustic instabilities. This susceptibility becomes evident when pushing the equivalence ratio ( $\phi$ ) towards leaner mixtures, as illustrated in Figure 1.1. These instabilities can result in a narrower range of viable operating conditions, indirectly leading to reduced power or increased emissions under certain conditions (Candel, 2002). In severe instances, these instabilities can escalate, potentially shortening the operational lifespan of the engine or compromising its structural integrity.

## **1.2 THERMOACOUSTIC INSTABILITY PHENOMENON**

### **1.2.1 Thermoacoustic instability and its consequences**

The phenomenon of thermoacoustic instability is characterized by self-excited periodic pressure oscillations, which originate due to the coupling between the acoustic pressure and unsteady heat release rate from the flame (Lieuwen and Yang, 2005; Sujith and Pawar, 2021; Zhao, 2023). The unsteady heat release is a potential source, producing acoustic waves that propagate within the combustor. The acoustic waves after getting

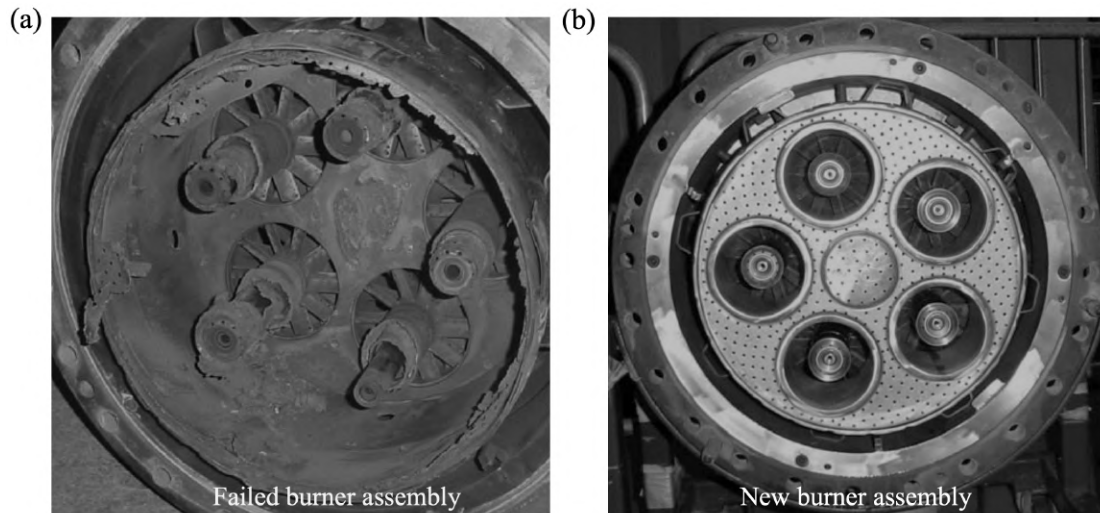


Figure 1.2: Combustion chamber assembly of the gas turbine engine (a) damaged by large amplitude thermoacoustic instability and (b) a new burner assembly. Adapted from [Lieuwen and Yang \(2005\)](#) with permission from AIAA.

reflected from the combustor boundary reach the combustion zone; these reflected waves now perturb the heat release rate further. The fluctuating heat release rate when in phase with the acoustic pressure, amplifies the acoustic pressure fluctuations. This positive feedback loop between the unsteady flame(s) and the combustor acoustic modes can have devastating consequences. The transition from a stable operation characterized by broadband combustion noise to thermoacoustic instability occurs when the heat release rate fluctuations evolve in phase with acoustic pressure oscillations ([Rayleigh, 1945](#)), and the total acoustic energy arising through the nonlinear feedback from the flame is greater than the net acoustic losses across the boundary of the combustion chamber ([Chu, 1965](#); [Putnam, 1971](#)).

Thermoacoustic instability, which is characterized by large amplitude pressure oscillations, presents a significant risk of engine damage. As depicted in figure 1.2, these oscillations can lead to pronounced vibrations within the engine, causing mechanical and thermal stress that can compromise engine components ([McManus \*et al.\*, 1993](#); [Candel, 2002](#); [Lieuwen and Yang, 2005](#); [Juniper and Sujith, 2018](#)). The intense growth in pressure amplitude may cause severe damage to crucial combustor components such as liners, fuel

injectors, and turbine blades or may degrade their performance (Culick and Kuentzmann, 2006). Moreover, the elevated acoustic pressure levels can escalate heat transfer, which in turn overwhelms the thermal protection system. Importantly, electronic components in the control system or the payload can fail due to the high level of acoustic ambience. Consequently, these oscillations generate intolerably loud noise, causing health risks for engine operators and making them highly undesirable, both in terms of safety and comfort.

### 1.2.2 Mechanism of thermoacoustic instability

The driving mechanism behind thermoacoustic instabilities was first recognized by Rayleigh (1878). He observed amplification in the amplitude of oscillations when acoustic pressure and heat release fluctuations were in phase. Figure 1.3 provides an illustration of the interaction between the acoustic field and the heat release rate fluctuations. Any fluctuations in the acoustic velocity and pressure field can cause fluctuations in the heat release rate. Importantly, the energy transfer from the heat release rate field to the acoustic environment does not always imply that the combustion system will experience thermoacoustic instability. Only when the rate of energy supplied by the combustion process to the acoustic field in the combustor exceeds the rate at which acoustic energy is dissipated within the duct or transmitted across its boundaries, the system exhibits thermoacoustic oscillations (Zinn and Lieuwen, 2005). The Rayleigh criteria suggest that the thermoacoustic instability arises from a positive relationship between heat release rate and pressure fluctuations, which is expressed as:

$$\int_V \int_T p'(x, t) \dot{q}'(x, t) dt dV > 0 \quad (1.1)$$

where  $p'(x, t)$  and  $\dot{q}'(x, t)$  are the acoustic pressure and the heat release rate fluctuations, respectively. Here,  $V$  and  $T$  are the combustor heat release volume and period of the oscillations. The correlation encapsulated by the  $p'\dot{q}'$  is commonly known as the Rayleigh index. This condition is widely employed for providing bounds of thermoacoustic stability with detailed discussions available in works by Lieuwen and Yang (2005), Poinsot (2017)

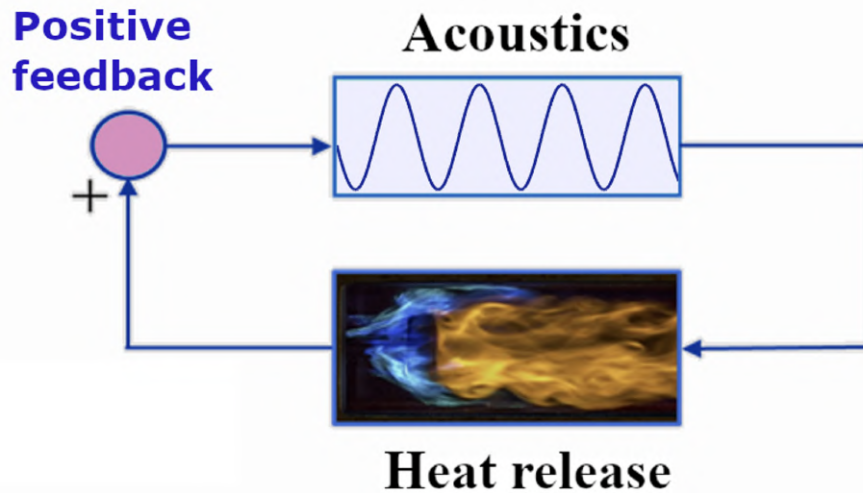


Figure 1.3: Schematic of the positive feedback loop formed between the unsteady flame and the acoustic field within the combustor responsible for driving self-excited thermoacoustic instabilities.

and [Juniper and Sujith \(2018\)](#).

The fundamental idea is that the propagation of the acoustic waves within the combustor perturb the flame surface, and influence the compression and expansion of the gas surrounding the flame. When the heat released by the perturbed flame is consistently higher during local pressure maxima, the work done by the gas is more during the acoustic expansion phase than during the acoustic compression phase. If the excess work is not effectively dissipated, the acoustic energy within the combustor amplifies, leading to an increase in the amplitude of acoustic pressure oscillations ([Rayleigh, 1878](#); [Chu, 1965](#)). The coupling mechanism between heat release rate and acoustic pressure fluctuations is strongly dependent on various factors. These factors include combustion mechanisms, the acoustic modes of the combustor, hydrodynamic instabilities through density gradients in the flow field, and turbulence levels. For a comprehensive understanding, one can refer to the reviews by [Lieuwen \(2012\)](#).

It is evident that any fluctuations in the heat release rate, when coupled with acoustic pressure, can potentially excite thermoacoustic instability. There are a number of physical

mechanisms which generate heat release rate fluctuations; these include equivalence ratio fluctuations (Lieuwen *et al.*, 1998; Kim *et al.*, 2010), swirl number fluctuations (Komarek and Polifke, 2010), flame-vortex interactions (Poinsot *et al.*, 1987; Renard *et al.*, 2000), and entropy fluctuations (Polifke *et al.*, 2001; Goh and Morgans, 2013). The equivalence ratio starts fluctuating when the acoustic wave propagates upstream along the fuel and air supply. These variations in equivalence ratio subsequently trigger fluctuations in the heat release rate and lead to oscillations in the flame speed (Lieuwen *et al.*, 1998; Lieuwen and Zinn, 1998; Shreekrishna and Lieuwen, 2010). Lee *et al.* (2000a) utilized an infrared absorption technique to measure the equivalence ratio fluctuations and shows that the equivalence ratio fluctuations are strongly linked to the heat release rate fluctuations during unstable combustor operation. This relation suggests a substantial influence of equivalence ratio fluctuations in driving the thermoacoustic instability.

Palies *et al.* (2010) illustrates the effect of fluctuation in swirl number on the heat release rate of a swirling flame. The study highlights the rise in the heat release rate fluctuations resulting from a combination of processes, specifically the vortex roll-up of the flame and perturbations caused by fluctuations in the swirl number. Notably, these fluctuations in swirl number arise from the interaction between incoming acoustic disturbances and the swirler, leading to the generation of both a transmitted acoustic wave and a convective vorticity wave. Thus, the interplay between the heat release rate and acoustic pressure oscillations due to fluctuations in swirl number leads to thermoacoustic instability. Further, Komarek and Polifke (2010) explores how fluctuations in the swirl number affect the heat release rate of a premixed flame within a combustor equipped with an adjustable axial swirl generator. Their findings reveal that the position of the swirl generator notably influences the dynamic response of the flame, despite not significantly altering the time-averaged heat release distribution. This dynamic response of the flame after interacting with the acoustic field results in self-excited thermoacoustic oscillations in the combustor.

Another potential mechanism for exciting thermoacoustic instability involves the interplay between the flame and vortex. Flame-vortex interaction can be driven by large-scale coherent structures in the flow that distort the flame, consequently influencing the heat release rate (Poinsot *et al.*, 1987; Shanbhogue *et al.*, 2009a). In particular, vortices in the flow can entrain fresh reactants and cause the flame to roll up, which significantly increases the flame surface area, thereby enhancing heat release rate fluctuations. This coherent oscillation in the heat release rate feeds back into the acoustic pressure fluctuations, establishing a self-sustaining thermoacoustic instability (Renard *et al.*, 2000).

Moreover, the generation of entropy waves within the flame zone acts as a source of entropy noise and can affect thermoacoustic instability within the combustor. This indirect combustion noise is excited due to the acceleration of flow with nonuniform entropy distribution or convective entropy modes, potentially contributing to thermoacoustic instability. A comprehensive review on this topic can be found in Morgans and Duran (2016). Additionally, Polifke *et al.* (2001) highlighted the coupling between the entropy waves and acoustic waves both constructively and destructively, showcasing their potential to influence combustion stability.

### **1.2.3 Origin of nonlinearities in thermoacoustics**

Thermoacoustic systems inherently exhibit nonlinear characteristics (Sujith and Pawar, 2021), notably demonstrated by the emergence of limit cycle oscillations during the onset of thermoacoustic instability within the combustor (Culick, 1994). As the acoustic driving is greater than the damping, the periodic oscillations grow exponentially in the system, eventually saturating at constant-amplitude periodic oscillations. This happens when nonlinearities dominate in the combustor, establishing a balance between acoustic driving and damping processes. Therefore, understanding the nonlinear nature of the thermoacoustic system becomes crucial in predicting the amplitude of limit cycle oscillations. Notably, both the acoustic sub-system and the unsteady flame can display nonlinear behavior. However, in gas turbine combustors the acoustic pressure fluctuations

have comparatively low amplitude relative to the mean pressure. Therefore, acoustic wave propagation is often viewed as a linear process. Conversely, the response of the flame to acoustic perturbations is highly nonlinear (Dowling, 1997; Sujith and Unni, 2020). Consequently, modeling the acoustic waves is relatively straightforward and well established. In contrast, modeling the nonlinear response of the flame is exceedingly challenging.

In order to characterize the response of the flame, Bellows *et al.* (2006) investigate the effect of the external acoustic forcing on the flame. They show that at a low value of the perturbation amplitude, the heat release rate fluctuations are linear and the response becomes nonlinear only when the forcing amplitude is high. The significance of these nonlinear effects in heat release rate fluctuations arises when the magnitude of acoustic velocity fluctuations is of the order of the mean flow velocity ( $v'_z \sim \bar{v}_z$ ). Balachandran *et al.* (2005) experimentally show the nonlinear response of the flame dominates when the velocity ratio ( $v'_z/\bar{v}_z$ ) is around 15%. Numerous other sources contribute to system nonlinearities, including phenomena such as flow-flame interaction (Dowling, 1997; Emerson and Lieuwen, 2015), equivalence ratio fluctuations (Peracchio and Proscia, 1999; Shreekrishna and Lieuwen, 2010), flame front kinematics (Baillot *et al.*, 1992; Lieuwen, 2003), burning rate (McIntosh, 1999), flame speed and stretch rate (Kelley and Law, 2009) have been found in the past. As a result, considering the impact of nonlinearities on the thermoacoustic system is of fundamental importance which leads to different kinds of unexpected behaviors of the system dynamics.

### **1.3 LONGITUDINAL INSTABILITY IN THERMOACOUSTIC SYSTEMS**

#### **1.3.1 Bifurcations and transition to thermoacoustic instability**

In the previous section, we explored various mechanisms underlying the phenomena of thermoacoustic instability. Understanding the onset of thermoacoustic instability in the combustor is of great practical relevance. The transition to thermoacoustic instability

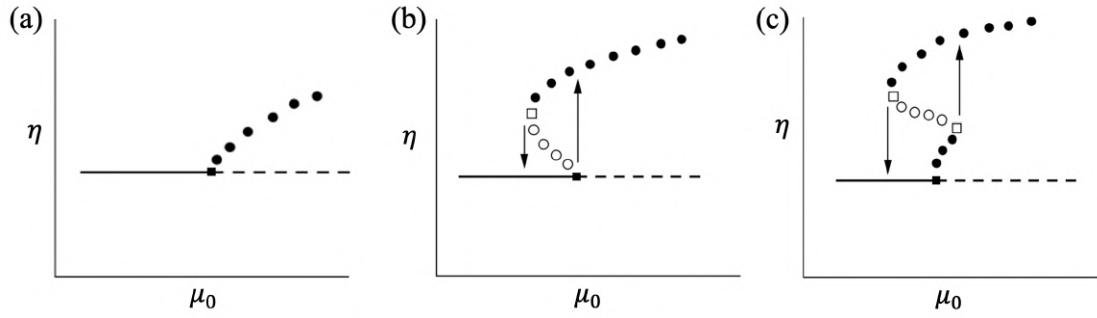


Figure 1.4: Normal form of (a) supercritical Hopf, (b) subcritical Hopf, and (c) secondary bifurcation for a Van der Pol oscillators with nonlinear terms depicting the change in the nature of a bifurcation as a function of control parameter  $\mu_0$ . Adapted from [Ananthkrishnan \*et al.\* \(1998\)](#) with permission from Elsevier.

from the state of stable operation is achieved when some control parameter is varied. For instance, thermoacoustic instability is observed in real combustors used in power plants (or aircrafts) when the equivalence ratio or flow velocity is altered to deal with an increase or decrease in power demand. Consequently, the focus often lies in transitioning from a stable state of combustor operation to a state characterized by limit cycle oscillations.

### Hopf bifurcations to limit cycle oscillations

Traditionally, the onset of thermoacoustic instability has been viewed as the loss of stability of the fixed point solution within the linearized system. Once we vary the critical parameter value past the Hopf point, a pair of complex conjugate eigenvalues cross the imaginary axis, leading to the emergence of limit cycle oscillations through a Hopf bifurcation ([Lieuwen, 2002](#); [Strogatz, 2018](#)). This transition can occur via primary supercritical or subcritical bifurcations ([Lieuwen, 2002](#); [Laera \*et al.\*, 2017b](#)) or through a secondary bifurcation of an initially stable, primary limit cycle oscillations ([Ananthkrishnan \*et al.\*, 1998](#); [Wang \*et al.\*, 2021](#); [Bhavi \*et al.\*, 2023](#)). The exact nature of the bifurcation depends on the type and order of nonlinearity inherent in the system ([Kuehn and Bick, 2021](#)).

Supercritical Hopf bifurcation is realized when a change in the value of the control parameter  $\mu$  beyond the Hopf point ( $\mu_H$ ), leads to a gradual increase in the amplitude of

limit cycle oscillations (see figure 1.4a). In contrast, if the system abruptly jumps from a stable fixed point to a limit cycle attractor of large amplitude, the bifurcation is referred to as subcritical Hopf bifurcation (see figure 1.4b). In this case, the system is bistable in the range  $\mu_F < \mu < \mu_H$ , i.e., the fixed point solution is linearly stable to small-amplitude perturbations and unstable to perturbations above a threshold value. At  $\mu = \mu_H$ , the system jumps from the stable fixed point to a limit cycle attractor with a large amplitude. To revert to the stable solution, the control parameter must be reversed past the Hopf point till the fold point ( $\mu_F$ ) is reached such that  $\mu_F < \mu_H$ . Thus, subcritical transitions are associated with hysteresis and bistability in the solution (Strogatz, 2018).

Whether the transition occurs through a supercritical or subcritical Hopf bifurcation depends on the stabilizing or destabilizing nature of the dominant nonlinearities in the system when a parameter is varied (Etikyala and Sujith, 2017). The dependence of the nonlinearity on the critical parameter leading to a change in the nature of the bifurcation is referred to as *change in criticality* of a Hopf bifurcation (Marsden and McCracken, 2012). In general, the source of nonlinearities in a thermoacoustic system is the acoustic damping and acoustic driving (Culick and Kuentzmann, 2006). Both of these quantities depend on the amplitude of acoustic pressure and also the control parameters. Any variation in these quantities can change the balance between driving and damping and can lead to the usual case of supercritical or subcritical bifurcation to limit cycle oscillations.

In extraordinary scenarios, higher-order nonlinearities in the system can destabilize the stable branch of the limit cycle solution generated through a primary Hopf bifurcation, leading to a secondary fold bifurcation to a high-amplitude limit cycle (Ananthkrishnan *et al.*, 1998), as shown in figure 1.4(c). An analogous transition to high-amplitude limit cycle oscillations has been noted in aircraft flight dynamics, specifically in wing rock phenomena, characterized by high-amplitude oscillatory rolling motion (Ananthkrishnan and Sudhakar, 1996). In thermoacoustic systems, the theoretical prediction of a secondary bifurcation to high-amplitude thermoacoustic instability was established

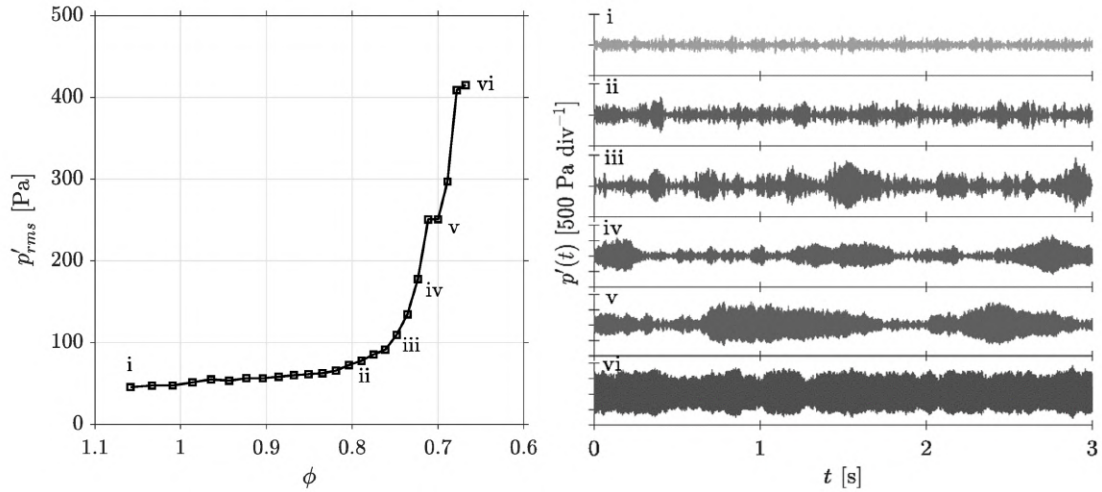


Figure 1.5: Typical bifurcation diagram showing amplitude of acoustic pressure fluctuations ( $p'_{rms}$ ) as a function of the equivalence ratio ( $\phi$ ). State (i) corresponds to the state of combustion noise, (ii-v) intermittency, and (vi) thermoacoustic instability. The bifurcation and associated dynamical states are observed in a bluff-body stabilized combustor. Figure is adapted from [George \*et al.\* \(2018\)](#) with permission from Cambridge University Press.

by [Ananthkrishnan \*et al.\* \(2005\)](#). The recent publication by [Bhavi \*et al.\* \(2023\)](#) is built upon experimental results on secondary bifurcation reported in this thesis, where they examine the secondary bifurcation using a low-order stochastic thermoacoustic model. They seamlessly incorporate findings from other experimental configurations to corroborate the universality of secondary bifurcation in turbulent combustors. Generally, the aforementioned distinct bifurcations to limit cycle oscillations have been observed in many practical combustors ([Lieuwen, 2002](#); [Campa and Juniper, 2012](#); [Etikyala and Sujith, 2017](#)).

### **Intermittency route to limit cycle oscillations**

While the paradigm of Hopf bifurcation is frequently utilized in both experimental and modeling studies of laminar and turbulent combustors, it encounters inherent challenges when applied to the discussion of transitions in turbulent thermoacoustic systems.

During the stable operation of the turbulent combustor, the flame generates sound through

non-steady volumetric expansion and convective entropy modes (Candel *et al.*, 2009; Dowling and Mahmoudi, 2015). The radiated sound lacks any characteristic time scale, appears noisy, and possesses a broadband signature (see figure 1.5i). These broadband fluctuations, rooted in turbulence, thus exhibit scale invariance and multifractal behavior (Nair and Sujith, 2014; Sujith and Pawar, 2021). The sound generated during combustion is colloquially referred to as combustion noise (Candel *et al.*, 2009) and is a deterministic phenomenon (Tony *et al.*, 2015). The mechanism of transition from such a low-amplitude chaotic state of combustion noise to a high-amplitude periodic state of thermoacoustic instability is a continuing problem of significant practical relevance and intense theoretical interest.

Turbulence plays a crucial role in determining how nonlinearities manifest in the dynamics of the system during the transition to thermoacoustic instability. Upon varying the control parameters such as equivalence ratio or Reynolds number systematically, the transition from combustion noise to thermoacoustic instability has often been reported to occur through the state of intermittency (Nair *et al.*, 2014; Nair and Sujith, 2015; George *et al.*, 2018; Kheirkhah *et al.*, 2017; Guan *et al.*, 2020). Intermittency is a deterministic phenomenon rooted in turbulence and refers to a dynamically stable state consisting of low-amplitude chaotic fluctuations randomly interspersed with high-amplitude periodic fluctuations (see figure 1.5ii-v). Consequently, the aforementioned characteristics cannot be well represented by the Hopf bifurcation. The transition to thermoacoustic instability shows a continuous increase in the amplitude of pressure oscillations as a result of a progressive increase in the duration of bursts of periodic oscillations until the state of full-blown thermoacoustic instability is reached (see figure 1.5vi), manifesting in a continuous “sigmoid” type transition diagram.

### **Mixed-mode oscillations route to thermoacoustic instability**

Besides the intermittency route, the transition to constant amplitude limit cycle oscillations can take place through a state where pressure oscillations alternate between low-amplitude

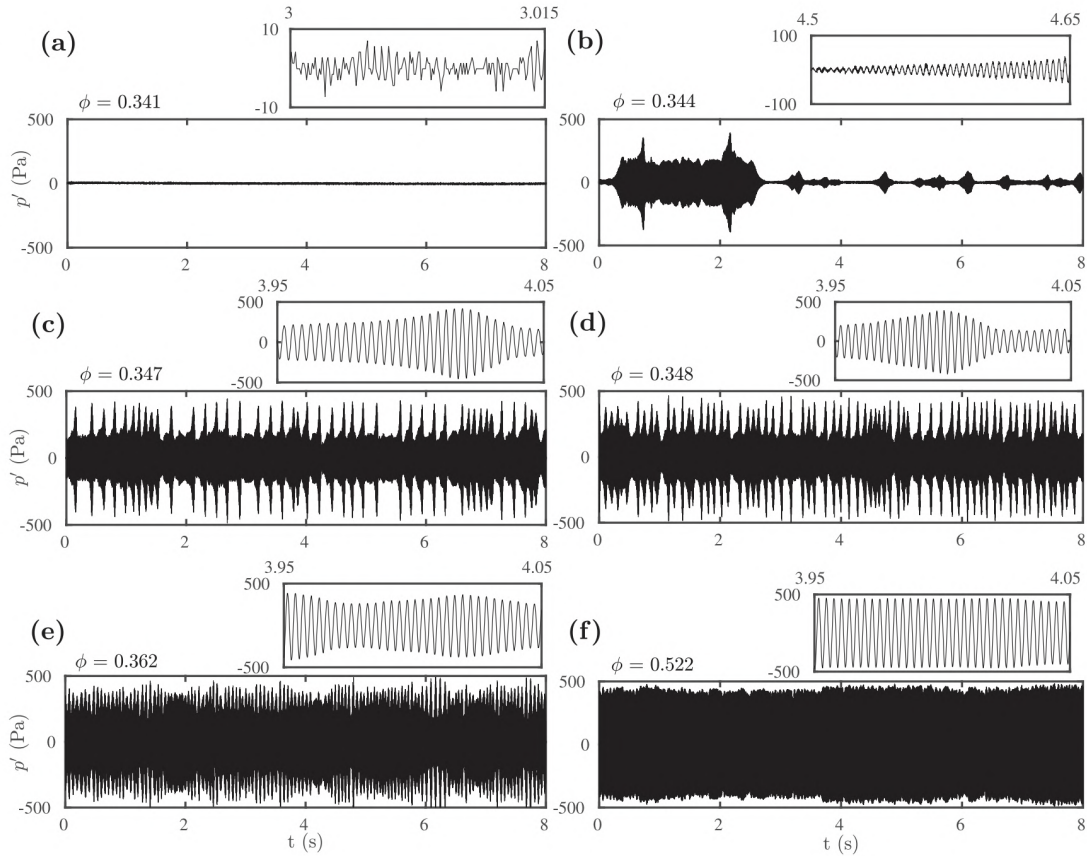


Figure 1.6: Time series of acoustic pressure oscillations  $p'$  inside the matrix burner during the state of (a) stable operation, (b) bursting oscillations, (c-e) mixed-mode oscillations, and (f) thermoacoustic instability. Figure is adapted from [Kasthuri \*et al.\* \(2019\)](#) with permission from the American Institute of Physics.

and high-amplitude periodic oscillations, known as mixed-mode oscillations ([Desroches \*et al.\*, 2012](#); [Kuehn, 2011](#)). Mixed-mode oscillations appear in systems with characteristic slow time scales in addition to fast time scales ([Kuehn, 2011](#); [Kasthuri \*et al.\*, 2019](#)). [Kasthuri \*et al.\* \(2019\)](#) observed the transition from stable operation to thermoacoustic instability through mixed-mode oscillations in a ducted matrix burner (see figure 1.6). Interestingly, the findings reveal the existence of bursting oscillations followed by mixed-mode oscillations. Within the bursting oscillations, there is a switching of oscillations between bursts of periodic oscillations and a nearly quiescent state. During mixed-mode oscillations, a periodic oscillation switches between two different amplitudes. In combustion literature, amplitude-modulated limit cycle oscillations are often termed

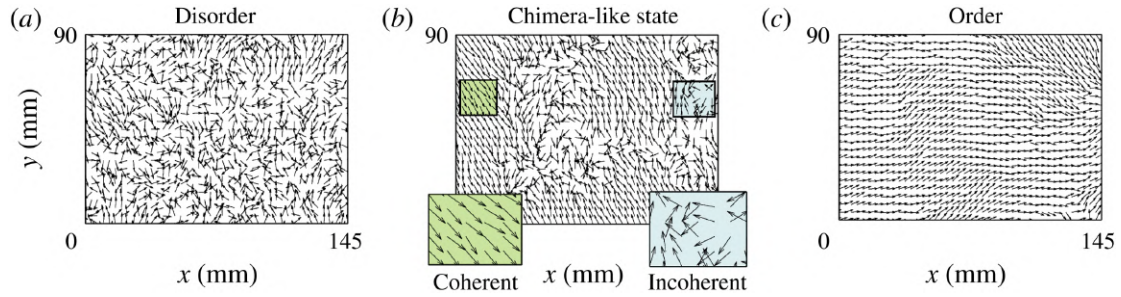


Figure 1.7: Illustration of the emergence of global phase synchronization during the transition from (a) combustion noise, followed by (b) intermittency to (c) thermoacoustic instability in a bluff-body turbulent combustor. Spatial view of the combustor showing the instantaneous phase difference ( $\psi$ ) between the acoustic pressure ( $\Phi$ ) and heat release rate ( $\theta_i$ ) oscillations. Adapted with permission from [Mondal \*et al.\* \(2017b\)](#), courtesy of Cambridge University Press.

as beats ([Weng \*et al.\*, 2016](#); [Kim \*et al.\*, 2019](#); [Han \*et al.\*, 2020](#)). These beats typically result from the linear superposition of acoustic modes with small frequency differences, displaying constructive and destructive interference patterns ([Kim \*et al.\*, 2019](#); [Han \*et al.\*, 2020](#)). However, the concept of beats is applicable only in linear systems. The oscillations depicted in figure 1.6(c-e) differ from standard beats due to nonlinearities and the absence of clear constructive and destructive interference patterns. As a result, the framework of mixed-mode oscillations seems a more fitting description for these amplitude-modulated oscillations.

### 1.3.2 Spatiotemporal dynamics of thermoacoustic systems

The flow field also presents many interesting features when the combustor transitions from stable operation to thermoacoustic instability. Most of the initial investigations concentrated solely on the spatiotemporal dynamics during combustion noise and the onset of thermoacoustic instability. These studies provided valuable insights into the emergence of large-scale coherent structures at the onset of thermoacoustic instability and how these flow structures alter the dynamics of the flame ([Rogers and Marble, 1956](#); [Smith, 1985](#); [Poinsot \*et al.\*, 1987](#); [Schadow and Gutmark, 1992](#); [Coats, 1996](#); [Renard \*et al.\*, 2000](#); [Schwing \*et al.\*, 2011](#); [Emerson \*et al.\*, 2012](#)).

Turbulent combustors by nature are spatially extended systems, wherein thermoacoustic instability results from the nonlinear interaction of various spatially extended subsystems (Sujith and Unni, 2020; Sujith and Pawar, 2021). These include the turbulent flow field, reaction field, and chamber acoustics, interacting across diverse temporal and spatial scales. The oscillations in the CH\* chemiluminescence field of the flame are predominantly governed by a complex interplay of hydrodynamic fluctuations, vortex formation, equivalence ratio fluctuations, flame stabilization mechanisms, and the boundaries of the combustor (Lieuwen, 2012). During the transition to thermoacoustic oscillations through intermittency, the spatial field unveils interesting characteristics. This gradual emergence of periodic dynamics is associated with the emergence of order or coherence in the spatial field (Mondal *et al.*, 2017b; George *et al.*, 2018; Hashimoto *et al.*, 2019; Guan *et al.*, 2019b).

A recent study by Mondal *et al.* (2017b) computes the instantaneous phase relationship between acoustic pressure and unsteady heat release rate fluctuations to examine the phase field across three distinct dynamical states: combustion noise, intermittency, and thermoacoustic instability. During the occurrence of combustion noise, the phasor field displays spatial incoherence (refer to figure 1.7a). Conversely, during thermoacoustic instability, the phasor field shows perfect alignment, indicating a spatially coherent flame extending across extensive regions (refer to figure 1.7c). However, during the intermediate state of intermittency, a unique scenario emerges: patches of both incoherent and coherent phasor fields coexist simultaneously (refer to figure 1.7b), resembling a chimera state (Abrams and Strogatz, 2004). Moreover, during the occurrence of combustion noise and during the epochs of aperiodic oscillations within intermittency, small vortices are shed aperiodically, maintaining spatial incoherence in the heat release rate field (George *et al.*, 2018). In contrast, during the state of thermoacoustic instability and the epochs of periodic oscillations in intermittency, vortices are shed periodically from the backward-facing step of the combustor. These vortices carrying the air and fuel mixtures develop into large-scale coherent structures, which collide with the bluff-body

and combustor walls. The collision results in intense mixing zones, leading to regions with intense heat release rate (George *et al.*, 2018; Premchand *et al.*, 2020). Hence, both the temporal and spatiotemporal dynamics significantly contribute to the onset of thermoacoustic instability.

## 1.4 AZIMUTHAL AND LONGITUDINAL INSTABILITIES IN ANNULAR COMBUSTOR

Gas turbine combustors in practical applications often adopt an axially shorter design, ensuring a more uniform turbine inlet temperature profile. They frequently incorporate multiple swirling flames arranged around an annular chamber. This arrangement gives rise to both longitudinal and azimuthal acoustic modes, each exhibiting distinct behaviors in the acoustic field structure and flame responses. Notably, due to the perimeter of the annular combustor typically being the largest physical dimension in industrial gas turbines, the occurrence of thermoacoustic oscillations, particularly associated with the azimuthal acoustic eigenmode, becomes more probable (Krebs *et al.*, 2002). On the other hand, real engine designs often feature axial lengths that are of a similar order of magnitude as their perimeters. This proximity in dimensions enhances the potential for interactions between the longitudinal and azimuthal modes (Mazur *et al.*, 2021).

### 1.4.1 Self-excited thermoacoustic modes in annular combustor

In order to comprehend the dynamics of both longitudinal and azimuthal modes, investigating real annular configurations becomes imperative to enhance our understanding of these modes. While initial data was obtained from experiments conducted on full-scale commercial gas turbines (see Seume *et al.*, 1998; Krebs *et al.*, 2002; Paschereit *et al.*, 2006, for a review), these configurations are geometrically very complex and entail high operational costs. Motivated by these challenges, simplified annular combustion chambers capable of showcasing self-excited thermoacoustic instabilities were developed in the past decade (Worth and Dawson, 2013b; Bourgouin *et al.*, 2013). Figure 1.8

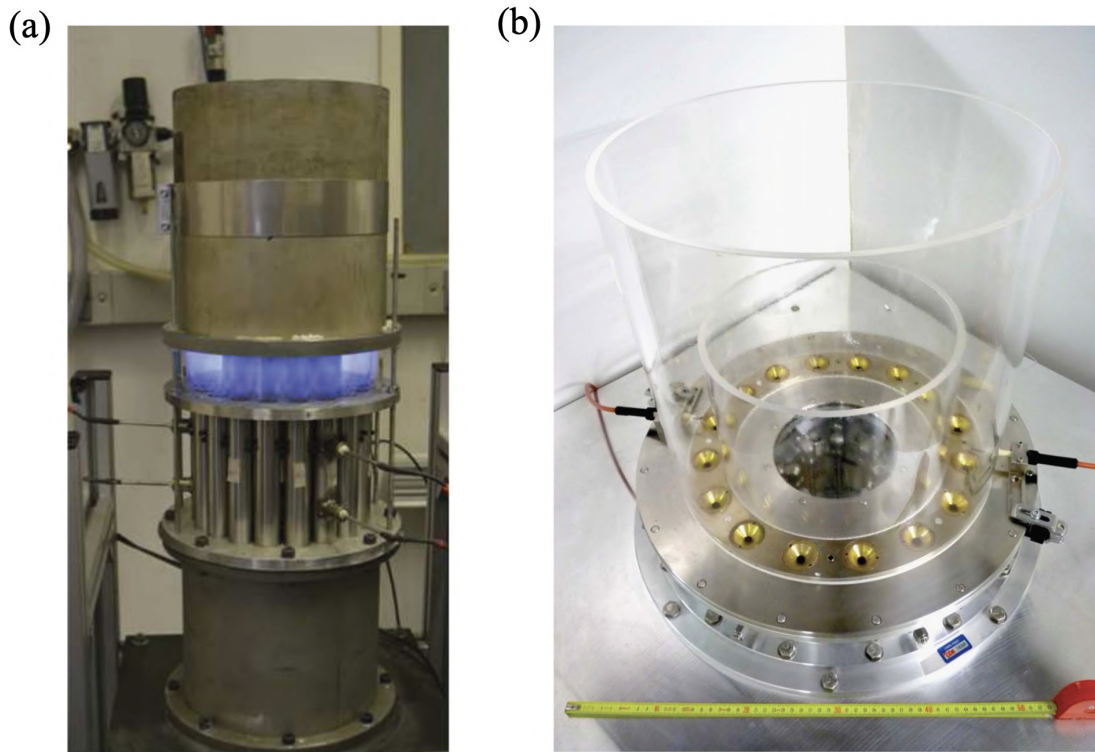


Figure 1.8: First lab-scale atmospheric annular combustors to exhibit self-sustained azimuthal instabilities at (a) Cambridge University (Worth and Dawson, 2013a,b) and (b) EM2C laboratory. Reproduced from (a) Worth and Dawson (2013a) and (b) Bourgouin *et al.* (2013) with permission from Elsevier and ASME, respectively.

presents an external view of lab-scale annular combustor designed by Worth and Dawson (2013b) and Bourgouin *et al.* (2013) that exhibits self-excited thermoacoustic instabilities. These two annular combustors are independently developed at Cambridge University and EM2C laboratory.

During the unstable operation of an annular combustor, numerous interactions occur concurrently: turbulent flow interacts with premixed flames, flames interact with neighboring flames, and both the flow and flames interact with the acoustic field of the chamber (Candel *et al.*, 2014; O'Connor *et al.*, 2015). In these combustors, the interaction among neighboring flames results in intricate three-dimensional flame dynamics. The structure and behavior of interacting flames undergo substantial changes based on the distance between them and their flame-holding characteristics. In a study by Worth and

Dawson (2012), they investigated the impact of separation distance between flames in a setup with two bluff-body stabilized flames. Their findings highlighted that shorter distances between burners lead to the merging of flames on a large scale, altering the mean flame structure and its corresponding thermoacoustic response. Subsequently, Worth and Dawson (2013b) extended this analysis to a complete annular combustor, revealing a shift in flame structure from helical to a merged large-scale configuration as the inter-burner distance decreased. Another study by Bourgouin *et al.* (2013), focused on a swirl-stabilized annular combustor, and analysed the modal dynamics related to heat release rate perturbations during both longitudinal and azimuthal instabilities. Their observations indicated a certain level of desynchronization in flame dynamics during longitudinal instability. Together, these studies shed light on how flame-flame interactions impact thermoacoustic responses across a range of annular combustor configurations. Hence, it is essential to gain a comprehensive understanding of the thermoacoustic behavior exhibited by annular combustors.

Due to rotational symmetry, thermoacoustic instabilities in annular combustors often manifest as eigenmodes featuring an azimuthally modulated distribution of acoustic pressure. The azimuthal modes are classified into three categories: (i) standing modes characterized by spatial nodes and anti-nodes, exhibiting either a fixed location or slow drift relative to the speed of sound, (ii) spinning modes propagating in either a clockwise (CW) or counter-clockwise (CCW) direction, and (iii) mixed modes, representing a linear combination of spinning and standing modes (Noiray *et al.*, 2011; Ghirardo and Juniper, 2013; Worth and Dawson, 2013a). Recent observations have unveiled a unique form of thermoacoustic dynamics known as the “slanted mode”, identified in the annular combustor by Bourgouin *et al.* (2015). This mode arises from the concurrent presence of a standing azimuthal mode and a longitudinal mode, both exhibiting coinciding frequencies. Subsequent investigation on this dynamic was conducted by Prieur *et al.* (2017) within the same experimental framework. Additionally, Moeck *et al.* (2019) developed a model depicting this phenomenon as a synchronization between a pure longitudinal mode

and an azimuthal mode characterized by remarkably close eigenfrequencies. Another interesting finding by [Fang \*et al.\* \(2021\)](#) reported a new dynamic state in the annular combustor, revealing the coexistence of both longitudinal and azimuthal modes at different frequencies.

In general, these interesting dynamical state in the combustor arises due to the nonlinear interaction between the azimuthal eigenmodes. The interplay between the azimuthal eigenmodes was initially explored by [Paschereit \*et al.\* \(2006\)](#), who considered a nominally axisymmetric system with degenerate eigenmodes. Their investigation focused on the nonlinear interaction of two orthogonal standing modes of azimuthal instability. They demonstrated that, under conditions of linear instability, the system evolves into a limit cycle where both standing modes coexist due to their degeneracy. The combination of two standing eigenmodes results in a single spinning wave, rotating either in the clockwise or counter-clockwise direction, solely determined by initial conditions. Building upon this work, [Hummel \*et al.\* \(2016, 2017\)](#) investigated a similar problem, framing it in terms of two counter-rotating eigenmodes within a nominally axisymmetric system. Unlike the earlier study, they allowed for non-degeneracy, introducing different frequencies and/or growth rates for clockwise and counterclockwise eigenmodes. In alignment with the findings of [Paschereit \*et al.\* \(2006\)](#), they confirmed that only spinning waves dominate the system during limit cycle conditions. However, they further revealed that non-degeneracy introduces a preference for one spinning wave over the other. To summarize, these studies collectively emphasize that a nominally axisymmetric system predominantly exhibits spinning wave behavior at the limit cycle, and does not capture the potential presence of standing waves.

Of paramount significance, various factors such as non-degeneracy ([Bauerheim \*et al.\*, 2015](#)), non-uniformity ([Noiray \*et al.\*, 2011](#)), and background noise ([Faure-Beaulieu \*et al.\*, 2021a](#)) can have considerable influence, capable of altering the direction, orientation, and characteristics of thermoacoustic modes. Numerous studies have incorporated

the impact of non-uniformities within their models. These non-uniformities can exist in geometry, flow dynamics, or flame characteristics, arising from factors such as azimuthal fluctuations in fuel-air ratio, distinct swirl directions of individual nozzles, or a discrete arrangement of nozzles distributed azimuthally. For instance, [Noiray \*et al.\* \(2011\)](#) analyzed a non-degenerate combustor system, considering non-uniform flame-acoustic coupling and mean temperature distributions. They demonstrated that weak non-uniformities could allow two standing modes to coexist, potentially resulting in a spinning or mixed wave. However, when non-uniformities were sufficiently high, only a single standing mode persisted, with the specific mode dependent on the shape of the non-uniformities. Similarly, a study by [Bauerheim \*et al.\* \(2015\)](#) considered a system with non-degeneracy arising from non-uniformities and azimuthal bulk flow. Their findings suggested that while non-uniformities tend to promote standing waves, azimuthal flow tends to promote spinning waves. When both non-uniformities and azimuthal bulk flow coexisted, a mixed wave emerged as a possibility. Moreover, [Ghirardo \*et al.\* \(2016\)](#) tackled a scenario involving degenerate eigenmodes and identical flames, where azimuthal variation resulted from discrete nozzles positioned azimuthally. Their study revealed the potential coexistence of standing and spinning waves, with the relative strengths of these modes determined by the spacing between the nozzles.

Quite notably, the thermoacoustic behavior of a combustor can exhibit a relatively fixed modal character or intermittently switch between one wave direction and another ([Fang \*et al.\*, 2021](#)), or between standing and spinning dominant wave ([Indlekofer \*et al.\*, 2021b](#)). More importantly, the influence of other factors such as non-degeneracy ([Bauerheim \*et al.\*, 2015](#)), non-uniformity ([Noiray \*et al.\*, 2011](#)), and background noise ([Faure-Beaulieu \*et al.\*, 2021a](#)) can change the direction, orientation as well as nature of the thermoacoustic modes. For example, [Krebs \*et al.\* \(2002\)](#) and [Worth and Dawson \(2013a,b\)](#) experimentally observed standing and spinning modes, as well as switching between them, depending on the operating conditions or burner arrangements. Another interesting point about azimuthal modes is the behavior of the nodal line during the limit cycle. In a system

characterized by rotational symmetry, the nodal line during azimuthal mode oscillations is not bound to remain fixed, in contrast to axial or radial mode oscillations. For instance, experimental observations by [Vignat \*et al.\* \(2020\)](#) showed the movement of the nodal line as seemingly erratic. However, the presence of system non-uniformities can anchor the nodal line at specific azimuthal locations, as demonstrated in experiments ([Prieur \*et al.\*, 2018](#)) and through reduced-order models ([Faure-Beaulieu \*et al.\*, 2021a](#); [Ghirardo \*et al.\*, 2021](#)). On the contrary, the deterministic motion of the nodal line has been observed in a few scenarios. Experimental investigations by [Kim \*et al.\* \(2021b,a\)](#) and [Worth and Dawson \(2013a\)](#) indicated that the nodal line periodically oscillates around a fixed azimuthal position on a slow time scale. Therefore, to comprehend the underlying principles resulting in the onset of azimuthal thermoacoustic instabilities, it becomes essential to systematically vary control parameters.

#### **1.4.2 Transition to azimuthal instabilities**

Studies that capture the dynamical transition to thermoacoustic instability in annular combustors through smooth variation of parameters remain few. One such notable study is by [Prieur \*et al.\* \(2017\)](#), wherein the authors mapped combustor dynamics on a parametric plane defined by equivalence ratio and bulk-flow velocity. They observed both longitudinal and azimuthal instability and noted a hysteresis cycle when the equivalence ratio varied in the fuel-rich limit. They showed the transitions in the combustor from chugging to spinning and finally to standing azimuthal modes. Recently, [Indlekofer \*et al.\* \(2021a\)](#) reported the transition from stable operation to self-excited azimuthal thermoacoustic modes. They showed a fascinating phenomenon wherein the self-oscillating azimuthal mode periodically alternates between CW and CCW spinning directions through standing mode. They termed this intricate behavior a beating azimuthal mode. The underlying deterministic mechanism driving this phenomenon was elucidated by [Faure-Beaulieu \*et al.\* \(2021b\)](#). Additionally, a recent study by [Ahn \*et al.\* \(2022\)](#) explored the variations in the amplitude of self-excited azimuthal instabilities as a function of equivalence ratio and hydrogen power fraction. Their work examined the heat release rate response

during self-excited azimuthal thermoacoustic instabilities within a pressurized annular combustor, specifically investigating hydrogen/methane blended flames.

## **1.5 SUPPRESSION OF THERMOACOUSTIC INSTABILITIES**

In the foregoing discussion, we highlighted the mechanisms behind the development of thermoacoustic instability and characterized the states that emerge during the transition to thermoacoustic instability. Now, we briefly review some of the practical approaches utilized for tackling thermoacoustic instability. Control of thermoacoustic instability is crucial for enhancing the stable operation of a gas turbine engine. Broadly, we can mitigate thermoacoustic instability by (1) disrupting the coupling between the unsteady heat release rate fluctuations and the acoustic field within the combustor, (2) enhancing damping within the system, (3) employing anti-sound to suppress limit cycle oscillations, and (4) implementing secondary fuel injection. Traditionally, approaches to mitigate thermoacoustic instability fall into two categories: active control (McManus *et al.*, 1993; Zhao *et al.*, 2018) and passive control (Richards *et al.*, 2003; Zhao and Li, 2015).

### **1.5.1 Active and passive control of thermoacoustic instabilities**

Active control involves employing external excitation, such as acoustic forcing and/or fuel modulation, to control thermoacoustic instability. It relies on three main components: (1) sensors, (2) controllers, and (3) actuators. There are two primary approaches to implementing active control, as detailed by Candel (2002): closed-loop and open-loop control. During closed-loop active control, the state of the combustor is continuously monitored and control measures are adopted based on the specific state of the system (Zhao *et al.*, 2018). In contrast, open-loop active control is achieved by forcing the system using actuators, without any feedback from controllers or sensors monitoring the dynamics in the combustor (Ćosić *et al.*, 2012). Active control methods often use external acoustic forcing (Bellows *et al.*, 2008; Balusamy *et al.*, 2015) or fuel-air modulation (Seume *et al.*, 1998; Uhm and Acharya, 2005) to achieve suppression, relying on the

forced synchronization of the thermoacoustic system (Balusamy *et al.*, 2015; Guan *et al.*, 2019a; Roy *et al.*, 2020).

Passive control involves altering specific aspects of the combustor, such as the acoustic characteristics or the heat release rate dynamics, changed independently of its regular operation (Zhao and Li, 2015). This alteration can be achieved through various means: adjusting acoustic characteristics using acoustic damping resonators (Duperé and Dowling, 2005), modifying heat release dynamics via fuel injection strategy (Steele *et al.*, 2000) or fuel staging (Samarasinghe *et al.*, 2017). Notably passive control strategies are effective only over a limited range of frequencies, requiring expensive and time-consuming design adjustments, and may be detrimental to engine performance.

Implementing these techniques poses significant challenges. Acoustic forcing mechanisms struggle to scale up to match the amplitude levels of the real turbulent combustors. In addition, ensuring the durability of actuators operating in the harsh environments of combustors is unreliable over the extremely long lifespan of turbulent combustors (Gang *et al.*, 2018; Guan *et al.*, 2019a).

### **1.5.2 Recent strategies for mitigating thermoacoustic instabilities**

Modern controlling strategies are expected to deliver effective solutions for mitigating thermoacoustic instability under diverse operating conditions, considering that gas turbine engines are designed to function across varying power levels and with different fuels. The quest for such solutions calls for mitigating methods that are versatile, intelligent, and cost-effective.

In alignment with this pursuit, Gopakumar *et al.* (2016) proposed a novel strategy involving the use of an actuated swirler for altering the coupling between the flame and the acoustic fluctuations. They found that actuating the static swirler, used for flame stabilization inside the combustion chamber, even at moderate rotation rates significantly altered the flow field and the flame structure (Mahesh *et al.*, 2018). This alternation

in the flow field caused by the actuating swirler was associated with the suppression of thermoacoustic instability, where low amplitude aperiodic oscillations are observed through an intermittency route, hinting towards the de-synchronization of the acoustic pressure and the heat release rate fluctuations during the state of suppression. The underlying mechanism of suppression was then modeled by [Dutta \*et al.\* \(2019\)](#) based on the synchronization of flame oscillators through the Kuramoto model ([Kuramoto, 1975](#)), which was able to quantitatively capture the heat release rate response observed in the experiments.

Several other studies have shown that by modifying the spatiotemporal dynamics of the flame/flow through injection of secondary air/fuel, mitigation of thermoacoustic instability is possible ([Lee \*et al.\*, 2000b](#); [Altay \*et al.\*, 2010](#); [Krishnan \*et al.\*, 2019](#); [Roy \*et al.\*, 2021](#)). Many passive control strategies are based on suppressing visible large-scale patterns such as large-scale coherent structures. Focusing on these large-scale coherent structures emerges as a possible way of controlling thermoacoustic instability. Thus, in recent years, a necessity has arisen to investigate thermoacoustic instability through non-conventional approaches focusing on disrupting the coupling between the acoustic pressure field and the unsteady heat release rate fluctuations.

## **1.6 THEORETICAL ANALYSIS OF THERMOACOUSTIC INSTABILITIES**

As previously mentioned, the origin of heat release rate fluctuations in a thermoacoustic system can add energy to the acoustic oscillations if the Rayleigh criterion is satisfied. This addition of energy to the acoustic pressure or velocity oscillations is known as acoustic driving. As a result, modeling the source of heat release rate fluctuations plays a crucial part in developing an accurate model for the thermoacoustic system. This section focuses on examining prevalent thermoacoustic models extensively utilized to capture longitudinal thermoacoustic instability.

### 1.6.1 Time delay model

The Rayleigh criterion in Eq. (1.1) shows the phase between the acoustic pressure and heat release rate fluctuations is important to the stability of the system. The most crucial aspect of modeling thermoacoustic instability is to explain the phase difference between the unsteady heat release rate fluctuations and the acoustic field. Such a model is the key to providing closure to the linear system of equations. The seminal work by Crocco and Cheng (1956) introduced a linearized model that addresses this aspect within a thermoacoustic system. This model, often termed the *n-tau* model or the sensitive time lag hypothesis, offers a simplified expression:  $\dot{q}' = n[u'(z_f, t - t_\tau)]$ . Here, the model encapsulates the interaction between the unsteady heat release rate and the acoustic field. According to this model, the fluctuations in the heat release rate are directly linked to the fluctuation in acoustic velocity at the flame location ( $z_f$ ), albeit delayed by a time lag  $t_\tau$ . The non-dimensional scaling factor, denoted as  $n$ , signifies the interaction index. The time lag  $t_\tau$  amalgamates several components: the time required for fuel to convect from the injection point to the flame front, the duration for the fuel-air mixture to mix with hot products, and the ignition delay. This model has found extensive use in investigating combustion instabilities, initially in liquid propellant rocket motors (Culick, 1988) and subsequently in gas turbine combustors (Dowling, 1995; Dowling and Stow, 2003).

### 1.6.2 FTF/FDF approach

One of the most successful approaches in modeling thermoacoustic systems is through the measurement of flame response decoupled from the acoustic analysis of the combustor. This approach, when expressed in the frequency domain, is referred to as a flame transfer and describing functions (FTF/FDF) (Merk, 1957, 1958; Schuller *et al.*, 2020), and when obtained in the time domain, leads to the concept of impulse response functions (Polifke, 2020). In FTF/FDF modeling, the flame response is illustrated using Bode plots discerning the gain and phase of frequency response. This is complemented by a linear stability analysis of the acoustic network in the frequency domain that reveals the growth rate of eigenmodes in terms of complex eigenfrequencies (Noiray *et al.*, 2008;

[Schuller \*et al.\*, 2020](#)). The measurement of the flame impulse response in the method of time delays, on the other hand, allows for a straightforward interpretation of the convective processes underlying the thermoacoustic system. When a transition to limit cycle oscillations is concerned, a bifurcation analysis is usually performed by modeling the flame response and its feedback on the acoustic fluctuations as a nonlinear oscillator ([Dowling, 1995](#); [Nicoud \*et al.\*, 2007](#); [Balasubramanian and Sujith, 2008](#); [Subramanian \*et al.\*, 2013](#); [Agharkar \*et al.\*, 2013](#); [Noiray \*et al.\*, 2011](#); [Ghirardo and Juniper, 2013](#); [Nair and Sujith, 2015](#)). Insights gained from FTF/FDF and time delay approaches are often utilized for estimating the dynamical flame models utilized in bifurcation studies ([Noiray and Schuermans, 2013](#); [Laera \*et al.\*, 2017b](#); [Noiray, 2017](#); [Bonciolini \*et al.\*, 2021](#)).

### **1.6.3 Kicked oscillator model**

In an alternative approach, [Matveev and Culick \(2003\)](#) formulated a reduced-order model that captures interactions among vortex shedding, the acoustic field, and combustion processes within a combustor. They modeled the interaction between the heat release rate fluctuations and the acoustic field as a kicked oscillator system, where the vortices that impinge on the bluff body impulsively force the acoustic field. Here, the periodic formation of coherent vortices induces oscillations in the flame and subsequently drives the acoustic field. Moreover, the shedding of vortices and their periodic impact on the combustor walls or flame stabilization mechanisms result in temporally localized instances of high heat release rates. While their model adeptly captured both stable and unstable combustor operations, it did not account for intermittency preceding thermoacoustic instability.

[Nair and Sujith \(2015\)](#) expanded upon this model by introducing turbulence effects as stochastic fluctuations in velocity that influenced the timing of kicks. This modification allowed the model to replicate the transition to thermoacoustic instability through intermittency within a bluff body-stabilized dump combustor. Further investigations by [Nair \*et al.\* \(2013\)](#) and [Tony \*et al.\* \(2015\)](#) suggested that aperiodic pressure fluctuations in

a combustor during stable operation exhibited deterministic characteristics. However, the model proposed by [Nair and Sujith \(2015\)](#) integrated stochastic elements to capture intermittency. Addressing this, [Seshadri \*et al.\* \(2016\)](#) introduced an enhanced deterministic model that eliminates the need for stochastic fluctuations to capture intermittency. They achieved this by establishing a refined feedback mechanism between the timing of kicks and the acoustic pressure/heat release rate oscillations. Within this framework, the thermoacoustic system is modeled as a kicked oscillator. The kicks, which are in feedback with pressure fluctuations, represent the energy added to the acoustic oscillator by localized intense heat release events. Adapted modification in the kicked oscillator model reproduces various synchronization states observed in bluff body combustors ([Pawar \*et al.\*, 2017](#)) and also exhibits the capability to predict the amplitude of oscillations during thermoacoustic instability in a turbulent combustor ([Seshadri \*et al.\*, 2018](#)).

#### **1.6.4 Van der Pol type model with nonlinear terms**

In this modeling approach, [Ananthkrishnan \*et al.\* \(1998\)](#) employed the Van der Pol oscillator with higher-order nonlinear terms to explain supercritical, subcritical, and secondary bifurcation in the system. They show that higher-order nonlinearities in the system can destabilize the stable branch of the limit cycle solution generated through a primary Hopf bifurcation, leading to a secondary fold bifurcation to a high-amplitude limit cycle. Building on this theoretical groundwork, [Ananthkrishnan \*et al.\* \(2005\)](#) proposed the theoretical feasibility of secondary bifurcation leading to thermoacoustic instability.

Recently, [Noiray and Schuermans \(2013\)](#) employed a noise-driven Van der Pol oscillator as a model for thermoacoustic oscillations in a turbulent combustor. Their study established a methodology for identifying the linear growth rates of a system by analyzing acoustic pressure fluctuations measured during limit cycle oscillations. They approached the fluctuations in limit cycle amplitudes during thermoacoustic instability as a response

of an oscillator perturbed by strong stochastic forcing due to turbulence. Notably, they estimated the linear growth rate of the oscillator from these fluctuating amplitudes in the limit cycle oscillations. Additionally, this model exhibited intermittency-like behavior, characterized by intermittent bursts of high-amplitude periodic pressure oscillations within the region of aperiodic fluctuations.

Although these modeling approaches have been useful in revealing the nature of bifurcation and the resulting stability characteristics of the limit cycle, they remain specific to the nature of nonlinearity encoded in the assumed flame model. The explanation for other types of bifurcation in these models required the inclusion of additional higher-order nonlinear terms with little physical justification and sometimes scarce experimental support. Another fundamental drawback of these models is the assumption of a lumped system where the nonlinear contributions of a spatially-extended convective-diffusive-reaction system underlying the premixed flame are parameterized temporally using functions such as quadratic, cubic, quintic function of acoustic perturbations (Laera *et al.*, 2017b; Noiray, 2017; Bhavi *et al.*, 2023). Consequently, these models cannot explain the rich spatiotemporal synchronization developing concomitantly during the transition to limit cycles (Mondal *et al.*, 2017b; Pawar *et al.*, 2019; Guan *et al.*, 2019b). Finally, there has been no clear resolution on what causes thermoacoustic transitions to be abrupt or continuous which has necessitated disparate modeling approaches.

## **1.7 OBJECTIVE OF THE CURRENT WORK**

The overall objective of the present thesis is to investigate the thermoacoustic response of the turbulent combustion systems followed by providing a possible way of suppressing thermoacoustic instability. However, the detailed objectives are summarised in the following:

1. Develop a turbulent annular combustor rig incorporating multiple swirl-stabilized burners that exhibit both longitudinal and azimuthal instabilities.

2. Systematically conduct experiments to explore the transition from a stable state to thermoacoustic instability. Quantify various possible dynamics routes to thermoacoustic instability when the control parameters are varied within the turbulent annular combustor.
3. Elucidate the mechanism responsible for altering the nature of the bifurcation and excitation of interesting dynamical states.
4. Quantify flame-flame and flame-acoustic interactions during the transition to thermoacoustic instabilities (longitudinal and azimuthal modes). This investigation aims to understand the overall thermoacoustic response of a combustor.
5. Introduce a quaternion-based formalism to comprehend azimuthal modes within the annular combustor. Then, compare and contrast the effect of the amplitude of acoustic pressure oscillations on the flames during various azimuthal modes in the combustor.
6. Develop a theoretical model to capture the dynamics observed in the experiments. In particular, the modeling approach should explain the temporal as well as spatiotemporal dynamics, further elucidating the underlying dynamics.
7. Implement an optimisation algorithm for model parameter estimation that allows us to pinpoint the exact correspondence between the experimental and the model parameters.
8. Apply insights into the physics underlying thermoacoustic instability gained from experiments to develop mitigation strategies for practical turbulent combustion systems prone to thermoacoustic instabilities.

## 1.8 OVERVIEW OF THE THESIS

The outline of the rest of the thesis is briefly described as follows. In Chapter 2, we detail experimental facilities where extensive experiments are carried out. We provide details of the annular combustor, dump combustor with bluff-body and swirler configuration, and rotating swirler combustor. We explain the experimental procedure and diagnostic techniques used for measuring heat release rate and acoustic pressure oscillations.

In Chapter 3, we discuss the change of criticality in a bifurcation due to parametric variation in the annular combustor. We depict three different routes to longitudinal thermoacoustic instability. We further discuss the crossover of bifurcation and the corresponding stability map of the combustor. Later, we discuss the global and local flame behavior during various dynamical states. In particular, we discuss the flame-flame and flame-acoustic interactions during the thermoacoustic transitions.

In Chapter 4, we consider the two distinct modeling approaches to explain the criticality of a bifurcation obtained by varying along a two-parameter family. We derive the model starting from the acoustic wave equation and expound the thermoacoustic models. This is followed by an explanation of the numerical solution and the optimisation method for estimating model parameters from experimental data. We further present the results from the model and experiments. We then discuss the global phase synchronization during the different thermoacoustic transitions. In particular, we explain how our modeling approaches capture the criticality of a bifurcation and explain the temporal as well as spatiotemporal dynamics observed in the experiments.

In Chapter 5, we introduce the method of characterizing azimuthal modes in the annular combustor followed by a procedure to obtain the modes from our experimental data. We further discuss the transition to azimuthal thermoacoustic instability and various dynamical states observed during this transition. With the help of quaternion-formalism, we explain the existence of different azimuthal modes in the combustor on varying the

control parameter. We further discuss the behavior of sixteen flames during different dynamical states. Finally, quantify flame-flame interactions.

In Chapter 6, we characterize the possible route to the suppression state by actuating a swirler in the turbulent combustor. We discuss the flame dynamics and spatiotemporal behavior of the phasor field during the transition to the suppression state. We further extend the model discussed in Chapter 4 by including the effect of an active swirler. We then showcase the applicability of the model by exactly capturing the dynamics which is observed in the experiments. In particular, we discuss the relationship between the control parameter in the model and experiments.

We conclude our discussion in Chapter 7, where we highlight the key findings and discuss the context of these findings and their practical implications. We close our discussion by summarizing many exciting research directions arising out of the present thesis.

## CHAPTER 2

### EXPERIMENTAL SETUPS AND DIAGNOSTICS

In this chapter, we discuss the experimental facilities and diagnostics used for conducting experiments and acquiring data related to the results presented in this thesis. Four different studies were performed on primarily three different setups:

1. A swirl-stabilized turbulent annular combustor is used to study the change in criticality of a bifurcation along the two-parameter family.
2. The same annular combustor with certain modifications is used to study the transition to self-sustained azimuthal instability in the combustor.
3. Longitudinal dump combustor with bluff-body and swirler configurations is used to study continuous and abrupt transition, respectively<sup>1</sup>.
4. A rotating swirler combustor is used to investigate the mitigation of thermoacoustic instability in a turbulent environment<sup>2</sup>.

#### 2.1 ANNULAR COMBUSTOR FACILITY

We perform experiments on the laboratory-scale annular combustor comprising sixteen swirl-stabilized burners as shown in figure 2.1(a). The schematic of different parts of the experimental setup is shown in figure 2.1(b-d). Our combustor is close to the designs of the [Bourgouin \*et al.\* \(2013\)](#) and [Worth and Dawson \(2013a\)](#). This setup consists of the premixing chamber, settling chamber, burner tubes, and combustion chamber as

---

<sup>1</sup>We are thankful to a team consisting of Dr. Induja Pavithran, Dr. Manikandan Raghunathan, Mr. Midhun P. R., and Prof. R. I. Sujith for generously providing us with the datasets in February 2022.

<sup>2</sup>We extend our gratitude to Dr. Ankit K. Dutta for performing the experiments and Prof. Swetaprovo Chaudhuri for graciously providing us with the dataset in August 2021. The experiments were performed in the Turbulent Combustion and Spray Research Lab at the Indian Institute of Science, Bangalore, India.

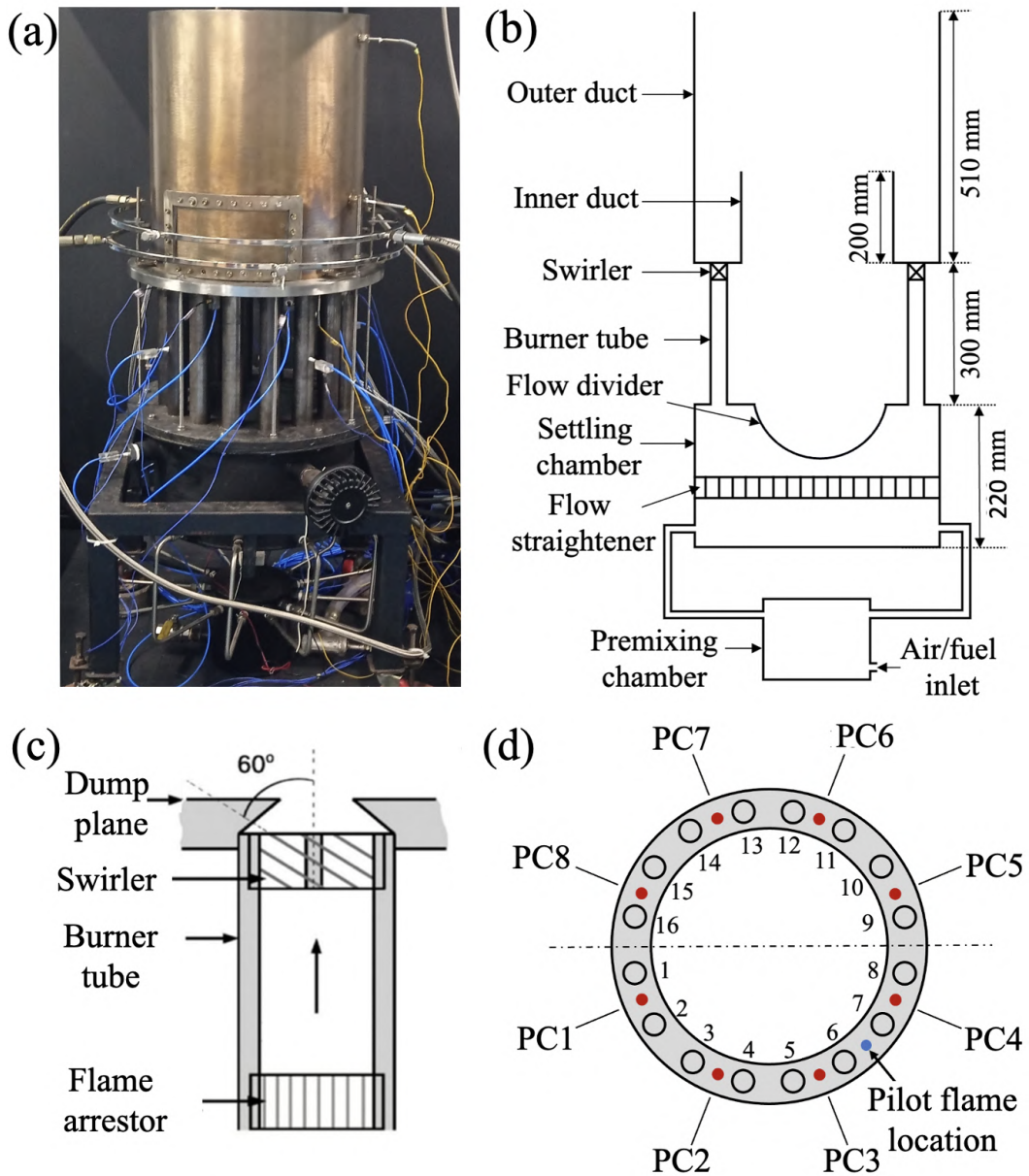


Figure 2.1: (a) Photograph of the annular combustor rig at IIT Madras, Chennai. Schematic of the (b) cross-section of the combustor, (c) the burner tube, and (d) the dump plane. The location of the eight pressure transducers is named as PC1, PC2, ..., PC8. The non-premixed pilot flame is used to ignite the sixteen flames in the combustion chamber. Eight flames are acquired during the longitudinal instability, while sixteen flames are acquired during the azimuthal instability.

shown in figure 2.1(b). Dehumidified air from a compressor was mixed with liquefied petroleum gas (LPG - 40% propane and 60% butane by volume) in a premixing chamber to produce a technically premixed air-fuel mixture. The mixture then enters the bottom

of the settling chamber through twelve equispaced inlet ports. Each port has an internal diameter of 9.5 mm and is mounted perpendicular to the axis of the combustion chamber. A mixture is then passed through a honeycomb mesh to arrest any transverse velocity fluctuations, followed by a hemispherical bluff body to improve flow uniformity through all the burners.

The reactant mixture is now divided into sixteen burner tubes, each burner tube comprises a flame arrestor at the bottom and a swirler on the top (refer figure 2.1c). Sixteen flame arrestors are circular disks of 10 mm thickness and 36 mm diameter with 179 holes of 1.5 mm diameter are mounted at the bottom of each burner tube to prevent flashback. The sixteen swirlers have a central shaft of 15 mm diameter on which six guide vanes are mounted at an angle of  $\delta_\alpha = 60^\circ$  relative to the shaft axis. The geometric swirl number is calculated as  $S = 2/3 \tan \delta_\alpha = 1.15$  (Candel *et al.*, 2014). A converging section having a contraction area ratio of 2, height of 18 mm, and exit diameter  $d = 15$  mm connects the burner tube to the dump plane (see figure 2.1c).

The dump plane consists of sixteen burner inlets, a port for a pilot flame, and eight pressure measurement ports (see figure 2.1d). A non-premixed pilot flame anchored between two injectors was used to ignite the premixed flames, which was extinguished following flame stabilization in the combustor. Finally, the air-fuel mixture enters the combustor chamber, where the chamber is made up of two concentric ducts of different lengths. Depending on the type of experiments we perform, we modify the dimensions of the settling chamber, burner tube, and concentric ducts.

### **2.1.1 Longitudinal thermoacoustic instability in annular combustor**

To excite self-sustain longitudinal thermoacoustic instability in the annular combustor, the dimensions of the settling chamber, burner tube, and concentric ducts are altered. The diameter and length of the settling chamber are 400 mm and 440 mm, respectively. The inner diameter and length of the burner tubes are 30 mm and 150 mm, respectively.

Moreover, the inner duct has a diameter of 300 mm and a length of 200 mm, while the outer duct has a diameter and length of 400 mm.

Air ( $\dot{m}_a$ ) and fuel ( $\dot{m}_f$ ) flow rates are controlled using mass flow controllers (MFC). Each MFC has an uncertainty of  $\pm 0.8\%$  and an additional  $0.2\%$  uncertainty of the full-scale. The equivalence ratio is controlled by keeping  $\dot{m}_a$  at  $2.86 \times 10^{-2} \text{ kgs}^{-1}$  fixed and varying  $\dot{m}_f$  from  $1.2 \times 10^{-3}$  to  $1.4 \times 10^{-3} \text{ kgs}^{-1}$ . The equivalence ratio is calculated as  $\phi = (\dot{m}_f/\dot{m}_a)_{\text{actual}}/(\dot{m}_f/\dot{m}_a)_{\text{stoichiometry}}$ . The Reynolds number for the reactive flow is computed using the expression  $Re = 4\dot{m}/\pi\mu_a d_0$ , where  $\dot{m} = \dot{m}_a + \dot{m}_f$  is the mass flow rate of the air–fuel mixture,  $\mu_a$  is the dynamic viscosity of the air–fuel mixture at the experimental conditions obtained by following [Wilke \(1950\)](#), and  $d_0$  is the diameter of the burner. Thus,  $\phi$  is varied in the range of 0.44 to 0.53 and  $Re$  is around  $8.6 \times 10^3$ . In these experiments, the parameter range is such that only longitudinal instability is excited, as verified by the negligible phase difference in the acoustic pressure fluctuations measured by the transducers mounted on the combustor backplane (refer to [Appendix A](#)).

A piezoelectric transducer and high-speed camera are used concomitantly to capture acoustic pressure and heat release rate fluctuations, respectively. The acoustic pressure fluctuations are recorded using three equispaced piezoelectric transducers (PCB Piezotronics, PCB103B02, sensitivity -  $217.5 \text{ mV/KPa}$ , uncertainty -  $\pm 0.15 \text{ Pa}$ ), at equidistant to each other, are mounted on a waveguide (diameter 4 mm and length 3.2 m) at a distance of 75 mm from the combustor backplane. The pressure signals were acquired for 3 s at a sampling frequency of 10 kHz and digitized using a National Instruments 16-bit PCI 6343 card.

A high-speed CMOS camera (Phantom V 12.1) with CH\* filter (bandwidth of  $435 \pm 10 \text{ nm}$ ) is used to capture chemiluminescence images of the flames. The camera is operated at a sampling frequency of 2 kHz and a pixel resolution of  $1280 \times 800$ . A combustor half-plane of size  $400 \text{ mm} \times 200 \text{ mm}$  consisting of eight flames is visualized with the aid

of an air-cooled mirror placed overhead of the combustor. The position of eight burners, as imaged by the camera, has been numbered as 1-8 in figure 2.1(d). The camera was outfitted with a Nikon AF Nikkor 70-210 mm  $f/4 - f/5.6$  camera lens. A total number of 5,563 images were acquired for each state of combustor operation. A pulse generated from a Tektronix AFG1022 function generator was used to trigger the camera and the PCI card to acquire measurements simultaneously.

### 2.1.2 Azimuthal thermoacoustic instability in annular combustor

To excite self-sustain azimuthal thermoacoustic instability in the annular combustor, the dimensions of the settling chamber, burner tubes, and concentric ducts are altered again. The diameter and length of the settling chamber are 400 mm and 220 mm, respectively. The inner diameter and length of the burner tubes are 30 mm and 300 mm, respectively. Moreover, the inner duct has a diameter of 300 mm and a length of 200 mm, while the outer duct has a diameter of 400 mm and a length of 510 mm. In these experiments, the equivalence ratio ( $\phi$ ) is controlled by keeping  $\dot{m}_a$  fixed at  $3.67 \times 10^{-2} \text{ kgs}^{-1}$  and varying  $\dot{m}_f$  from  $3.28 \times 10^{-3}$  to  $2.42 \times 10^{-3} \text{ kgs}^{-1}$ . Here,  $\phi$  is varied in the range of 1.38 - 1.02, and  $Re$  is around  $1.14 \times 10^4$ . The relevant properties of this combustor configuration are discussed in table 2.1

We concurrently measure the acoustic pressure fluctuations ( $p'$ ) and the heat release rate fluctuations ( $\dot{q}'$ ) using the eight piezoelectric pressure transducers (named PC1, PC2,..., PC8) and the two high-speed cameras, respectively. Pressure measurements are performed using a PCB103B02 piezoelectric transducer mounted on the backplane of the combustor between two burners at eight locations (see figure 2.1d). The sensitivity of all transducers is 217.5 mV/kPa (uncertainty of  $\pm 0.15$  Pa). To measure the fluctuating heat release rate around the annulus, a Phantom v12.1 CMOS camera and a Phantom VEO 710S CMOS camera equipped with CH\* filters are used. In order to protect the camera from the hot exhaust gases, the movies were acquired with the aid of two air-cooled mirrors placed overhead of the combustor. We used Nikon AF Nikkor 70 – 210 mm

<b>Feature</b>	<b>Annular combustor</b>
Flame holding mechanism	Swirler
Type of bifurcation	Continuous, Azimuthal
Reynolds number, $Re$	$1.14 \times 10^4$
Equivalence ratio, $\phi$	1.38 - 1.02
Pressure measurement	10 kHz
Photomultiplier tube	Not Available
High speed imaging	5 kHz

Table 2.1: Relevant properties of an annular combustor considered in this study for self-excited azimuthal instability.

$f/4$  to  $f/5.6$  camera lens in both cameras to focus on the region of interest in the experiments. The  $\text{CH}^*$  filters used in our experiments have a  $435 \pm 10$  nm bandwidth. The pressure signal was acquired for a duration of 5 s with a sampling rate of 10 kHz, and the cameras were operated at a frame rate of 5 kHz and a resolution of  $1280 \times 800$  pixels. A total number of 5,562 and 6,240 images were acquired for each state of combustor operation using the Phantom v12.1 and Phantom VEO 710S cameras, respectively. A pulse generated using the Tektronix AFG1022 function generator is used to trigger the camera and the PCI card to acquire measurements simultaneously.

## 2.2 TURBULENT DUMP COMBUSTOR

Two configurations of the dump combustor were considered: (1) circular bluff-body and (2) fixed-vane swirler stabilized flames. These two configurations show distinct routes to limit cycle oscillation, each exhibiting disparate dominant frequency and amplitude in the oscillations of acoustic pressure and heat release rate. The combustor comprises a plenum connected upstream of a burner tube of 40 mm diameter. The burner tube is connected to the combustion chamber of cross-sectional area  $90 \times 90$  mm (figure 2.2a). The burner supports a central shaft of diameter 16 mm, which holds the bluff-body or the swirler in place. Fuel is delivered to the burner tube by four injection holes in the shaft, each of diameter 1.7 mm, 120 mm upstream of the flame holder. Ignition of the

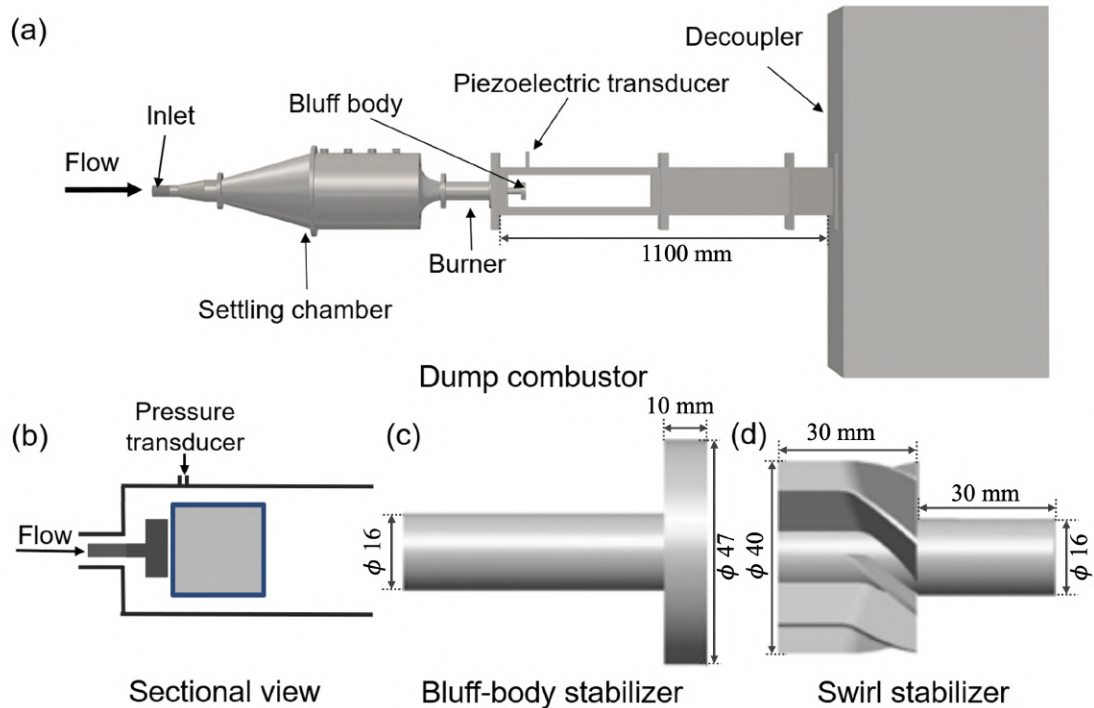


Figure 2.2: (a) Schematic of the dump combustor. (b) Schematic of the combustor cross-section indicating the chemiluminescence field of view. We use two different flame-holding mechanisms, (c) a bluff-body and (d) swirl, attached to the burner by a central shaft. The shaded area in (b) is captured using  $\text{CH}^*$  imaging. The box in (b) is the region chosen for synchronization analysis. The experiments on a bluff-body configuration were conducted by Dr. Manikandan Raghunathan and a swirl-stabilized configuration by Dr. Induja Pavithran under the guidance of Prof. R. I. Sujith at IIT Madras, Chennai.

combustible air-fuel mixture is facilitated by an 11 kV spark plug, flush mounted on the dump plane. Combustion by-products are exhausted into the atmosphere via an acoustic decoupler of size  $1000 \times 500 \times 500$  mm. The relevant properties of the annular combustor and two configurations of dump combustor that exhibit longitudinal instability are discussed in table 2.2.

### 2.2.1 Bluff-body stabilized configuration

The flame holder is a cylindrical bluff-body (diameter 47 mm and width 10 mm) mounted on the central shaft, located 45 mm downstream of the dump plane (figure 2.2c). The combustion chamber is 1100 mm in length. In this configuration, experiments were

<b>Feature</b>	<b>Dump combustor</b>	<b>Dump combustor</b>	<b>Annular combustor</b>
Flame holding mechanism	Bluff-body	Swirler	Swirler
Type of bifurcation	Continuous	Secondary, abrupt	Secondary, abrupt
Reynolds number, $Re$	$2.2 \times 10^4$ - $3.2 \times 10^4$	$1.7 \times 10^4$ - $2.7 \times 10^4$	$8.6 \times 10^3$
Equivalence ratio, $\phi$	0.56 - 0.86	0.53 - 0.81	0.44 - 0.53
Pressure measurement	20 kHz	10 kHz	10 kHz
Photomultiplier tube	20 kHz	10 kHz	Not Available
High speed imaging	5 kHz	Not Available	2 kHz

Table 2.2: Relevant properties of the turbulent combustors considered in this study for self-excited longitudinal instability.

performed by maintaining a constant rate of fuel flow  $\dot{m}_f = 8 \times 10^{-4} \text{ kgs}^{-1}$  and varying the rate of air flow in steps from  $\dot{m}_a = 1.0 \times 10^{-2}$  to  $1.6 \times 10^{-2} \text{ kgs}^{-1}$ . Consequently, the equivalence ratio varies from  $\phi = 0.86$  to  $0.56$  and  $Re$  from  $2.2 \times 10^4$  to  $3.2 \times 10^4$ .

A photomultiplier tube (PMT) and pressure transducers are used for measuring the heat release rate and acoustic pressure oscillations in the combustor at a sampling frequency of 20 kHz. The PMT is equipped with a  $\text{CH}^*$  filter. High-speed  $\text{CH}^*$  chemiluminescence images are also obtained using a CMOS camera capturing  $400 \text{ mm} \times 90 \text{ mm}$  of the combustor onto  $1200 \text{ pixels} \times 800 \text{ pixels}$  of the sensor and a framing rate of 5 kHz. A total number of 7,418 images were acquired for each state of combustor operation. For this combustor, a rectangular region of size  $50 \text{ mm} \times 50 \text{ mm}$  after the bluff-body, as shown by the box in figure 2.2(b), is used for spatiotemporal analysis. All three measurements were obtained simultaneously.

### 2.2.2 Swirl-stabilized configuration

The swirler consists of eight guided vanes of 1 mm thickness and is mounted on a central shaft and positioned at the exit of the burner (figure 2.2d). The guided vanes are inclined at  $40^\circ$  with respect to the injector axis. The swirler has a length of 30 mm and a diameter of 40 mm. At the outer end of the swirler, a center body of diameter 16 mm and length 30 mm is attached to aid flame stabilization. In these experiments,  $\dot{m}_f$  is maintained

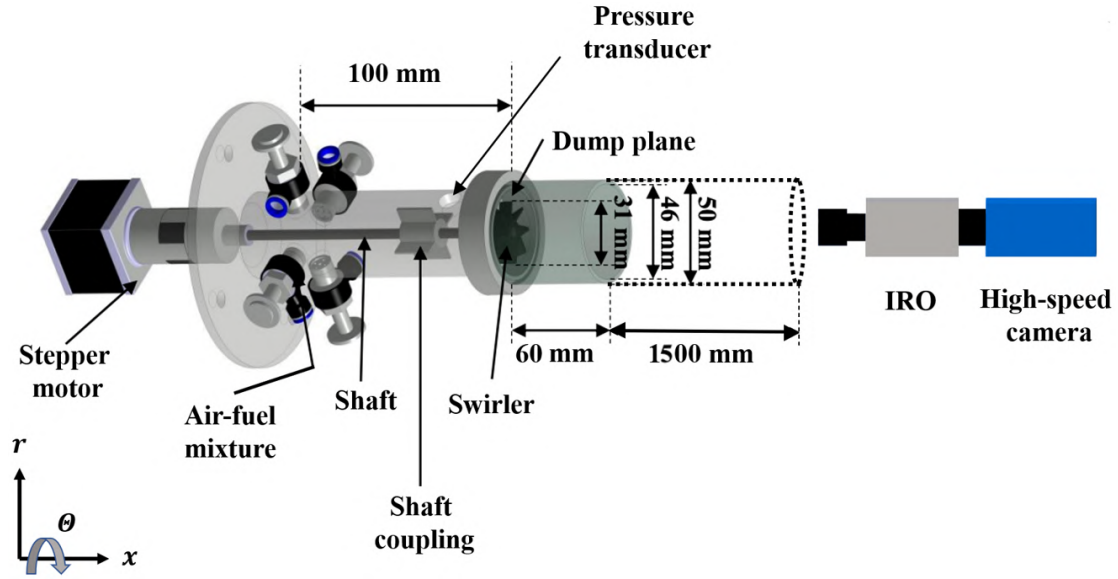


Figure 2.3: A schematic of the experimental setup used for suppressing thermoacoustic instability along with the diagnostic tools. The swirler is actuated using the stepper motor for mitigation of thermoacoustic instability. The experiments were performed in the Turbulent Combustion and Spray Research Lab at IISC, Bangalore.

at  $7 \times 10^{-4} \text{ kgs}^{-1}$  and  $\dot{m}_a$  is varied from  $0.8 \times 10^{-2}$  to  $1.4 \times 10^{-2} \text{ kgs}^{-1}$ . As a result,  $\phi$  varies in the range of 0.81 to 0.53, and  $Re$  varies in the range of  $1.7 \times 10^4$  to  $2.7 \times 10^4$ . In this arrangement, only the pressure and the heat release rate fluctuations are measured using a pressure transducer and PMT at 10 kHz, respectively.

### 2.3 ROTATING SWIRLER COMBUSTOR

The experiments on the laboratory-scale turbulent combustor at IISC, Bangalore were used to control thermoacoustic instability by actuating the swirler. The schematic of the lab-scale premixed turbulent combustor is shown in figure 2.3. The combustor was characterized in previous work (Gopakumar *et al.*, 2016; Mahesh *et al.*, 2018; Dutta *et al.*, 2019) in a vertical configuration and is used in the present experiments in a horizontal configuration to facilitate length variation and imaging. The mitigation of thermoacoustic instability upto  $\sim 20$  dB is achieved for the horizontal setup under similar operating conditions as the vertical one, reported in the earlier works (Dutta *et al.*, 2019; Mahesh

<b>Feature</b>	<b>Rotating swirler combustor</b>
Flame holding mechanism	Swirler
Type of bifurcation	Continuous
Reynolds number, $Re$	$6 \times 10^3$
Equivalence ratio, $\phi$	0.68
Pressure measurement	10 kHz
Photomultiplier tube	Not Available
High speed imaging	2 kHz

Table 2.3: Relevant properties of the turbulent combustor considered in this study for suppressing thermoacoustic instability.

*et al.*, 2018). This establishes that the overall functioning and observations from the experimental setup remain unaffected by the change in orientation. A lean mixture ( $\phi = 0.68$ ) consisting of 6.5 SLPM (standard liter per minute) of methane and 90 SLPM of air (Reynolds number,  $Re = 6 \times 10^3$  based on swirler diameter, with an uncertainty of  $\pm 0.8\%$ ) is supplied into the settling chamber through four equally spaced inlet ports. The relevant properties of this combustor configuration for suppressing thermoacoustic instability are discussed in table 2.3.

The reactant mixture flows into the combustion chamber made of quartz, having a diameter of 46 mm and a length of 60 mm, where it is ignited. An aluminum duct of 1.5 m in length is mounted over the quartz duct which act as a resonator to generate self-excited thermoacoustic instability in the combustor. The flame stabilization is achieved using the swirler having a diameter of 30 mm and consisting of eight straight vanes inclined at  $\delta_\alpha = 30^\circ$  with the axis mounted on the central shaft of the motor. The geometric swirl number is obtained as  $S = 2/3 \tan \delta_\alpha = 0.385$ . The swirler is actuated through a stepper motor to a maximum speed of 2100 rpm for the suppression experiments.

The airflow rate ( $\dot{m}_a$ ) and the fuel flow rate ( $\dot{m}_f$ ) are controlled using digital mass flow controllers (Alicat Scientific, MCR series) with a measurement uncertainty of  $\pm(0.8\%$

of reading + 0.2% of full-scale). Acoustic signatures from the combustor are acquired using a Kistler pressure transducer (sensitivity 1.84 V/bar, uncertainty  $\pm 0.2$  %) mounted 20 mm upstream of the dump plane. The pressure signals are acquired for a duration of 5 s at a sampling frequency of 10 kHz and digitized using a National Instruments 16-bit PCI 6251 card. A high-speed CMOS camera (Photon SA5) fitted with LaVision IRO (Intensified Relay Optics) and Tamaron 150-600 mm  $f/5-6.3$  telephoto lens is used to capture the unfiltered chemiluminescence images of the flame. The camera recorded 60 mm  $\times$  60 mm of the combustion chamber onto 480 pixels  $\times$  480 pixels of the sensor at a framing rate of 2 kHz while focused at the  $r - \Theta$  plane at 5 mm height from the swirler exit. A total number of 10,000 images were acquired at each state of the combustor operation. The acoustic pressure and imaging measurements were recorded simultaneously for making quantitative assessments.



## CHAPTER 3

# CRITICALITY OF BIFURCATION IN ANNULAR COMBUSTOR

In this chapter, we quantify various possible dynamical transitions to longitudinal thermoacoustic instability in the swirl-stabilized annular combustor. The current configuration of the annular combustor exhibits longitudinal thermoacoustic instability and is discussed in Section 2.1.1. Our focus is on understanding how varying the bulk velocity alters the characteristics of the bifurcations leading to thermoacoustic instability obtained by changing the equivalence ratio alone. We aim to compare and contrast the response of global flame structure during different dynamical states. We also assess the local flame response by determining the normalized amplitude and phase of the heat release rate fluctuations of each burner during each of the dynamical states. The primary objective is to discuss possible routes to longitudinal thermoacoustic instability in a natural setting without resorting to external forcing. Additionally, quantify the flame-flame and flame-acoustic interaction in the annular combustor during the transition from combustion noise to longitudinal thermoacoustic instability.

### 3.1 ROUTES TO LONGITUDINAL THERMOACOUSTIC INSTABILITY

To study the dependence of the characteristics of bifurcation transitioning to longitudinal thermoacoustic instability in the annular combustor, we vary the bulk flow velocity in

---

The results presented in this chapter are published in the following two papers:

1. Singh, S., Roy, A., Reeja, K. V., Nair, A., Chaudhuri, S., Sujith, R. I. (2021). Intermittency, Secondary Bifurcation and Mixed-Mode Oscillations in a Swirl-Stabilized Annular Combustor: Experiments and Modeling. *J. Eng. Gas Turbine Power*, 143 (5), 051028.
2. Roy, A., Singh, S., Nair, A., Chaudhuri, S., Sujith, R. I. (2021). Flame dynamics during intermittency and secondary bifurcation to longitudinal thermoacoustic instability in a swirl-stabilized annular combustor. *Proc. Combust. Inst.*, 38 (4), 6221-6230.

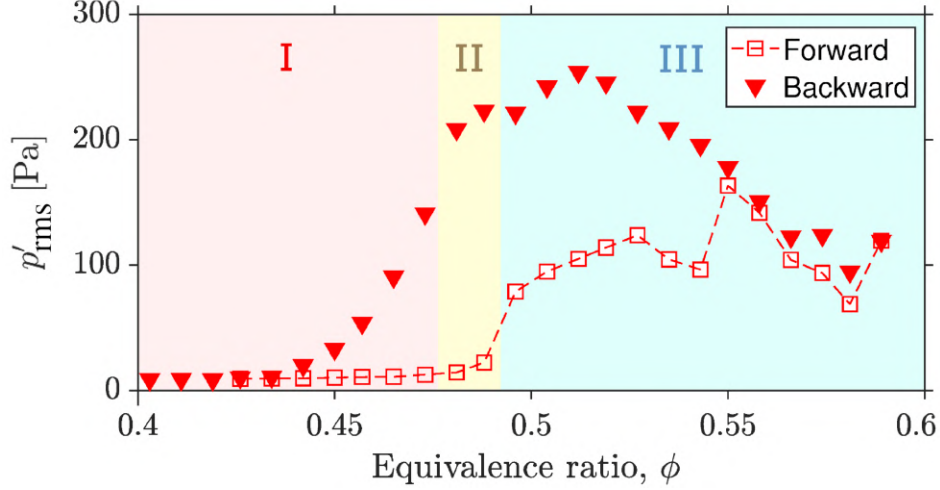


Figure 3.1: Transition from combustion noise (CN) to thermoacoustic instability (TAI) when  $\phi$  is increased ( $\square$ ) for  $v_z \approx 6.09$  m/s. Region I to III corresponds to the states of CN, intermittency, TAI.

the range  $v_z = 5.5$  to  $12$  m/s ( $Re = 0.56 - 1.22 \times 10^4$ ). For each value of  $v_z$ , we vary  $\phi$  in the range of  $0.4 - 0.62$ .

### 3.1.1 Transition to thermoacoustic instability through continuous bifurcation

Figure 3.1 shows the variation of root-mean-square (rms) value of pressure oscillations ( $p'_{rms}$ ) as a function of equivalence ratio ( $\phi$ ) corresponding to bulk flow velocity  $v_z \approx 6.09$  m/s. For  $\phi \leq 0.47$  (region I), we observe the state of combustion noise (CN) with  $p'_{rms} \sim 20$  Pa. For  $\phi$  between  $0.47$  to  $0.49$  (region II), we observe intermittency in pressure oscillations with  $p'_{rms} \sim 60$  Pa. For  $\phi > 0.49$ , we observe the state of low-amplitude TAI with  $p'_{rms} \sim 100$  Pa. On decreasing  $\phi$  from  $0.60$  to  $0.40$ , hysteresis is seen in the system dynamics. The amplitude of low-amplitude TAI decreases gradually as  $\phi$  is lowered. The hysteresis and the difference in the amplitude of oscillations in the forward and reverse path possibly arise due to thermal inertia of the combustor walls (Bonciolini *et al.*, 2019).

For low bulk velocities from  $v_z \approx 6$  to  $6.5$  m/s, the transition from CN to low-amplitude TAI of the acoustic subsystem takes place through a bifurcation similar to supercritical Hopf bifurcation (Nair *et al.*, 2014), as illustrated in 3.1. Since the flow is turbulent,

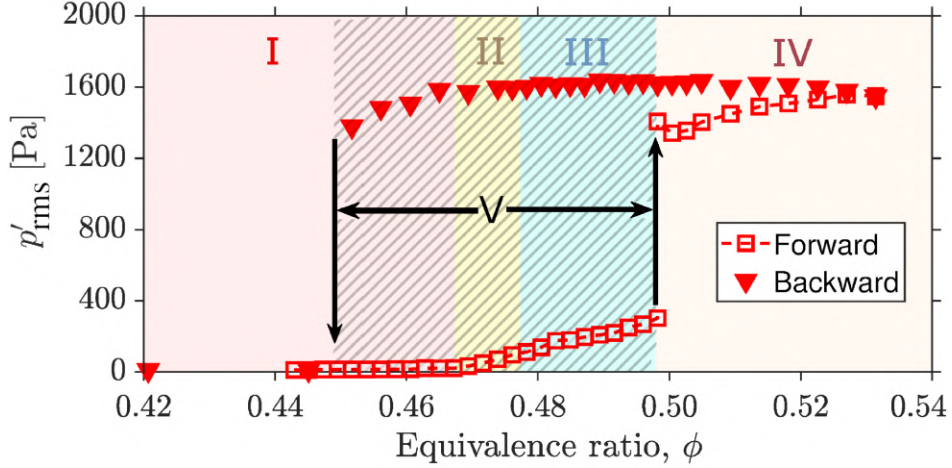


Figure 3.2: Observed transition from combustion noise (CN) to thermoacoustic instability (TAI) when  $\phi$  is increased ( $\square$ ) and back to CN when  $\phi$  is decreased ( $\blacktriangledown$ ) for  $v_z \approx 8.51$  m/s. Region I to V correspond to the states of CN, intermittency, low-amplitude TAI, high-amplitude TAI and bistable region (hatched region).

the transition is associated with an intermittent state between the state of CN and TAI. This is different from a conventional supercritical bifurcation where the dynamics are expected to change smoothly from CN to TAI.

### 3.1.2 Transition to thermoacoustic instability through abrupt bifurcation

In figure 3.2, we plot the variation of  $p'_{\text{rms}}$  as a function of  $\phi$  at  $v_z \approx 8.51$  m/s. For  $\phi \leq 0.47$  (region I), the amplitude of pressure fluctuations is very low, indicating the state of combustion noise (CN). Upon increasing  $\phi$  up to 0.50 (region II and III), we first notice the state of intermittency followed by low-amplitude TAI. On increasing  $\phi$  past 0.50 (region IV), we observe an abrupt increase in the amplitude of  $p'_{\text{rms}}$  indicating a secondary bifurcation to high-amplitude TAI. At the fold point ( $\phi = 0.49$ ), the low-amplitude stable limit cycle loses stability and jumps to a secondary limit cycle, which has a higher amplitude. The bistable region (hatched region V in figure 3.2) is obtained for  $\phi = 0.54$  to 0.45. The difference of about 400 Pa between the forward and reverse path is possibly due to different boundary conditions of the combustor as a result of prolonged operations.

In figure 3.3, we plot the time series and the power spectrum of  $p'$  during different states

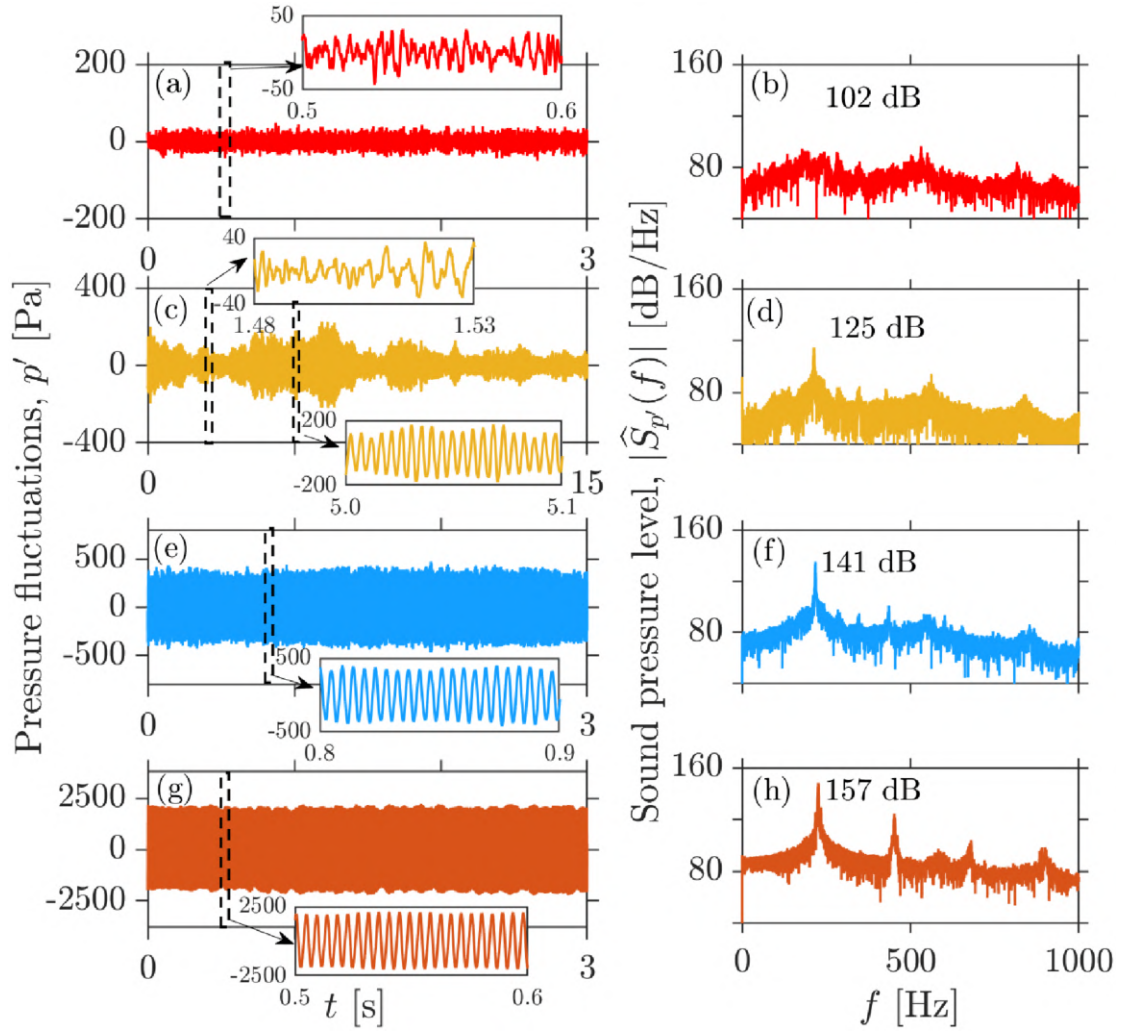


Figure 3.3: Time series and the power spectrum of pressure fluctuations observed during the states of (a,b) combustion noise (CN), (c,d) intermittency (INT), (e,f) low-amplitude TAI, and (g,h) high-amplitude TAI for  $v_z \approx 8.51$  m/s. Experimental conditions: (a, b)  $\phi = 0.44$ , (c, d)  $\phi = 0.48$ , (e, f)  $\phi = 0.49$ , and (g, h)  $\phi = 0.5$ .

of combustor operation for  $v_z \approx 8.51$  m/s acquired in the forward direction. At  $\phi = 0.44$ , we observe aperiodic oscillations having broadband spectrum, indicating the state of CN (figures 3.3a,b). At  $\phi = 0.48$ , there are intermittent bursts of high-amplitude periodic pressure oscillations amidst low-amplitude aperiodic pressure fluctuations (see insets), corresponding to the state of intermittency (figure 3.3c) (Nair *et al.*, 2014). In order to ensure that the state of intermittency is statistically stable, we show a long time series of 15 s. We also notice that the power spectrum narrows at  $f_n \approx 213$  Hz associated with the

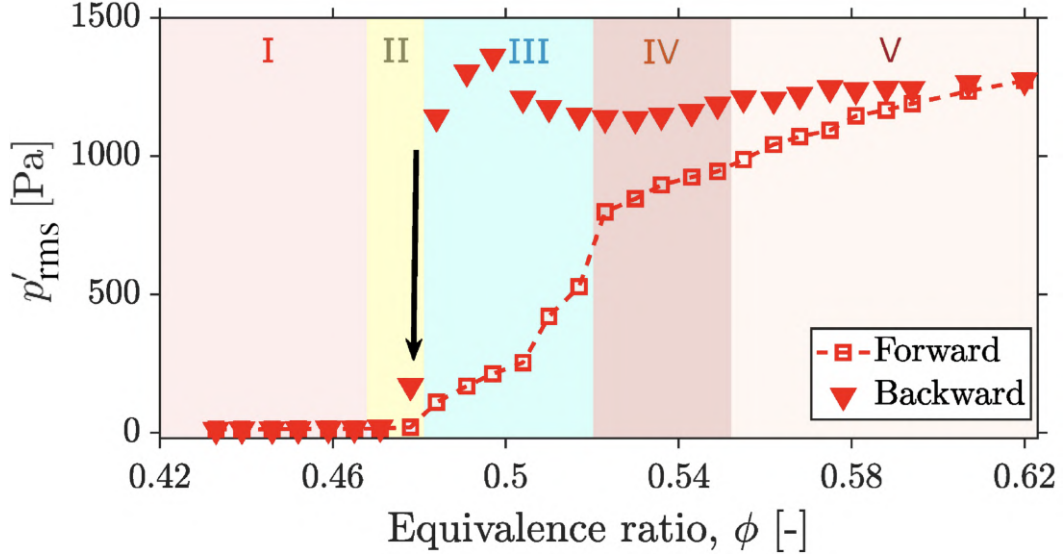


Figure 3.4: Transition from CN to high-amplitude TAI when  $\phi$  is varied for  $v_z \approx 7.3$  m/s. The transition from low-amplitude TAI to high-amplitude TAI takes place through MMO. Region I to V corresponds to CN, intermittency, low-amplitude TAI, MMO, and high-amplitude TAI.

first longitudinal mode of the combustor with an intensity of 125 dB (figure 3.3d). At  $\phi = 0.49$ ,  $p'$  is periodic with a dominant peak at  $f_n \approx 218$  Hz and intensity of 141 dB (figures 3.3e,f). The characteristics of low-amplitude TAI are very similar to what was reported in (Bourgouin *et al.*, 2013). We refer to this state as low-amplitude TAI. Finally, at  $\phi = 0.50$ ,  $p'$  is periodic with  $p'_{\text{rms}} \approx 1425$  Pa corresponding to  $f_n \approx 227$  Hz and intensity of 157 dB (figures 3.3g,h). This state is referred to as high-amplitude TAI. Similar high-amplitude TAI has also been reported for a standing mode of azimuthal thermoacoustic instability in a similar configuration (Vignat *et al.*, 2020), further exemplifying the relevance of the problem.

### 3.1.3 Transition to thermoacoustic instability through mixed-mode oscillations

As we discussed, for  $v_z < 7$  m/s, the combustor dynamics exhibit the state of low-amplitude TAI, while for  $v_z > 7.5$  m/s there is a secondary fold bifurcation of low-amplitude TAI to high-amplitude TAI. Figure 3.4 shows  $p'_{\text{rms}}$  as a function of  $\phi$  for  $v_z \approx 7.3$  m/s. As before, we observe the state of CN (region I), intermittency (region II),

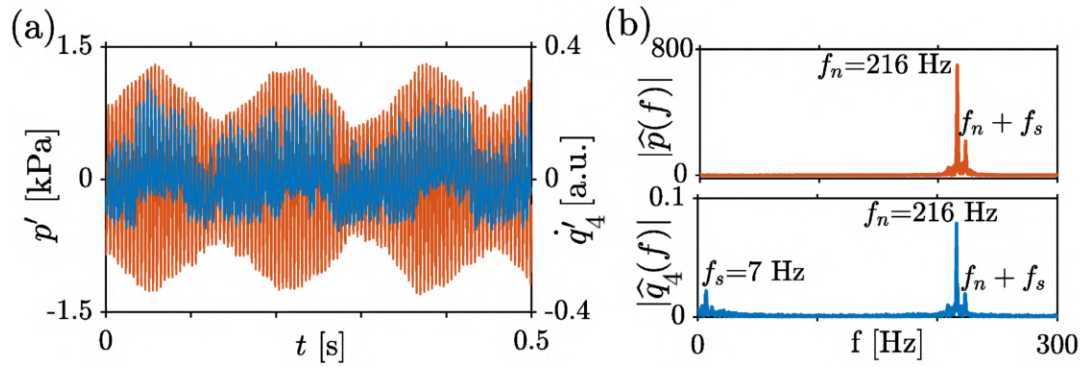


Figure 3.5: (a,b) Time series of  $p'$  (orange) and  $q'_4$  (blue), and the corresponding amplitude spectrum during MMO at  $\phi = 0.54$ .

low-amplitude TAI (region III), and high-amplitude TAI (region V). Of special interest here is the transition from low-amplitude TAI to high-amplitude TAI. The transition is not abrupt, but takes place smoothly with a monotonic increase in the value of  $p'_{\text{rms}}$  (figure 3.4). Here, the transition from low-amplitude TAI to high-amplitude TAI takes place through mixed-mode oscillations (see figure 3.5a).

A representative time series of  $p'$  during the mixed-mode oscillations (MMO) at  $\phi = 0.54$  (region IV) is shown in orange in figure 3.5(a). The associated amplitude spectrum  $|\hat{p}(f)|$  is shown in figure 3.5(b). The peaks at  $f_n = 216$  Hz and  $f_n + f_s = 223$  Hz are indicated. The low-frequency modulation calculated from the envelope of  $p'$  is  $f_s = 7$  Hz. Next, we calculate the instantaneous heat release rate  $\dot{q}'_k(t)$  from the chemiluminescence images by considering a region circumscribing the  $k^{\text{th}}$  burner and summing over all the intensity values. An example of such a region for burner 4 is shown in figure 3.7(d). The fluctuations in the local heat release rate (HRR) oscillations  $\dot{q}'_4$  from burner 4 is shown in figure 3.5(a) (in blue) and the corresponding amplitude spectrum  $|\hat{q}_4(f)|$  in figure 3.5(b) (in blue). We observe a peak at  $f_n = 216$  Hz and  $f_s = 7$  Hz and their combination at  $f_n + f_s$ .

In combustion literature, amplitude-modulated limit cycle oscillations are usually referred to as beats (Weng *et al.*, 2016; Kim *et al.*, 2019; Han *et al.*, 2020). The phenomenon

of beats is associated with the linear superposition of acoustic waves with a very small frequency difference. Beats are characterized by the constructive and destructive interference pattern, as was observed in (Kim *et al.*, 2019; Han *et al.*, 2020). However, the applicability of beats is restricted only to linear systems. The amplitude-modulated oscillations in figure 3.5(a) are different from beats because of two key reasons. First, the oscillations do not show the well-known constructive and destructive pattern usually observed for beating (e.g., figure 12a in Han *et al.* (2020)). Second, the parametric value ( $v_z = 7.3$  m/s) for which we observe these amplitude-modulated oscillations separates the region for which we get low-amplitude TAI and secondary bifurcation from low-amplitude TAI to high-amplitude TAI. Consequently, slow scale ( $f_s = 7$  Hz) oscillations associated with  $\dot{q}'$  causes the parameter to increase past the bifurcation point affecting high-amplitude oscillations. When the parameter value decreases due to slow oscillations, it crosses the bifurcation point, and the system dynamics switch back to low-amplitude oscillations. The latter is a well-known mechanism associated with MMO (Kuehn, 2011) and has been discussed in the context of Rijke tube recently (Tandon *et al.*, 2020). Thus, we refer to these oscillations as MMO.

## 3.2 THE CROSSOVER OF BIFURCATION

### 3.2.1 Change of criticality across two-parameter family

We now discuss the change in the nature of the bifurcation along the two control parameters in the combustor. In particular, we focus on the effect of variation of the control parameters on the characteristics of the bifurcations to thermoacoustic instability. In figure 3.6(a), we show the variation in amplitude of acoustic pressure ( $p'_{\text{rms}}$ ) as a function of equivalence ratio ( $\phi$ ) and bulk velocity ( $v_z$ ). For every experiment, depending upon the bulk velocity, we observe various routes to thermoacoustic instability when the equivalence ratio is varied. For visual clarity, the bottom surface is plotted only till the secondary fold point where the oscillations abruptly transition from low-amplitude TAI to high-amplitude TAI, indicated with the up arrow. The top surface is plotted till the fold

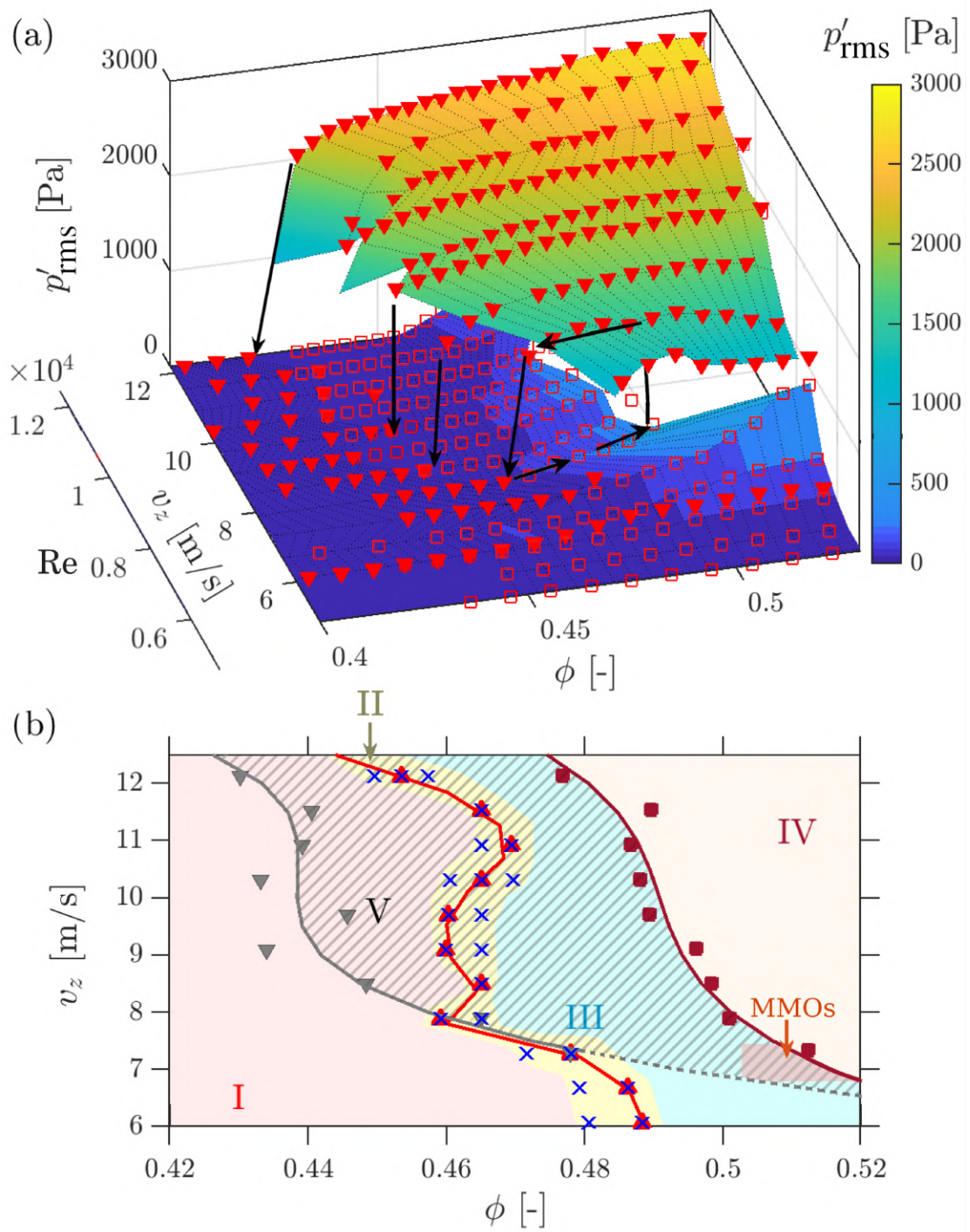


Figure 3.6: (a) Change in criticalities of bifurcations to the state of TAI when  $v_z$  and  $\phi$  are sequentially varied. The forward path is indicated by  $\square$  and the backward path by  $\blacktriangledown$ . (b) Interpolated stability map of the system.  $\triangle$  Hopf point,  $\times$  intermittent dynamics,  $\square$  secondary bifurcation point,  $\nabla$  fold point. A dashed line indicates an extrapolated boundary. The frequency of the oscillations was in the range of 215 – 230 Hz.

point where the dynamics of pressure oscillations abruptly jump from high-amplitude TAI to combustion noise (CN) (down arrows).

In the range of low bulk velocities, specifically from  $v_z \approx 6$  to 6.5 m/s, the transition from CN to low-amplitude TAI of the acoustic subsystem takes place through a bifurcation similar to supercritical Hopf bifurcation (see figure 3.1). For  $v_z \approx 7.3$  m/s (see figure 3.4), there is a transition from CN to high-amplitude TAI through the state of intermittency, low-amplitude TAI, and MMO. In the range of high bulk velocities, for  $v_z > 7.5$  m/s, the transition from CN to high-amplitude TAI takes the following route: CN to low-amplitude TAI via intermittency followed by a secondary bifurcation from low-amplitude TAI to high-amplitude TAI (figure 3.2). The variation in the nature of these bifurcations along the two-parameter family is commonly referred to as the *criticality of a bifurcation*.

### 3.2.2 Stability map of the combustor

We now discuss the stability map of the annular combustor obtained by varying the two control parameters ( $\phi, v_z$ ). In figure 3.6(b), we show the interpolated boundary between different dynamical states in the parametric  $\phi - v_z$  plane. A cubic spline has been used to interpolate and extrapolate the boundary between different regions. Since we do not observe secondary bifurcation to high-amplitude TAI below  $v_z < 6$  m/s, we have limited the ordinate to  $v_z \geq 6$  m/s. The approximate boundary separating regions I and III marks the transition from CN to low-amplitude TAI. This transition is always associated with the state of intermittency (indicated with ‘ $\times$ ’ markers in region II highlighted in yellow). The boundary between III and IV indicates the boundary of the secondary fold bifurcation to high-amplitude TAI. The small parametric region for which we observe MMO is also indicated in figure 3.6(b). The bistable region has been hatched, and the boundary between regions V and I shows the fold point of the system. Several salient features can be observed from the stability diagram. First, the onset of low-amplitude TAI and high-amplitude TAI takes place at a progressively lower value of  $\phi$  as  $v_z$  is increased. Second, the range of  $\phi$  over which we observe low-amplitude TAI decreases,

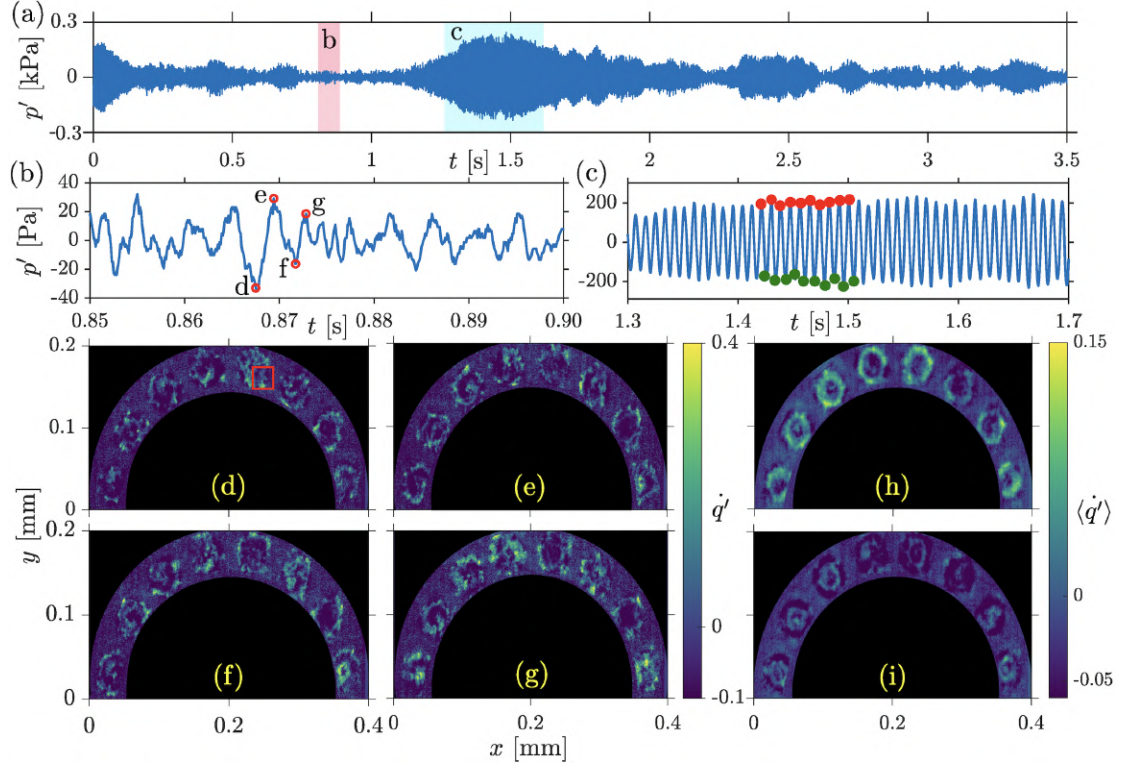


Figure 3.7: (a) Time series of acoustic pressure oscillations obtained during intermittency observed at  $\phi = 0.47$ . (b) Aperiodic and (c) periodic part of intermittency. (d-g) Mean-subtracted instantaneous chemiluminescence images corresponding to the indicated points in the aperiodic region in (b). (h,i) Phase-averaged chemiluminescence image at the pressure maxima ( $90^\circ$ ) and minima ( $270^\circ$ ) measured from the points indicated in (c).

and high-amplitude TAI increases on increasing  $v_z$ . Finally, there is also an increase in the width of the bistable region with an increase of  $v_z$ .

### 3.3 FLAME DYNAMICS DURING THE THERMOACOUSTIC TRANSITIONS

In this section, we discuss the flame dynamics observed across various dynamical states during the thermoacoustic transitions. We discuss global and local flame dynamics during intermittency, low-amplitude TAI, high-amplitude TAI, and MMO. We then compare and contrast to highlight the intriguing behaviors exhibited by the flames in these distinct dynamic states.

During combustion noise (CN), as the flames are only subjected to broadband turbulent

velocity fluctuations, the heat release rate (HRR) field largely remains incoherent and the acoustic pressure fluctuations remain aperiodic and have not been shown here for brevity.

We focus on the flame dynamics observed during the state of intermittency (INT). The intermittent acoustic pressure oscillations observed when  $\phi = 0.47$  are shown in figure 3.7(a). In the enlarged portion in figures 3.7(b) and (c), we observe aperiodic and periodic pressure oscillations. Instantaneous images corresponding to the points indicated in figure 3.7(b) have been shown below the time signal. For the periodic part of intermittency, phase-averaged chemiluminescence images at maxima ( $90^\circ$ ) and minima ( $270^\circ$ ) determined from the red and green points in figure 3.7(b), have been shown in figures 3.7(h) and (i). The flames are identified as 1 to 8 going in an anti-clockwise direction.

Figure 3.7(d) corresponds to the local minima of aperiodic pressure oscillations observed during intermittency. We observe that flames 5 and 7 show very high heat release rate fluctuations. However, at the next minima (figure 3.7f), we observe that flames 6 and 8 are at a maximum. Similar observations can be made from the points corresponding to local pressure maxima (figures 3.7e,g). In other words, the intensity levels are incoherent across different burners. In contrast, from the phase-averaged image taken at pressure maxima (figure 3.7h), we distinguish the swirling flame structure. For all the burners, we observe that the intensity is at maxima along the periphery of the swirling flame. At the pressure minima, the phase-averaged flame image shows a very low heat release.

It is worth noting that the phase-averaged images ( $\langle\langle\dot{q}'\rangle\rangle$ ) were calculated from mean-subtracted chemiluminescence images. As a result, the phase-averaged images at pressure minima in figure 3.7(i) show negative values. Additionally, we note that  $\langle\dot{q}'\rangle$  is not centered around zero, which could be a consequence of the apparent nonlinear interaction between heat release rate and acoustic pressure fluctuations.

Now, we analyze the local HRR dynamics during the periodic part of intermittency.

The local HRR is determined by summing over all the intensity values present in a rectangular region as shown for the 4<sup>th</sup> flame in figure 3.7(d). To calculate HRR from each burner, the rectangular region was chosen instead of the entire burner to avoid phase cancellation effects from affecting the HRR time series. A similar region is chosen for all the burners and a time series of local HRR fluctuations is obtained. Since the local HRR signals contain phase noise, we bandpass the signal centered around the frequency of dominant oscillations ( $f_n$ ) with a width of  $\pm f_n/4$ . Here,  $f_n$  is the frequency of limit cycle oscillations which is approximately around  $220 \pm 50$  Hz. We normalize the HRR signals to compare the amplitude of oscillations and use the Hilbert transform to obtain the phase of the time signals (Gabor, 1946; Pikovsky *et al.*, 2003). From the HRR signal for the  $k^{\text{th}}$  burner  $\dot{q}'_k$ , we construct a complex analytic signal  $\zeta(t) = \dot{q}'_k(t) + i\mathcal{H}[\dot{q}'_k(t)] = A_k(t) \exp(i\theta_k t)$ . Here  $\theta_k(t)$  is the instantaneous phase and  $A_k(t)$  is the instantaneous amplitude of the analytic signal associated with  $\dot{q}'_k$ . The Hilbert transform is defined as:

$$\mathcal{H}[\dot{q}'_k(t)] = \text{PV} \int_{-\infty}^{\infty} \frac{\dot{q}'_k(\tau)}{t - \tau} d\tau, \quad (3.1)$$

evaluated at the Cauchy principal value (PV). It is important to note that for the interpretation of the calculated quantity using the Hilbert transform as phase, the trajectories of the signal in the analytic plane [ $\mathcal{T}(\mathcal{H}) - \mathcal{R}(\mathcal{H})$ ] should rotate around a fixed center (Romano *et al.*, 2005). During limit cycle oscillations, the trajectories of the acoustic pressure signal  $p'(t)$  possess a unique center of rotation in the analytic plane. However, during combustion noise, the signal trajectories do not revolve around an origin in the analytic plane. This absence of a distinct center of rotation implies that the acoustic pressure signal  $p'(t)$  is not strictly analytic during the state of combustion noise. To determine the phase during the state of combustion noise, Mondal *et al.* (2017b) instead evaluated the correlation and used the probability of recurrence to determine the phase of the pressure and heat release rate oscillations. The resulting phases were qualitatively similar to the phase obtained through the Hilbert transform, despite the

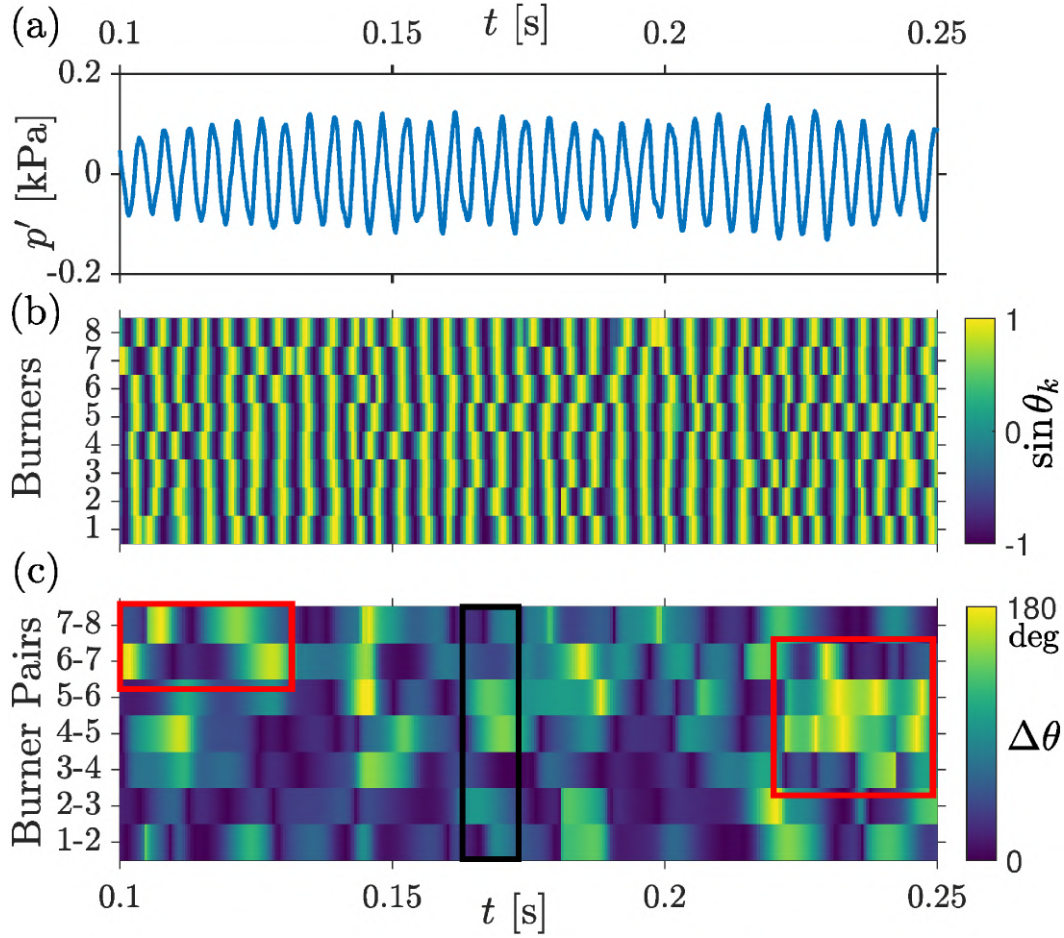


Figure 3.8: (a) Periodic part of intermittency observed at  $\phi = 0.47$ . Temporal variation of (b) normalized amplitude and (c) phase difference (in deg) of HRR between burners and burner pairs.

limitation imposed by the definition of analytic signals. So, we also utilize the phase of the analytic signal computed using the Hilbert transform in our analysis to visualize the changes in the phase field during the transition from combustion noise to thermoacoustic instability. The normalized HRR can then be evaluated as:  $\dot{q}'_k(t)/A_k(t) = \sin \theta_k$ .

In figure 3.8(a), we show the periodic part of intermittency in  $p'$ . In figure 3.8(b), we plot the temporal variation of the amplitude of HRR oscillations for all the burners. This phase difference between different pairs of burners is shown in figure 3.8(c). We observe some phase mismatch between the cycles of oscillations among different flames. We notice that the phase difference of different burners are different. For instance, in the region

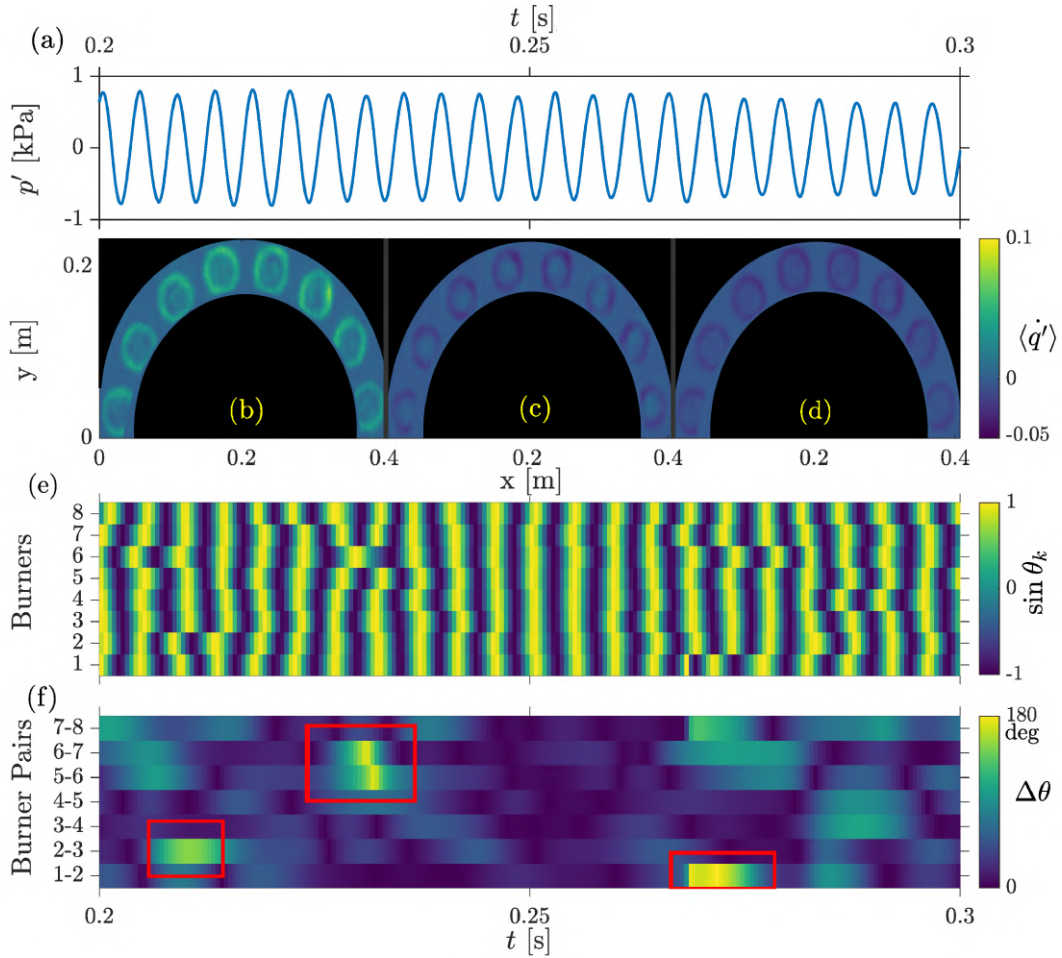


Figure 3.9: (a) Time series of  $p'$  during low-amplitude TAI at  $\phi = 0.49$ . Phase-averaged CH\* images at pressure (b) maxima ( $90^\circ$ ), (c) mean ( $0^\circ$ ) and (d) minima ( $270^\circ$ ) value. (e) Variation in the normalized amplitude of  $\dot{q}'$  for each burner measured from each of the flames. (f) Relative phase (in degrees) evolution between  $\dot{q}'$  measured from the indicated pair of burners.

indicated by the black rectangle, burner 1-2 are in-phase, while burner pair 4-5 is  $180^\circ$  out-of-phase. However, there are many burner pairs that become out-of-phase (indicated by the red rectangle). Thus, even though the burners are frequency synchronized, they have a significant amount of desynchronized behavior. In summary, we observe that during periodic bursts of intermittency, although the burners have the same frequency, their phase differences show significant phase slips in time. As a consequence, the flames are in a state of partial (intermittent phase) synchronization with each other.

Figure 3.9(a) shows the time series of pressure fluctuations obtained during a low

amplitude limit cycle with an amplitude of around 800 Pa obtained at  $\phi = 0.49$ . Phase-averaged CH\* images obtained at the phase of pressure maxima ( $90^\circ$ ), mean ( $0^\circ$ ) and minima ( $270^\circ$ ) are plotted in figures 3.9(b-d), respectively. From the phase-averaged CH\* images at pressure maxima during low-amplitude TAI (figure 3.9b), we see a hollow flame structure for every burner along the annulus. This is in contrast to the case of intermittency where we observed the hollow flame structure for some burners and distributed flames for others (figure 3.7h). The flame is bounded by the inner and outer recirculation zone. Consequently, there is a minima in the HRR at the center of each flame and a large HRR along the flame edges. We can also notice a difference in the heat release field during the phase of pressure maxima and minima.

Next, we calculate the local HRR from all eight flames and compare their dynamics in the manner discussed previously. We plot the temporal variation in the amplitude of the HRR obtained from each of the eight burners in figure 3.9(e). We observe that the burners have the same frequency, as observed from the temporal match of their normalized amplitudes. In the temporal variation of the phase difference between neighboring pairs of burners (figure 3.9f), we find that the phase differences are predominantly close to zero. In other words, most of the burners are in-phase synchronized with each other. We also see the random appearance of phase slips between different pairs of burners (indicated by the red rectangles). Phase slips indicate an increase in phase difference by  $180^\circ$ . In comparison to the periodic part of intermittency, there are much fewer phase slips between different pairs of burners during low-amplitude TAI. We refer to this state where the flames are not perfectly synchronized as a state of weak synchronization.

Figure 3.10(a) shows high-amplitude TAI obtained at  $\phi = 0.52$ . The amplitude of TAI is around 2 kPa and is about an order of magnitude larger than the low-amplitude TAI. We plot the phase-averaged CH\* images at the phase of pressure maxima ( $90^\circ$ ), mean ( $0^\circ$ ) and minima ( $270^\circ$ ) in figures 3.10(b-d), respectively. We observe that the flame dynamics are significantly different from that during low-amplitude TAI. First, during pressure

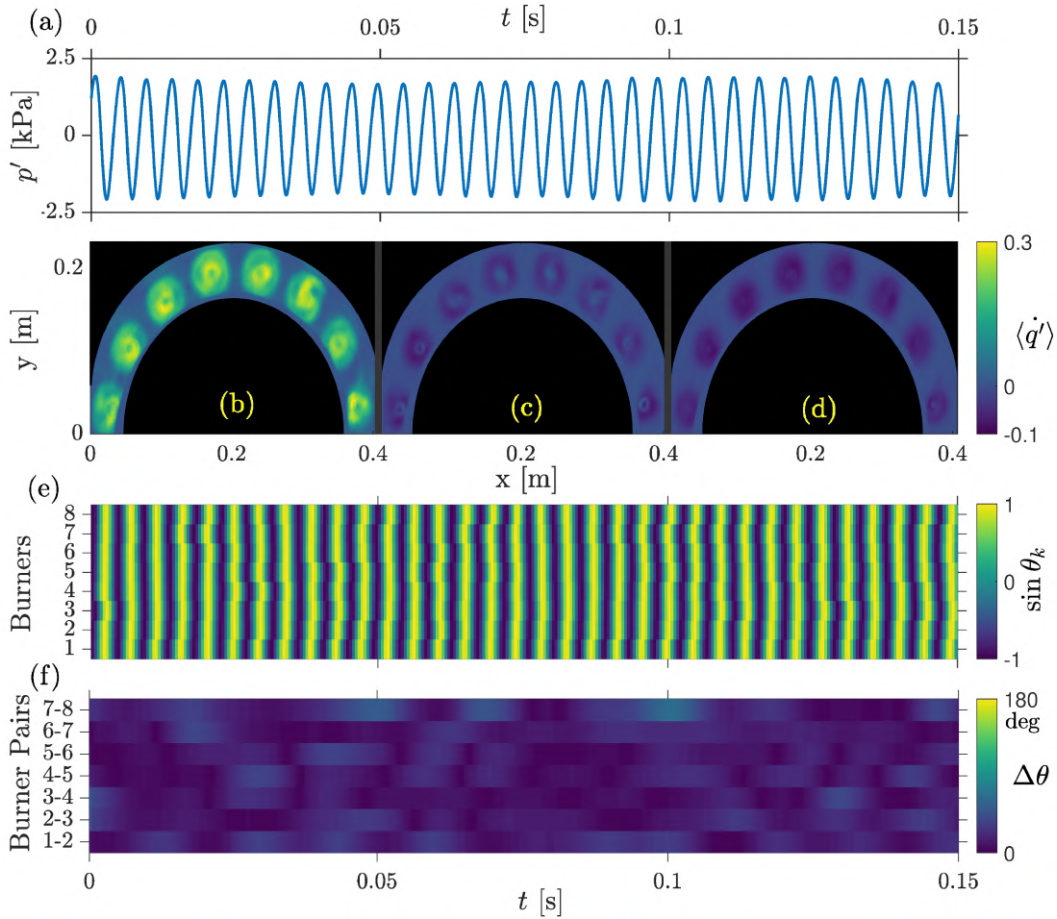


Figure 3.10: (a) Time series of  $p'$  during high-amplitude TAI at  $\phi = 0.52$ . Phase-averaged CH\* images at pressure (b) maxima ( $90^\circ$ ), (c) mean ( $0^\circ$ ), and (d) minima ( $270^\circ$ ) value. (e) Variation in the normalized amplitude of  $\dot{q}'$  for each burner measured from each of the flames. (f) Relative phase (in degrees) evolution between  $\dot{q}'$  measured from the indicated pair of burners.

maxima, the highest HRR intensity is concentrated at the center of each flame. This possibly indicates intense heat release in the inner recirculation zone during the pressure maxima. At  $0^\circ$  and  $270^\circ$  phase, we can observe that the flame does not propagate along the inner recirculation zone.

We now analyze the individual flames by evaluating the local HRR for each burner. The temporal variation in amplitude of the HRR for each of the flames is plotted in figure 3.10(e). We observe that each of the burners attains maxima in the HRR at the same time instant, indicating in-phase synchronization among each of the burner pairs. This

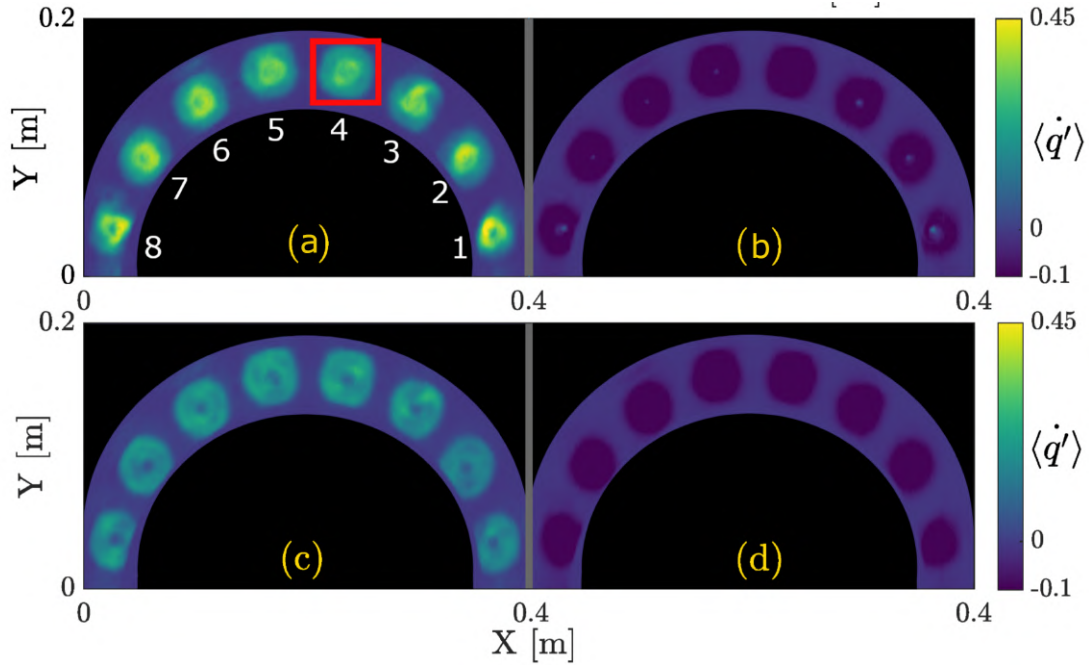


Figure 3.11: Phase-averaged  $\text{CH}^*$  chemiluminescence images at (a) pressure maxima ( $90^\circ$ ) and (b) pressure minima ( $270^\circ$ ) during epochs of high-amplitude oscillations in MMO, and (c) pressure maxima ( $90^\circ$ ) and (d) pressure minima ( $270^\circ$ ) during epochs of low-amplitude oscillations in MMO. This experimental investigation was conducted under the condition of  $\phi = 0.54$ .

is further corroborated by the temporal evolution of the phase difference between the pair of burners in figure 3.10(f). We can observe that the burners are always in-phase synchronized and the phase difference is always below  $90^\circ$ . Hence, we refer to the flame interactions between burners during high-amplitude TAI as perfect synchronization.

As previously mentioned, mixed-mode oscillations (MMO) involve the periodic alternation between high-amplitude and low-amplitude TAI. Figures 3.11(a-d) correspond to phase-averaged  $\text{CH}^*$  images for pressure maxima ( $90^\circ$ ) and minima ( $270^\circ$ ) during epochs of high-amplitude oscillations are shown in figures 3.11(a,b), and for the low-amplitude oscillations in figures 3.11(c,d). At the pressure maxima during epochs of high-amplitude oscillations (figure 3.11a), intense HRR oscillations manifest in the high intensity at the center of each burner in the phase-averaged images. The intense central region of the burners indicates the presence of a well-developed inner

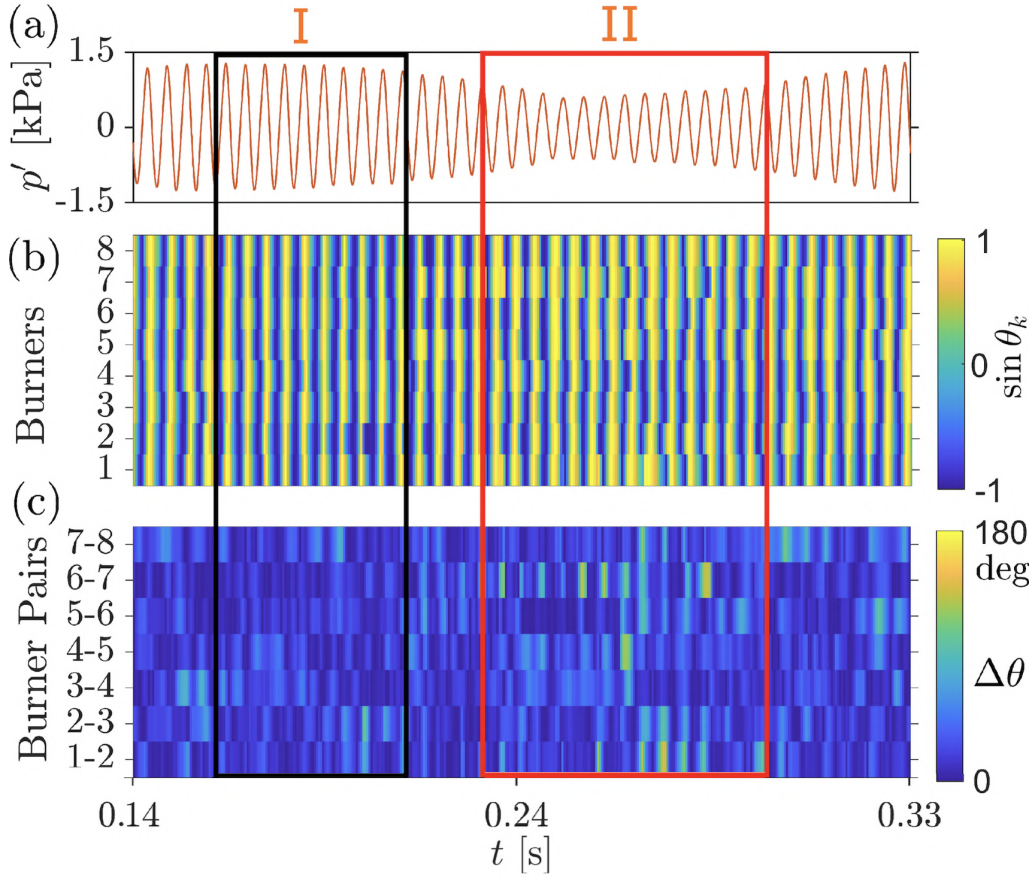


Figure 3.12: (a) Enlarged portion of  $p'$  during MMO at  $\phi = 0.54$ . (b) Temporal variation in the normalized amplitude of heat release rate ( $\sin \theta_k$ ) measured from all the burners. (c) Temporal variation in the relative phase (in degrees) from the indicated pair of burners.

recirculation zone. In addition, all of the eight flames have almost the same intensity with a very similar flame structure. The flame intensity levels are low at the pressure minima (figure 3.11b). The behavior is remarkably different during the epochs of low-amplitude fluctuations of MMO. At pressure maxima (figure 3.11c), the intensity is much lower. The flame structure shows that the flames are stabilized along the central shear layer separating the inner and outer recirculation zones and indicates the absence of the vortex bubble at the centerline. At pressure minima (figure 3.11d), we notice very low intensities for all the flames. The global phase-averaged flame dynamics observed in figures 3.11(a-d) are qualitatively similar to the phase-averaged flame dynamics observed during high-amplitude TAI and low-amplitude TAI.

Next, we discuss the local flame behavior during MMO by analyzing the mutual interaction of adjacent flames. Figure 3.12(a) shows an enlarged portion of the acoustic pressure oscillations during the MMO consisting of alternate epochs of high-amplitude and low-amplitude oscillations. We observe that during the epochs of high-amplitude oscillations (region I), all of the burners attain maxima and minima in the HRR concurrently with almost the same amplitude (figure 3.12b). In contrast, during epochs of low-amplitude oscillations (region II), we observe that all of the burners do not attain maxima and minima in the HRR at the same time instants. Instead, there is some phase mismatch in the HRR oscillations associated with the different flames (figure 3.12b). This contrasting behavior is well captured from the instantaneous relative phase. During high-amplitude oscillations (region I), the burners are in-phase synchronized, and the phase difference between various pairs of burners always remains well below  $90^\circ$  (figure 3.12c). However, during low-amplitude oscillations (region II), we observe that some burner pairs are in-phase while others are out-of-phase. For instance, burners 2-3 are initially in-phase and, after some time, go  $180^\circ$  out-of-phase, while burners 6-7 are  $90^\circ$  out-of-phase for almost the entirety of the duration of low-amplitude oscillations. Similar observations can be drawn for other pairs of burners.

For a better understanding of the above-mentioned scenario, we further investigate the instantaneous interactions between burner pairs 2-3 and 6-7 and contrast the synchronous behavior during low and high-amplitude oscillations over one cycle of oscillations. Figure 3.13(a) shows one cycle of low-amplitude oscillations during MMO. Figures 3.13(b-f) show the corresponding instantaneous flame image of burner pairs 2-3 and 6-7 at various points over the cycle. In figure 3.13(b), we observe high-intensity levels for burner 6 while the rest of the burners have lower intensity levels. In addition, burner 6 is  $100^\circ$  out-of-phase with burner 7 at the beginning of the cycle and has a mean phase difference of  $\langle \Delta\theta_{67} \rangle = 53^\circ$  over the cycle. In comparison, burner 2 is in-phase with burner 3 for all the points over the cycle with a mean phase difference of  $\langle \Delta\theta_{23} \rangle = 16^\circ$  (figures 3.13b-f). In figure 3.13(g), we show the high-amplitude oscillation during MMO over

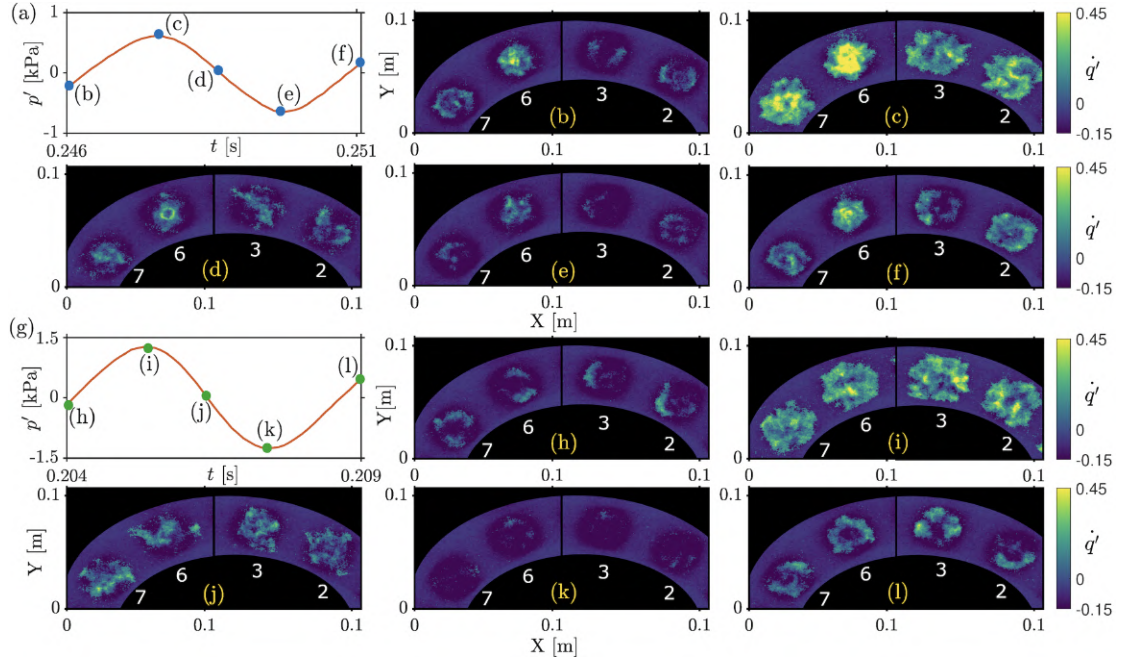


Figure 3.13: (a) Low-amplitude pressure oscillations over one cycle during the state of MMO. (b-f) Portion of CH\* images depicting the flame-flame interaction between burner pairs 2-3 and 6-7 corresponding to the points marked in (a). (g) High-amplitude pressure oscillations over one cycle during the state of MMO and (h-l) the corresponding CH\* images.

a cycle along with the instantaneous images of the burner pairs 2-3 and 6-7 in figures 3.13(h-l). Compared to the behavior of burner pairs over a cycle of low-amplitude pressure oscillation (figures 3.13b-f), the intensity of heat release rate at each of the burner is almost the same over the cycle of high-amplitude pressure oscillation (figures 3.13h-l). The averaged phase difference over the points of the cycle are  $\langle \Delta\theta_{23} \rangle = 13^\circ$  and  $\langle \Delta\theta_{67} \rangle = 5^\circ$ . The flame structures at each of the burners are also quite similar over different points in the cycle.

### 3.4 QUANTIFICATION OF FLAME-FLAME AND FLAME-ACOUSTIC INTERACTIONS

In this section, we quantify the relative degree of synchronization amongst different pairs of burners and with the acoustic pressure oscillations. We define the phase-locking value

(PLV) for any given pair of oscillators  $x_1$  and  $x_2$  as (Pikovsky *et al.*, 2003):

$$\text{PLV} = \frac{1}{N_p} \left| \sum_{j=1}^{N_p} \exp(i\Delta\phi_{x_1, x_2}(t_j)) \right|, \quad (3.2)$$

where, the phase difference between the signals at the instant  $t_j$  is  $\Delta\phi_{x_1, x_2}(t_j) = \phi_{x_1}(t_j) - \phi_{x_2}(t_j)$  and  $N_p$  is the length of the time series. The PLV indicates the absolute value of the mean phase difference between two signals where the instantaneous phase differences ( $\Delta\phi$ ) are expressed as complex unit-length vectors, i.e.,  $e^{i\Delta\phi}$  (Mondal *et al.*, 2017a). The PLV has a value close to 0 for desynchronized signals and close to 1 for perfectly synchronized signals. For cases with partial synchronization such as intermittent phase-locking, the PLV lies between 0 and 1.

We also define the Kuramoto order parameter to quantify the synchronous behavior for the spatially distributed oscillators (the eight burners) as (Mondal *et al.*, 2017b):

$$R(t) = \frac{1}{N_b} \left| \sum_{k=1}^{N_b} \exp(i\theta_k(t)) \right| \quad (3.3)$$

where,  $\theta_k$  is the phase of the  $k^{\text{th}}$  burner and  $N_b$  is the total number of burners. At any time instant,  $R = 0$  indicates spatial desynchrony, while  $R = 1$  indicates spatial synchrony.

We show the variation in PLV between the HRR from different pairs of burners in figure 3.14(a) observed during the state of CN, intermittency, low amplitude TAI, and high-amplitude TAI. We also show the PLV between each burner with respect to pressure fluctuations observed during the above-mentioned states in figure 3.14(b) for the different states of combustor operation. During CN (figures 3.14a,b), the PLV between different burner pairs and burner and acoustic pressure fluctuations remain close to zero, indicating desynchronized behavior among them. During intermittency (figures 3.14a,b), the PLV between different pairs of burners is very low ( $< 0.5$ ) indicating the desynchronized nature of their interaction with each other. However, the PLV between different burners and the acoustic pressure fluctuations are close to 0.4 indicating partial synchronization between them (figure 3.14b).

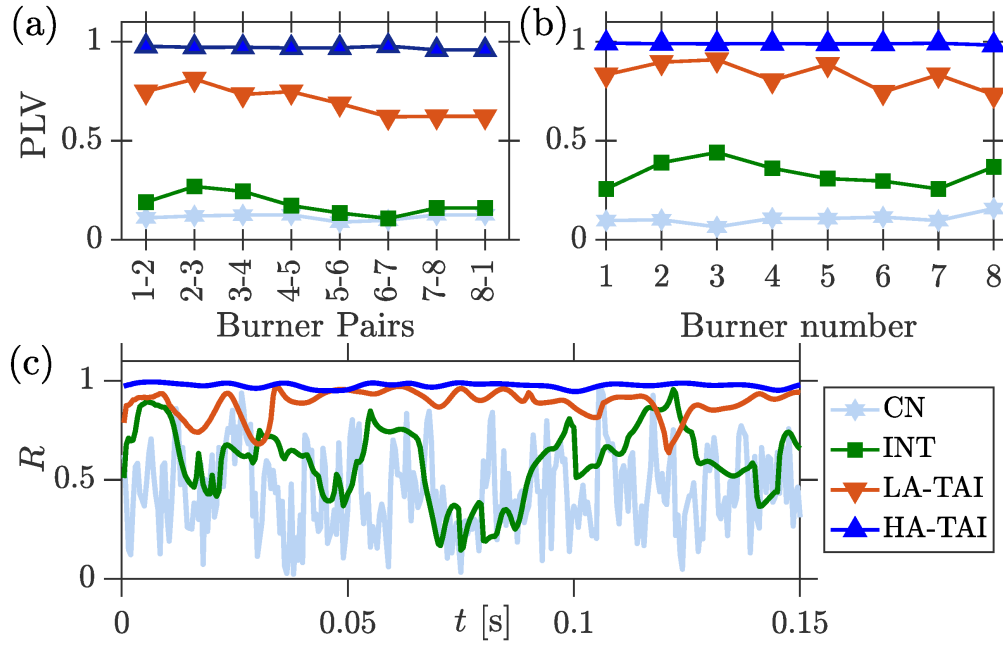


Figure 3.14: Phase-locking value (PLV) between (a)  $\dot{q}'$  measured from individual burners, and between (b)  $\dot{q}'$  from each burner and  $p'$  during combustion noise (CN), intermittency (INT) at  $\phi = 0.47$ , low amplitude TAI at  $\phi = 0.49$ , and high-amplitude TAI at  $\phi = 0.52$ , respectively. (c) Kuramoto order parameter ( $R$ ) determined from the eight burners during different states of combustor operation.

As noted during the discussion following figure 3.9, during low-amplitude TAI, some oscillators are only weakly synchronized with each other due to phase-slips in their relative phases. As a consequence, PLV lies between 0.5 and 1, indicating weak synchronization among different burners (figure 3.14a). We also note that the PLV of different burners with the acoustic pressure oscillations follows suit and lies between 0.5 and 1 showing partial synchrony (figure 3.14b). For high-amplitude TAI, the PLV between different pairs of burners and different burners with pressure lies very close to 1, indicating perfect synchronization of the burners with each other and with the pressure oscillations (figures 3.14a,b).

Next, the Kuramoto order parameter is plotted as a function of time in figure 3.14(c) during different dynamical states. The order parameter indicates the different degrees of spatial coherence of the oscillators over time. During CN,  $R$  fluctuates around

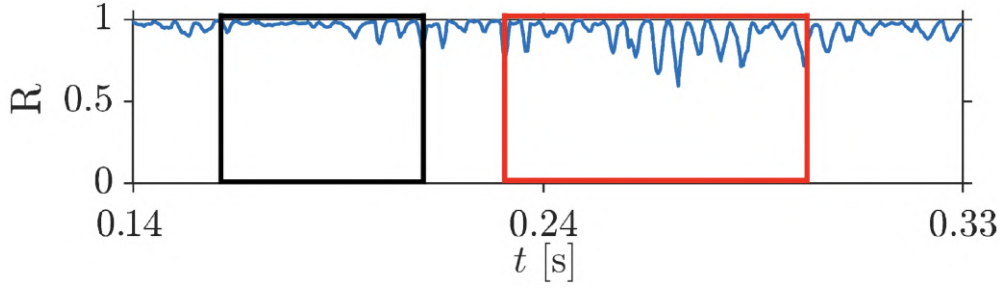


Figure 3.15: Temporal variation in the Kuramoto order parameter ( $R$ ) measured from the eight flames during mixed-mode oscillations (MMO) at  $\phi = 0.54$ .

time-averaged value of  $\bar{R} = 0.41$ . During the periodic and aperiodic part of intermittency,  $R$  fluctuates around  $\bar{R} = 0.49$  and  $\bar{R} = 0.37$ . This indicates that spatially, the flames are intermittently coherent during the periodic part of intermittency and incoherent otherwise. During low-amplitude TAI,  $R$  fluctuates around a mean value of  $\bar{R} = 0.84$ . Thus, the burners are in a state of weak spatial synchronization. And, during high-amplitude TAI,  $R$  fluctuates around a mean value of  $\bar{R} = 0.97$ , indicating perfect spatial synchronization.

Finally, in figure 3.15, we plot the temporal variation of the Kuramoto order parameter during the mixed-mode oscillations (MMO). We observe the value of  $R$  is near 1 for the epochs of high-amplitude oscillations (region I marked in black). While, during low-amplitude pressure oscillations, the value of  $R$  fluctuates between 0.50 and 1 (region II marked in red). Thus, during the epochs of high-amplitude oscillations, all the flames get perfectly synchronized, while during epochs of low-amplitude oscillations, they are weakly synchronized.

### 3.5 INTERIM SUMMARY

In this chapter, we evaluated the criticality of a bifurcation by systematically varying the equivalence ratio and bulk flow velocity in the annular combustor. We demonstrate the effect that change of control parameters has on determining the characteristics of the bifurcations leading to longitudinal thermoacoustic instability. We observe different dynamical states depending upon the values of  $v_z$  and  $\phi$ , namely, combustion noise,

intermittency, low-amplitude TAI, high-amplitude TAI, and MMO. We then focused on the flame dynamics during various dynamics states observed in the experiments. We find that during the periodic part of the intermittency, the phase-averaged flame structure changes from incoherent to a ring-like structure. During low-amplitude TAI, we find that the flame exhibits a well-defined ring-like structure anchored along with the space between the inner and outer recirculation zone. During high-amplitude TAI, the flame propagates into the inner reaction zone, resulting in intense heat release at the center of the burner. Remarkably, in the case of MMO, we find that the flame behavior encompasses features from both low- and high-amplitude oscillations.

Further, we analyze the interactions between neighboring flames along the annulus. Upon comparing the amplitude and phase of the HRR response of neighboring burners, we find different degrees of spatiotemporal synchronization during different dynamical states. We show that even in the case of longitudinal TAI, the flame-flame interactions are non-trivial. In particular, we find a transition from partially synchronized response of the burners during INT to weakly synchronized behavior with sporadic phase slips during low-amplitude TAI, followed by perfect synchronization among the burners during high-amplitude TAI. During MMO, the flame interaction periodically alternates between weak and perfect synchronization. We quantify the degree of spatiotemporal synchronization using the phase-locking value (PLV) and the Kuramoto order parameter ( $R$ ). Most importantly, we characterize the nonlinear dependence of the flame response on the dissimilar amplitude perturbations encountered during the MMO, low-amplitude TAI, and high-amplitude TAI.

## CHAPTER 4

# MODELING CRITICALITY OF BIFURCATION IN THERMOACOUSTIC SYSTEMS

In our discussion regarding the criticality of bifurcation in Chapter 3, we highlighted various routes to thermoacoustic instability and the underlying spatiotemporal behavior of the flame across various dynamical states. However, the differences in the transition mechanisms make evident the challenge in the development of thermoacoustic models capable of explaining all these transition scenarios. Here, we present two distinct thermoacoustic models to explain the criticality of a bifurcation and the underlying mechanism leading to a change in the nature of the bifurcation. In the first approach, the phenomenological thermoacoustic model successfully captures the nature of bifurcation by introducing the nonlinearity that is encoded in the assumed flame model. In the second approach, we develop a general model of thermoacoustic interactions capable of capturing the bifurcations and their criticalities, and the rich phase dynamics which underlie thermoacoustic transitions in disparate combustion systems. Importantly, the second approach provides an explanation of spatiotemporal synchronization and pattern-formation underlying the transition to thermoacoustic instability while encapsulating the statistical properties of desynchronization, chimeras, and global phase synchronization. The generality of these modeling approaches in capturing different types of transitions and underlying physics highlights the possibility of extending the present model to a broad range of fluid-dynamical phenomena beyond thermoacoustics.

---

The results presented in this chapter are published in the following two papers:

1. Singh, S., Roy, A., Reeja, K. V., Nair, A., Chaudhuri, S., Sujith, R. I. (2021). Intermittency, Secondary Bifurcation and Mixed-Mode Oscillations in a Swirl-Stabilized Annular Combustor: Experiments and Modeling. *J. Eng. Gas Turbine Power*, 143 (5), 051028.
2. Singh, S., Roy, A., Dhadphale, J. M., Chaudhuri, S., and Sujith, R. I. (2024). Continuous and explosive synchronization transition in turbulent combustors. *AIP Advances*, 14, 065106.

#### 4.1 GOVERNING EQUATION FOR THE ACOUSTIC FIELD

The examination of longitudinal thermoacoustic instability in the combustor, as discussed in the previous chapter, allows us to capture its dynamics with a simple one-dimensional thermoacoustic model. We begin by considering a one-dimensional thermoacoustic system assuming negligible mean flow and temperature gradient effects. In such a case, the linearized equations of momentum and energy with a heat source can be expressed as (Nicoud and Wieczorek, 2009; Balasubramanian and Sujith, 2008):

$$\frac{1}{\rho_0} \frac{\partial \tilde{p}'}{\partial \tilde{z}} + \frac{\partial \tilde{u}'}{\partial \tilde{t}} = 0, \quad (4.1a)$$

$$\frac{\partial \tilde{p}'}{\partial \tilde{t}} + \gamma p_0 \frac{\partial \tilde{u}'}{\partial \tilde{z}} = (\gamma - 1) \dot{q}' \delta(\tilde{z} - \tilde{z}_f), \quad (4.1b)$$

where  $\tilde{u}'$  and  $\tilde{p}'$  are the velocity and acoustic pressure fluctuations, respectively. Here,  $\gamma$  is the ratio of specific heat capacities,  $\tilde{t}$  is the time,  $\tilde{z}$  is the distance along the axial direction in the duct, and  $\rho_0$  and  $p_0$  are the density and pressure at mean flow condition. We assume that the flame is acoustically compact and concentrated at  $\tilde{z}_f$ , which is indicated in (4.1b) with the Dirac delta function  $\delta(\tilde{z} - \tilde{z}_f)$ .

We use a Galerkin modal expansion to simplify the system of partial differential equations (Lores and Zinn, 1973). We project Eq. (4.1a) and Eq. (4.1b) onto the Galerkin modes and reduce the partial differential equations to a set of ordinary differential equations. The spatially and temporally varying acoustic pressure and velocity signals are decomposed in terms of spatial basis functions (sine, cosine) satisfying appropriate boundary conditions along with time-varying coefficients ( $\eta, \dot{\eta}$ ). Here, we choose the basis as the eigenmodes of the self-adjoint part of the linearized system. As a result, the acoustic pressure  $\tilde{p}'$  and the velocity fluctuations  $\tilde{u}'$  can be expanded as a series of orthogonal basis functions, which satisfy the boundary conditions associated with the close-open duct (Culick and Kuentzmann, 2006; Nair and Sujith, 2015):

$$\tilde{p}'(\tilde{z}, \tilde{t}) = p_0 \sum_{j=1}^n \frac{\dot{\eta}_j(\tilde{t})}{\tilde{\Omega}_j} \cos(\tilde{k}_j \tilde{z}), \quad \tilde{u}'(\tilde{z}, \tilde{t}) = \frac{p_0}{\rho_0 c_0} \sum_{j=1}^n \eta_j(\tilde{t}) \sin(\tilde{k}_j \tilde{z}). \quad (4.2)$$

Here, the time-varying coefficients  $\eta_j$  and  $\dot{\eta}_j$  are associated with  $j^{\text{th}}$  mode of  $\tilde{u}'$  and  $\tilde{p}'$ . The wavenumber and the natural frequency of the system are given by:  $\tilde{k}_j = (2j-1)\pi/2\tilde{L}$  and  $\tilde{\Omega}_j = c_0\tilde{k}_j$ , respectively. By substituting Eq. (4.2) in Eq. (4.1b), we get:

$$\sum_{j=1}^n \frac{\ddot{\eta}_j(\tilde{t})}{\tilde{\Omega}_j} \cos(\tilde{k}_j\tilde{z}) + \frac{\gamma p_0}{\rho_0 c_0} \sum_{j=1}^n \eta_j(\tilde{t}) \tilde{k}_j \cos(\tilde{k}_j\tilde{z}) = \frac{(\gamma-1)}{p_0} \dot{q}' \delta(\tilde{z} - \tilde{z}_f). \quad (4.3)$$

We then project the resultant equation along the basis function by multiplying Eq. (4.3) with  $\cos(\tilde{k}_j\tilde{z})$  and evaluating the inner product over the domain. Thus, we obtain a set of second-order ordinary differential equations:

$$\frac{\ddot{\eta}_j(\tilde{t})}{\tilde{\Omega}_j} + c_0 \tilde{k}_j \eta_j(\tilde{t}) = \frac{2(\gamma-1)}{\tilde{L} p_0} \int_0^{\tilde{L}} \dot{q}' \delta(\tilde{z} - \tilde{z}_f) \cos(\tilde{k}_j\tilde{z}) d\tilde{z}, \quad (4.4)$$

where,  $c_0 = \sqrt{\gamma p_0/\rho_0}$  is the average speed of sound in the duct and  $\int_0^{\tilde{L}} \cos^2(\tilde{k}_j\tilde{z}) d\tilde{z} = \tilde{L}/2$ .

As a first approximation, we assume that the influence of higher modes can be neglected, and a single-mode analysis captures the thermoacoustic transition reasonably well (Lieuwen, 2003; Culick and Kuentzmann, 2006; Subramanian *et al.*, 2013). Thus, upon considering only a single mode for our analysis, we obtain:

$$\ddot{\eta}(\tilde{t}) + \tilde{\zeta} \dot{\eta}(\tilde{t}) + \tilde{\Omega}_0^2 \eta(\tilde{t}) = \frac{2(\gamma-1)}{\tilde{L} p_0} \tilde{\Omega}_0 \int_0^{\tilde{L}} \dot{q}' \delta(\tilde{z} - \tilde{z}_f) \cos(\tilde{k}\tilde{z}) d\tilde{z}, \quad (4.5)$$

where following Matveev and Culick (2003), the term  $\tilde{\zeta}\dot{\eta}$  is introduced to account for acoustic damping, which plays a crucial role in determining the amplitude of limit cycle oscillation,  $\tilde{\zeta}$  being the damping coefficient.

## 4.2 MODELING HEAT RELEASE RATE USING NONLINEAR FUNCTIONS

Based on the insights gained from the experiments discussed in the previous chapter, here, we present a minimal nonlinear model that can capture the different criticalities of bifurcation observed in the turbulent combustor. Since the observed dynamics in thermoacoustic systems arise from the nonlinear flame-response to acoustic perturbations

(Noiray and Schuermans, 2013). As a result, the heat release rate response can be expressed as a nonlinear function of  $\eta$  and  $\dot{\eta}$ , i.e.,  $\dot{q}' \equiv \dot{Q}'(\eta, \dot{\eta})$ .

By substituting for  $\dot{q}'$  in Eq. (4.5), we obtain the following set of ordinary differential equations:

$$\ddot{\eta}(\tilde{t}) + \omega^2 \eta(\tilde{t}) = f(\eta, \dot{\eta}), \quad (4.6)$$

where  $\omega = \tilde{\Omega}_0$  and  $f(\eta, \dot{\eta}) = \dot{Q}'(\eta, \dot{\eta}) - \tilde{\zeta} \dot{\eta}(\tilde{t})$  is the nonlinear driving term. Using a truncated Taylor series expansion of the source term  $f(\eta, \dot{\eta})$  following Ananthkrishnan *et al.* (1998), we express Eq. (4.6) as:

$$\ddot{\eta}(\tilde{t}) + \left( \mu_6 \eta^6(\tilde{t}) + \mu_4 \eta^4(\tilde{t}) + \mu_2 \eta^2(\tilde{t}) - \mu_0 \right) \dot{\eta}(\tilde{t}) + \omega^2 \eta(\tilde{t}) + \xi(\tilde{t}) = 0, \quad (4.7)$$

where,  $\mu_i$  are the coefficients of the nonlinear terms, for  $i = 0, 2, 4, 6$  and  $\xi(\tilde{t})$  is Gaussian white noise. We start by considering  $\mu_4 = \mu_6 = 0$  and absence of noise. In such a case,  $\mu_2 \eta^2$  makes up the nonlinear damping term while  $\mu_0$  controls the driving. Setting  $\mu_2 = 1$  (for convenience), it is easy to see that  $\mu_2 \eta^2$  positively damps the system and counteracts the driving induced by  $\mu_0 > 0$  for large  $\eta$ . Thus, the system undergoes a supercritical Hopf bifurcation for  $\mu_2 = 1$  when  $\mu_0$  is increased above 0. For  $\mu_2 = -1$ , a family of unstable limit cycle exists, which can be stabilized by introducing fourth-order nonlinearity. For  $\mu_4 > 0$ , the unstable limit cycle undergoes a fold bifurcation and jumps to a stable limit cycle solution. Thus, fourth-order nonlinearity is required for subcritical Hopf bifurcation (Ananthkrishnan *et al.*, 1998). The fold point of the subcritical system depends on the choice of  $\mu_4$ . Laera *et al.* (2017a) considered a similar flame model reducible to Eq. (4.7) for  $\mu_6 = 0$  to predict supercritical and subcritical bifurcation in longitudinal and annular combustors.

In order to capture the secondary bifurcation to high-amplitude TAI discussed in the previous chapter, we need to consider higher-order nonlinearity such that there is a fold bifurcation on stable low-amplitude limit cycle oscillations (LCO) to high-amplitude LCO.

This form has been considered by [Campa and Juniper \(2012\)](#) in modeling thermoacoustic instability (TAI) in a Rijke tube by considering the flame response to depend on the mass flow rate through sixth-order nonlinearity.

We include delta-correlated Gaussian white noise  $\xi(\tilde{t}) = \sigma^2 \delta(\tilde{t})$  to the governing equation to account for the noisy behavior associated with the state of combustion noise (CN) and aperiodic epochs of intermittency. Here,  $\delta(\cdot)$  is the Dirac-Delta function and  $\sigma^2$  indicates the strength of white noise. We solve this equation numerically using stochastic Runge-Kutta method ([Gopalakrishnan and Sujith, 2015](#)) for 1000 time steps with  $d\tilde{t} = 0.01$ ,  $\sigma_2 = 0.001$ ,  $\mu_2 = 1$ , and  $\mu_4 = -1$  chosen for convenience from previous discussion. The frequency of limit cycle oscillations is set as  $\omega = 2\pi f = 1$  rad/s. The initial conditions for the forward path are:  $\eta(0) = 0.10$  and  $\dot{\eta}(0) = 0$ . For the reverse path,  $\dot{\eta}(0) = 0$  and  $\eta(0)$  are chosen as the amplitude of limit cycle oscillations of  $\eta(t)$  obtained for a given  $\mu_0$  in the forward path.

Figure 4.1(a) depicts the variation of  $\eta_{rms}$  as a function of  $\mu_0$  and  $\mu_6$ . As with the experimental results, the bottom surface is plotted till the secondary fold bifurcation where the dynamics abruptly transitions from low to high-amplitude LCO, and the top surface is plotted till the fold point where the dynamics transition from high-amplitude LCO to a fixed-point solution. For  $\mu_6 > 0.25$ , there is a supercritical-like bifurcation to low-amplitude LCO through the state of intermittency. For  $0.15 < \mu_6 < 0.25$ , there is a transition from the fixed point solution to low-amplitude LCO through intermittency, followed by secondary bifurcation to high-amplitude LCO. Figure 4.1(b) shows the stability diagram observed from the model. The different regions are serialized as per figure 3.6. We observe that figures 4.1(a,b) and 3.6(a,b) are qualitatively similar. We find the two different final dynamical states. First, there is a transition from a fixed point to low-amplitude LCO through intermittency. Second, there is a transition from a fixed point to intermittency to low-amplitude LCO followed by a secondary bifurcation to high-amplitude LCO. Moreover, the bistable region broadens when  $\mu_6$  is decreased. The

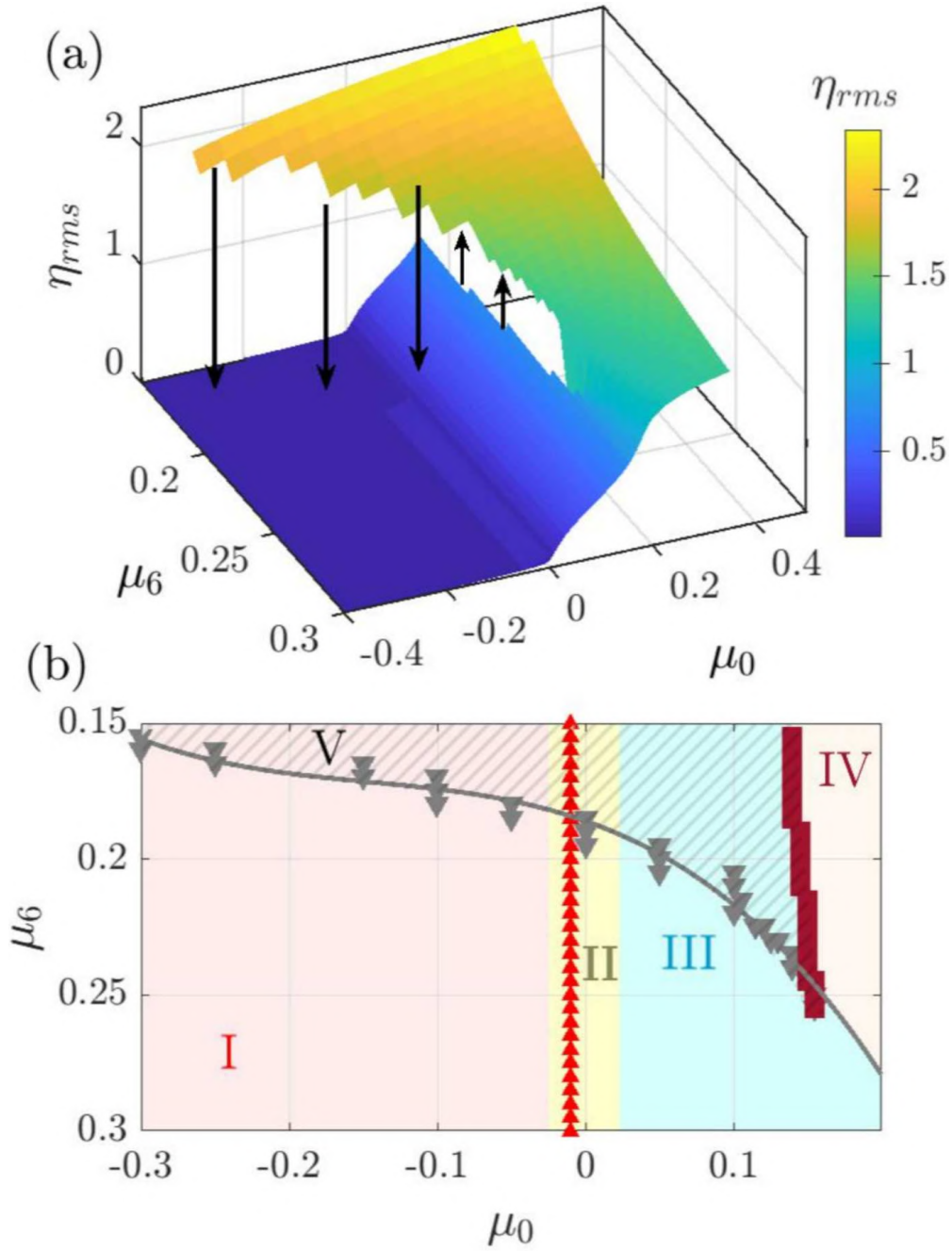


Figure 4.1: (a) Change of criticalities of bifurcations observed from the model in Eq. (4.7) and the corresponding (b) stability diagram.

parameters  $\mu_0$  and  $\mu_6$  in the model capture the respective effects of  $\phi$  and  $v_z$ .

Finally, we note that secondary bifurcation can occur only when stable limit cycle solution arising from supercritical Hopf bifurcation, arising from a change in leading-order control  $\mu_0$ , loses its stability and give rise to an unstable branch of limit cycle oscillations and

stable limit cycle solution of significantly higher-amplitude. The loss of stability of limit cycle oscillations can only be effected when higher-order nonlinearities become significant (Ananthkrishnan *et al.*, 1998). Thus, we infer that  $\phi$  and  $v_z$  influence the physical processes which affect the higher-order nonlinearities in the system, thereby leading to a secondary bifurcation. However, we also note the limitations of the model in predicting the exact nature of the boundaries separating different dynamical states (figures 3.6b and 4.1b). Also, we observe that the trend of bifurcation captured by  $\mu_6$  is the opposite of what we observed when  $v_z$  is changed (see figure 3.6a).

### 4.3 MEAN-FIELD SYNCHRONIZATION MODEL FOR THERMOACOUSTIC TRANSITIONS

#### 4.3.1 Phase-oscillator based heat release rate model

To complete the thermoacoustic model discussed in Eq. (4.5), we need to know the exact form of  $\dot{q}'$ . The heat release rate field, say  $\dot{q}'(x, y, t)$ , of the turbulent flame, which fluctuates due to turbulent flow regardless of the presence of the acoustic field, is a continuous field decomposable in terms of amplitude and phase. We approximate the continuous phase field as a discrete (sufficiently large) set of amplitude-weighted phase oscillators, which evolve under the influence of acoustic fluctuations. This can be expressed in terms of a general response function ( $\mathcal{G}$ ) which expresses the evolution of the phase of the population of oscillators as (Strogatz, 2000; Kuramoto, 2003):

$$\frac{d\theta_l(\tilde{t})}{d\tilde{t}} = \tilde{\omega}_l + \mathcal{G} [\hat{R}(\tilde{t}), \Phi(\tilde{t}), \theta_l(\tilde{t})], \quad (4.8)$$

where  $\tilde{\omega}_l$  is the mean subtracted frequency of the  $l^{\text{th}}$  oscillator, where  $l = 1, \dots, N$ , and  $\mathcal{G}$  is a function of the phase of the oscillators ( $\theta_l$ ), normalized amplitude ( $\hat{R}$ ) and phase ( $\Phi$ ) of the acoustic pressure or velocity. The frequencies of the oscillators are distributed according to the probability density  $g(\tilde{\omega})$  centered around the acoustic frequency  $\tilde{\Omega}_0$ .

The relation between  $\Phi$  and  $\theta_l$  can be obtained by assuming that  $\mathcal{G}$  shifts  $\theta_l$  closer or away

from  $\Phi$ :  $\mathcal{G}$  is positive when  $\theta_l$  lags  $\Phi$ , and  $\mathcal{G}$  is negative when  $\theta_l$  leads  $\Phi$ . It is evident that the simplest periodic function that satisfies these requirements leads to:  $\mathcal{G} \propto \sin(\Phi - \theta_l)$  (Kuramoto, 1975). We further assume that  $\mathcal{G} \propto \hat{R}$  implies that the influence of the pressure oscillations becomes stronger as the amplitude of the pressure oscillations on the phase oscillators increases. This amplitude dependence of  $\mathcal{G}$  determines the maximum rate of phase shift for a given amplitude of pressure oscillations and so determines the *sensitivity* of an oscillator to the amplitude of acoustic perturbation. Thus, the modified expression for the evolution of the phase oscillator is:

$$\frac{d\theta_l(\tilde{t})}{d\tilde{t}} = \tilde{\omega}_l + \tilde{K} \hat{R}(\tilde{t}) \sin [\Phi(\tilde{t}) - \theta_l(\tilde{t})], \quad (4.9)$$

where the interaction amongst the oscillators is weighted equally using the coupling strength  $\tilde{K}$ . In the absence of acoustic feedback,  $\tilde{K}$  determines the level of interaction among the oscillators and hence, controls the degree of coherence and synchrony among the oscillators. Thus, the term  $\tilde{K} \hat{R}$  makes up the effective coupling strength due to intra-oscillator coupling and acoustic feedback. The distribution of frequency of the oscillators  $g(\tilde{\omega})$  is estimated from the amplitude spectrum of heat release rate fluctuations during the occurrence of combustion noise. Hence, the nonlinear flame response due to turbulence, acoustic feedback, etc., are indirectly accounted through the initial distribution  $g(\tilde{\omega})$  and the mean-field interactions of the oscillators.

Finally, the individual contribution from each of the phase oscillators can be added to obtain the overall heat release rate fluctuations (Dutta *et al.*, 2019), as shown below:

$$\dot{q}' = \tilde{q}_0 \sum_{i=1}^N \sin [\tilde{\Omega}_0 \tilde{t} + \theta_l(\tilde{t})], \quad (4.10)$$

where  $\tilde{q}_0$  (N/m $\cdot$ s) is introduced to keep the dimensions consistent. It is important to highlight that  $\tilde{q}_0$  remains constant and does not contribute to heat release rate fluctuations. On a fundamental level, the summation in Eq. (4.10) is a model-reduction of the spatially distributed heat release rate field in terms of interacting phase oscillators. The overall heat release rate fluctuations in Eq. (4.10) is thus high when oscillators are in synchrony

and low otherwise, as has been corroborated in multiple studies (Mondal *et al.*, 2017b; Pawar *et al.*, 2019).

### 4.3.2 Flame-acoustic coupling

Now we combine the mean-field model of the heat source with the oscillator equation for the temporal dynamics of the acoustic mode. Substituting (4.10) into (4.5), we obtain:

$$\ddot{\eta}(\tilde{t}) + \tilde{\zeta}\dot{\eta}(\tilde{t}) + \tilde{\Omega}_0^2\eta(\tilde{t}) = \tilde{\beta}\tilde{\Omega}_0 \cos(\tilde{k}\tilde{z}_f) \sum_{i=1}^N \sin[\tilde{\Omega}_0\tilde{t} + \theta_i(\tilde{t})], \quad (4.11)$$

where  $\tilde{\beta} = 2(\gamma - 1)\tilde{q}_0/\tilde{L}p_0$ . We non-dimensionalize Eqs. (4.11) and (4.9) using the following transformations:

$$z = \frac{\tilde{z}}{\tilde{L}}; \quad t = \tilde{\Omega}_0\tilde{t}; \quad k = \tilde{k}\tilde{L}; \quad \zeta = \frac{\tilde{\zeta}}{\tilde{\Omega}_0}; \quad \omega_l = \frac{\tilde{\omega}_l}{\tilde{\Omega}_0}; \quad \beta = \frac{\tilde{\beta}}{\tilde{\Omega}_0}; \quad K = \frac{\tilde{K}}{\tilde{\Omega}_0}. \quad (4.12)$$

Using the above non-dimensionalization in Eq. (4.9) and Eq. (4.11), we obtain:

$$\ddot{\eta}(t) + \zeta\dot{\eta}(t) + \eta(t) = \beta \cos(kz_f) \sum_{i=1}^N \sin[t + \theta_i(t)], \quad (4.13a)$$

$$\dot{\theta}_l(t) = \omega_l + K\hat{R}(t) \sin[\Phi(t) - \theta_l(t)]. \quad (4.13b)$$

Thus, Eq. (4.13a) and Eq. (4.13b) denote the set of  $(N + 1)$  coupled ordinary differential equations making up the thermoacoustic mean-field model. It is easy to observe that an increase in the effective coupling strength through an increase in  $K$  or amplitude of acoustic pressure  $\hat{R}$  would lead to phase synchronization of the phase oscillators to a common phase. The synchronized state would, in turn, produce the largest driving to the damped harmonic oscillator equation governing the acoustic fluctuations through the summation in Eq. (4.13a), consequently leading to the state of thermoacoustic limit cycle oscillations.

### 4.3.3 Slow flow amplitude and phase representation of the mean-field model

We now seek the limit cycle solution for the set of equations given by Eq. (4.13) which will then be used for obtaining the feedback of acoustic fluctuations  $(\hat{R}, \Phi)$  on the phase

oscillators. We begin by assuming that the acoustic fluctuations are quasi-harmonic such that  $\eta(t)$  can be decomposed as (Krylov and Bogolyubov, 1947):

$$\eta(t) = -R(t) \cos [t + \Phi(t)], \quad (4.14)$$

where  $R(t)$  is the envelope amplitude and  $\Phi(t)$  is the phase of the ensuing limit cycle and varies much slower than the fast time scale  $2\pi/\Omega_0$ . Thus, the autonomous equation describing the evolution of pressure fluctuations in Eq. (4.13a) can be decomposed further in terms of slow variables ( $R$  and  $\Phi$ ). We next calculate  $\dot{\eta}(t)$  and  $\ddot{\eta}(t)$  by differentiating Eq. (4.14) with respect to  $t$  and get:

$$\dot{\eta}(t) = -\dot{R}(t) \cos [t + \Phi(t)] + R(t) \sin [t + \Phi(t)] + R(t)\dot{\Phi}(t) \sin [t + \Phi(t)]. \quad (4.15)$$

By representing the solution in the form of Eq. (4.14), we express  $\eta(t)$  as a function of  $R(t)$  and  $\Phi(t)$ , which introduces additional ambiguity in the equation. To remove the introduced ambiguity, we have to prescribe one arbitrary relationship between these quantities, which we take as (Balanov *et al.*, 2008):

$$-\dot{R}(t) \cos [t + \Phi(t)] + R(t)\dot{\Phi}(t) \sin [t + \Phi(t)] = 0. \quad (4.16)$$

Therefore, the derivative of  $\eta(t)$  is a simple expression of the form:

$$\dot{\eta}(t) = R(t) \sin [t + \Phi(t)]. \quad (4.17)$$

We follow Balanov *et al.* (2008) for expressing  $\eta(t)$ ,  $\dot{\eta}(t)$  and  $\ddot{\eta}(t)$  in terms of exponents of complex arguments. We start by reformulating the solution for  $\eta(t)$  as:

$$\eta(t) = -\frac{1}{2} (R(t)e^{i\Phi(t)} e^{it} + R(t)e^{-i\Phi(t)} e^{-it}) = -\frac{1}{2} (ae^{it} + a^* e^{-it}). \quad (4.18)$$

We introduce a complex function of time  $a$ , such that  $a = R(t)e^{i\Phi(t)}$  and  $a^* = R(t)e^{-i\Phi(t)}$ , where the asterisk denotes the complex conjugate. Next, reformulating  $\dot{\eta}(t)$ , we get:

$$\dot{\eta}(t) = \frac{1}{2i} R(t) e^{i(t+\Phi(t))} - e^{-i(t+\Phi(t))} = -\frac{i}{2} (ae^{it} - a^* e^{-it}). \quad (4.19)$$

Finally, reformulating  $\ddot{\eta}(t)$  in terms of exponent of complex arguments, we obtain:

$$\ddot{\eta}(t) = -\frac{i}{2}(\dot{a}e^{it} - \dot{a}^*e^{-it}) + \frac{1}{2}(ae^{it} + ae^{-it}). \quad (4.20)$$

We now substitute  $\eta(t)$ ,  $\dot{\eta}(t)$  and  $\ddot{\eta}(t)$  ( Eqs. (4.18), (4.19) and (4.20), respectively) into Eq. (4.13a) and we get:

$$\begin{aligned} & -i(\dot{a}e^{it} - \dot{a}^*e^{-it}) + (ae^{it} + ae^{-it}) - i\zeta(ae^{it} - a^*e^{-it}) \\ & - (ae^{it} + a^*e^{-it}) = -i\beta \cos(kz_f) \sum_{i=1}^N (e^{i(t+\theta_i(t))} - e^{-i(t+\theta_i(t))}). \end{aligned} \quad (4.21)$$

By canceling the second and fourth terms in the above equation and then multiplying the whole equation by  $e^{-it}$ , we obtain:

$$(\dot{a} - \dot{a}^*e^{-2it}) + \zeta(a - a^*e^{-2it}) = \beta \cos(kz_f) \sum_{i=1}^N (e^{i\theta_i(t)} - e^{-2it}e^{-i\theta_i(t)}). \quad (4.22)$$

We now note that  $a$ ,  $\dot{a}$  and their complex conjugates are slow functions of time as compared to the functions  $e^{\pm nit}$ , where  $n$  is an integer. This means that the slow flow variables do not change much during one period of fast oscillations. If we average the whole equation over one period of fast oscillations, i.e.,  $T = 2\pi$ , we can eliminate the fast terms, and only the slow terms remain. The time average  $\bar{f}$  of a smooth function  $f(t)$  over the time interval  $T$  is defined as  $\bar{f} = \frac{1}{T} \int_0^{2\pi} f(t) dt$ . It is easy to see that all the terms containing  $e^{-2it}$  would integrate to zero over the time oscillation period  $T$ . Therefore, we apply time averaging on Eq. (4.22) and obtain:

$$\dot{a} + \zeta a = \beta \cos(kz_f) \sum_{i=1}^N e^{i\theta_i(t)}. \quad (4.23)$$

Recalling that  $a = R(t)e^{i\Phi(t)}$  and substituting it in the above equation, we get:

$$\dot{R}(t)e^{i\Phi(t)} + iR(t)\dot{\Phi}(t)e^{i\Phi(t)} + \zeta R(t)e^{i\Phi(t)} = \beta \cos(kz_f) \sum_{i=1}^N e^{i\theta_i(t)}. \quad (4.24)$$

We multiply Eq. (4.24) by  $e^{-i\Phi(t)}$  and then equate the real and imaginary parts of the equation. This gives us the evolution equations for the slowly varying amplitude and

phase variables as:

$$\dot{R}(t) = \beta \cos(kz_f) \sum_{i=1}^N \cos [\theta_l(t) - \Phi(t)] - \zeta R(t), \quad (4.25a)$$

$$\dot{\Phi}(t) = \frac{\beta}{R(t)} \cos(kz_f) \sum_{i=1}^N \sin [\theta_l(t) - \Phi(t)]. \quad (4.25b)$$

These equations are the *truncated equations* (Balanov *et al.*, 2008) for the evolution of  $R(t)$  and  $\Phi(t)$ . Similarly, applying the method of averaging on Eq. (4.13b), we observe that the equation is associated with only the slow flow variables, i.e.,  $R$ ,  $\Phi$ , and  $\theta_l$ , and hence, remains unchanged.

#### 4.3.4 Limit cycle solution

From Eq. (4.25a), it is straightforward that the limit cycle solution is given by  $\dot{R}(t) = 0$ , i.e., when the rate of change of envelope of acoustic pressure tends to zero. Although Eqs. (4.25a) and (4.25b) appear compact, their analysis is quite involved as it is difficult to separate the amplitude and phase variables. To make further progress, we recast them from polar to Descartes coordinates through the following variable transformation:  $A(t) = R(t) \cos \Phi(t)$  and  $B(t) = R(t) \sin \Phi(t)$ . The time derivatives of the new variables ( $A$  and  $B$ ) can be expressed through  $R$  and  $\Phi$  as:

$$\dot{A}(t) = \dot{R}(t) \cos \Phi(t) - R(t) \dot{\Phi}(t) \sin \Phi(t), \quad (4.26a)$$

$$\dot{B}(t) = \dot{R}(t) \sin \Phi(t) + R(t) \dot{\Phi}(t) \cos \Phi(t). \quad (4.26b)$$

On substituting Eq. (4.26) into Eqs. (4.25a) and (4.25b), we obtain the truncated equations in Descartes coordinates:

$$\dot{A}(t) = \beta \cos(kz_f) \sum_{i=1}^N [\cos (\theta_l(t) - \Phi(t)) \cos \Phi(t) - \sin (\theta_l(t) - \Phi(t)) \sin \Phi(t)] - \zeta A(t), \quad (4.27a)$$

$$\dot{B}(t) = \beta \cos(kz_f) \sum_{i=1}^N [\cos (\theta_l(t) - \Phi(t)) \sin \Phi(t) - \sin (\theta_l(t) - \Phi(t)) \cos \Phi(t)] - \zeta B(t), \quad (4.27b)$$

On simplifying the above equation (Eq. (4.27)), we obtain:

$$\dot{A}(t) = \beta \cos(kz_f) \sum_{i=1}^N \cos \theta_i(t) - \zeta A(t), \quad (4.28a)$$

$$\dot{B}(t) = \beta \cos(kz_f) \sum_{i=1}^N \sin \theta_i(t) - \zeta B(t). \quad (4.28b)$$

Imposing the condition for limit cycle oscillations, viz.,  $\dot{A}(t) = 0$ ,  $\dot{B}(t) = 0$  in the above equation, the resultant amplitude of limit cycle oscillations is obtained as:

$$R_{\text{LCO}}(t) = \beta \cos(kz_f) N r(t) / \zeta, \quad (4.29)$$

where  $r(t)$ , the order parameter, is defined as (Strogatz, 2000):

$$r(t) = \frac{1}{N} \sqrt{\left( \sum_{i=1}^N \sin \theta_i(t) \right)^2 + \left( \sum_{i=1}^N \cos \theta_i(t) \right)^2}. \quad (4.30)$$

We know that during limit cycle oscillations, all the oscillators are perfectly synchronized, resulting in  $r(t) \approx 1$ . Thus, the amplitude of the limit cycle oscillations is expressed as  $R_{\text{LCO}} = \beta \cos(kz_f) N / \zeta$ . This is used for normalizing the amplitude of oscillations as  $\hat{R} = R / R_{\text{LCO}}$

To compare with experimental observations, we normalize the model Eq. (4.13) with the amplitude of limit cycle oscillation ( $R_{\text{LCO}}$ ). Consequently, we obtain:

$$\ddot{\hat{\eta}}(t) + \zeta \dot{\hat{\eta}}(t) + \hat{\eta}(t) = \zeta \frac{1}{N} \sum_{i=1}^N \sin[t + \theta_i(t)], \quad (4.31a)$$

$$\dot{\theta}_i(t) = \omega_i + K \left\{ \dot{\hat{\eta}}(t) \cos[t + \theta_i(t)] + \hat{\eta}(t) \sin[t + \theta_i(t)] \right\}, \quad (4.31b)$$

where  $\hat{\eta}(t) = \eta(t) / R_{\text{LCO}}$ . Similarly,  $R$  and  $\Phi$  in Eq. (4.13b) are rewritten in terms of  $\eta$  and  $\dot{\eta}$  using Eq. (4.14).

#### 4.4 NUMERICAL SIMULATION FOR THE MEAN-FIELD MODEL

In this section, we give details about the numerical setup and parameter initialization for solving the model Eq. (4.31). We also discuss the procedure for estimating the model

parameters from experimental data.

#### 4.4.1 Initialization and bifurcation analysis

The initial phase distribution is determined as  $\theta_l(0) = \theta_m + \epsilon$ , where  $\theta_m$  represents the mean of the distribution of  $\theta$  and  $\epsilon$  is normally distributed as  $\epsilon \sim \mathcal{N}(0, \sigma^2)$ . The initial frequency distribution  $g(\omega)$  is obtained by uniformly distributing oscillators proportional to the amplitude of the heat release rate spectrum during the state of combustion noise. The procedure for numerically sampling the frequency is detailed in Appendix B. The number of oscillators  $N$  determines how well the spectrum  $\hat{q}(f)$  is resolved by  $g(\omega)$ . We fix  $N = 2 \times 10^3$  oscillators for which  $g(\omega)$  resolves  $\hat{q}(f)$  sufficiently well. The procedure for optimisation of  $N$  is included in Appendix C. The initial frequency distribution of the oscillators so obtained from the heat release rate spectrum during the occurrence of combustion noise for the three combustors (bluff-body stabilized, swirl-stabilized and annular combustor) is shown in figure 4.2.

With these inputs, the transition is obtained by sequentially changing  $K$  and numerically solving Eqs. (4.31a) and (4.31b) using the adaptive fourth-order Runge-Kutta method (Zheng and Zhang, 2017). We first verify the transition predicted by the model with that observed in experiments. Upon verification, we perform a parameter estimation to identify the correspondence between the control parameters in the model and our experiments, as discussed next.

#### 4.4.2 Parametric identification

Many techniques have been used for identifying parameters while modeling thermoacoustic instabilities. For instance, system identification has been used for estimating parameters in models involving transfer functions or impulse response functions (Polifke, 2014; Bonciolini *et al.*, 2017) and coupled oscillator models (Lee *et al.*, 2020, 2021). Similarly, uncertainty quantification has been used for estimating parameters in level-set flame models (Yu *et al.*, 2019, 2021). Here, we implement an

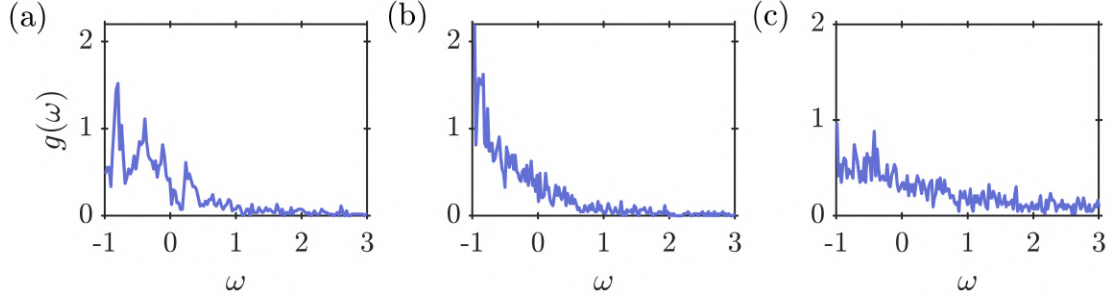


Figure 4.2: Frequency distribution  $g(\omega)$  of  $N = 2 \times 10^3$  phase oscillators obtained from the amplitude spectrum of heat release rate during the state of combustion noise for the (a) bluff-body stabilized dump combustor, (b) swirl-stabilized dump combustor and (c) annular combustor. Here,  $\omega$  is distributed relative to the acoustic frequency  $\tilde{\Omega}_0$  and also normalized by  $\tilde{\Omega}_0$ .

optimisation algorithm that identifies model parameters by minimizing the error between experimental data and model predictions.

We optimise the model parameters ( $\zeta$  and  $K$ ) along with the initial conditions  $\eta(0)$ ,  $\dot{\eta}(0)$  and  $\theta_l(0)$ . The initial conditions are included in the optimisation to accurately reproduce experimental features during the state of intermittency featuring the presence of random bursts of periodic oscillations. When initial conditions are instead randomised and not included in the optimisation, statistical features (such as PDF, spectrum, etc.) are reproduced by the model during all the states. However, the location of periodic bursts is not accurately predicted (see Appendix D). Therefore, we estimate the parameter vector,  $\mathbb{P} = [\zeta, K, \eta(0), \dot{\eta}(0), \theta_m, \sigma]$ .

Constructing the vector  $\mathbf{Y} = [\eta, \dot{\eta}, \theta_l]^T$  and re-writing the nonlinear set of equations in Eq. (4.31) as:

$$\dot{\mathbf{Y}} = f(\mathbb{P}, \mathbf{Y}). \quad (4.32)$$

Starting from an initial state  $\mathbf{Y}_0$  at  $t_0$ , the state of the system at time  $t_n = t_0 + n\Delta t$  can be obtained from the model as:

$$\mathbf{Y}_m(\mathbb{P}; t_n) = \int_{t_0}^{t_n} f(\mathbb{P}, \mathbf{Y}) dt + \mathbf{Y}_0. \quad (4.33)$$

The fourth-order Runge-Kutta scheme is used for numerically integrating the above equations with a time step of  $\Delta t$ . Using Eqs. (4.2) and (4.10), we obtain:

$$p'_m = \dot{\hat{\eta}}(t); \quad \dot{q}'_m = \frac{1}{N} \sum_{i=1}^N \sin [t + \theta_i(t)]. \quad (4.34)$$

Thus, from the model we obtain:  $\mathbf{X}_m(\mathbb{P}; t_n) = [p'_m, \dot{q}'_m]$ .

Next, from the experimental data, we construct the vector  $\mathbf{X}_{\text{exp}}(\phi; t_n) = [p', \dot{q}']^T$ , where  $\phi$  is the equivalence ratio or the control parameter in the experiments,  $p'$  and  $\dot{q}'$  are the normalized acoustic pressure and global heat release rate fluctuations, respectively. Thus, we can obtain the parameter values that minimize the error between the model  $\mathbf{X}_m$  and the experiments  $\mathbf{X}_{\text{exp}}$ . This minimisation of the error can be done by constructing the loss function ( $\mathcal{L}$ ) based on the mean square error:

$$\mathcal{L}(\mathbb{P}) = \frac{1}{N} \sum_{n=1}^N \|\mathbf{X}_m(\mathbb{P}; t_n) - \mathbf{X}_{\text{exp}}(\phi; t_n)\|_2^2. \quad (4.35)$$

Finally, the parameter estimation can be cast in terms of a minimisation problem subject to the parameter vector  $\mathbb{P}$ . The minimisation is performed using the gradient descent method (Boyd *et al.*, 2004):

$$\mathbb{P}_{i+1} = \mathbb{P}_i - \alpha_l \nabla_{\mathbb{P}} \mathcal{L}, \quad (4.36)$$

where  $\alpha_l$  is the learning rate which gives the rate at which the parameter updates per unit gradient of the loss function with respect to the parameter. We used a learning rate of  $\alpha_l = 1 \times 10^{-3}$  to optimise the parameter estimates. We use the automatic differentiation method to evaluate the gradient of  $\mathcal{L}$  with respect to  $\mathbb{P}$  (Baydin *et al.*, 2018). Kindly see Appendix E.1 for more details about convergence and loss minimisation.

It is worth noting that randomizing initial conditions does not have any reasonable effect on the  $K - \phi$  relation that is obtained following the optimisation procedure, as shown in Appendix D.

## 4.5 MODEL PREDICTION OF TRANSITIONS TO THERMOACOUSTIC INSTABILITY

The model is numerically implemented by choosing the frequency distribution of oscillators  $g(\omega)$  from the amplitude spectrum  $\hat{q}(f)$  of the heat release rate fluctuations obtained during the state of combustion noise from different combustors. The damping coefficient ( $\zeta$ ) is obtained from the experimental data during the state of combustion noise using parameter optimisation Eq. (4.36) and is subsequently fixed for determining other states during the transition. Using these inputs, the transition to the state of the limit cycle is obtained by increasing the coupling strength  $K$ . Once the transition is qualitatively verified with the experiments by systematically varying the coupling strength  $K$  and randomly choosing the initial conditions, parameter optimisation of the vector  $\mathbb{P}$  is performed according to Eq. (4.36) and shown in Appendix I.1. The parameter optimisation technique is applied on all the experimentally observed states to identify the relationship between the coupling strength  $K$  and the control parameter observed in the experiments  $\phi$ . The  $K - \phi$  relationship enables us to map the bifurcation obtained from experiments onto the bifurcation plot obtained from the model.

Let us now compare how our model fares in predicting continuous and abrupt transitions observed in turbulent thermoacoustic systems.

### 4.5.1 Continuous transition to thermoacoustic instability

The bluff-body stabilized combustor, shown in figure 2.2(a,c), exhibits a continuous transition to the state of thermoacoustic instability through intermittency when the equivalence ratio  $\phi$  is decreased. Figure 4.3(a) shows the variation in the amplitude of acoustic pressure fluctuations ( $p'_{\text{rms}}$ ) as a function of the equivalence ratio ( $\phi$ ) and coupling strength ( $K$ ). The amplitude is normalized with the amplitude of limit cycle oscillations to aid the comparison of the observed transition with that predicted by the model Eq. (4.31). Figure 4.3(b-d) shows the characteristics of pressure ( $p'$ ) and heat release rate ( $q'$ ) fluctuations during the state of combustion noise, intermittency and

thermoacoustic instability, as marked in the bifurcation diagram.

At  $\phi = 0.86$  ( $K = 0.23$ ), we observe the occurrence of combustion noise (figure 4.3b) where the fluctuations ( $p'$ ,  $q'$ ) are visibly aperiodic. These fluctuations are associated with an unimodal distribution and possess broadband spectra. As  $\phi$  is decreased ( $\phi = 0.72$ ,  $K = 0.75$ ), we observe intermittency where periodic fluctuations appear amidst aperiodic fluctuations (figure 4.3c). A further decrease in  $\phi$  leads to an increase in the frequency of occurrence and the amplitude of these periodic bursts. The appearance of these periodic bursts leads to a sharp, albeit low-amplitude, peak in the spectrum  $|\hat{p}(f)|$  and  $|\hat{q}(f)|$ . Further decrease in the value of  $\phi$  leads to a gradual increase in the amplitude and the number of occurrences of these bursts and manifests as a continuous increase in the value of  $p'_{\text{rms}}$  observed in figure 4.3(a). The transition has a “sigmoid” shape which is a characteristic feature of such continuous transitions (Nair *et al.*, 2014). Finally, at  $\phi = 0.56$  ( $K = 2$ ), we observe limit cycle oscillations associated with the state of thermoacoustic instability. The fluctuations possess a bimodal distribution and are periodic with narrowband amplitude spectra at a frequency of 146.5 Hz (figure 4.3d).

The transition predicted by the model (continuous line) is also shown in figure 4.3(a). To aid the comparison of specific states depicted by the model, the envelopes of the time series obtained from the model (in darker shade) are overlaid on top of each of the time series obtained from experiments (in lighter shade) in figure 4.3(b-d). Similarly, the PDF and the spectra indicated in the darker shade are the predictions of the model. The broadband spectrum  $|\hat{q}(f)|$  during the occurrence of combustion noise shown in figure 4.3(b) is used for obtaining the distribution  $g(\omega)$  shown in figure 4.2(a).

We notice that the model captures many features of the experimental data. Foremost, we observe that the model predicts the transition observed in the experiments very well. The continuous, sigmoid-type transition to the state of limit cycle oscillation is well captured (figure 4.3a). Quite notably, the prediction from this model shows a qualitative

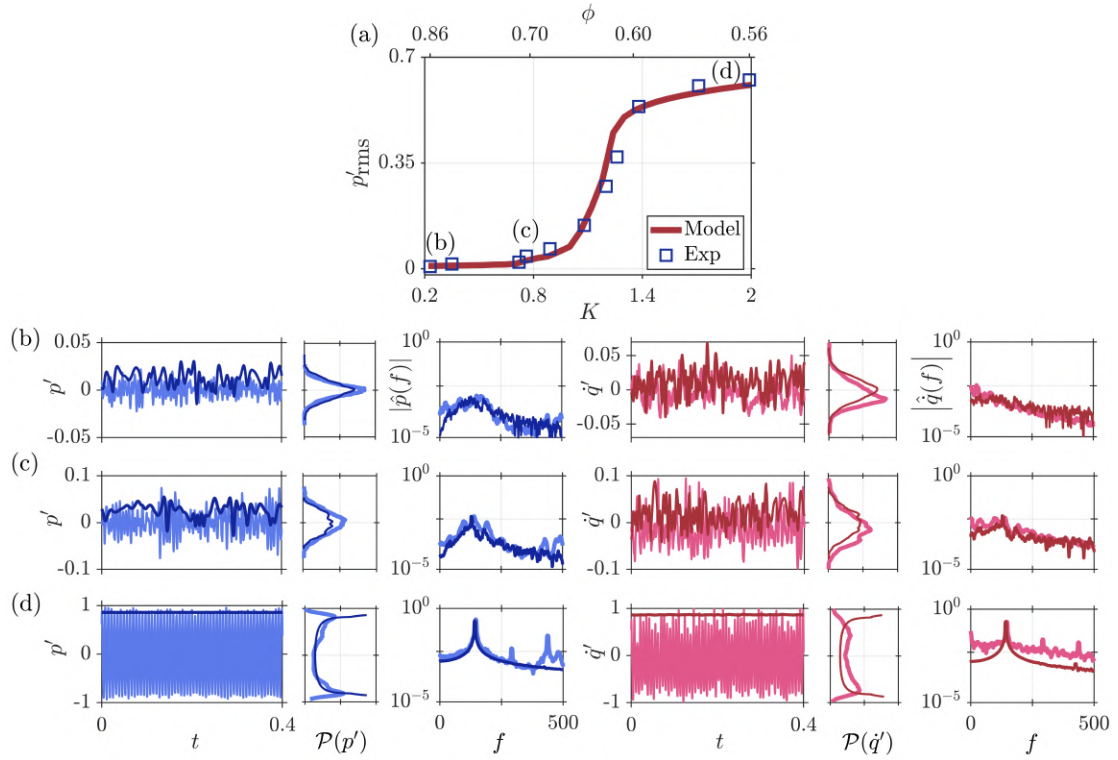


Figure 4.3: Continuous transition to thermoacoustic instability through the state of intermittency observed in the bluff-body stabilized combustor. (a) Comparison of the normalized amplitude  $p'_{\text{rms}}$  obtained from the experiments ( $\square$ ) and model ( $-$ ) as a function of the equivalence ratio ( $\phi$ ) and the model parameter ( $K$ ). The time series ( $p'$ ,  $q'$ ), probability distribution function [ $\mathcal{P}(p')$ ,  $\mathcal{P}(q')$ ] and amplitude spectrum [ $|\hat{p}(f)|$ ,  $|\hat{q}(f)|$ ] are shown during the states of (b) combustion noise ( $\phi = 0.86$ ,  $K = 0.23$ ), (c) intermittency ( $\phi = 0.72$ ,  $K = 0.75$ ) and (d) thermoacoustic instability ( $\phi = 0.56$ ,  $K = 2$ ). In panels (b-d) the experimental data are shown using a lighter shade, while the model result is shown using a darker shade. Only the envelope of the time series from the model is shown for clarity.

match with the time series of pressure fluctuations obtained from experiments. The model captures various features of the time series of pressure fluctuations. For instance, the distribution  $\mathcal{P}(p')$  and spectrum  $|\hat{p}(f)|$  during the state of combustion noise and intermittency are well approximated. Similarly, the envelope of the limit cycle obtained from the model is a good estimate of the limit cycle amplitude observed in figure 4.3(d). Finally, the spectrum  $|\hat{p}(f)|$  from the model shows a close match with that observed in experiments.

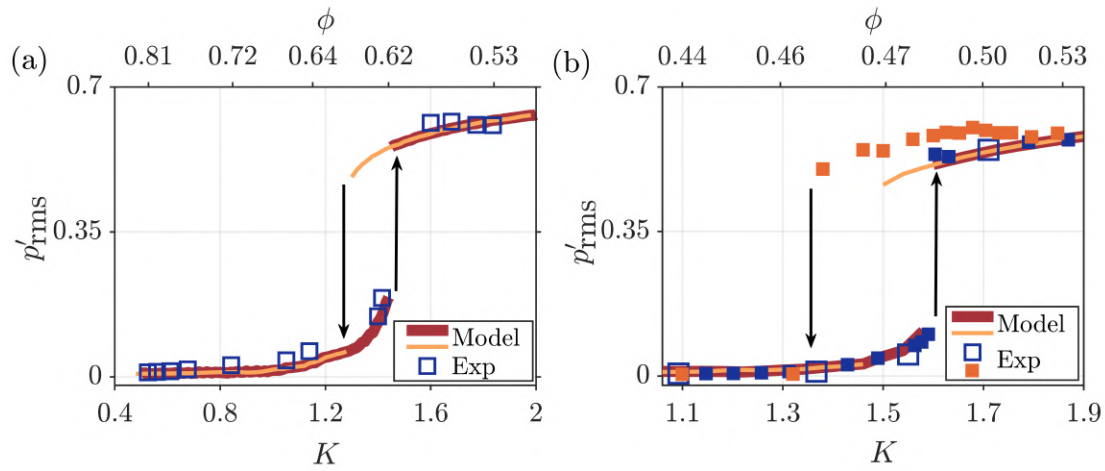


Figure 4.4: Abrupt secondary bifurcation to limit cycle oscillations in (a) swirl-stabilized dump combustor and (b) annular combustor. The bifurcation plots illustrate the comparison of the normalized amplitude  $p'_{rms}$  obtained from the experiments ( $\square$ ) and the model (—) as a function of equivalence ratio ( $\phi$ ) and the model parameter ( $K$ ). The forward and reverse transitions in the experiments are indicated as ( $\square$ ) and ( $\blacksquare$ ), while in the model are indicated as (—) and (—), respectively. In panel (b), heat release rate data is available only at the four points indicated by ( $\square$ ). For the remaining points (depicted by  $\blacksquare$ ) only pressure data is available, we interpolated these points from the optimisation at the four points shown in figure 4.6.

#### 4.5.2 Secondary bifurcation to high-amplitude thermoacoustic instability

Both swirl-stabilized dump combustor (figure 2.2a, d) and annular combustor (figure 2.1) undergo abrupt secondary bifurcation to the state of thermoacoustic instability on varying the control parameter ( $\phi$ ) systematically (see figure 4.4). For the former, the transition is observed when  $\phi$  is decreased from 0.81 to 0.53, while for the latter, the transition is observed upon increasing  $\phi$  from 0.44 to 0.53. The transition for both the combustors are shown in figure 4.4 where the normalized root mean square of the acoustic pressure ( $p'_{rms}$ ) is plotted as a function of the equivalence ratio ( $\phi$ ) and the model parameter  $K$ . For the annular combustor (figure 4.4b), chemiluminescence data was acquired only at four locations marked by  $\square$ . For the remaining states, pressure data alone was acquired. The dynamical states corresponding to the four points representative of the secondary bifurcation in the annular combustor are shown in figure 4.5.

The annular combustor is in a state of combustion noise close to  $\phi = 0.44$  (figure 4.5a). Both pressure and heat release rate fluctuations exhibit noisy behavior, possessing a unimodal PDF and broadband amplitude spectrum. When  $\phi$  is increased, we observe intermittent periodic oscillations (figure 4.5b). The appearance of intermittent bursts is associated with a continuous increase in the amplitude of oscillations (see figure 4.4b for  $\phi = 0.47$  and  $K = 1.37$ ). In addition, the peak of the distribution  $\mathcal{P}(p')$  and  $\mathcal{P}(\dot{q}')$  widens. A narrowband starts to appear in the amplitude-spectrum at  $f = 218$  Hz (figure 4.5b). Upon further increase to  $\phi = 0.49$  ( $K = 1.55$ ), we observe low-amplitude limit cycle oscillations along with a bimodal distribution  $\mathcal{P}(p')$  possessing additional peaks at  $|p'| \neq 0$  (figure 4.5c). During the state of low-amplitude limit cycle oscillations, we observe  $\tilde{p}'_{\text{rms}} \approx 0.3$  kPa. The distribution  $\mathcal{P}(\dot{q}')$  depicts a distinct bimodal shape along with a narrowband peak in the amplitude-spectrum at  $f = 223$  Hz. Finally, there is an abrupt secondary fold bifurcation from low-amplitude to very high-amplitude limit cycle oscillations beyond  $\phi = 0.49$  ( $K = 1.55$  in figure 4.4b). The amplitude of pressure fluctuations at this state is  $\tilde{p}'_{\text{rms}} \approx 2$  kPa. The distribution remains bimodal with the distribution peaks appearing at large values of  $p'$  (figure 4.5d). Accordingly, the spectrum shows a dominant peak at  $f = 227$  Hz.

A similar transition is also observed in the swirl-stabilized dump combustor (see figure 4.4a) when  $\phi$  is decreased from 0.81 to 0.53. There is a secondary bifurcation from low-amplitude ( $\tilde{p}' \approx 1.5$  kPa) limit cycle to very high-amplitude ( $\tilde{p}' \approx 5.6$  kPa). The frequency of limit cycle oscillations is  $f = 201$  Hz. The dynamical states during the secondary bifurcation are similar to those observed for the annular combustor that is depicted in figure 4.5.

Secondary bifurcation predicted by the model for each of the two combustors is also shown in figure 4.4. We notice that the model, numerically simulated by considering the spectrum  $|\hat{q}(f)|$  during the state of combustion noise for obtaining  $g(\omega)$  (see figure 4.5a), predicts the secondary bifurcation very well. The normalized limit cycle amplitude

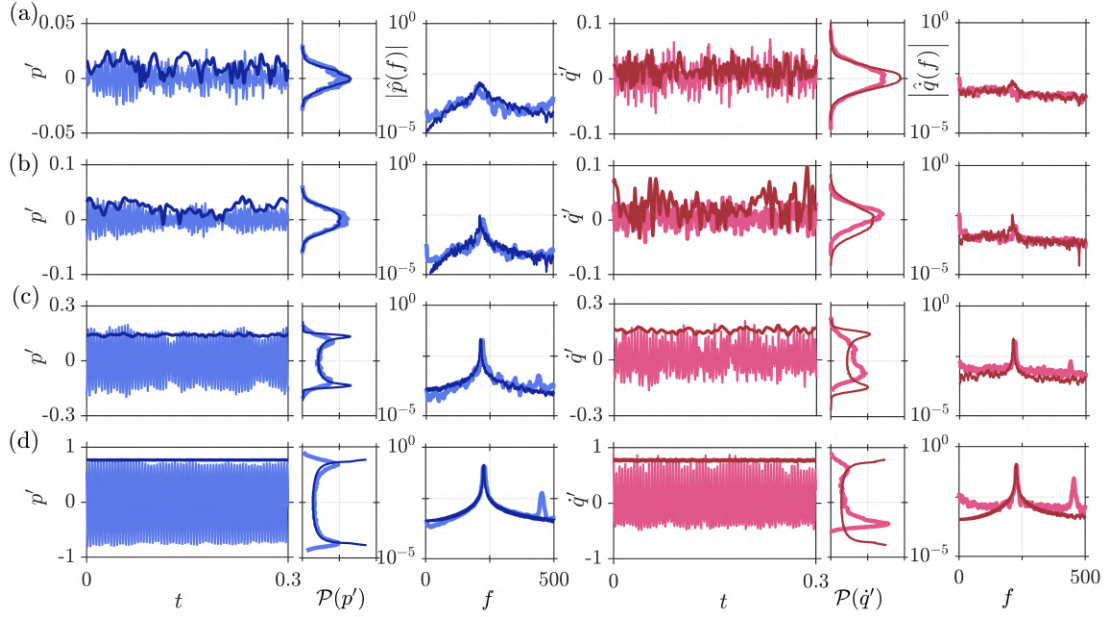


Figure 4.5: Representative states observed during secondary bifurcation in the annular combustor. The time series ( $p'$ ,  $q'$ ), probability distribution function [ $\mathcal{P}(p')$ ,  $\mathcal{P}(q')$ ] and amplitude spectrum [ $|\hat{p}(f)|$ ,  $|\hat{q}(f)|$ ] are shown during the states of (a) combustion noise ( $\phi = 0.44$ ,  $K = 1.09$ ), (b) intermittency ( $\phi = 0.47$ ,  $K = 1.37$ ), (c) low-amplitude thermoacoustic instability ( $\phi = 0.49$ ,  $K = 1.55$ ) and (d) high-amplitude thermoacoustic instability ( $\phi = 0.52$ ,  $K = 1.71$ ). The experimental data are shown using a lighter shade, while the model result is shown using darker shade.

following the secondary fold bifurcation is well approximated. The dynamics of pressure and heat release fluctuations obtained from the model are also shown in figure 4.5. We observe that the model captures the amplitude of pressure and heat release rate oscillations associated with the different states of combustor operation. In addition, the probability density functions and amplitude spectrum of the pressure and the heat release rate fluctuations are well estimated by the model. Furthermore, our model simulation confirms the presence of type-II intermittency in both continuous and abrupt transitions, which is consistent with the findings from the experiments corresponding to both the bluff-body stabilized combustor and annular combustor. Please refer to Appendix F for more details.

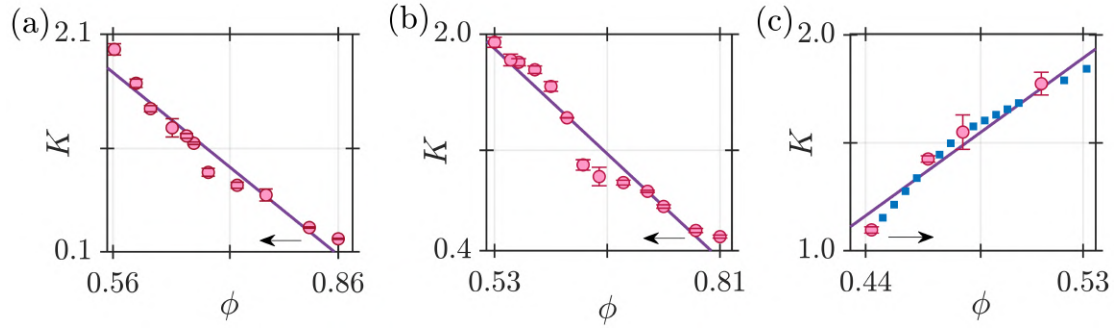


Figure 4.6: Correspondence between the control parameter in the model ( $K$ ) and experiments ( $\phi$ ) obtained using gradient descent optimisation for the (a) bluff-body stabilized dump combustor, (b) swirl-stabilized dump combustor, and (c) annular combustor. For all the cases, we obtain a linear relation between  $\phi$  and  $K$  where the fits are: (a)  $K = -5.35\phi + 4.68$ , (b)  $K = -4.85\phi + 4.28$  and (c)  $K = 8.59\phi - 2.66$ . The goodness-of-fit corresponding to different combustors is 0.95, 0.94, and 0.96, respectively. The arrows in each panel indicate the direction in which  $\phi$  was varied in experiments. In panel (c), heat release rate data were obtained only at four points. The remaining points were interpolated. Error bars correspond to the standard deviation in the estimation of  $K$  by sliding the window used during optimisation (Appendix E.1).

### 4.5.3 Relation between the control parameters in experiments and model

The correspondence between the control parameters in experiments and the parameters of the model is quite important. Knowing how parameters observed in the experiments are related to the model allows for the interpretation of experimental observations in terms of the physics embodied in the model. Thus, we perform parameter optimisation as explained in Section 4.4 to obtain the relation between the experimentally controlled equivalence ratio  $\phi$  and model parameter  $K$ . The relationship between  $K$  and  $\phi$  estimated using parameter optimisation for the three combustors are shown in figure 4.6. The indicated error in the relation is determined from a distribution of  $K$  obtained by estimating  $K$  from  $\mathbf{X}_{\text{exp}}$  for a window of size  $t_w = 0.5$  s and sliding the window across the entire time series. The choice of window size is explained in Appendix E.1. These  $K - \phi$  relations were used for constructing the bifurcation diagram in terms of  $K$  in figures 4.3(a) and 4.4. Note that for the annular combustor, optimisation was performed only at four data points for which heat release rate data was available.

For the bluff-body and swirl-stabilized dump combustors, the transition is attained by decreasing  $\phi$ . For each of these cases,  $\phi$  is a linearly decreasing function of  $K$ . In contrast, the transition is attained by increasing  $\phi$  in the annular combustor, and we obtain a linearly increasing relationship between  $\phi$  and  $K$ . For all these cases, note that the linear relation between  $\phi$  and  $K$  is such that (increasing/decreasing) change in the control parameter  $\phi$  is translated to an increase in  $K$ . This linear dependence makes the model highly interpretable: a change in the control parameter leads to an increase in the coupling strength of the phase oscillators, promoting global phase synchronization and hence, limit cycle oscillations.

Here, we reiterate that the excellent agreement between the experiments and model is not a result of parameter optimisation. The parameter optimisation only determines the specific mapping from  $K$  to  $\phi$  once the transition in the model has been determined for a given parameter input. The accuracy of prediction and optimisation depends upon how well the model represents the behavior of the system. Our results show that the model captures the combustor dynamics very well, lending support to our methodology.

On the flip-side however, the model does not capture some experimentally observed features. For instance, we observe that the higher order modes appearing in the spectrum  $|\hat{p}(f)|$  (cf. figures 4.3 and 4.5) are not captured, as only the fundamental mode was considered in the formulation of the model Eq. (4.5). The results can be improved by incorporating the higher modes in the current model. Further, the presence of highly turbulent flow in the experiments introduces phase-jitter in the heat release rate signal (Shanhogue *et al.*, 2009b; Shin and Lieuwen, 2013). This is manifested in terms of highly turbulent fluctuations in the time series of  $\dot{q}'$  and asymmetric PDF during the transition to thermoacoustic instability (cf. figures 4.3 and 4.5). Bonciolini *et al.* (2021) reported a similar asymmetry in the PDF during limit cycle oscillations, and were able to model it through the use of a Van der Pol type model with quadratic nonlinearity and stochastic forcing. Hence, model estimates of  $\dot{q}'$  can potentially be improved by

introducing stochastic terms in Eq. (4.13) (see Appendix G).

Finally, we notice that the annular combustor depicts hysteresis along with secondary bifurcation (figure 4.4b). While, the model also shows a hysteresis, the width of the region of hysteresis is not consistent with experiments. This discrepancy can be attributed to variations in gas/wall temperatures during the reverse path (Bonciolini *et al.*, 2019). Modeling the width of hysteresis correctly requires precise knowledge of the nonlinear damping effects arising from temperature changes introduce nonlinear damping effects.

For the present discussion in the context of modeling and prediction of thermoacoustic transitions along with the underlying synchronization behavior, the above mentioned dissimilarities are ignored in view of simplicity and parsimony.

To understand the reason for the observation of continuous and abrupt transitions across disparate combustion systems under seemingly identical operating conditions, we next consider the characteristics of synchronization in more detail.

#### 4.6 CONTINUOUS AND EXPLOSIVE SYNCHRONIZATION TRANSITION TO THERMOACOUSTIC INSTABILITY

Let us now consider the characteristics of synchronization which underlies the two different kinds of transitions in more detail. To make this connection substantive, we compare the behavior of phase oscillators in the mean-field model devoid of any spatial inputs with the phase dynamics of spatially distributed heat release rate oscillations obtained through chemiluminescence imaging in our experiments.

Figure 4.7 shows the instantaneous spatial distribution of phasors ( $\psi_l = \theta_l - \Phi$ ) for the bluff-body stabilized combustor and the annular combustor, where  $\theta_l$  and  $\Phi$  are the instantaneous phase of  $\dot{q}'(x, y, t)$  and  $p'(t)$ . The phase difference is related to the correlation over a small time window of the time series (Sethares, 2007; Balasubramanian

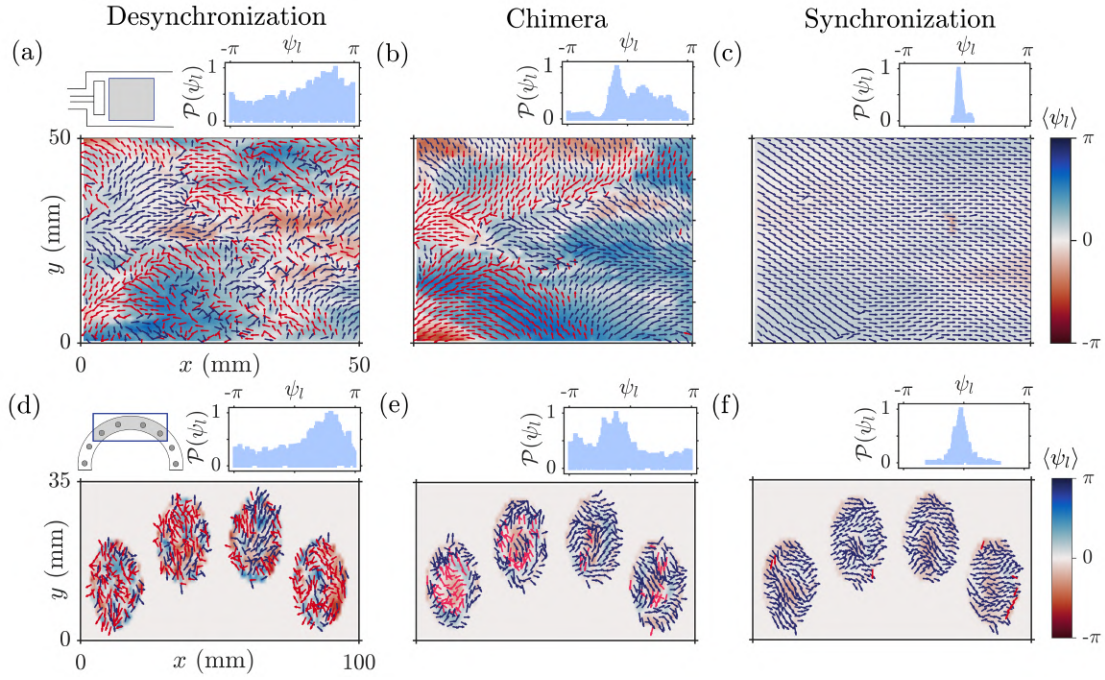


Figure 4.7: Emergence of global phase synchronization during the transition to thermoacoustic instability in a bluff-body combustor (a-c) and annular combustor (d-f). Spatial view of the combustor showing the instantaneous (phasors,  $\psi_l$ ) and time-averaged (colormap,  $\langle \psi_l \rangle$ ) phase difference between the acoustic pressure ( $\Phi$ ) and heat release rate ( $\theta_l$ ) oscillations. Phasors have been colored as blue if  $|\psi| < \pi/2$  (Rayleigh criteria) and red otherwise to delineate local acoustic power sources from sinks. The phase of pressure oscillations remains spatially uniform as the cases correspond to the longitudinal instability. The probability distribution of the relative phase  $\mathcal{P}(\psi_l)$  for each state has also been shown to highlight the appearance of global phase synchronization during thermoacoustic instability. The experimental conditions for the bluff-body and annular combustor correspond to the states shown in figure 4.3 and figure 4.5, respectively.

and Sujith, 2008):

$$\cos \psi_l = \int_0^t p'(t') \dot{q}'(x, y, t') dt' \left/ \left[ \int_0^t (p'(t'))^2 dt' \int_0^t (\dot{q}'(x, y, t'))^2 dt' \right]^{1/2} \right., \quad (4.37)$$

which is the local Rayleigh index and is related to the acoustic power added to the acoustic field due to the flame fluctuations. Here, we measure the phase of heat release rate fluctuations from arbitrary pixels in chemiluminescence images and pressure fluctuations using the Hilbert transform. To reduce the effect of noisy fluctuations, the chemiluminescence images obtained from the bluff-body and annular combustor are

coarse-grained over  $8 \times 8$  pixels and  $6 \times 6$  pixels, respectively. While the signals  $p'(t)$  and  $\dot{q}'(x, y, t)$  at various conditions are not always strictly analytic, the Hilbert transform can still be used for the purposes of visualization. Indeed, [Mondal \*et al.\* \(2017b\)](#) explicitly evaluated the correlation Eq. (4.37) as well as used the probability of recurrence to determine the phase of the heat release rate field. The resulting phases were qualitatively similar to the phase obtained through the Hilbert transform. Hence, we adopt the same in the following.

In addition, we also ensured that there were no acoustic phase delay effects in our experimental measurements. To this end, the pressure oscillations are measured at 25 mm from the dump plane in the bluff-body combustor and remain nearly constant across the domain of spatial measurements (cf. figure 2.2b). In the case of the annular combustor, the acoustic pressure is measured on the combustor backplane such that there is no acoustic phase delay (cf. figure 2.1d). We also mask out the regions between the swirling flames in the annular combustor and do not consider their contribution in our calculations. This is done because heat release rate fluctuations from the inter-flame region are not significant and remain noisy for all the dynamical states (cf. figure 4.7d-f).

Figure 4.7 illustrates the distinct patterns in the phase-field obtained from experiments. During the occurrence of combustion noise, the phase-field is randomly oriented and incoherent (cf. figure 4.7 a,d). This state is more generally referred to as *phase turbulence* ([Shraiman, 1986](#); [Shraiman \*et al.\*, 1992](#)). In the present context, the phase-turbulent state indicates that the heat release rate response of the flame is dominated only by the highly turbulent flow, leading to an incoherent and desynchronized field of the phase difference between the pressure and the heat release rate fluctuations. As the phasors are distributed  $\psi_l > |\pi/2|$ , the acoustic power production remains very low as shown in Eq. (4.37), resulting in low-amplitude aperiodic fluctuations. In contrast, during the state of thermoacoustic instability, the phasors are aligned in a coherent manner, highlighting the global phase synchronization (cf. figure 4.7 c,f). The phasors distributed in  $\psi_l < |\pi/2|$ ,

affect substantially high acoustic power production driving thermoacoustic instability in the two combustors.

While there are similarities in the characteristics of phase turbulence and phase synchronization during the occurrence of combustion noise and thermoacoustic instability, the manner in which synchronization is attained is quite different. For the bluff-body stabilized and annular combustor, the emergence of a globally synchronized state takes place through the state of intermittency where the phase-field shows both phase turbulence and phase synchronization, as can be observed in figure 4.7(b,e). Thus, clusters of synchronized regions appear amidst phase turbulence. The states of co-existence of clusters of phase turbulence and synchronization are referred to as *chimeras* (Kuramoto and Battogtokh, 2002; Abrams and Strogatz, 2004). Additionally, for the annular combustor, the transition takes place through the state of intermittency and low-amplitude instability. The phase-field is shown for the state of intermittency in figure 4.7(e).

To quantify the characteristics of synchronization, we define the Kuramoto order parameter:

$$\bar{r} = \left\langle \left| \frac{1}{N} \sum_{i=1}^N \exp(i\theta_i(t)) \right| \right\rangle_t, \quad \bar{r} \in [0, 1], \quad (4.38)$$

where  $\langle \cdot \rangle_t$  implies time average and  $\theta_l$  is the phase at  $l$ -th oscillator. The order parameter quantifies the degree of synchrony among the oscillators as the bifurcation parameter varies. Kuramoto order parameter is close to zero for desynchronized states and is close to one for synchronized states.

Figure 4.8(a,b) illustrates the variation of the order parameter when the coupling strength  $K$  is varied. The order parameter is determined according to Eq. (4.38) from the model in Eq. (4.31). The procedure for obtaining  $\bar{r}$  from chemiluminescence images is detailed in Appendix H. The oscillator distributions on the  $\dot{\theta}_l - \psi_l$  plane for different states are shown in figure 4.8(c-j). Characteristics of oscillators from spatiotemporal images are

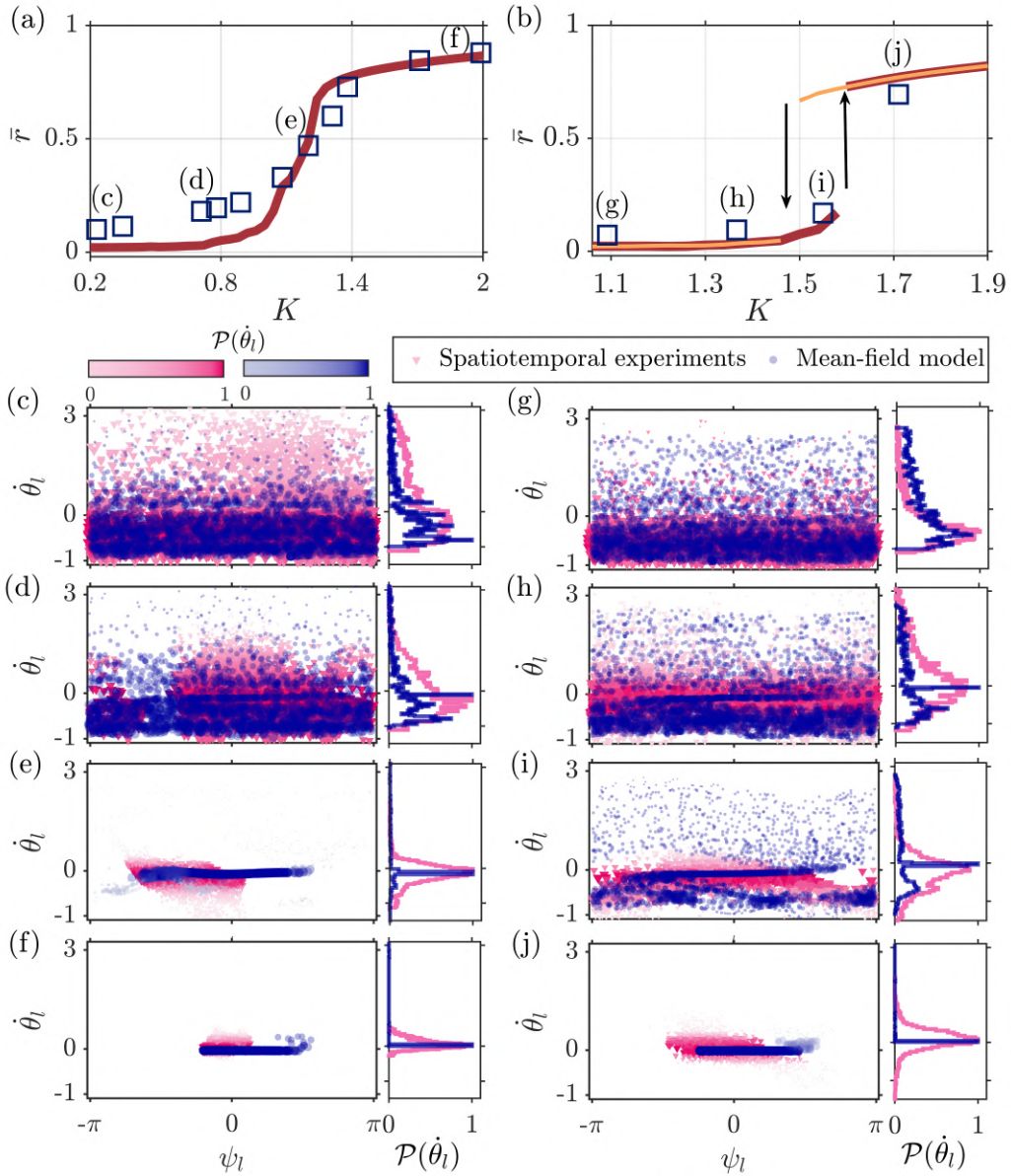


Figure 4.8: The variation of time-averaged Kuramoto order parameter  $\bar{r}$  in Eq. (4.38) as a function of coupling strength  $K$  shows (a) a continuous *second-order* synchronization transition for the bluff-body stabilized combustor and (b) abrupt *first-order* explosive synchronization transition for the annular combustor. Panels (c-j) depict the instantaneous oscillator distribution in the  $\dot{\theta}_l - \psi_l$  phase space along with the distribution  $\mathcal{P}(\dot{\theta}_l)$  representative of various dynamical states indicated in panels (a) and (b). Here,  $\dot{\theta}_l$  is the normalized frequency of the  $l^{\text{th}}$  oscillator, and  $\psi_l$  is the relative phase of the oscillator obtained by subtracting the phase of the heat release rate oscillator by phase of the acoustic pressure. In panels (c-f), the distribution of oscillators obtained from spatiotemporal imaging of the combustors is depicted using a pink shade, while the oscillators from the mean-field model using a blue shade.

depicted using pink shade markers, while that from the model are illustrated using blue shade markers. As the heat release rate oscillators in experiments evolve in physical space, a comparison of oscillator properties in the phase space  $\dot{\theta}_l - \psi_l$  allows us to gauge how closely the spatiotemporal synchronization of oscillators are captured by the low-dimensional dynamical mean-field model. Note that during the occurrence of combustion noise, the initial mean subtracted frequency distribution is  $\dot{\theta}_l = \omega_l$ , where  $\omega_l = \tilde{\omega}_l/\tilde{\Omega}_0$  according to Eq. (4.12), and  $\tilde{\omega}_l = 2\pi\tilde{f}_l - \tilde{\Omega}_0$ . Here,  $\tilde{\Omega}_0$  is the frequency of the acoustic pressure during thermoacoustic instability. Thus, the lower bound of the oscillators is given by  $\tilde{f}_l = 0$ , which leads to  $\dot{\theta}_l = -1$ .

For the bluff-body dump combustor, which shows a continuous transition to thermoacoustic instability through intermittency, the order parameter also shows a continuous and monotonous increase as  $K$  is varied (figure 4.8a). For  $K < 0.75$  corresponding to the state of combustion noise (figure 4.3b), we observe the oscillators to have a broad distribution of  $\dot{\theta}_l = \omega_l$  and  $\psi_l$  (figure 4.8c). As the oscillators are desynchronized,  $\bar{r}$  is close to zero. As  $K$  is increased past 0.75, intermittency appears in the system dynamics (figure 4.8d). This results in the appearance of the phase-synchronized cluster, which is small at first but grows in size with increasing  $K$ . At  $K = 0.95$ , we notice that the frequency of oscillators is no longer broadly distributed and instead have a narrowband distribution around the mean frequency  $\tilde{\Omega}_0$  (figure 4.8e). Due to a higher degree of synchronization among oscillators,  $\bar{r}$  increases monotonously and continuously till the state of thermoacoustic instability. This can be observed at  $K = 2$ , at which  $\dot{\theta}_l$  is close to zero, and all the oscillators fluctuate at the mean acoustic frequency, as can be observed from the sharp peak in  $\mathcal{P}(\dot{\theta}_l)$  (figure 4.8f). Further, we notice that the oscillators are phase-locked with distribution in  $\psi_l < |\pi/2|$ . Accordingly, the order parameter is  $\bar{r} = 0.88$ , implying global phase synchronization among the oscillators.

In the case of the annular combustor, which undergoes a secondary bifurcation to

thermoacoustic instability,  $\bar{r}$  shows a discontinuous transition as  $K$  is increased (figure 4.8b). As noted earlier, during the occurrence of combustion noise ( $K < 1.3$ ), the oscillators show broad frequency and phase distributions (figure 4.8g). The frequency distribution narrows close to zero during the state of intermittency (figure 4.8h). As  $K$  is increased further, the state of low-amplitude limit cycle is reached, we observe a bimodal frequency distribution with a peak close to zero and another peak at  $\dot{\theta}_l \approx -0.6$  (figure 4.8i). Upon increasing  $K > 1.6$ , there is an abrupt jump in the value of  $\bar{r}$  as the state of phase synchronization is reached, as confirmed from the sharp peak in  $\mathcal{P}(\dot{\theta}_l)$  (figure 4.8j). This is associated with the state of high-amplitude thermoacoustic instability in the annular combustor.

It is worth noting here that some phase oscillators remain desynchronized even during the state of thermoacoustic instability (figure 4.8f,j). Such a distribution is expected due to various reasons such as phase-jitter in the heat release rate signal due to turbulence. Such a source of noise can induce random phase-slips in certain oscillators. In addition, some oscillators are not synchronized to the main cluster because their initial frequency difference was too large to be synchronized by the mean-field coupling (Kuramoto, 2003).

To clarify the picture of synchronization, it is instructive to plot the distribution of relative phases  $\psi_l = \theta_l - \Phi$  in polar coordinates. Since, by definition, the frequency of oscillators is centered around the acoustic frequency ( $\tilde{\Omega}_0$ ), the frame of reference of the oscillators is co-rotating with respect to  $\tilde{\Omega}_0$ . Figure 4.9 shows the instantaneous distribution of  $\psi_l$  corresponding to four representative states observed in the annular combustor (cf. figure 4.8b). The experimental data are shown using a pink shade, while the model results are shown using a blue shade. The instantaneous averaged relative phase obtained from the model  $\langle \psi_m \rangle$  and the experiments  $\langle \psi_e \rangle$  are also shown along with the respective Kuramoto order parameter ( $\bar{r}$ ) obtained using Eq. (4.38) and Eq. (H.1) (in Appendix H). The plot shows a drastic change where initially asynchronous oscillators during the state of combustion noise become synchronous during high-amplitude thermoacoustic

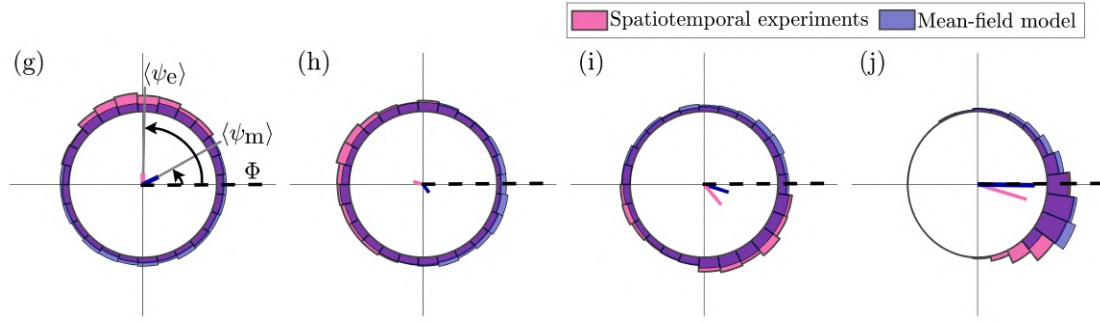


Figure 4.9: Polar plot in the co-rotating frame showing the variation in the instantaneous distribution of relative phases ( $\psi_l$ ) between the phase of the oscillators ( $\theta_l$ ) and acoustic pressure ( $\Phi$ ) obtained from the experiments (dark shade) and model (light shade) during (g) combustion noise, (h) intermittency, (i) low-amplitude and (j) high-amplitude thermoacoustic instability. The representative states correspond to the points indicated in figure 4.8b observed during the abrupt *first-order* explosive synchronization in the annular combustor. Averaged relative phase from the experiments and the model are indicated using  $\langle \psi_e \rangle$  and  $\langle \psi_m \rangle$  along with the Kuramoto order parameter ( $r$ ) showing the level of synchrony among the oscillators, respectively. The dashed line indicates the reference phase of the acoustic pressure oscillations ( $\Phi$ ).

instability.

In figure 4.9, during the occurrence of combustion noise, the oscillators are uniformly distributed. The average phase also drifts with respect to  $\Phi$ , indicating desynchronization amongst the oscillators. During the transition to thermoacoustic instability, we observe a clear shift from a uniform broadband distribution to a narrowband distribution, implying the emergence of synchronization among oscillators. The average phase remains locked to  $\Phi$ , and the exact phase difference never exceeds  $\pm\pi/2$ . In summary, we see that this behavior is very well approximated by the model.

The stark contrast in the bifurcation behavior of the order parameter  $\bar{r}$  shown in figure 4.8(a,b) highlights the difference in the characteristics of synchronization underlying the two bifurcations. Indeed, the continuous change in  $\bar{r}$  exemplifies a *second-order* synchronization phase-transition. On the other hand, the abrupt bifurcation in  $\bar{r}$  embodies a *first-order* phase transition and is more appropriately referred to as *explosive*

synchronization (Strogatz, 2000; Pazó, 2005; Leyva *et al.*, 2013; Kuehn and Bick, 2021).

Whether the synchronization transition will be continuous or explosive is crucially contingent on the initial frequency distribution. It is well-known that the second-order continuous transitions appear in the standard Kuramoto model whenever the frequency distribution of phase oscillators is symmetric and unimodal (Kuramoto, 1975; Strogatz, 2000). This is due to the presence of a clear peak in the distribution, which ensures that upon increasing coupling strength, a large cluster of oscillators gets synchronized around the peak in the distribution. Further increase in coupling strength leads to entrainment of drifting oscillators to the large cluster resulting in the gradual increase in the size of the coherent cluster (Strogatz, 2000; Basnarkov and Urumov, 2007).

The picture becomes complicated when the frequency distribution undergoes symmetry breaking to non-unimodal and asymmetric distribution in non-standard extensions of the Kuramoto model (Zhou *et al.*, 2015; Terada *et al.*, 2017; de Oliveira and Abud, 2020). For instance, in the case of bimodal distribution, the appearance of two frequency peaks means that an increase in the coupling strength leads to the entrainment of oscillators distributed around the two frequency peaks. When the coupling strength becomes too large, these peaks and the two clusters coalesce abruptly, leading to non-standard, first-order explosive synchronization (Terada *et al.*, 2017; Zhang *et al.*, 2020). Similar observation has been made when the frequency distribution is flat (Basnarkov and Urumov, 2007; Pietras *et al.*, 2018) or asymmetric unimodal (Zhou *et al.*, 2015; de Oliveira and Abud, 2020). While the above-mentioned studies are important steps in understanding second-order and first-order transitions, a clear resolution is still missing.

Here also, the key to discerning the reason behind second-order and first-order transitions lies in the characteristics of the frequency distribution. Evidently, the distributions  $g(\omega)$  obtained from the three experiments are non-standard and asymmetric, as can be observed in figure 4.2. The distributions are more clearly shown in figure 4.8(c,g). Now,

the observation of such a non-standard initial distribution (figure 4.2) makes it difficult to relate the present results to the observed theoretical results in the existing literature. However, the observed first and second-order transitions can still be reconciled by observing the behavior of the distributions during the intermediate states of intermittency and low-amplitude thermoacoustic instability.

The distribution  $g(\omega)$  for the bluff-body stabilized combustor is multimodal, where the peaks are centered very close to the frequency of acoustic oscillations (see figure 4.8c). Now, as the coupling strength increases, oscillators at these frequencies get entrained, and a single peak is established in the frequency distribution (cf. figure 4.8e). Further increase in the coupling strength leads to a gradual increase in the size of the largest entrained cluster. Hence, we observe a continuous, second-order synchronization transition. In contrast, for the annular combustor, the distribution  $g(\omega)$  is initially asymmetric with a peak that is comparatively farther away from the frequency of acoustic fluctuations (cf. figure 4.8g). Now, as the coupling strength is increased, a secondary peak becomes clearly visible (cf. figure 4.8i). Thus, oscillators are entrained around two different clusters associated with the two peaks. An increase in  $K$  beyond a critical value leads to an abrupt coalescence of these two clusters, resulting in the first-order explosive synchronization.

To summarize, we have seen that although the model is dynamical with no spatial input, it captures the characteristics of spatiotemporal synchronization patterns observed in experiments very well while also predicting the nature of bifurcation to limit cycle oscillations—a feature that has yet to be captured in other thermoacoustic models. Thus, the above results strongly suggest the usefulness of the proposed mean-field model for analyzing the thermoacoustic transitions in turbulent combustion systems.

It is worth mentioning here that explosive synchronization has been reported in power-grids (Motter *et al.*, 2013), neurological activity (Kim *et al.*, 2016), chemical reactions

(Kumar *et al.*, 2015; Călugăru *et al.*, 2020). Our study is the first experimental evidence of explosive synchronization in a strongly-coupled fluid dynamical system.

#### **4.7 INTERIM SUMMARY**

In this chapter, we presented two distinct thermoacoustic models to study the change in nature of the bifurcation observed in the turbulent combustors. In the first model based on the nonlinear function, we vary the nonlinear terms to reproduce the crossover of the bifurcation and the stability map observed in the annular combustor. In the second model, we assume that the turbulent flame comprises an ensemble of phase oscillators evolving under the influence of mean-field interactions and acoustic feedback. These interactions encode the nonlinearities in the flame response subjected to acoustic and turbulent fluctuations.

We showed that the mean-field model captures continuous and abrupt transitions observed in three distinct (bluff-body stabilized, swirl-stabilized, and annular) combustor configurations. These transitions are captured by the model by taking the heat release rate spectrum during the stable operation as the only input. Further, the model captures the characteristics such as time series, PDF, and spectrum of the different states – combustion noise, intermittency, limit cycle oscillations – en route to the state of thermoacoustic instability in these systems. We then estimated the relationship between experimental and model parameters using a gradient descent algorithm. In all three combustors, we find that the coupling strength is a linear function of the equivalence ratio, indicating that a change in the control parameter leads to an increase in the coupling strength of the phase oscillators.

Importantly, we show that our second modeling approach naturally provides an explanation of spatiotemporal synchronization and pattern formation observed in turbulent thermoacoustic systems. We showed that the model closely captures the statistical behavior of spatial desynchronization, chimera, and global phase

synchronization underlying the transitions. Our results strongly indicate that continuous and abrupt thermoacoustic transitions are associated with synchronization transition of second-order and first-order, respectively. This observation of disparate phase transitions is further rationalized based on the frequency spectrum of the phase oscillators. We observe the appearance of an unimodal peak around which all the oscillators get entrained, giving rise to a second-order transition. On the other hand, the first-order explosive transition is associated with the appearance of a bimodal distribution where two synchronized clusters of oscillators get entrained. An increase in the coupling strength beyond a critical point results in a sudden, abrupt coalescence into one large synchronized cluster.

## CHAPTER 5

# INTERMITTENCY TRANSITION TO AZIMUTHAL INSTABILITIES IN ANNULAR COMBUSTOR

In this chapter, we study the transition to azimuthal instabilities in the annular combustor. The current combustor is introduced to resemble the main features of modern aero and land-based gas turbine combustors and enable the study of azimuthal combustion instabilities in a well-controlled and accessible environment. The lab-scale annular combustor used for azimuthal thermoacoustic instability experiments is comprehensively described in Section 2.1.2. The primary motivation of this chapter is to understand the nature of the azimuthal modes using temporal and spatiotemporal measurements. Specifically, our attention is directed towards the nonlinear flame response during different dynamical states as a function of the equivalence ratio.

### 5.1 CHARACTERIZATION OF AZIMUTHAL MODES

To understand the nature of the azimuthal mode in the annular combustor, we apply the quaternion-based formalism on the azimuthal pressure fluctuation. Recently, [Ghirardo and Bothien \(2018\)](#) proposed a new approach for describing the azimuthal pressure eigenmodes in annular combustors by utilizing the quaternions ansatz. The quaternion formulation defines the system using state space variables that directly characterize the

---

The results presented in this chapter are showcased at the conference and published in the journal paper:

1. Singh, S., Bhavi R., P. R. Midhun, Bhaskaran A., Mishra P., Chaudhuri S., and Sujith R.I., Intermittency transition to azimuthal instability in a turbulent annular combustor. *Symposium on Thermoacoustics in Combustion: Industry meets Academia, ETH Zurich, Switzerland*, (2023).
2. Singh, S., Bhavi R., Midhun P. R., Bhaskaran A., Mishra P., Chaudhuri S., and Sujith R. I. (2024). Intermittency transition to azimuthal instability in a turbulent annular combustor. *Int. J. Spray Combust. Dyn.*, 16 (3), 119-136.

nature of the mode. This approach is particularly of interest to experimentalists seeking a clear and insightful understanding of the system dynamics in complicated combustion systems. Utilizing acoustic pressure data acquired from eight distinct locations, as illustrated in figure 2.1, we employ the quaternion-based ansatz to decompose the azimuthal pressure fluctuations ( $p'$ ) as:

$$p'(\Theta, t) = A \cos(\Theta - \theta) \cos(\chi) \cos(\Omega t + \Phi) + A \sin(\Theta - \theta) \sin(\chi) \sin(\Omega t + \Phi), \quad (5.1)$$

where  $\Omega$  is the acoustic frequency,  $t$  is the time, and  $\Theta$  is the azimuthal coordinate. A set of four state variables, namely  $A$ ,  $\chi$ ,  $\theta$ , and  $\Phi$ , is then extracted from the time series of acoustic pressure. These variables vary slowly with respect to the fast acoustic timescale  $T = 2\pi/\Omega$ , and provide a well-defined description of the state of an azimuthal thermoacoustic mode. The slow variation in the angles  $\theta$  and  $\chi$  describes the position of the antinodal line and the nature of the azimuthal eigenmode (standing wave, pure CW or CCW spinning wave, or a mix of both), respectively. Additionally, the angle  $\Phi$  represents the slow temporal phase drift. We can express the pressure field in the form:

$$p'(\Theta, t) = \frac{A}{2} (\cos \chi - \sin \chi) \cos(\Theta - \theta + \Omega t + \Phi) + \frac{A}{2} (\cos \chi + \sin \chi) \cos(\Theta - \theta - \Omega t - \Phi). \quad (5.2)$$

These two traveling waves yield:

$$A_+ = (A/2)(\cos \chi + \sin \chi), \quad (5.3)$$

$$A_- = (A/2)(\cos \chi - \sin \chi), \quad (5.4)$$

and

$$\theta = (\Phi_- - \Phi_+)/2, \quad \Phi = (\Phi_- + \Phi_+)/2, \quad (5.5)$$

where  $A_+$  and  $A_-$  denotes the slowly varying amplitudes of the two counter-rotating spinning waves. Further, the slowly varying amplitude  $A$  represents the amplitude of

acoustic pressure oscillations in Eq. (5.1) can be deduced from Eqs. (5.3) and (5.4) as:

$$\frac{A}{\sqrt{2}} = \sqrt{|A_+|^2 + |A_-|^2}, \quad (5.6)$$

The relation of the two amplitudes defines whether the mode is standing ( $|A_+| = |A_-|$ ) or spinning in clockwise (CW) ( $|A_+| = 0$ ) or counter-clockwise (CCW) ( $|A_-| = 0$ ) direction. In addition to the slowly varying variables, we introduce the spin ratio to characterize the nature of the azimuthal mode (Bourgouin *et al.*, 2013). This convenient indicator for the nature of the mode is based on the projection on two spinning waves and defined as  $SR = (|A_+| - |A_-|)/(|A_+| + |A_-|)$ . The relation between the spin ratio  $SR$  and the nature angle  $\chi$  is described by the equation as:

$$\chi = \arctan(SR) = \arctan\left(\frac{|A_+| - |A_-|}{|A_+| + |A_-|}\right). \quad (5.7)$$

Since the characteristic features of a given azimuthal mode are the amplitude  $A$ , the nature angle  $\chi$  and the orientation angle  $\theta$ , it is natural to describe a given mode as a point on a Poincaré-Bloch sphere (Ghirardo and Bothien, 2018) (see figure 5.1). The amplitude  $A$  determines the distance from the point to the origin of the sphere. The orientation angle  $\theta$  is the angle in the equatorial plane relative to the reference angle of the coordinate system and varies between  $-\pi$  and  $\pi$ . Twice the nature angle ( $2\chi$ ) determines the angle between the equatorial plane and the point representing the thermoacoustic mode. Here,  $\chi$  indicates whether the azimuthal eigenmode is a standing wave ( $\chi = 0$ ), a pure clockwise or counterclockwise spinning wave ( $\chi = \pm\pi/4$ ) or a mix of both for  $0 < |\chi| < \pi/4$ . Taken together, these slow-flow variables and spin ratio provide a comprehensive description of the acoustic field  $p'$  as a function of time and azimuthal position.

## 5.2 DETERMINATION OF AZIMUTHAL MODE FROM OUR EXPERIMENTS

In this section, we outline the process of deriving the slow flow variables within the quaternion framework from experimental measurements. We begin with azimuthally

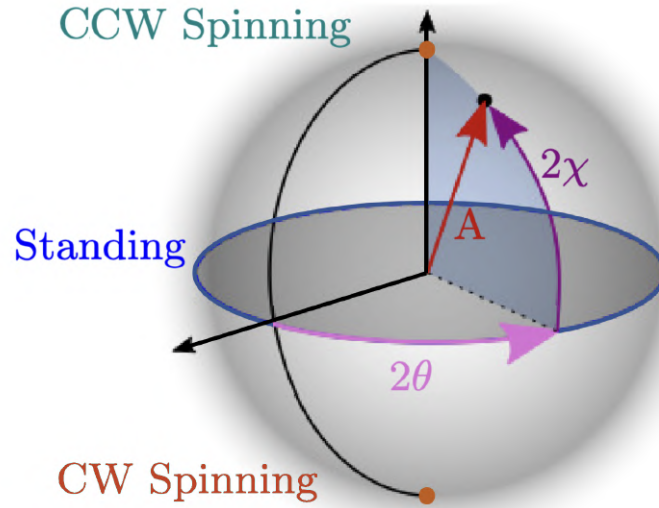


Figure 5.1: Poincaré-Bloch sphere representation of the azimuthal mode in the quaternion formalism. The amplitude  $A$  corresponds to the radius,  $2\chi$  the latitude and  $\theta$  the longitude. Thermoacoustic states at the poles correspond to spinning modes, standing modes are located near the equator and mixed modes at intermediate latitudes.

distributed pressure signals, denoted as  $p'(\Theta, t)$ , which provide time series data for acoustic pressure at specific azimuthal locations represented by  $\Theta_k$ . To capture the acoustic pressure signals, we have installed eight pressure transducers, each designated as PC1, PC2, .. PC8, positioned at intervals of  $45^\circ$  from one another on the backplane of the combustor (see figure 2.1d). To identify the dominant mode and its corresponding frequency, we employ a Fast Fourier Transformation (FFT) on the pressure signals. We apply a bandpass filter on each pressure time series to improve the quality of the data by removing the unwanted noise and harmonic components. This filter has a bandwidth of  $\Delta f = 50$  Hz centered around the peak frequency  $f_p$  associated with each transducer. The framework takes a starting point in the description of the acoustic field by two orthogonal eigenmodes:

$$p'(\Theta, t) = \xi_1(t) \cos(n\Theta) + \xi_2(t) \sin(n\Theta), \quad (5.8)$$

where  $n$  is the order of the azimuthal mode having value  $n = 1$  in our case, and  $\cos(n\Theta)$  and  $\sin(n\Theta)$  are the two orthogonal modes. The projected signals  $\xi_1$  and  $\xi_2$  are obtained

from the filtered pressure transducer timetraces by inverting the system:

$$\begin{bmatrix} p_0 \\ p_1 \\ \vdots \\ p_k \end{bmatrix} = \begin{bmatrix} \cos(n\Theta_0) & \sin(n\Theta_0) \\ \cos(n\Theta_1) & \sin(n\Theta_1) \\ \vdots & \vdots \\ \cos(n\Theta_k) & \sin(n\Theta_k) \end{bmatrix} \begin{bmatrix} \xi_1 \\ \xi_2 \end{bmatrix} \quad (5.9)$$

where  $k$  describes the number of the pressure signals which are acquired at specific azimuthal positions  $\Theta_k$ . The corresponding complex analytic signals of  $\xi_1$  and  $\xi_2$  are defined as:

$$\xi_{a,1}(t) = \xi_1(t) + j\mathcal{H}(\xi_1(t)); \quad \xi_{a,2}(t) = \xi_2(t) + j\mathcal{H}(\xi_2(t)), \quad (5.10)$$

where  $\mathcal{H}$  is the Hilbert transform and  $j$  is the second quaternion imaginary unit. The quaternion analytic signal of  $\xi(t)$  is defined as  $\xi_a(t) = \xi_{a,1}(t) + i\xi_{a,2}$  which turn out as:

$$\xi_a(t) = \xi_1(t) + j\mathcal{H}(\xi_1(t)) + i\xi_2(t) + k\mathcal{H}(\xi_2(t)), \quad (5.11)$$

with  $i, j, k$  as the quaternion imaginary units. From this point, the slow-flow variables  $A, \chi, \theta, \phi$  are extracted from  $\xi_a$  with the step by step description presented rigorously in the appendix of [Ghirardo and Bothien \(2018\)](#).

### 5.3 ROUTE TO AZIMUTHAL THERMOACOUSTIC INSTABILITY

In this section, we discuss the transition from a stable state to azimuthal thermoacoustic instability in the annular combustor, as shown in figure 5.2. For the frequency analysis of the acoustic pressure ( $p'$ ) signal, we employed the fast Fourier transform algorithm (FFT). The datasets were sampled at 10 kHz to accurately capture the limit cycle signal. We have utilized 1 second duration of data for the current analysis, resulting in approximately 10000 data points. To avoid any spectral leakage, we have implemented the FFT with a frequency resolution of 0.3 Hz per bin, spanning a total of 8193 bins. Figure 5.2(a) illustrates the variation in the amplitude of acoustic pressure ( $A$ ), calculated using

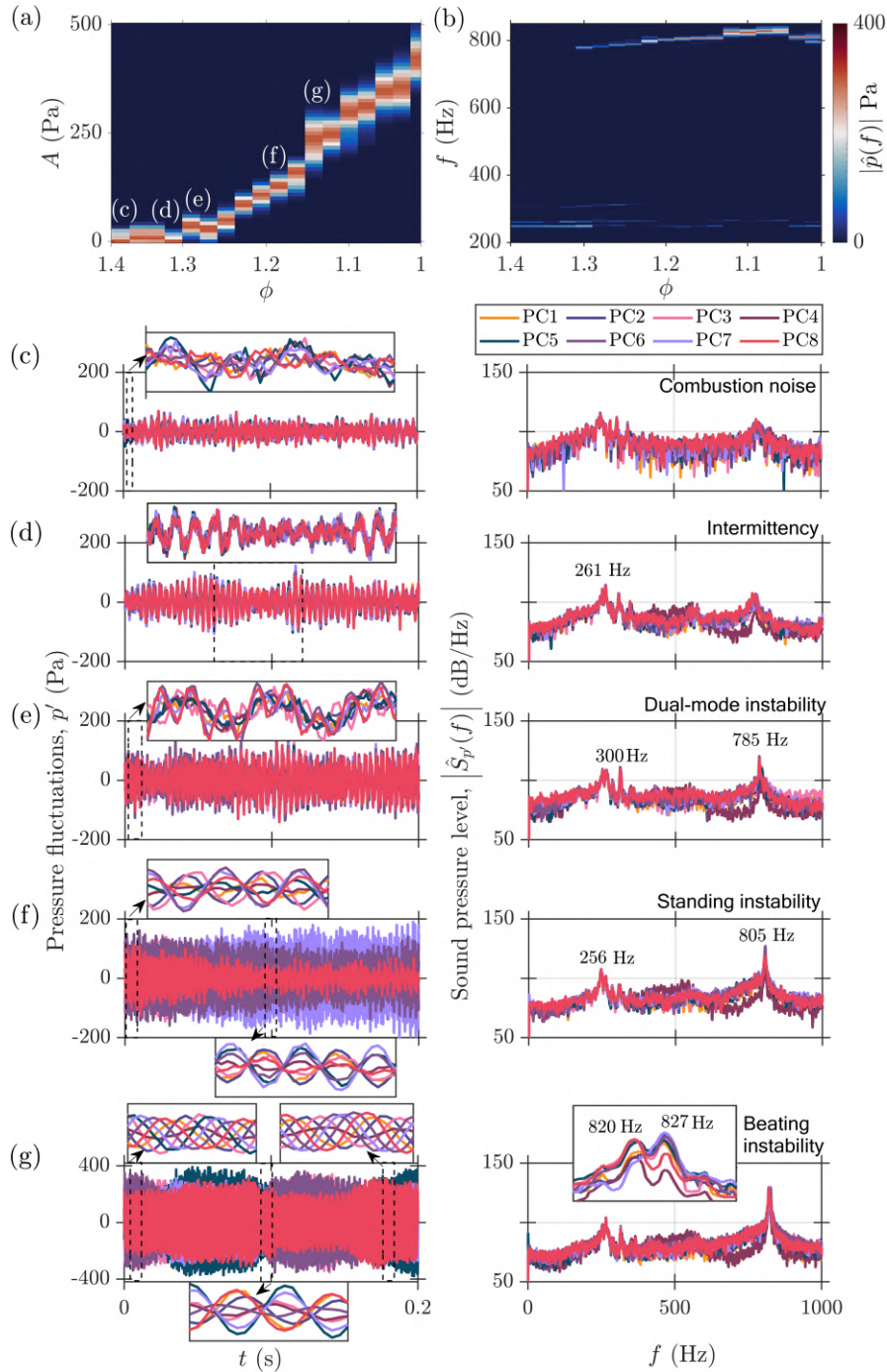


Figure 5.2: Observed transition from a state of combustion noise to azimuthal thermoacoustic instability in a turbulent annular combustor. (a) The variation of  $A$  and (b) the frequency of  $p'$  from position PC2 as a function of equivalence ratio ( $\phi$ ). Time traces and the sound pressure level of the acoustic pressure fluctuations ( $p'$ ) from eight equispaced pressure sensors during (c) combustion noise, (d) intermittency, (e) dual-mode instability, (f) standing azimuthal instability, and (g) beating azimuthal instability. The transition involves a frequency shift – from a low frequency associated with the longitudinal mode to a higher frequency associated with the azimuthal mode. Experimental conditions: (c)  $\phi = 1.38$ , (d)  $\phi = 1.32$ , (e)  $\phi = 1.28$ , (f)  $\phi = 1.20$ , and (g)  $\phi = 1.14$ .

equation (5.6), as a function of the equivalence ratio ( $\phi$ ). Figure 5.2(b) highlights the change in the dominant frequency of the acoustic pressure at position PC2 (Figure 2.1d). Each  $\phi$  value corresponds to a specific dominant frequency, which shifts from the low-frequency range of approximately  $270 \pm 30$  Hz to the high-frequency range of around  $810 \pm 30$  Hz. The frequency variation of  $\pm 30$  Hz is obtained through visual inspection from figure 5.2(b). As we vary the equivalence ratio, we observed a continuous increase in  $A$  (Figure 5.2a), and a notable shift in frequency from a lower to a higher range in figure 5.2(b). This shift in the frequency of the acoustic pressure signifies the transition from longitudinal to azimuthal thermoacoustic instability.

In figure 5.2(c-g), we show the time series and sound pressure level of  $p'$  from all eight locations during different states of combustor operations in a sequence as marked in figure 5.2(a). At  $\phi = 1.38$ , in figure 5.2(c), we observe aperiodic pressure fluctuations in the time series of  $p'$  (see insets) and broadband spectrum in the sound pressure level, indicating the state of combustion noise. As we decrease  $\phi$  to 1.32, in figure 5.2(d), we notice intermittent bursts of longitudinal periodic oscillations amidst aperiodic fluctuations (see insets), indicating the occurrence of intermittency (Nair *et al.*, 2014). We confirmed that the epochs of the periodic fluctuations during the current state are predominantly longitudinal in nature, given the negligible phase difference observed among all eight pressure signals (not shown here). Notably, the sound pressure level corresponding to this state starts narrowing around 260 Hz, which corresponds to the longitudinal mode of the combustor. Upon further decreasing  $\phi$  to 1.28, figure 5.2(e) displays a coexistence of both azimuthal mode and longitudinal mode with distinct frequencies in the time series of  $p'$ . For a closer look at the time series of  $p'$ , refer to the zoomed-in view provided in figure 5.4(a). The coexistence of two modes strongly indicates the presence of dual-mode instability, first observed by Fang *et al.* (2021) in their experimental study. Interestingly, the corresponding sound pressure level shows almost equal amplitudes for the longitudinal and azimuthal modes. The dominant frequency for the longitudinal mode has shifted from 261 Hz to 300 Hz, while the azimuthal thermoacoustic mode is

around 785 Hz. Upon closer examination, we observed two peaks in the low frequency range, where one peak is located around 260 Hz, and the other is around 300 Hz. Recent studies have shown that combustors can exhibit multiple acoustic modes, which can either coexist or compete, depending on nonlinear interactions [Noiray *et al.* (2008); Moeck and Paschereit (2012); Lieuwen (2021)]. The presence of these two closely-spaced modes in our combustor corresponds to longitudinal modes, as confirmed in figure 5.4. Given that the sharp peak at 300 Hz exhibits a higher amplitude compared to the broader peak around 260 Hz, we consider the peak at 300 Hz as indicative of the longitudinal mode. The combined longitudinal and azimuthal modes exhibit specific time-varying modal dynamics during their occurrence, necessitating further analysis discussed in the next section.

In figure 5.2(f), we observe standing azimuthal oscillations with a slow rotation of the nodal line when  $\phi$  reaches 1.20 (also refer to figure 5.6a for a zoomed-in view). In the corresponding spectral plot, we identify two prominent peaks: one at approximately 256 Hz, indicating the presence of the longitudinal mode, and another at around 805 Hz, indicating the azimuthal mode. Remarkably, we notice the amplitude of the peak at 805 Hz is significantly higher than that of the peak at 256 Hz. Recent experimental studies have reported the rotation of the nodal line in a random (Vignat *et al.*, 2020) and deterministic fashion (Worth and Dawson, 2017; Kim *et al.*, 2021b). In our case, the motion of the nodal line appears to oscillate periodically in a deterministic fashion discussed in figure 5.6(d). With further decrease in  $\phi$ , we observe a complex sequence of dynamical states between spinning and standing azimuthal modes along with amplitude modulation in figure 5.2(g) (at  $\phi = 1.14$ ). Please also refer to figure 5.7(a) for a zoomed-in view. The combustor exhibits a CCW spinning mode, followed by standing mode, CW spinning mode, and again standing mode. The dominating peak frequency associated with the azimuthal thermoacoustic mode displays two peaks: one at approximately 820 Hz and the other at  $f_1 = 820 + f_0$ . Upon closer inspection of the spectrum, we notice two peaks separated by approximately  $f_0 = 7$  Hz, which corresponds to the frequency

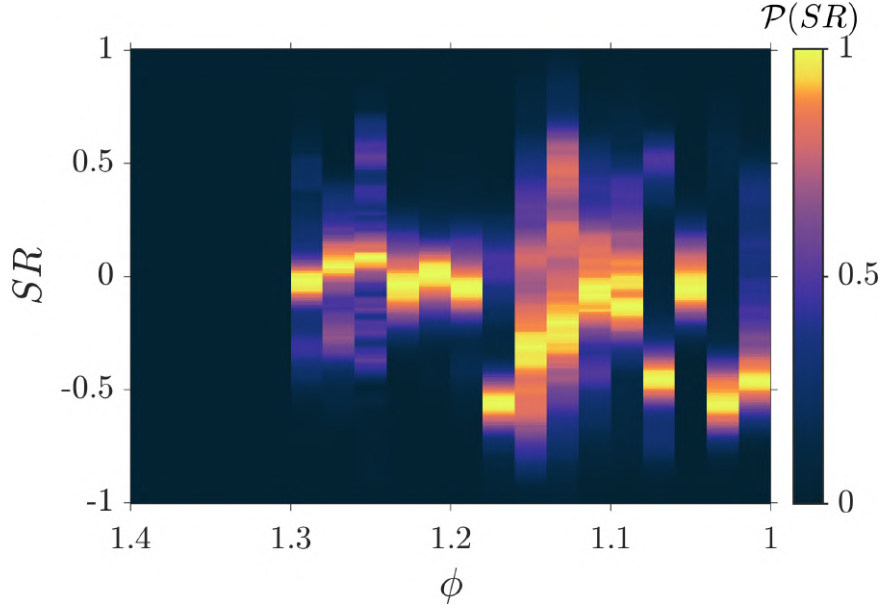


Figure 5.3: The variation in the distribution of spin ratio ( $SR$ ) as a function of equivalence ratio ( $\phi$ ) indicates the change in the azimuthal mode dynamics during the thermoacoustic transition.

of beating. This dynamical state is referred to as the beating azimuthal instability in literature (Indlekofer *et al.*, 2021a; Faure-Beaulieu *et al.*, 2021a). This dynamical state can arise due to tiny non-uniformities in the geometry, impedance variations of the cavity walls, or flow irregularities.

#### 5.4 AZIMUTHAL MODAL DYNAMICS DURING THE THERMOACOUSTIC TRANSITION

Using the mode indicator discussed in Eq. 5.7, we investigate the change in the azimuthal modal dynamics as a function of  $\phi$ . We assess the modal dynamics by examining the distribution of spin ratio ( $SR$ ) across different  $\phi$  values, as shown through the probability density function of spin ratio  $\mathcal{P}(SR)$  distributions. In figure 5.3, we show the distribution in  $SR$  as a function of  $\phi$ . For the value of  $\phi$  between 1.4 and 1.3, we observed the state of combustion noise and intermittency, denoted by ‘(c)’ and ‘(d)’ in figure 5.2.

Given our emphasis on azimuthal modal dynamics, we neglect these states and commence analysis from  $\phi = 1.3$  onwards. Detailed explanations of these two dynamic states,

namely combustion noise and intermittency, are provided in Chapter 3. We first apply a bandpass filter to each pressure time series with a bandwidth of  $\Delta f = 50$  Hz, centered around the peak frequency to calculate  $SR$ . At  $\phi = 1.3$ , we observe  $SR \approx 0$ , indicating a standing azimuthal mode as  $|A_+| = |A_-|$ . The spread in the  $\mathcal{P}(SR)$  suggests the time-varying spin ratio between -0.5 and 0.5 with the maximum probability of forming standing azimuthal mode. This state is denoted as ‘(e)’ in figure 5.2(a) and referred to as the dual-mode instability. As  $\phi$  is decreased, we notice a sharp peak in  $\mathcal{P}(SR)$  distribution. Specifically, at  $\phi = 1.2$ ,  $SR$  is very close to zero, indicating pure standing azimuthal mode. This state is denoted as ‘(f)’ in figure 5.2(a). As the value of  $\phi$  past 1.2, we observe a spread in  $SR$  between -1 and 1, indicating the beating phenomenon in the combustor. For instance, at  $\phi = 1.14$ , we observe that the probability of  $SR$  remains between -1 to 1 with the highest probability around 0. Here,  $\mathcal{P}(SR)$  indicates that the azimuthal mode switching between CCW and CW spinning waves is always through the standing wave. On further decreasing  $\phi$ , we notice irregular switching between CCW and CW spinning mode through the standing mode.

## 5.5 CHARACTERIZING DYNAMICAL STATES DURING THE TRANSITION TO AZIMUTHAL THERMOACOUSTIC INSTABILITY

In order to further understand each dynamical state observed in the annular combustor during the transition to azimuthal thermoacoustic instability, we examine the temporal behavior of different dynamical states. For brevity, we have not shown the temporal and flame dynamics during the state of combustion noise and intermittency as they are discussed in Chapter 3.

Figure 5.4 shows the portion of the original time series and scalogram of  $p'$ , filtered time series of  $p'$  associated with the longitudinal and azimuthal modes, and the corresponding probability density function ( $\mathcal{P}(\Delta\Psi)$ ) of the phase difference ( $\Delta\Psi$ ) during the dual-mode instability discussed in figure 5.2(e). To improve clarity, the time series from four

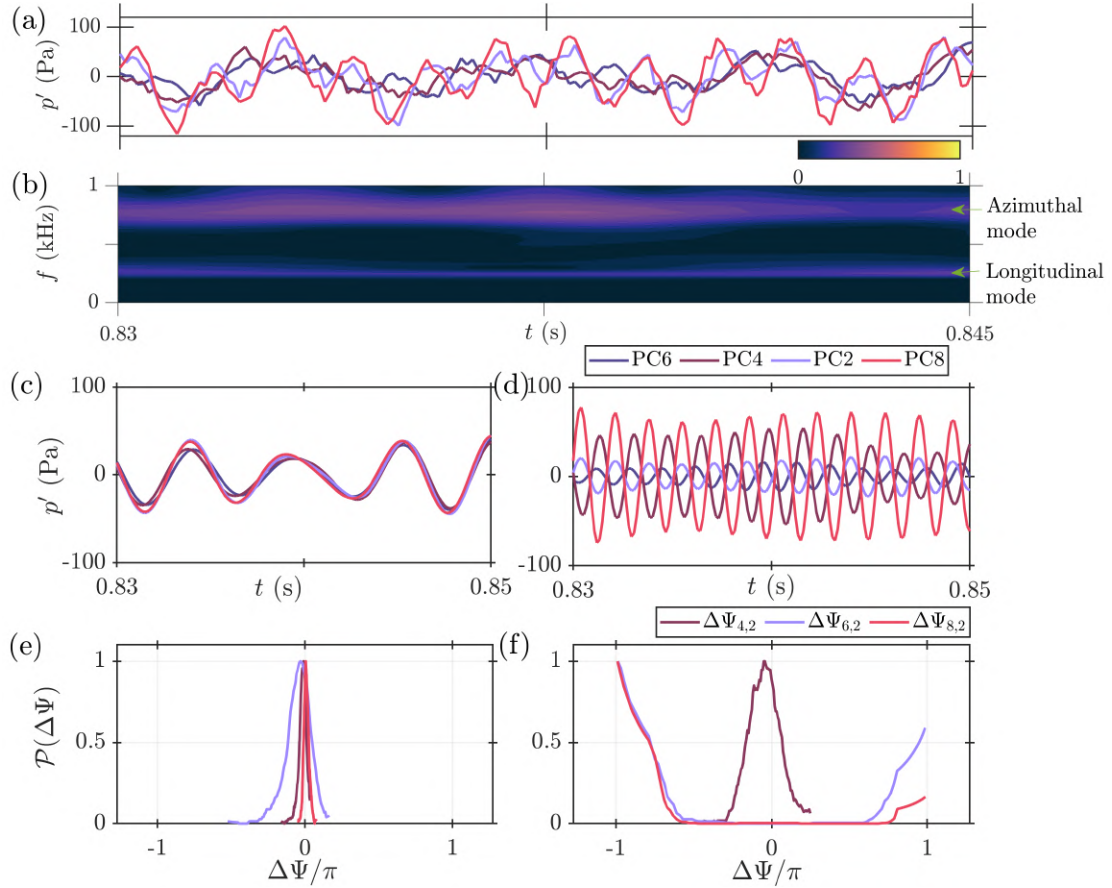


Figure 5.4: (a,b) Evolution of time series and scalogram of the acoustic pressure oscillations during the dual-mode instability at  $\phi = 1.28$ . (c) and (d) Selected windows in the pressure time series are bandpass filtered in the range [250, 350] Hz and [734, 834] Hz, respectively. (e) and (f) Probability density function of the phase difference ( $\mathcal{P}(\Delta\Psi)$ ) of all pressure signals with respect to the signal in PC2.

pressure transducers (PC2, PC4, PC6, and PC8) located  $90^\circ$  apart are displayed, and the scalogram plot for PC2 is shown. In figure 5.4(a), the periodic amplitude modulation of  $p'$  is associated with dual tonal peaks before applying any spectral filtering. Specifically, the  $p'$  signal corresponding to azimuthal mode modulates at the frequency of longitudinal mode. The scalogram displaying two tonal peaks around 251 Hz and 785 Hz is shown in figure 5.4(b). The tonal peaks are of almost equal strength, where 251 Hz is associated with the longitudinal mode and 785 Hz is associated with the azimuthal mode. We apply a bandpass filter on the time series of  $p'$  to decouple the two modes, which simplifies our analysis.

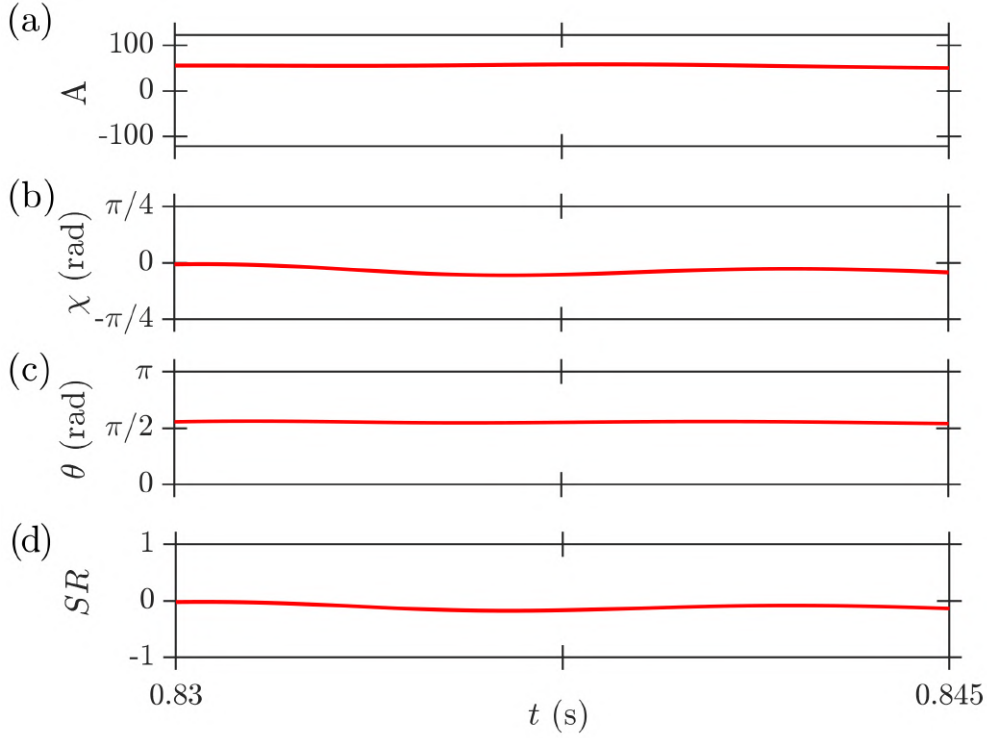


Figure 5.5: Evolution of (a) amplitude ( $A$ ), (b) nature angle ( $\chi$ ), (c) orientation angle ( $\theta$ ), and (d) spin ratio ( $SR$ ) exacted using time series of  $p'$  during the azimuthal mode of dual-mode instability.

Figure 5.4(c) shows the time series of  $p'$  associated with the longitudinal mode when bandpass filtered in the range [250, 350] Hz, while figure 5.4(d) shows the same time series but now associated with the azimuthal mode when bandpass filtered in the range [727, 834] Hz. Figure 5.4(c) depicts the signals from all four pressure transducers are in-phase during the longitudinal mode, while in figure 5.4(d) PC2 and PC4 are out-of-phase to PC6 and PC8, further confirms standing azimuthal mode in the combustor. Moreover,  $\mathcal{P}(\Delta\Psi)$  associated with the longitudinal mode shows the phase difference of PC4, PC6, and PC8 with respect to PC2 is negligible (see figure 5.4e). In contrast,  $\mathcal{P}(\Delta\Psi)$  associated with the azimuthal mode shows the phase difference of PC4 with respect to PC2 is negligible, and the phase difference of PC6 and PC8 with respect to PC2 is  $|\pi|$  (see figure 5.4f).

To better understand the azimuthal thermoacoustic mode during the dual-mode instability

shown in figure 5.4(d), we adopt the quaternion-based formalism elucidated in Section 5.1. We decompose the acoustic pressure oscillations ( $p'$ ) into clockwise and counterclockwise waves using slow flow variables obtained from the eight pressure transducers (PC1, PC2, ..., PC8), allowing a reconstruction of the pressure amplitude ( $A$ ), nature angle ( $\chi$ ), orientation angle ( $\theta$ ), and spin ratio ( $SR$ ). In figure 5.5, panel (a) depicts the evolution of the amplitude of the azimuthal mode ( $A$ ). Panel (b) shows the evolution of  $\chi$ , which oscillates around 0 and corresponds to a mode near the equator in the Bloch sphere. This behavior indicates the presence of the standing azimuthal mode in the combustor (Ghirardo and Bothien, 2018; Ghirardo and Gant, 2021; Kim *et al.*, 2021b). Panel (c) represents the evolution of the orientation angle  $\theta$ , which determines the location of the pressure antinodes of the standing azimuthal wave. It is worth noting that the angle  $\theta$  for the dual-mode instability exhibits oscillations around  $\pi/2$ , which strongly suggests that the position of the nodal line is almost constant in time. Finally, panel (d) displays the temporal variation of the spin ratio ( $SR$ ), which exhibits oscillations centered around zero. This variation of  $SR$  around zero provides further evidence for the existence of a standing azimuthal mode in the combustor when decoupled from the longitudinal mode.

We next discuss the temporal dynamics of the pure standing azimuthal mode with a moving nodal line, which corresponds to marker '(f)' in figure 5.2(a). In figure 5.6, panel (a) illustrates the time series of  $p'$  along with the zoomed-in views at two distinct windows in the same time series. These two time series windows reveal the modulation in amplitude and phase difference of  $p'$  from the eight pressure transducers (shown four here) around the annulus. Panel (a) also depicts the evolution of the amplitude of the standing azimuthal instability ( $A$ ) indicated in red color. Panel (b) presents the evolution of the frequency from four transducers (PC2, PC4, PC6, and PC8), demonstrating the modulation in the amplitude of  $p'$  in the scalogram plots. For instance, at around  $t = 0.85$  s, all four scalogram plots distinctly exhibit a nearly identical amplitude of  $p'$ , while at around  $t = 1.1$  s, a noticeable disparity emerges: PC2 and PC4 manifest higher amplitudes of  $p'$ , whereas PC1 and PC3 display a minimized amplitudes. Therefore, we

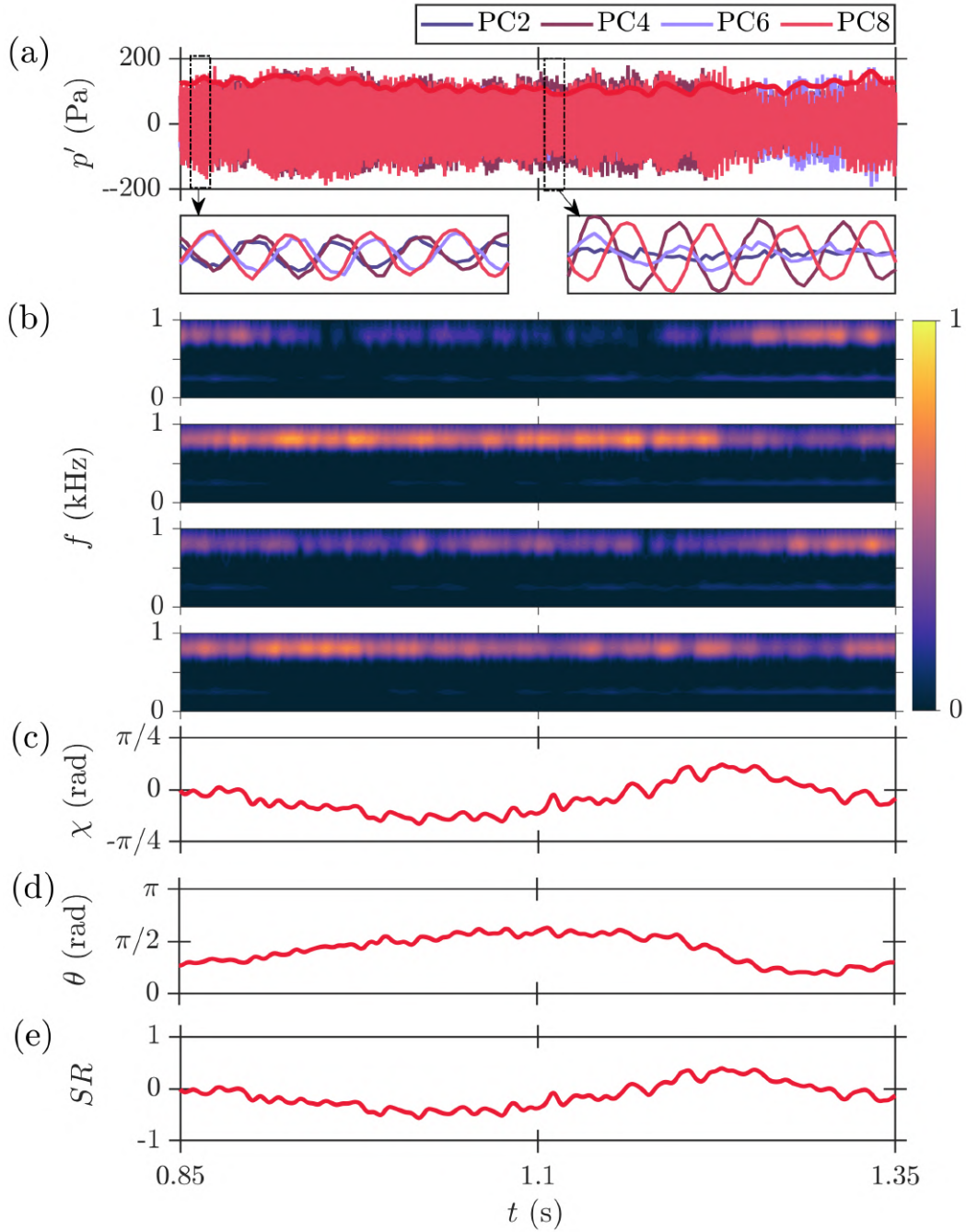


Figure 5.6: (a) Time series of the acoustic pressure along with the slowly varying amplitude ( $A$ ) and (b) corresponding scalogram during the pure standing azimuthal instability at  $\phi = 1.20$ . (c-e) Evolution of nature angle ( $\chi$ ), orientation angle ( $\theta$ ), and spin ratio ( $SR$ ) defining the dynamical state of the azimuthal thermoacoustic mode.

can be certain of the transitional switching of standing azimuthal mode and the nodal line position in the combustor. Panel (c) shows the evolution of  $\chi$ , which oscillates around 0,

indicating the standing azimuthal mode as the mode is oscillating near the equator in the Bloch sphere. Panel (d) represents the evolution of the orientation angle  $\theta$ , which determines the location of the pressure antinodes of the standing azimuthal wave. It is worth noting that the angle  $\theta$  exhibits oscillations between  $\pi/4$  and  $3\pi/4$ , which strongly suggests that the nodal line is moving in seemingly periodic motion. Lastly, panel (e) displays the temporal variation of the spin ratio ( $SR$ ), which exhibits oscillations centered around zero, implying that the amplitudes of the counterclockwise (CCW) and clockwise (CW) waves are nearly equal in strength.

In figure 5.7, we show the temporal dynamics of the beating azimuthal instability corresponding to marker ‘(g)’ in figure 5.2(a). Here, panel (a) depicts the time series of  $p'$ , complemented by the concurrently varying amplitude ( $A$ ) highlighted in red. Additionally, zoomed-in views are presented in three distinct temporal windows within the same time series. Moving from left to right, we can clearly identify the presence of a CCW spinning mode, a standing mode, and a CW spinning mode. Panel (b) displays the scalogram of the acoustic pressure obtained from PC2, PC4, PC6, and PC8 locations. The scalogram shows the CCW and CW spinning mode at the extreme left and right of the panel, where all four time series exhibit nearly equivalent amplitudes of  $p'$ . However, at  $t = 0.07$  s, in the middle of the time series of  $p'$ , we observe the narrowband spectrums in PC2 and PC6 due to periodic oscillations in  $p'$ , while PC4 and PC8 exhibit broadband spectrum due to aperiodic fluctuations. This arrangement of the scalograms from four pressure transducers at  $90^\circ$  to each other indicates the existence of the standing azimuthal mode. Panel (c) illustrates the oscillation in  $\chi$  is between  $-\pi/4$  to  $\pi/4$  (known as poles in Ghirardo and Bothien (2018)), indicating the switching from CCW spinning to CW spinning through the standing mode ( $\chi \approx 0$ ). Panel (d) shows that the location of the pressure antinode ( $\theta$ ) remains constant during the standing azimuthal mode, indicating a fixed nodal line at  $\theta \approx 3\pi/4$ . Finally, in panel (e), we observe that the spin ratio ( $SR$ ) oscillates between 1 and -1 at the extremes and remains at 0 in the middle, indicating the switching from CCW spinning mode ( $SR = 1$ ) to CW spinning mode ( $SR = -1$ ) through

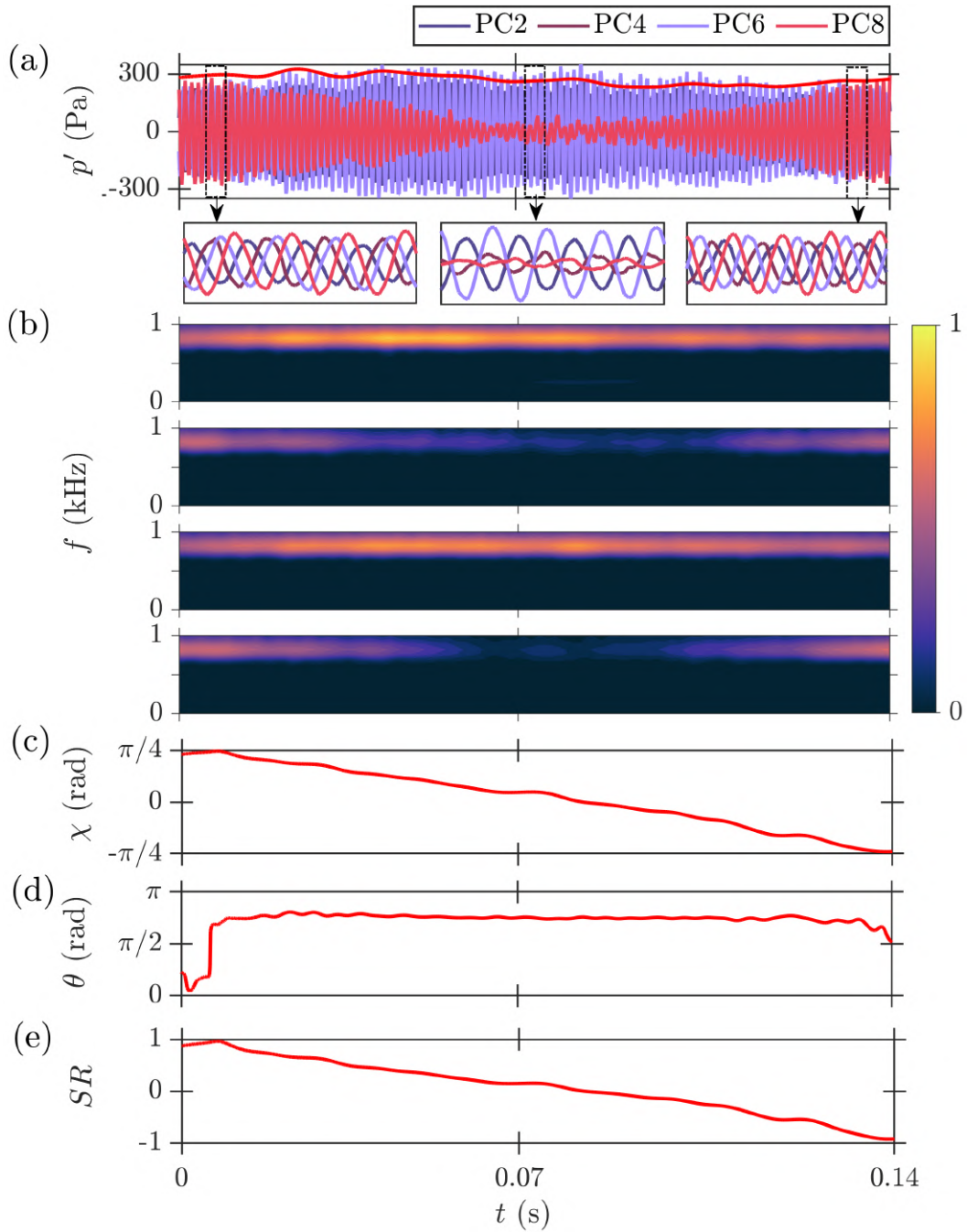


Figure 5.7: (a) Time series of the acoustic pressure along with the slowly varying amplitude ( $A$ ) and (b) corresponding scalogram during the beating azimuthal instability at  $\phi = 1.14$ . (c-e) Evolution of nature angle ( $\chi$ ), orientation angle ( $\theta$ ), and spin ratio ( $SR$ ) defining the dynamical state of the azimuthal thermoacoustic mode.

the standing mode ( $SR = 0$ ).

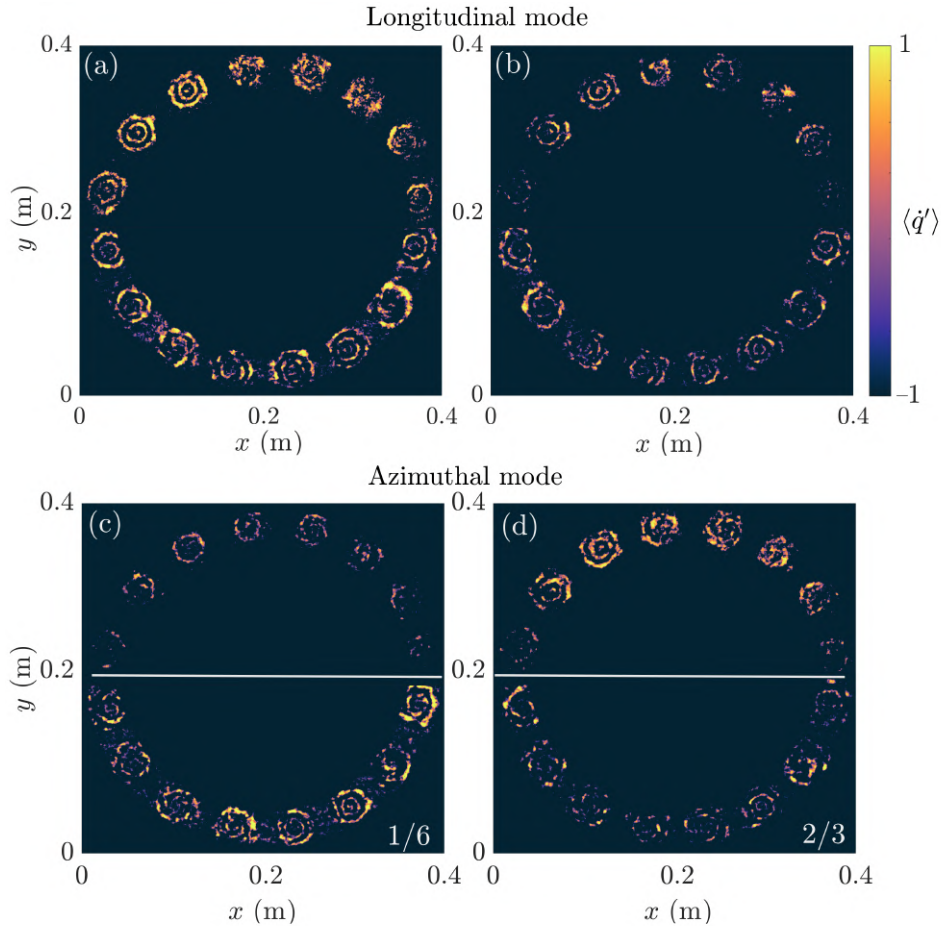


Figure 5.8: Phase-averaged global heat release rate viewed from above the annulus in two distinct scenarios: (a-b) during the pressure maxima and minima associated with the longitudinal mode of the dual-mode instability, and (c-d)  $\psi = 1/6$  and  $\psi = 2/3$  in the acoustic cycle associated with the azimuthal mode of the dual-mode instability. The white line represents the nodal line. This experimental investigation was conducted under the condition of  $\phi = 1.28$ .

## 5.6 FLAME DYNAMICS DURING THE TRANSITION TO AZIMUTHAL THERMOACOUSTIC INSTABILITY

In this section, we investigate the flame dynamics through the phase-average heat release distribution along the annulus associated with the different dynamical states discussed in the previous section. We show the normalized phase-averaged value of the heat release rate from the mean-subtracted chemiluminescence images at non-dimensional time steps of the acoustic pressure cycle. Here, the phase-averaged heat release rate field is indicative of the evolution of the flame structure at different points in the acoustic cycle.

We highlight the large-scale features of the global flame dynamics by calculating the phase-averaged contours of  $\dot{q}' - \dot{\bar{Q}}/\langle\dot{\bar{Q}}\rangle$ , first introduced by [Worth and Dawson \(2013b\)](#). Here,  $\dot{\bar{Q}}$  represents the time-averaged mean heat release rate, while  $\langle\dot{\bar{Q}}\rangle$  indicates its spatially averaged heat release rate fluctuations. This approach of phase averaging is particularly relevant as the dominant oscillations in the present combustion chamber is primarily governed by oscillations centered around a single frequency. For our study, we divide the data into six non-dimensional time steps ( $\psi$ ) in the acoustic cycle during the azimuthal mode and nineteen  $\psi$  in the acoustic cycle during the longitudinal mode. During the azimuthal mode, the non-dimensional time steps are considered as follows:  $\psi = 0$ ,  $\psi = 1/6$ ,  $\psi = 1/3$ ,  $\psi = 1/2$ ,  $\psi = 2/3$ , and  $\psi = 5/6$  of the acoustic pressure cycle.

During the longitudinal mode of the dual-mode instability (figure 5.4c), we illustrate the phase-averaged chemiluminescence image corresponding to the maxima and minima of  $p'$  in figure 5.8(a-b). The phase-averaged heat release rate field is shown at the pressure maxima and minima to facilitate a clear differentiation of the global swirling flame structures within flames. Across the majority of the sixteen burners, we observe the intensity is maximum along the periphery of the swirling flames during the pressure maxima (see figure 5.8a). These flames are bounded by the inner and outer shear layer with little recirculation, corroborating our earlier findings within the context of the low-amplitude longitudinal instability state discussed in Chapter 3. . Since the two modes (longitudinal and azimuthal modes) are coupled, we notice certain burners such as burner 14, 15, 16 as per figure 2.1(c), exhibit weak responses to the azimuthal mode. In contrast, during instances of pressure minima, the phase-averaged heat release rate field shows significantly diminished intensity along the periphery of the flame (see figure 5.8b).

During the azimuthal mode of the dual-mode instability (figure 5.4c,d), we show the phase-averaged heat release rate field corresponding to two non-dimensional time-steps of the acoustic pressure cycle, specifically at  $\psi = 1/6$  and  $\psi = 2/3$ . In figure 5.8(c-d),

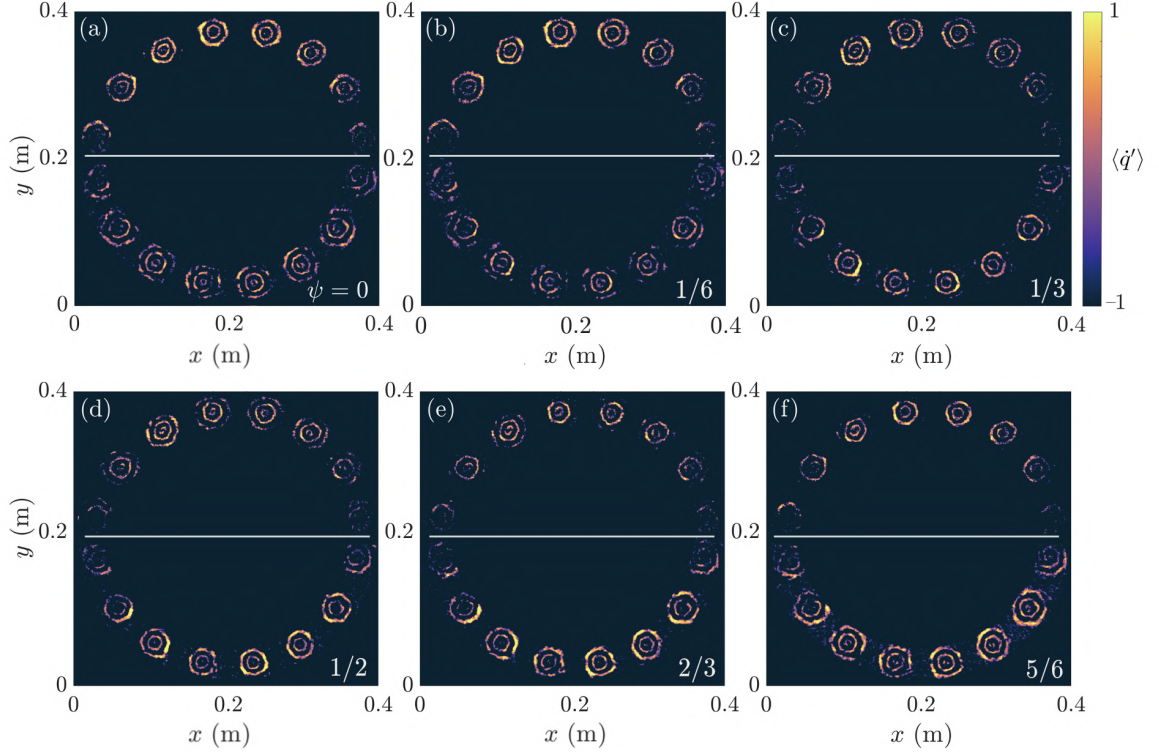


Figure 5.9: Phase-averaged chemiluminescence images at six normalized time steps ( $\psi$ ) in the acoustic cycle during the pure standing azimuthal instability. Phase averaging is conducted across the time trace of acoustic pressure fluctuations in the interval from 1.05 s to 1.15 s. The white line represents the nodal line. This experimental investigation was conducted under the condition of  $\phi = 1.20$ .

close to the pressure anti-node ( $90^\circ$  from the nodal line indicated in white), the flame response appears to be largely symmetric, which is associated with large axial and low transverse velocity fluctuations. In comparison, close to the pressure nodes (near the nodal line), a more asymmetric heat release distribution is observed, corresponding to negligible axial but strong transverse velocity fluctuations. Further, we notice the effect of the longitudinal mode on burners 14 and 15 in figure 5.8(c) and burners 1 and 7 in figure 5.8(d). The two coupled modes (longitudinal and azimuthal) clearly demonstrate the influence on the flame dynamics during the dual-instability mode.

Next, we discuss the flame dynamics during the pure standing azimuthal instability, whose corresponding time series of  $p'$  is earlier discussed in figure 5.6(a). In figure 5.9,

the pressure node regions are near the center of the flame image, indicated with a white line, while the pressure antinode regions are on the top and bottom. The non-dimensional time-steps  $\psi = 1/6$  and  $\psi = 2/3$  correspond to the instants in the cycle where the pressure oscillations are respectively maximum and minimum in the pressure signal from PC3. During these two non-dimensional time steps ( $\psi$ ), we observe the largest fluctuations in heat release rate appear close to the outer ring-like flame structures, which spans almost half the annulus. These flame structures in the previous studies have been understood as the formation of coherent vortical structures responding to the acoustic pressure fluctuations (Dawson and Worth, 2014). Specifically, these structures in the swirling flames are correlated to the roll-up of vortex structures on the shear layers, which rotate locally around every burner when advected downstream. We further notice these ring-like flame structures are clearly symmetric in terms of width and oscillation magnitude where the pressure is maximum in the combustor. Nevertheless, these flame structures are no longer continuous in the region of the combustor where the acoustic pressure reaches its minimum level.

Finally, we discuss the flame dynamics during the beating azimuthal instability (refer figure 5.7a), where the temporal analysis shows the spin ratio ( $SR$ ) oscillating between 1 and -1. From top to bottom, figure 5.10(I-III) consists of the time series of acoustic pressure (a) and the flame dynamics (b-g) over the acoustic cycle at six normalized positions during the epochs of CCW spinning ( $SR \approx 1$ ), standing ( $SR \approx 0$ ), and CW spinning ( $SR \approx -1$ ) mode, respectively. In panel (I), four pressure signals show sinusoidal oscillations of similar amplitudes and with phase shifts of  $90^\circ$  between them. The order of the time traces indicates a CCW spinning direction. Figures 5.10(I)(b-g) illustrates the phase-averaged images of the fluctuating component of the heat release rate for a CCW spinning mode at six normalized time steps ( $\psi$ ). At  $\psi = 0$ , we notice a high intensity of heat release rate fluctuations in the top right-hand quadrant and low intensity of heat release rate fluctuations at diametrically opposite. We observe that this flame structure rotates around the annulus in the counterclockwise direction over the duration of the

acoustic pressure cycle as shown in Figure 5.10(I)(c-g). These ring-like fluctuating flame structures are clearly symmetric in terms of width and oscillation magnitude near the pressure maxima. Moreover, larger oscillations in the heat release rate are present on the sides of the flame aligned in the CCW azimuthal direction away from the pressure maxima.

In panel (II), we show four acoustic pressure signals oscillating in phase or anti-phase, but with different amplitudes indicating the standing azimuthal mode in the combustor (figure 5.10IIa). Figure 5.10(II)(b-g) illustrates the phase-averaged images of the fluctuating component of the heat release rate for a standing azimuthal mode at six different  $\psi$ . In all six phase-averaged images, the amplitude of the acoustic pressure obtained from PC4 and PC8 is low, indicating the nodal line should be positioned near to the PC4 and PC8. We notice a symmetric flame response close to the pressure anti-node located near PC2 and PC6. The flame response near anti-nodal locations appears to be largely symmetric, which is associated with large axial and low transverse velocity fluctuations. In comparison, close to the pressure nodes locations, we notice a more asymmetric heat release distribution, corresponding to negligible axial but strong transverse velocity fluctuations.

In panel (III), again all the pressure signals show sinusoidal oscillations of similar amplitudes and with phase shifts of  $90^\circ$  between them. However, the order of the time traces now indicates a CW spinning direction (figure 5.10IIIa). Figure 5.10(III)(b-g) illustrates the phase-averaged images of the fluctuating component of the heat release rate for a CW spinning azimuthal mode at six different  $\psi$ . At  $\psi = 0$ , we notice high intensity of heat release rate fluctuations in the bottom right-hand quadrant and low intensity of heat release rate fluctuations at the diametrically opposite position. We observe that this flame structure rotates around the annulus in the clockwise direction over the duration of the acoustic pressure cycle as shown in Figure 5.10(III)(c-g). These ring-like flame structures are clearly symmetric in terms of width and oscillation magnitude near the

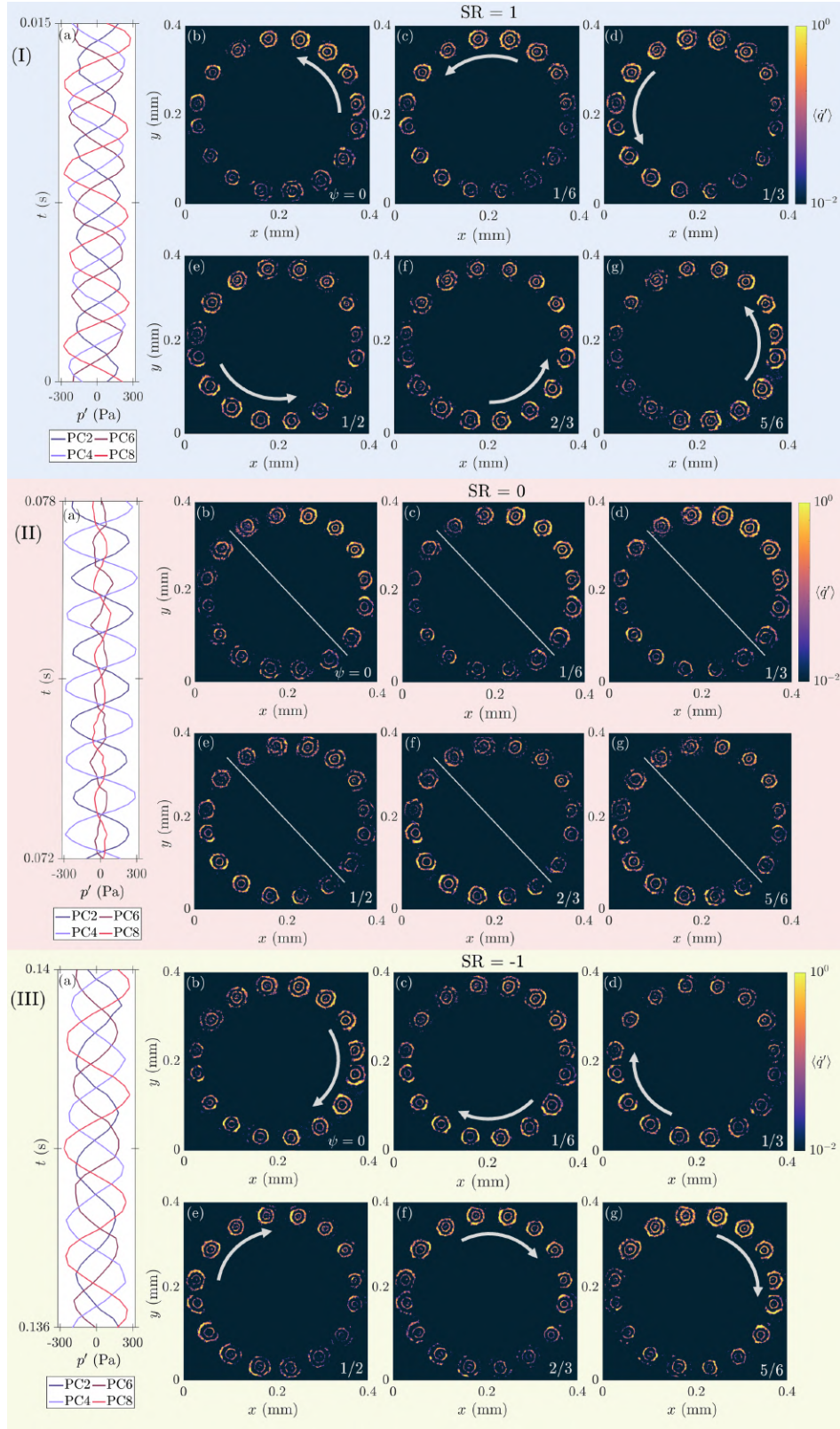


Figure 5.10: Time traces of acoustic pressure oscillations and associated phase-averaged chemiluminescence images at six normalized positions in the acoustic pressure cycle ( $\psi$ ) during the epochs of (I) counterclockwise spinning mode ( $SR = 1$ ), (II) standing azimuthal mode ( $SR = 0$ ), and (III) clockwise spinning mode ( $SR = -1$ ) in the beating azimuthal instability. This experimental investigation was conducted with  $\phi = 1.14$ .

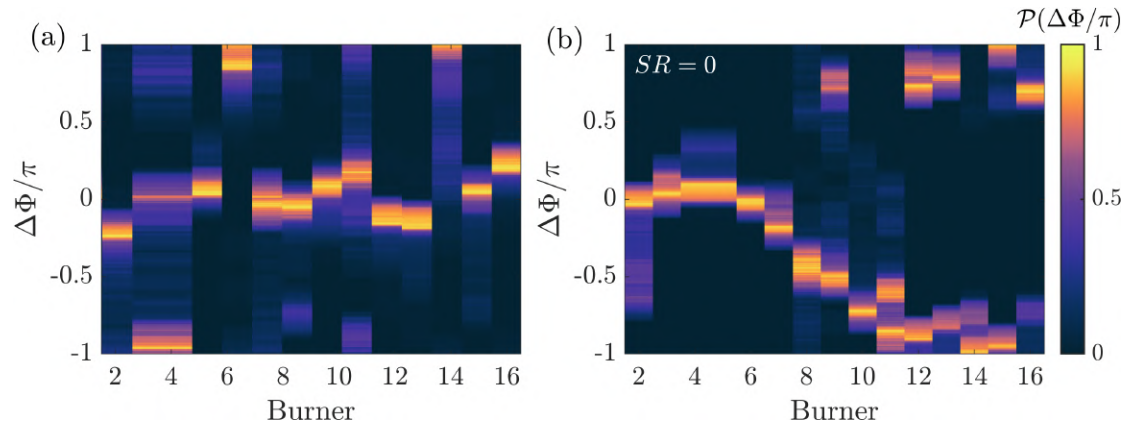


Figure 5.11: Distribution of the normalized phase difference of heat release rate fluctuations from flames is examined as a function of burner number during the (a) longitudinal and (b) azimuthal modes of the dual-mode instability.

pressure maxima. During the CW spinning azimuthal mode, the larger oscillations in the phase-averaged heat release rate fluctuations are observed on the sides of the flames aligned in the CW azimuthal direction when away from the pressure maxima. Thus, the global flame behavior offers the details of the overall thermoacoustic response of the annular combustor across various azimuthal modes.

## 5.7 QUANTIFY FLAME-FLAME INTERACTIONS DURING DIFFERENT DYNAMICAL STATES

To quantify the flame-flame interaction across various dynamical states observed during the thermoacoustic transition, we present the distribution of phase differences in heat release rate fluctuations ( $\Delta\Phi$ ) with respect to the burner number. The calculation of  $\Delta\Phi$  involves subtracting the phase of heat release rate fluctuations from each flame, positioned from 2 to 16 by the phase of heat release rate fluctuations from the flame at position 1. The arrangement of the burners is depicted in figure 2.1.

In Figure 5.11(a-b), we show the distribution of normalized  $\Delta\Phi$  as a function of burner number during the dual-mode instability, associated with longitudinal and azimuthal

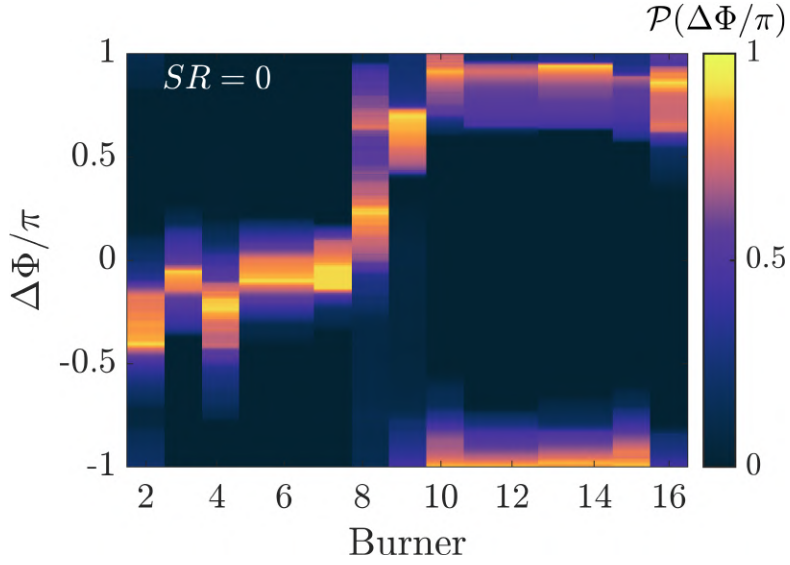


Figure 5.12: Distribution of the normalized phase difference of heat release rate fluctuations from all the flames in the annular combustor is examined across burners during the pure standing azimuthal instability.

mode separately (marked as ‘e’) in Figure 5.2). During the occurrence of the longitudinal mode, Figure 5.11(a) shows the distribution of normalized  $\Delta\Phi$  is near zero for almost all the burners with a few burners near  $-\pi$  and  $\pi$ . This suggests that most of the flames are oscillating in-phase during this mode with a few flames exhibiting slight out-of-phase behavior. In contrast, during the azimuthal mode of the dual-mode instability, as shown in Figure 5.11(b), flames positioned from 2 to 8 exhibit in-phase behavior, while flames at positions 9 to 16 are out-of-phase. Notably, flames 1 to 8 are located on one side of the nodal line, whereas the remaining eight flames are positioned on the opposite side, as illustrated in Figure 5.8(c-d). The spread observed in the distribution of normalized  $\Delta\Phi$  for certain burner numbers could be due to the coupling between the two modes.

In Figure 5.12, we show the distribution of normalized  $\Delta\Phi$  across the burner numbers during the state of pure standing azimuthal instability, denoted as ‘f’) in Figure 5.2. We observe the flames positioned from 2 to 8 exhibit the distribution in  $\Delta\Phi$  around zero, indicating their in-phase behavior. Conversely, flames located at positions 9 to 16 predominantly show the distribution in  $\Delta\Phi$  near  $\pi$  and  $-\pi$ , representing their out-of-phase

characteristics. As before, flames 1 to 8 are situated on one side of the nodal line, while the remaining eight flames are positioned on the opposite side, as illustrated in Figure 5.9. Remarkably, the pattern in the distribution of relative phase during the pure standing azimuthal instability appears more distinct compared to the pattern observed during the azimuthal mode of the dual-mode instability.

Finally, in Figure 5.13(a-c), we show the distribution of normalized  $\Delta\Phi$  across the burners during the beating azimuthal instability, marked as ‘(g)’ in Figure 5.2a. In particular, Figure 5.13(a) corresponds to the epochs of the CCW spinning wave, (b) corresponds to the epochs of the standing wave, and (c) corresponds to the epochs of the CW spinning wave. To maintain continuity in the observed pattern, we have rearranged the burner sequence, positioning burner 11 at the start and burner 10 at the end. In Figure 5.13(a), we notice the phase of heat release rate fluctuations from the flame at position 11 is entirely out-of-phase with respect to the fluctuations of the flame at position 1. The phase difference between flames at positions 12 to 16, relative to the flame at position 1, decreases and eventually reaches zero. As the burner number increases from 2 onwards, we observe the phase difference ( $\Delta\Phi$ ) starts to increase, reaching a maximum near burner 10. The observed pattern in the distribution of  $\Delta\Phi$  indicates that the wave is propagating from burner number 11 to 10 through burner 1, implying a spinning wave in the counterclockwise direction.

In Figure 5.13(b), the flames positioned from 11 to 2 exhibit the distribution in  $\Delta\Phi$  around zero, while flames located at positions 3 to 10 predominantly show the distribution in  $\Delta\Phi$  near  $\pi$  and  $-\pi$ . This flame behavior exhibits the standing wave pattern in the combustor. In Figure 5.13(c), we notice that the relative phase between the heat release rate fluctuations obtained from the flame at position 11 with the flame at position 1, is out-of-phase and has a value of  $\pi$ . As we approach the flame positioned closer to flame 2, there is a gradual reduction in the  $\Delta\Phi$  value. The value of  $\Delta\Phi$  is approximately zero when we reach the flame at position 2. Moreover, as we move from flame 2 towards flame

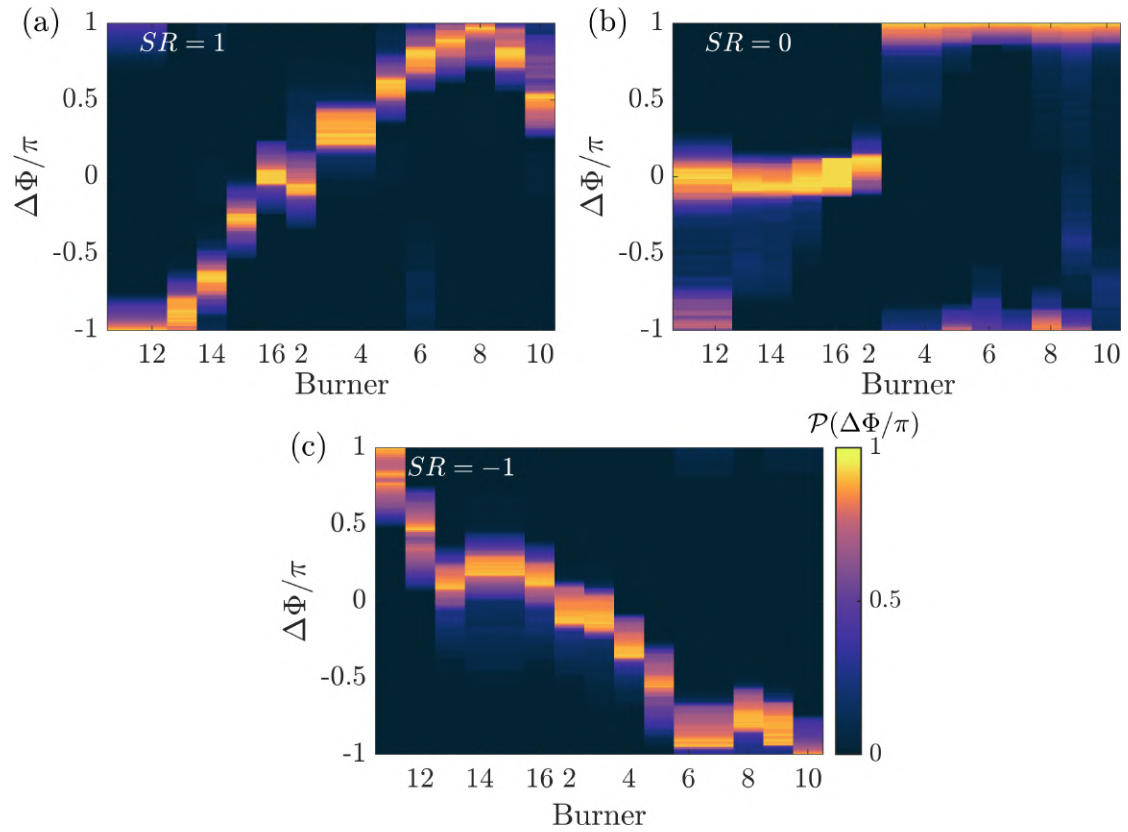


Figure 5.13: Distribution of the normalized phase difference of heat release rate fluctuations from all the flames is examined across burners during the epochs of (a) CCW spinning wave, (b) standing wave, and (c) CW spinning wave.

10, we observe that the value of  $\Delta\Phi$  reaches approximately  $-\pi$ . This smooth change in the distribution of  $\Delta\Phi$  from burner 11 to 10 through burner 1, indicates the presence of a clockwise spinning wave within the combustor.

## 5.8 INTERIM SUMMARY

In this chapter, we investigated the dynamics of the annular combustor to understand the transition from stable operation to azimuthal thermoacoustic instability. As we varied the equivalence ratio, we discovered a new route to azimuthal thermoacoustic instability through intermittency in the annular combustor. Employing a quaternion-based formalism to characterize the thermoacoustic modes within the combustor provided a concrete understanding of the system in terms of slow flow variables. Our finding

highlighted that the transition to azimuthal instability occurs through a frequency shift – from a low frequency corresponding to the longitudinal mode to a high frequency corresponding to the azimuthal mode.

Subsequently, we contrast the global flame behavior during the different dynamical states. During dual-mode instability, we illustrated how the coexistence of longitudinal and azimuthal modes influences the flame response. When it comes to pure standing azimuthal instability, we observe flames exhibiting a standing wave pattern. We show the maximum heat release rate fluctuations occur at pressure anti-nodes and the minimum fluctuations take place at pressure nodes. Moreover, during the beating azimuthal instability, we note distinct flame behaviors during epochs of counterclockwise (CCW) spinning, standing, and clockwise (CW) spinning modes.

Finally, we quantified the flame-flame interaction during various dynamical states by closely examining the distribution of relative phases among all burners with respect to one burner. During the azimuthal mode of the dual-mode instability, we observed that the phase differences among the eight consecutive flames, relative to the flame at position 1, remained in-phase. Conversely, the remaining eight flames exhibited out-of-phase behavior in relation to the flame at position 1. These observations pointed to the presence of a standing wave pattern within the combustor during this mode. A similar standing wave pattern was noted during the state of pure standing azimuthal instability. Intriguingly, during the beating azimuthal instability, we observed shifts in the pattern of the distribution of phase difference across burners during the epochs of counterclockwise (CCW) spinning, standing, and clockwise (CW) spinning modes. This quantification highlighted distinct patterns of relative phase during different azimuthal modes, emphasizing the significant role of flame-flame interaction in the observed behavior of the annular combustor.



## CHAPTER 6

# SUPPRESSING THERMOACOUSTIC INSTABILITY BY ACTUATING SWIRLER

From the investigation of the complex interaction between the unsteady heat release rate from the flame(s) and the acoustic pressure fluctuations in the previous chapters, it is evident that the coupling between these processes plays a vital role in the occurrence as well as controlling thermoacoustic instabilities in combustors. In this chapter, we discuss the experimental observations and a synchronization model for the suppression of thermoacoustic instability achieved by rotating the otherwise static swirler in a turbulent combustor. The experimental setup used to investigate the transition to the suppression state is discussed in Section 2.3 and the dataset is provided by Prof. Swetaprovo Chaudhuri's group. To understand the physical mechanism behind suppressing thermoacoustic instability using an actuating swirler, we extend the mean-field model of thermoacoustic transitions introduced in Chapter 4. We incorporate the effect of the active swirler in the model, to account for the time scale of the swirler rotation. The primary objective of the current work is to provide a possible way of suppressing notorious thermoacoustic instability and a model to explain the underlying principles behind suppression in self-excited thermoacoustic instability.

### 6.1 CHARACTERIZING THE ROTATING SWIRLER COMBUSTOR

In figure 6.1(a), we illustrate the variation of acoustic pressure amplitude of the first dominant mode as a function of the swirler rotation rate obtained from the rotating swirler turbulent combustor (see figure 2.3). The error bars in the plot show the variation

---

The results presented in this chapter are published in Singh, S., Kumar D., A., Dhadphale, J. M., Roy, A., Sujith, R. I., & Chaudhuri, S. (2023), Mean-field model of synchronization for open-loop, swirl controlled thermoacoustic system, *Chaos*, 33(4).

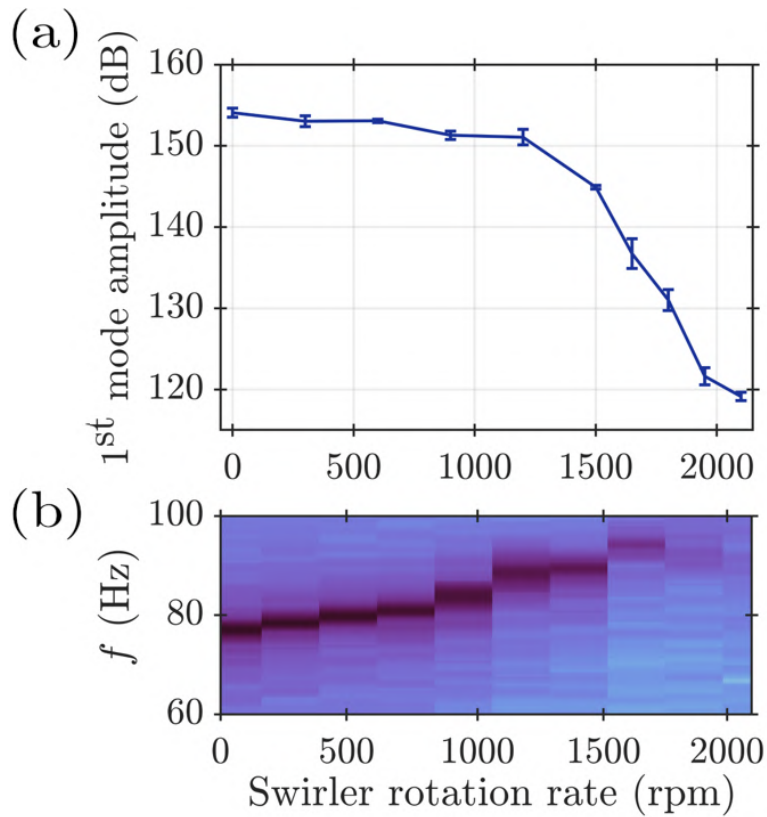


Figure 6.1: (a) Variation of the acoustic pressure amplitude of the first dominant mode as a function of the swirler rotation rate, depicting the suppression of thermoacoustic instability. (b) The frequency corresponding to the acoustic mode as a function of the swirler rotation rate. The error bar in (a) is associated with the variation of the amplitudes across three experimental runs.

between the amplitudes across three experimental runs. Figure 6.1(b) shows the change in the dominant frequency of the acoustic pressure during a transition from thermoacoustic instability to the state of suppression. The combustor remains at thermoacoustic instability for 0 rpm with a first mode amplitude of 153 dB and frequency of 76.9 Hz. At 1800 rpm, the amplitude reduces to about 130 dB and frequency of 94.2 Hz as intermittent oscillations emerge in the combustor. Finally, the system transitions to the state of suppression at 2100 rpm, where broadband sound replaces the dominant acoustic mode. Consequently, we observe a suppression of approximately 30 dB on varying the swirler rotation rate from 0 to 2100 rpm.

## 6.2 FLAME DYNAMICS DURING THE TRANSITION TO SUPPRESSION STATE

To understand the flame dynamics during the transition to the state of suppression, we illustrate the flame images obtained from the experiments. Figure 6.2 shows the phase-averaged unfiltered chemiluminescence images at pressure maxima (left column) and minima (right column) during the three dynamical states. The maxima and minima locations correspond to  $90^\circ$  and  $270^\circ$  phase, which are found from the instantaneous phase values of  $p'$  data using the Hilbert transform (Pikovsky *et al.*, 2002). During thermoacoustic instability, at pressure maxima (figure 6.2a), the mean-subtracted flame image depicts a well-defined circular shape with very high intensity, which reaches a negative value at pressure minima (figure 6.2b). Thus, the flame fluctuations are strongly correlated with the pressure fluctuations. Moreover, the flame structure shows flame stabilization along the central shear layer separating the inner and outer recirculation zones (Mahesh *et al.*, 2018).

Next, we consider the flame dynamics during the periodic part of intermittency (figures 6.2c-d). The phase-averaged flame image during maxima and minima still depict high and low-intensity values, respectively, albeit with lower intensity as compared to thermoacoustic instability. While the flame structure is similar to that observed during thermoacoustic instability, the distribution is diffused during both maxima and minima. This implies that some parts of the flame may not be attaining pressure maxima and minima at the instant of pressure maxima and pressure minima. Thus, the flame fluctuations are weakly correlated with the pressure fluctuations. Finally, figures 6.2 (e-f) correspond to the state of suppression. The phase-averaged chemiluminescence images corresponding to the pressure peaks (see figure 6.2e) and troughs (see figure 6.2f) are similar to each other. We observe incoherent and non-uniform flame structures with low intensity in comparison to the periodic part of intermittency and thermoacoustic instability. Moreover, the distributions of intensity between pressure maxima and minima are virtually indistinguishable, implying no correlation between flame fluctuations and

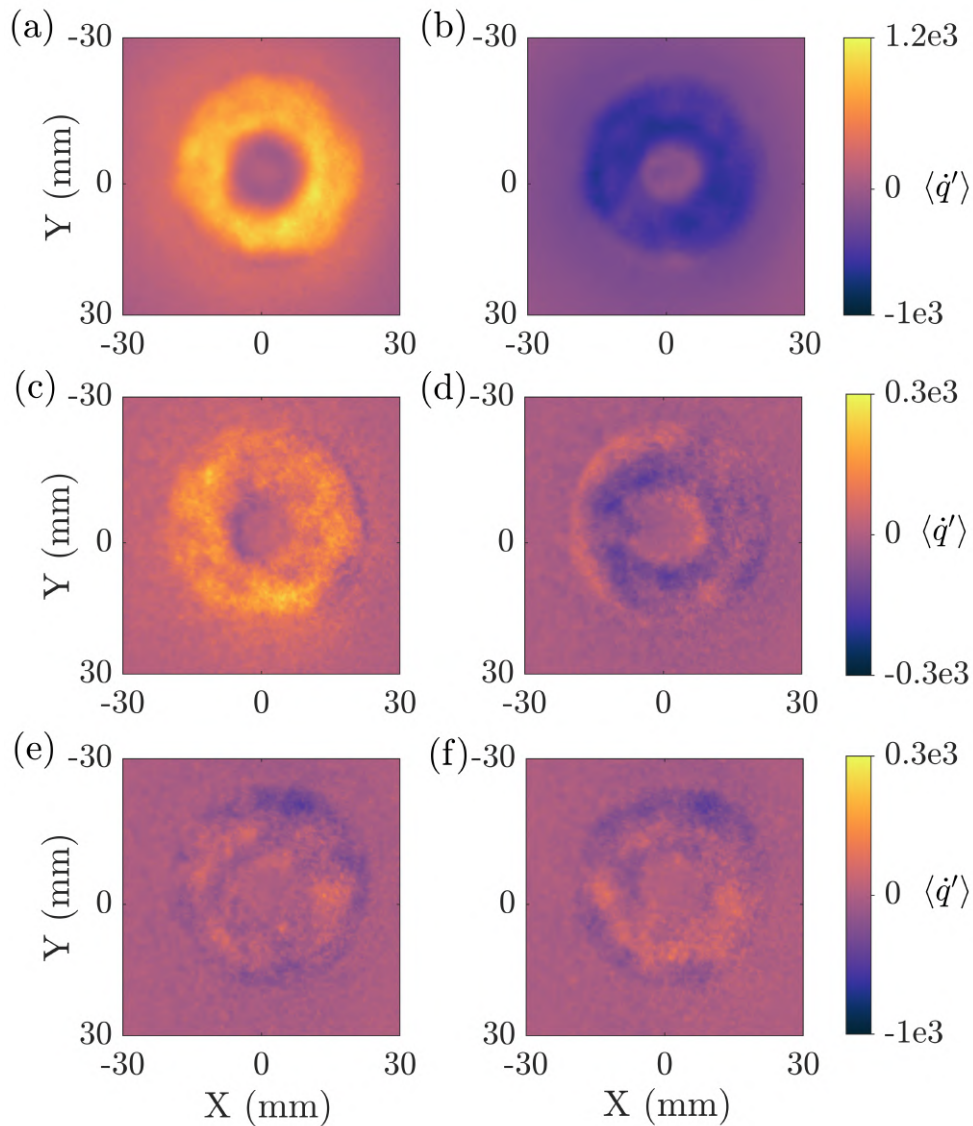


Figure 6.2: Mean-subtracted phase-averaged flame images at pressure maxima (left) and minima (right) during the dynamical states: (a-b) thermoacoustic instability, (c-d) periodic epochs of intermittency, and (e-f) suppression state. The flame image depicting a well-defined circular shape with very high intensity during thermoacoustic instability transitions to non-uniform flame structures with low intensity during the state of suppression.

acoustic fluctuations.

We are aware that any fluctuation in the flame results in an unsteady heat release rate which, in turn, causes acoustic disturbances in the combustion chamber and affects the flame when reflected from an appropriate acoustic boundary. The strength of the periodic

fluctuations in pressure and heat release rate starts increasing as the feedback between the acoustic field and heat release rate fluctuations increases. In figure 6.2, we notice the difference in the flame intensities when the swirler rotation rate is systematically varied. As a result, by varying the swirler rotation rate, we are disrupting the strength of a feedback loop to bring the sustained high-intensity oscillations in the flame at thermoacoustic instability to the low-intensity flame fluctuations at the state of suppression.

### 6.3 SPATIOTEMPORAL BEHAVIOR DURING THE TRANSITION TO SUPPRESSION STATE

Next, we investigate the spatiotemporal dynamics during the transition from thermoacoustic instability to the state of suppression. To that end, we analyze the characteristics of synchronization in a spatially extended thermoacoustic system by investigating the coupled behavior of the acoustic pressure  $p'(t)$  and the local heat release rate fluctuations  $\dot{q}'(x, y, t)$ . The local heat release rate fluctuations are extracted from the intensity variation observed at each pixel of the time-resolved chemiluminescence images. The flame images are coarse-grained over  $6 \times 6$  pixels to minimize the effect of noisy fluctuations in them. We install the pressure transducer near to the location of the flame imaging, to avoid acoustic phase delay effects in our experimental measurements. Figure 6.3 depicts the spatial distribution of instantaneous phase ( $\psi_I$ ) during a transition from thermoacoustic instability to the state of suppression through the state of intermittency when the swirler rotation rate ( $\tilde{\Omega}_r$ ) is increased. The instantaneous phasor field ( $\psi_I$ ) is obtained by subtracting the phase of the acoustic pressure ( $\Phi$ ) from the phase of the local heat release rate fluctuations ( $\theta_I$ ). The instantaneous phase of the local heat release rate fluctuations is obtained using Hilbert transformation.

In figure 6.3(a), when the swirler is static ( $\tilde{\Omega}_r = 0$  rpm), the acoustic pressure and heat release rate oscillate in phase, leading to a coherent field of the phasors. In the probability

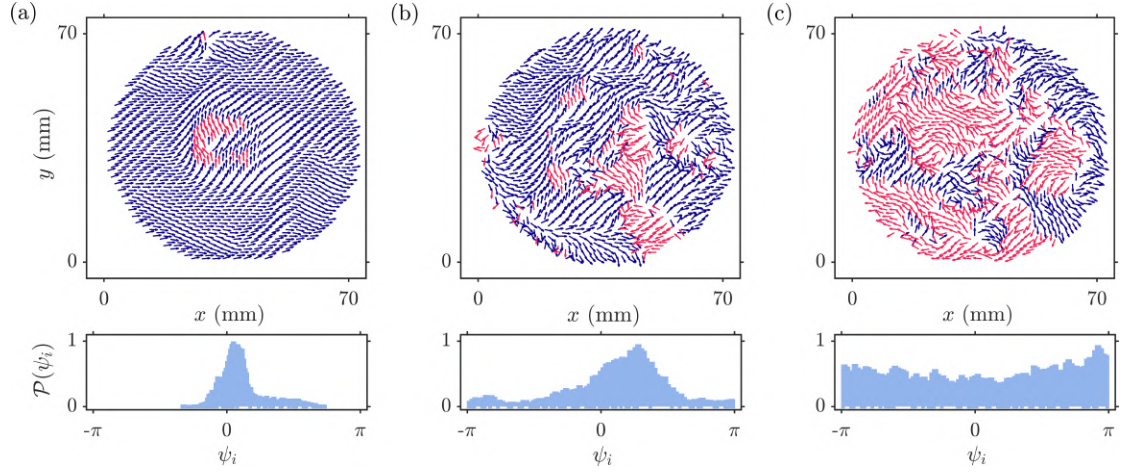


Figure 6.3: Disruption of order on varying the swirler rotation rate ( $\tilde{\Omega}_r$ ) from 0 to 2100 rpm in the turbulent combustor. A typical snapshot of the spatially distributed phasors ( $\psi_l$ ) is obtained by taking the phase difference between the local heat release rate ( $\theta_l$ ) and acoustic oscillations ( $\Phi$ ) during the state of (a) thermoacoustic instability, (b) intermittency, and (c) suppression. To delineate regions of acoustic power sources and sinks, phasors have been colored blue if  $|\psi_l| < \pi/2$  and red otherwise.

density function of  $\psi_l$ , we notice that the phase values are mostly  $\psi_l < |\pi/2|$  radians, leading to enhanced acoustic driving during the occurrence of thermoacoustic instability in the combustor and hence satisfying the Rayleigh criterion. We notice that the spatial synchrony in the phase plot starts reducing with an increase in  $\tilde{\Omega}_r$ . For instance, during the state of intermittency at  $\tilde{\Omega}_r = 1800$  rpm, the phase-field shows both coherent and incoherent fields of phasors shown in figure 6.3(b). The probability density function of  $\psi_l$  associated with intermittency is broadening in comparison with the probability density function of  $\psi_l$  obtained during thermoacoustic instability. In this state, there is the coexistence of clusters of both spatial synchrony and asynchrony in the phase field, referred to as a chimera state (Sujith and Unni, 2020). Further, increasing  $\tilde{\Omega}_r$  to 2100 rpm, we observe that the phase field is randomly oriented and incoherent (see figure 6.3c). In this state, the heat release rate fluctuations are dominated only by the turbulent flow, which results in a de-synchronized field of the phasors and a broadband distribution of  $\mathcal{P}(\psi_l)$ . This asynchronous behavior of the local heat release rate fluctuations during the state of suppression prevents the pressure oscillations from increasing in amplitude,

which leads to low-amplitude aperiodic fluctuations in the temporal dynamics of both acoustic pressure ( $p'$ ) and global heat release rate fluctuations ( $\dot{q}'$ ).

#### 6.4 THEORETICAL MODEL FOR SUPPRESSION OF THERMOACOUSTIC INSTABILITY

To understand the method of suppressing thermoacoustic instability, we provide a thermoacoustic model that not only captures temporal dynamics but also reproduces the features of the spatiotemporal synchronization during the transition to the suppression state.

We use the coupled non-dimensionalized flame-acoustic model discussed in Chapter 4 in Eq. (4.31) and reproduced here as:

$$\begin{aligned}\frac{d\hat{\eta}_j(t)}{dt} &= \hat{\eta}_j(t), \\ \frac{d\hat{\eta}_j(t)}{dt} &= \frac{\zeta}{N} \sum_{i=1}^N \sin [t + \theta_i(t)] - \zeta \dot{\hat{\eta}}(t) - \hat{\eta}(t), \\ \frac{d\theta_l(t)}{dt} &= \omega_l + K \left[ \dot{\hat{\eta}}(t) \cos (t + \theta_l(t)) + \hat{\eta}(t) \sin (t + \theta_l(t)) \right],\end{aligned}\tag{6.1}$$

where  $\hat{\eta}$  and  $\dot{\hat{\eta}}$  are the acoustic variables and normalized as  $\hat{\eta}(t) = \eta(t)/R_{\text{LCO}}$ . Here,  $R_{\text{LCO}}$  is the maximum amplitude of acoustic pressure during thermoacoustic instability, and the expression is derived in Eq. 4.29. And,  $\theta_l$  is the phase of the  $l^{\text{th}}$  heat release rate oscillator,  $N$  is the number of phase oscillators, and  $\zeta$  is the non-dimensionalized damping coefficient. Additionally,  $\omega_l$  is the non-dimensionalized and normalized frequency of the  $l^{\text{th}}$  phase oscillator.

In addition to the acoustic feedback, the swirler plays a crucial role in determining the flame response (Candel *et al.*, 2014). The swirler imparts a tangential velocity to the incoming flow through its geometry and actuation. The effect of swirl due to the geometry is quantified through the angular frequency of the geometric swirl  $\tilde{\Omega}_s$ , while the actuation is quantified through the frequency of shaft rotation  $\tilde{\Omega}_r$ . These two effects together make

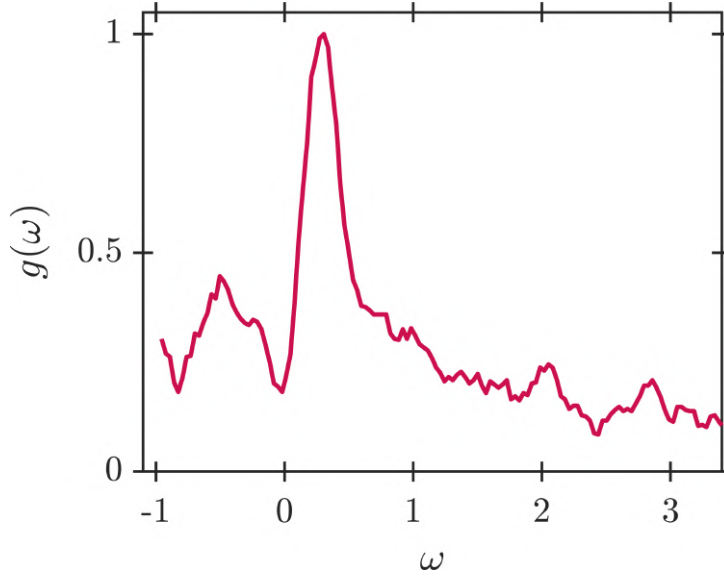


Figure 6.4: Oscillator frequency distribution  $g(\omega)$  as a function of  $\omega$  obtained from the heat release rate spectrum during a state of suppression.  $\omega$  is the normalized frequency centered around the acoustic frequency.

up the characteristic frequency of the swirler:  $\tilde{\Omega}_c = \tilde{\Omega}_s + \tilde{\Omega}_r$ . Thus, accounting for the competition in the acoustic ( $\tilde{\Omega}_0$ ) and swirler ( $\tilde{\Omega}_c$ ) frequencies, the coupling strength ( $\tilde{K}$ ) can be expressed as:

$$\tilde{K} = C [\tilde{\Omega}_0 - (\tilde{\Omega}_s + \tilde{\Omega}_r)] / \tilde{\Omega}_0, \quad (6.2)$$

where  $C$  is a model constant. The angular velocity ( $\tilde{\Omega}_s$ ) of a swirling flow is defined as  $\tilde{\Omega}_s = V \sin \delta_\alpha / r$  assuming solid body rotation of the fluid element (Dutta *et al.*, 2019). For incoming flow velocity  $V = 3$  m/s, swirler radius  $r = 11$  mm, and swirler blade angle  $\delta_\alpha = 30^\circ$ , the angular velocity imparted by the static swirler is  $\tilde{\Omega}_s = 137$  rad/s. We now normalized  $\tilde{\Omega}_0$ ,  $\tilde{\Omega}_r$ , and  $\tilde{\Omega}_s$  by  $\tilde{\Omega}_0$ .

## 6.5 MODEL PREDICTION OF TRANSITION TO SUPPRESSION STATE

We use the fourth-order Runge-Kutta method to solve Eq. (6.1). The damping coefficient ( $\alpha$ ) is estimated using the gradient descent method algorithm for parameter optimization during the state of suppression and is subsequently fixed for determining other states during a transition. We fix  $N \approx 3 \times 10^3$  phase oscillators for which frequency distribution

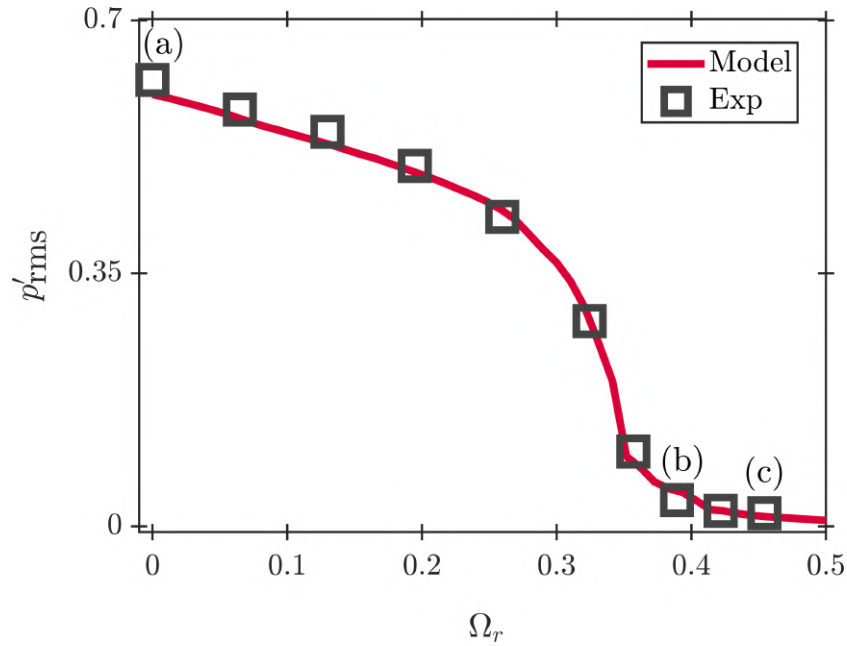


Figure 6.5: Comparison of the bifurcation diagrams obtained from the model (—) and experiments (□). The plot depicts the variation of the normalized  $p'_{rms}$  as a function of the non-dimensional swirler rotation rate ( $\Omega_r$ ).

(see figure 6.4) effectively resolves the heat release rate spectrum during the state of suppression and where a change in  $N$  has no effect on the simulation results. Using these inputs in the model, decreasing the coupling strength ( $K$ ) results in a transition to the state of suppression. We begin by confirming that a transition produced by the model is qualitatively similar to a transition obtained from the experiments. The relationship between the coupling strength ( $K$ ) and the swirler rotation rate ( $\Omega_r$ ) used in experiments is then determined by applying parameter optimization to each state observed in the experiments, which are tabulated in Appendix I.2.

Let us now compare the results from this model with the experimental observations.

### 6.5.1 Bifurcation diagram during the transition to suppression

Figure 6.5 illustrates the variation of the amplitude of the acoustic pressure ( $p'_{rms}$ ) as a function of the non-dimensional swirler rotation rate ( $\Omega_r$ ). In this figure, we show the comparison between the bifurcation diagram obtained from the model (—) with that

obtained from experiments ( $\square$ ). To compare the transition observed in the experiments with that obtained by the model (shown in Eq.(6.1)), we normalize each state with the amplitude of limit cycle oscillations. Initially, when the swirler is static ( $\Omega_r = 0$ ), the combustor exhibits thermoacoustic instability with limit cycle amplitude  $p'_{\text{rms}} = 0.62$ , at a frequency of  $f_0 = 76.9$  Hz as shown in figure 6.6(a). As  $\Omega_r$  increases, we notice a continuous decrease in  $p'_{\text{rms}}$ . At the highest  $\Omega_r$  value (0.455), we observe suppression, as the acoustic pressure fluctuations become low amplitude aperiodic with a broadband amplitude spectrum and low  $p'_{\text{rms}}$  value (see figure 6.6c).

A transition to the state of suppression occurs through the state of intermittency. This behavior can be observed at  $\Omega_r = 0.39$ , where bursts of the periodic pressure oscillations appear randomly amidst low amplitude aperiodic pressure fluctuations (see figure 6.6b). In figure 6.5, we notice that the model predicts a transition from thermoacoustic instability to the state of suppression as observed in the experiments. The monotonic decrease in  $p'_{\text{rms}}$  with increasing  $\Omega_r$  shows that the continuous, sigmoid-type transition observed in the experiments is well captured by the model.

## 6.5.2 Characterizing various dynamical states

Next, we contrast the dynamics obtained from the model with the dynamical states observed during experiments at three representative states. These states correspond to thermoacoustic instability, intermittency, and suppression state at three swirler rotation rates marked (a-c) in figure 6.5. We plot the time series, probability density function, and amplitude spectrum of  $p'$  in figure 6.6 and  $\dot{q}'$  in figure 6.7.

Figures 6.6(a) and 6.7(a) correspond to the state of thermoacoustic instability with  $\Omega_r = 0$ . We observe large-amplitude periodic oscillations in  $p'$  and  $\dot{q}'$ , and the probability density function of  $p'$  and  $\dot{q}'$  is characterized by a well-defined bimodal distribution. The amplitude spectrum corresponding to the same state indicates a sharp peak at  $f_0 = 76.9$

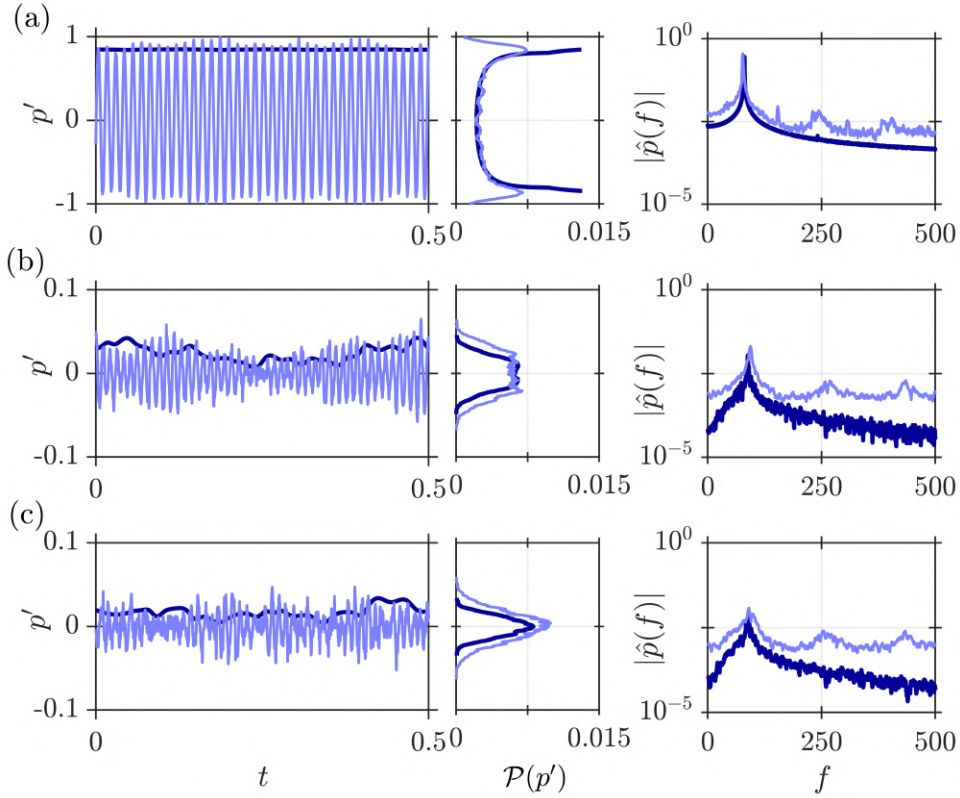


Figure 6.6: Comparison of the time trace, probability density function and amplitude spectrum of  $p'$  obtained from experiments (lighter shade) and that obtained from our model (darker shade) during the states of (a) thermoacoustic instability, (b) intermittency, and (c) suppression. (a-c) corresponds to the markers shown in figure 6.5. The envelope of the time series from the model is shown in the first column for clarity.

Hz. Figures 6.6(b) and 6.7(b) correspond to  $\Omega_r = 0.39$ , and depict intermittent oscillations in both  $p'$  and  $q'$ . These intermittent oscillations lead to a change from a bimodal to an unimodal distribution in the probability density function of  $p'$  and  $q'$ . We note that the model accurately depicts the location of epochs of periodic and aperiodic oscillations in both the time series ( $p'$  and  $q'$ ) while also depicting almost identical probability distribution function of both the time series. We also observe a good agreement between the amplitude spectrums of  $p'$  and  $q'$  obtained from the experiments and the model, each showing a dominant peak at 94.2 Hz during the state of intermittency. Finally, during the state of suppression at  $\Omega_r = 0.455$ , we observe low-amplitude aperiodic pressure fluctuations with a well-defined unimodal probability density function (figure 6.6c and

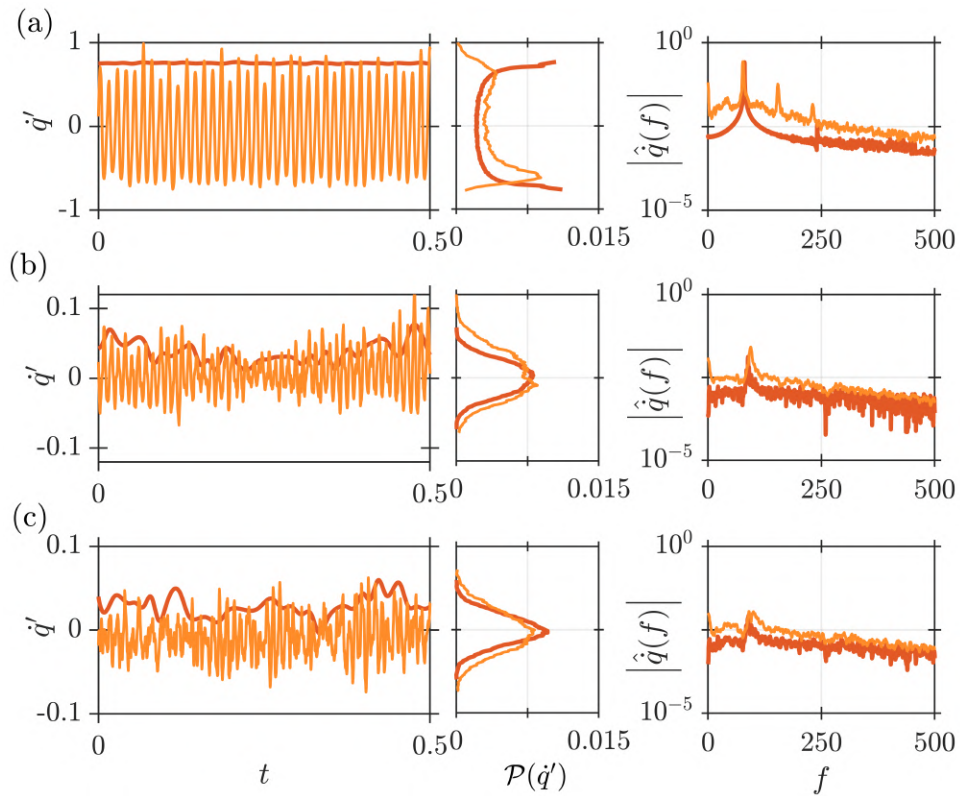


Figure 6.7: Comparison of the time trace, probability density function and amplitude spectrum of  $\dot{q}'$  obtained from experiments (lighter shade) and that obtained from our model (darker shade) during the states of (a) thermoacoustic instability, (b) intermittency, and (c) suppression. (a-c) corresponds to the markers shown in figure 6.5. Only the envelope of the time series from the model is shown.

6.7c). The amplitude spectrum of  $p'$  is broadband with a peak at 91 Hz. Again, the match between the experiments and the model is quite evident.

Quite notably, the model yields a good match in the characteristics of the time series of the pressure and heat release rate fluctuations during various dynamical states and only requires the heat release rate spectrum during the state of suppression as an input from the experiments for obtaining  $g(\omega)$ . Additionally, the amplitude spectrums and probability density functions of  $p'$  and  $\dot{q}'$  for the various states of combustor operation are well approximated. Our findings demonstrate that the model accurately represents the combustor dynamics, supporting our modeling approach.

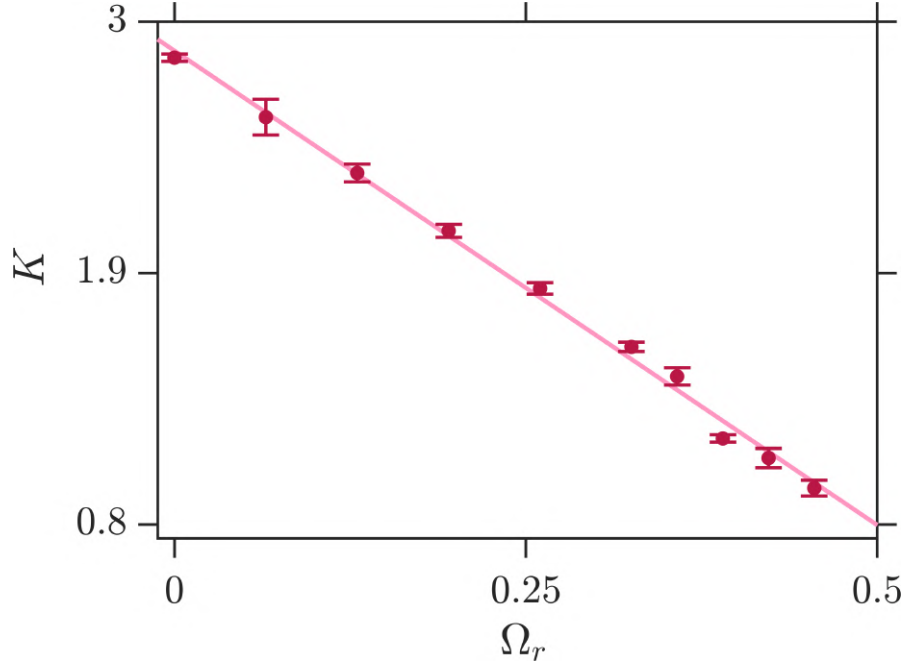


Figure 6.8: Mapping between the swirler rotation rate ( $\Omega_r$ ) and coupling strength ( $K$ ) during a transition to the state of suppression. The relation between  $\Omega_r$  and  $K$  is:  $K = 4.1(0.71 - \Omega_r)$  with the goodness-of-fit as 0.99. The error bars represent the standard deviation in estimating  $K$  by sliding the window of the time series used during optimization (Appendix E.2).

### 6.5.3 Relation between the coupling strength and swirler rotation rate

In figure 6.8, we show the mapping between the swirler rotation rate ( $\Omega_r$ ) and the coupling strength ( $K$ ), obtained by the gradient descent method using Eq. (4.36). The error bars in the figure are determined from a distribution of  $K$  for a window width of  $t_{\text{win}} = 0.7$  s using Eq. (4.36) and then sliding the window across the time series of  $\mathbf{Y}_{\text{exp}}$  and  $\mathbf{Y}_{\text{mod}}$ . Please refer to Appendix E.2 for a description of the window width selection process. The correspondence between the control parameters in the model and experiments will allow us to explain the experimental observations in terms of the physics embodied in the model. The estimated values strongly imply a linear relationship between the control parameter in our experiments ( $\Omega_r$ ) and the model ( $K$ ). The coupling strength linearly decreases according to the relation,  $K = 4.1(0.71 - \Omega_r)$ , thus providing *a posteriori* justification for assuming a linear relationship between  $K$  and  $\Omega_r$  in Eq. (6.2). The linear relation between the  $\Omega_r$  and  $K$  implies that when  $\Omega_r = 0$ , then coupling strength among

the phase oscillators is maximum, encouraging phase synchronization and leading to limit cycle oscillations. Increasing the value of  $\Omega_r$  leads to a decrease in the coupling strength ( $K$ ) among the phase oscillators, promoting phase de-synchronization and hence, the state of suppression. Thus, the model is easily interpretable in terms of experimentally relevant control parameters.

## 6.6 SYNCHRONIZATION TRANSITION TO SUPPRESSION STATE

We quantify the characteristics of synchronization through a measure called the Kuramoto order parameter described in Chapter 4 in Eq. (4.38) and reproduced here as:

$$\bar{r} = \frac{1}{N} \left\langle \left| \sum_{l=1}^N \exp(i\theta_l(t)) \right| \right\rangle_t, \quad (6.3)$$

where  $\theta_l$  is the phase of the  $l^{\text{th}}$  phase oscillator and  $\langle \cdot \rangle_t$  implies time average. The order parameter is defined as the degree of synchrony among the oscillators and it varies between  $[0, 1]$ . A value of  $\bar{r}$  close to zero indicates de-synchronized states, whereas a value of  $\bar{r}$  close to one indicates synchronized states.

Figure 6.9 depicts the variation of the order parameter as a function of the non-dimensional swirler rotation rate ( $\Omega_r$ ). The time-averaged order parameter ( $\bar{r}$ ) from the model is determined using Eq. (6.3), while  $\bar{r}$  from the experiments is determined according to Eq. (H.1) in Appendix H. The gradual decrease in the order parameter ( $\bar{r}$ ) indicates a transition from an ordered state where the heat release rate oscillators are in synchrony to a disordered state where the oscillators are in asynchrony. Note, that the minor deviation in the order parameter ( $\bar{r}$ ) from the model and experiment is due to the effect of background turbulent flow on the flame during the transition to the suppression state. For instance, figures 6.6 and 6.7 show the heat release rate spectrums are noisier than the acoustic pressure spectrums, indicating the phase jitter (Shanbhogue *et al.*, 2009b; Shin and Lieuwen, 2013) due to the turbulence is always stronger in the heat release rate signal than in the acoustic pressure signal. Furthermore, in figure 6.3(a), during

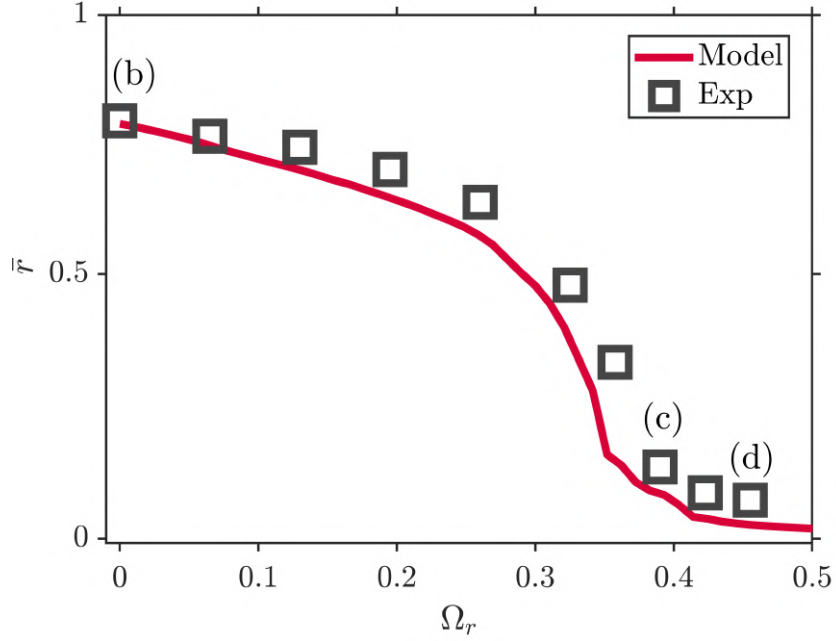


Figure 6.9: The synchronization bifurcation diagram depicts the variation of time-averaged order parameter ( $\bar{r}$ ) as a function of non-dimensional swirler rotation rate ( $\Omega_r$ )

the state of thermoacoustic instability, the majority of the phasors are aligned in one direction except for a few randomly distributed pockets in the center. A mean-field model of synchronization, on the other hand, does not account for the turbulence, resulting in a minor disagreement in the value of  $\bar{r}$ . These effects can potentially be incorporated through stochastic modeling, which will be taken up in the future.

To compare the synchronization observed in the spatial field of the experiments (figure 6.3) and from the model shown in Eq. (6.1), we plot the characteristics of the oscillators in the  $\dot{\theta}_l - \psi_l$  phase space. Here,  $\dot{\theta}_l$  is the instantaneous frequency and  $\psi_l$  is the phase difference between  $\theta_l$  and  $\Phi$ . Figure 6.10(a-c) shows the instantaneous oscillator distribution on the  $\dot{\theta}_l - \psi_l$  plane during different dynamical states (first column). These plots also include the distribution of instantaneous frequency  $\mathcal{P}(\dot{\theta}_l)$  in the middle column and the distribution of the instantaneous relative phase  $\mathcal{P}(\psi_l)$  along with the order parameter ( $r$ ) in the last column. The distribution of  $\psi_l$  is shown in polar coordinates (last column),

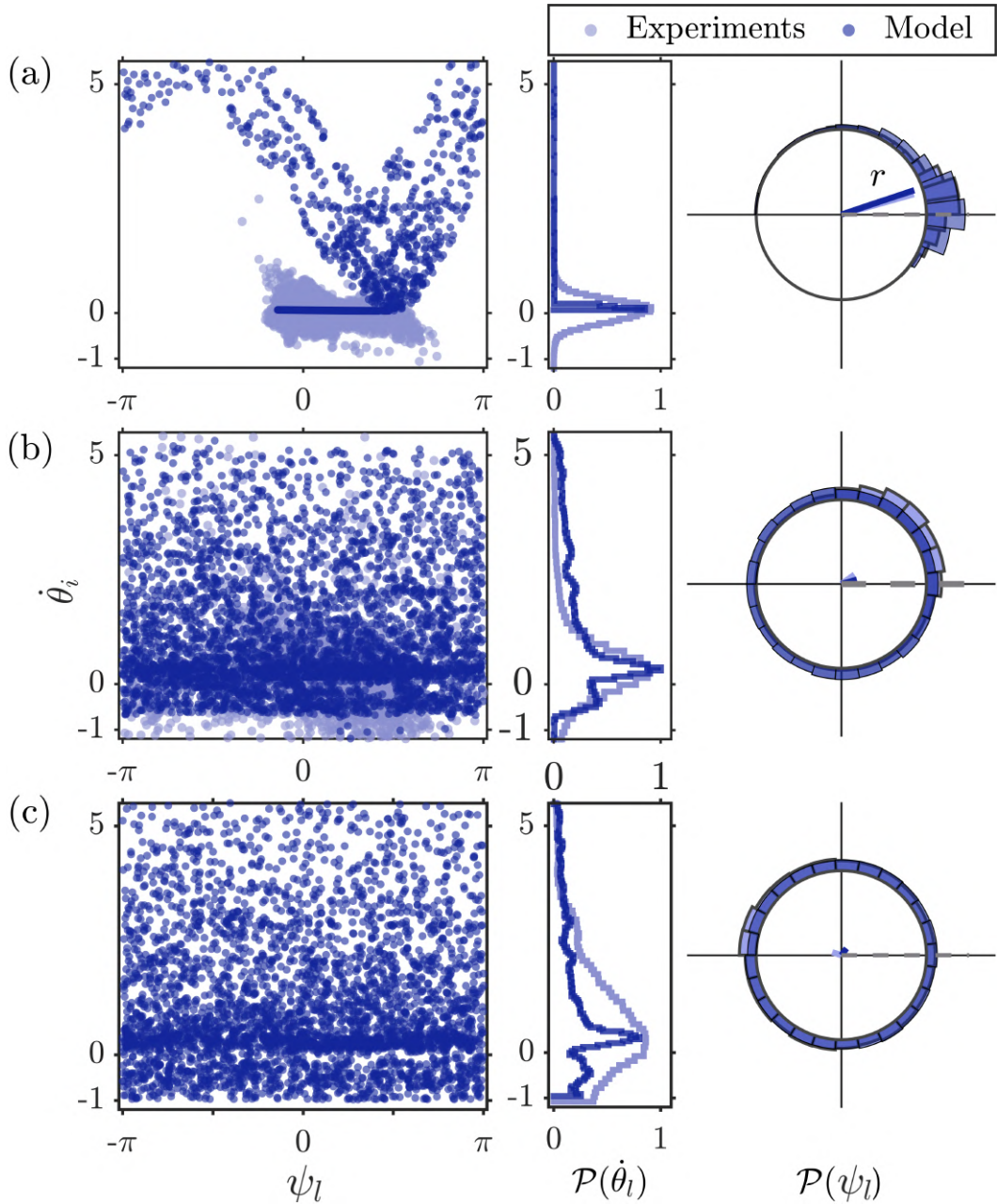


Figure 6.10: The typical instantaneous oscillator distribution in the  $\dot{\theta}_l - \psi_l$  plane, as well as the distribution of  $\mathcal{P}(\dot{\theta}_l)$  and  $\mathcal{P}(\psi_l)$  during the state of (a) thermoacoustic instability, (b) intermittency, and (c) suppression for experimental (lighter marker) and modeling (darker marker) dataset. The Kuramoto order parameter ( $r$ ) from the experiments and model (—) is shown in the last column.

and the frame of reference of the oscillators is co-rotating with the frequency of the acoustic pressure ( $\Omega_0$ ). The oscillators obtained from the spatiotemporal measurements are shown in lighter shades of marker, while those obtained from the model are shown in

darker shades of marker. Since the heat release rate fluctuations from the experiments are spatially distributed, comparing the characteristics of oscillators in the  $\dot{\theta}_l - \psi_l$  plane allows us to evaluate how well the low-dimensional mean-field synchronization model captures the characteristics of the spatiotemporal synchronization.

In figure 6.10(a), when the swirler is static ( $\Omega_r = 0$ ) corresponding to thermoacoustic instability (see figure 6.6a), we observe that the oscillators are entrained at the acoustic frequency and are phase-locked with the distribution of  $\psi_l$  mostly between  $-\pi/2$  and  $\pi/2$  radians (first column). In the last two columns, we notice a sharp peak, narrowband distribution of frequency  $\mathcal{P}(\dot{\theta}_l)$  and relative phase  $\mathcal{P}(\psi_l)$ . The value of order parameter  $\bar{r}$  is 0.8, implying global phase synchronization among the phase oscillators. In figure 6.10(b), when the swirler rotation rate is  $\Omega_r = 0.39$  corresponding to the state of intermittency (see figure 6.6b), we notice the larger regions of phase-synchronized clusters where  $\psi_l < |\pi/2|$  at some spatial locations and  $\psi_l > |\pi/2|$  at other locations, and comparatively less narrowband distribution of  $\mathcal{P}(\dot{\theta}_l)$  and  $\mathcal{P}(\psi_l)$ . The order parameter is  $\bar{r} = 0.13$  during the state of intermittency. Finally, in figure 6.10(c), when the swirler rotation rate is  $\Omega_r = 0.455$  corresponding to the state of suppression (see figure 6.6c), the oscillators are distributed in  $\psi_l > |\pi/2|$ , implying the phase de-synchronized among the oscillators. We also observe a broadband distribution in the distribution of  $\mathcal{P}(\dot{\theta}_l)$  and  $\mathcal{P}(\psi_l)$  and a value of  $\bar{r}$  close to zero. Thus, the gradual disappearance of the order among the oscillators, which is associated with the continuous shrinking of the size of the cluster of oscillators, leads to a continuous de-synchronized transition.

## 6.7 CHARACTERIZATION OF THE NONLINEAR TIME SERIES

In order to further demonstrate the ability of the model, we compare the dynamical features of the acoustic pressure fluctuations obtained from the experiments and the model.

We compute the permutation entropy ( $H_p$ ), which is an invariant measure of the

complexity of dynamics (Bandt and Pompe, 2002). Permutation entropy is often used to quantify the complexity of combustion (Gotoda *et al.*, 2012) and flame front dynamics (Gotoda *et al.*, 2010). Following Kobayashi *et al.* (2017), we first consider all  $D!$  possible permutations of successive data points in a time series consisting of  $\mathbf{p}(t) = \{p'(t), p'(t + \tau), p'(t + 2\tau), \dots, p'(t + (D - 1)\tau)\}$ , where  $p'(t)$  are the pressure fluctuations which is partitioned into subsets of length  $D$  (embedding dimension), with its elements being separated by a delay  $\tau$ . After obtaining the probability distribution of each permutation pattern  $p(\pi_l)$  where  $l = 1, 2, \dots, D!$ , we estimate the permutation entropy  $H_p$  normalized by the maximum permutation entropy  $\log_2 D!$  as:

$$H_p = -\frac{\sum_{l=1}^{D!} p(\pi_l) \log_2 p(\pi_l)}{\log_2 D!}, \quad (6.4)$$

where the lower bound of  $H_p = 0$  corresponds to a deterministic process, while the upper bound  $H_p = 1$  corresponds to an entirely random process.

Figure 6.11(a) shows the variation of permutation entropy ( $H_p$ ) as a function of the swirler rotation rate ( $\Omega_r$ ) obtained from the model (—) and experiments (□). We under-sampled the data to 2 kHz and took into account the embedding dimension  $D = 3$  with its elements separated by a delay  $\tau = 1$  s. The under-sampling is used to reduce the computational cost involved in obtaining  $H_p$ . During the state of thermoacoustic instability, we obtain the value of  $H_p$  from the experiments and model around 0.3. The value of  $H_p$  begins to rise during the intermittency state and reaches 0.65 during the suppression state. We can see that  $H_p$  from the model closely approximates  $H_p$  from the experiments.

The recurrence rate ( $RR$ ) is another nonlinear measure calculated following Nair *et al.* (2014) from the acoustic pressure time series. Many other experimental studies (Kabiraj and Sujith, 2012; Gotoda *et al.*, 2014; Baba *et al.*, 2023) have also elucidated the dynamic characteristics of acoustic pressure fluctuations during the state of stable operation and thermoacoustic instability through recurrence rate. The recurrence rate ( $RR$ ) is one of the statistical measures constructed through a recurrence quantification analysis and

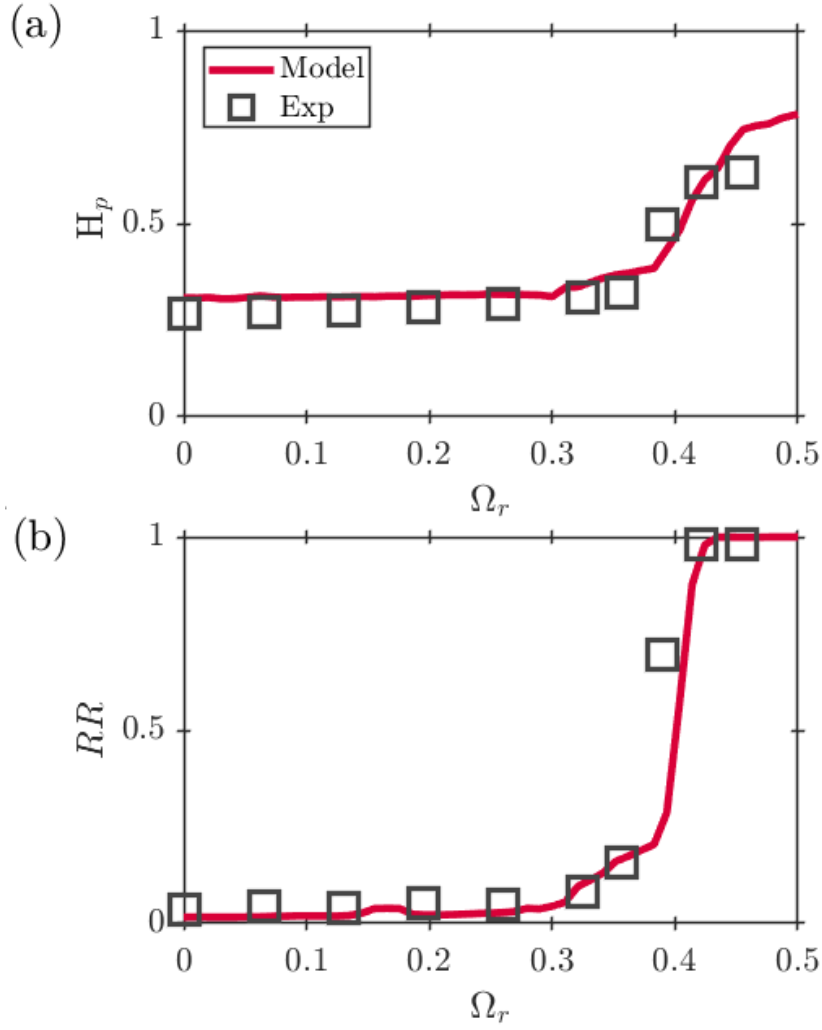


Figure 6.11: Comparison of the (a) permutation entropy ( $H_p$ ) and (b) recurrence rate ( $RR$ ) of dynamics as a function of swirler rotation rate ( $\Omega_r$ ) obtained from the model (—) and experiments ( $\square$ ) during the transition to suppression state in the rotating swirler combustor.

is a useful quantifier for measuring randomness in the signal (Marwan *et al.*, 2007). Recurrences in the phase space can be expressed as a matrix  $R_{ij} = \Theta(\epsilon - \|X_i - X_j\|)$ , where  $i, j = 1, 2, \dots, n$  and  $X_i, X_j$  represent the state vectors of the system at time  $t_i$  and  $t_j$ , respectively. Here,  $\Theta$  is the Heaviside step function and  $\epsilon$  is the size of the small neighborhood area considered around each point in the phase space. When the trajectory returns to the area within the threshold,  $R_{ij}$  is marked as 1 and 0 in the recurrence matrix to represent the white and black points in the recurrence plot, respectively. The density of black points in a recurrence plot represents the recurrence rate ( $RR$ ) in the dynamics

of the system and can be obtained as:

$$RR = \frac{1}{(N_0 - T)^2} \sum_{i,j=1}^{N_0-T} R_{ij}, \quad (6.5)$$

where  $T = d_0 \tau_{opt} F_s$  having value for  $d_0 = 10$ ,  $\tau_{opt} = 0.5$  ms,  $F_s = 2$  kHz. The threshold for the recurrence plot was chosen to be  $\epsilon = 0.2$  and signal was sampled at  $F_s$  of 2 kHz for 5 s to get  $N_0 = 10000$ . We obtained  $\tau_{opt}$  (optimum time delay) and  $d_0$  (minimum embedding dimension) using Average mutual information (AMI) and Averaged false nearest neighbor (AFNN) in [Hernandez-Rivera \*et al.\* \(2019\)](#).

Figure 6.11(b) demonstrates the variation of recurrence rate ( $RR$ ) of the dynamical state as a function of  $\Omega_r$ . On approaching thermoacoustic instability, the density of points in the recurrence plot decreases. This is expected because the number of black points in the recurrence plot would come down as the thermoacoustic instability is reached because the pairwise distances now exceed the threshold more often. We can notice the value of  $RR$  is around 0 during the state of thermoacoustic instability, 0.7 during intermittency, and 1 during the suppression state both from the model and experiments. This measure obtained from the experiments is also very well approximated by the model.

The close match of the measures ( $H_p$  and  $RR$ ) for the experiments and the model indicates that the nonlinear features of experiments are very well captured by the synchronization model presented here.

Although the model does well in capturing the bifurcation characteristics and aspects of synchronization, it does not capture the higher modes of the spectrum (see figures 6.6 and 6.7). This is by construction of the model as we did not consider higher modes in Eq. (6.1), to keep the analysis simple. Additionally, the prediction of dynamical states on further increase in swirler rotation rate beyond the state of suppression from the model is left for future studies.

## 6.8 INTERIM SUMMARY

In this paper, we report experiments and modeling of open-loop control of thermoacoustic instability in a turbulent combustion system using an actuated swirler. A systematic increase in the rotation rate of the swirler leads to the suppression of limit cycle oscillations as the dynamics of the combustor transitions to low-amplitude aperiodic oscillations through an intermediate state of intermittency. We extend a mean-field synchronization model for the flame response comprising an ensemble of non-identical phase oscillators evolving collectively under the effect of acoustic pressure discussed in Chapter 4. The effect of the active swirler is incorporated naturally into the model in terms of the relative time scales of swirler rotation and acoustic frequency. We further implement a parameter identification technique to obtain exact correspondence between the model parameter values and experimental observations. We find that the mapping between the swirler rotation rate in the experiments and the coupling strength in the model manifests as a linear relationship between them.

Through a comparison of the bifurcation diagram, time series, probability density functions and amplitude spectrums, we show that the model replicates the experimentally observed  $p'$  and  $\dot{q}'$  fluctuations very well. Further, we show that the model captures the characteristics of spatiotemporal synchronization underlying a transition to the state of suppression while depicting states such as synchronization, chimera, and de-synchronization. In particular, we find that the phase oscillators are synchronized during thermoacoustic instability, partially synchronized during intermittency, and undergo progressive de-synchronization during the suppression. Therefore, we notice a sigmoid-type transition to the suppression state happens through the underlying synchronization. As a consequence, using the mean-field thermoacoustic model, we establish that the active swirler suppresses thermoacoustic oscillations through a de-synchronization transition.



## CHAPTER 7

### CONCLUSION AND OUTLOOK

Our study offers a fresh perspective concerning the connection between synchronization theory and thermoacoustic transitions in turbulent combustors. In the broader context of nonlinear dynamics, our results provide valuable experimental evidence of both continuous and explosive synchronization in turbulent combustors. These findings contribute to a deeper understanding of the fundamental principles governing the emergence of different types of thermoacoustic transitions and states of pattern formation in spatially extended systems.

In the present thesis, our exploration began by examining how the nature of thermoacoustic transition changes systematically with variations in equivalence ratio and bulk flow velocity within the annular combustor. Through a comprehensive analysis of flame-flame and flame-acoustic interactions across various routes to longitudinal thermoacoustic instability, we identified distinct levels of synchronization. Comparisons of heat release rate responses among neighboring burners unveiled varying degrees of synchronization between the heat release rate and acoustic pressure fluctuations during different dynamical states. These differences underscore that thermoacoustic transitions can manifest gradually or abruptly, influenced by spatiotemporal synchronization. Significantly, even in cases of longitudinal thermoacoustic instability, our study reveals the non-trivial nature of flame-flame interactions.

Subsequently, we introduced a model to explain the spatiotemporal interactions giving rise to rich dynamical phenomena in turbulent combustors. This model is based on the assumption that the turbulent flame comprises an ensemble of phase oscillators evolving under the influence of mean-field interactions and acoustic feedback. These

interactions encode the nonlinearities in the flame response subjected to acoustic and turbulent fluctuations. The model successfully produces both continuous and abrupt transitions observed in three distinct combustor configurations (bluff-body stabilized, swirl-stabilized, and annular). Significantly, our modeling approach naturally provides an explanation of spatiotemporal synchronization and pattern formation observed in turbulent thermoacoustic systems – a feature that has yet to be captured in other thermoacoustic models. We showed that our model closely replicates the statistical behavior of spatial desynchronization, chimera, and global phase synchronization underlying the thermoacoustic transitions. Our findings strongly suggest that continuous and abrupt thermoacoustic transitions are associated with synchronization transition of second-order and first-order, respectively. Moreover, our model not only explains distinct types of bifurcation to limit cycle oscillations in disparate systems but also does so in a consistent manner based on the paradigm of synchronization, eliminating the need for disparate modeling approaches.

We proceeded to modify the annular combustor geometry to excite azimuthal thermoacoustic instability. The dynamics of the annular combustor is studied to understand the transition from stable operation to azimuthal thermoacoustic instability. As we varied the equivalence ratio, we discovered a new route to azimuthal thermoacoustic instability through intermittency in the annular combustor. Employing a quaternion-based formalism to characterize the thermoacoustic modes within the combustor provided a concrete understanding of the system in terms of slow flow variables. Our finding highlighted that the transition to azimuthal instability occurs through a frequency shift – from a low frequency corresponding to the longitudinal mode to a high frequency corresponding to the azimuthal mode. Furthermore, we quantified the flame-flame interaction during various dynamical states by closely examining the distribution of relative phases among all burners with respect to one burner. This quantification highlighted distinct patterns of relative phase during different azimuthal modes, emphasizing the significant role of flame-flame interaction in the

observed behavior.

Finally, we focused on the practical aspect of controlling thermoacoustic instability in a turbulent combustor by introducing an active swirler. Upon examining the flame dynamics and spatiotemporal behavior during the transition to the suppression state, we confirmed that the actuation of the swirler disrupts the strength of the feedback loop and effectively suppresses thermoacoustic instability. To understand the method of suppression, we extended the earlier proposed thermoacoustic model for studying thermoacoustic transitions by incorporating the effect of the active swirler and acoustics in the control parameter. Through a comparison of the statistical properties of the acoustic pressure and heat release rate fluctuations between the model and experimental data, we demonstrated that our model accurately reproduces the dynamics observed in experimental setups. Moreover, our model showcased its ability to capture the characteristics of spatiotemporal synchronization underlying a transition to the state of suppression while depicting states such as synchronization, chimera, and desynchronization.

The findings presented in this thesis offer potential solutions for resolving the issues surrounding the resolution of second-order and first-order synchronization in non-standard Kuramoto models. Moreover, our approach paves the way for exploring additional avenues in modeling related to fluid dynamical systems, particularly those involving aeroacoustic and flow-structure interactions, where complex spatiotemporal interactions give rise to diverse and rich dynamical phenomena.

### **7.0.1 Future directions**

The thesis opens doors to compelling future prospects. One direction involves enhancing the existing annular combustor by tilting the burner axes, thereby implementing a helical arrangement of flames ([Ariatabar \*et al.\*, 2016](#)). Implementing such an arrangement offers several potential benefits. It can promote more efficient mixing of fuel and air, enhance flame stability, and optimize combustion characteristics. Moreover, this

configuration can mitigate issues like flashback (where the flame propagates back into the fuel supply system) and reduce the susceptibility to thermoacoustic instabilities, ultimately contributing to better combustion performance and reduced emissions.

An alternative avenue for future exploration entails operating the annular combustor using blends of LPG and hydrogen to investigate the transition to thermoacoustic instabilities. Examining the impact of hydrogen fuel on flame behavior during the thermoacoustic transition stands as a crucial pursuit for the gas turbine community. Therefore, conducting comprehensive experiments to explain the response of the flames under various operational conditions can pave the way for utilizing existing aero and land-based combustors with the goal of achieving zero-carbon operation. This research direction holds the potential to contribute significantly to the development of eco-friendly and sustainable combustion technologies.

Moreover, it would be interesting to look into the critical regions within the annular combustor during thermoacoustic instabilities. Utilizing spatiotemporal data gathered from sixteen burners, we can assess the spatial distribution of turbulent velocity amplitudes at the acoustic frequency, time-averaged vorticity, time-averaged heat release rate, and Rayleigh index. By identifying and characterizing these significant regions, we can aim to implement a passive control strategy (Roy *et al.*, 2021). This involves directing a steady injection of secondary micro-jets of air to optimize injection locations and pinpoint the critical region. This approach seeks to develop a potential mitigation strategy for suppressing azimuthal instabilities in the annular combustor.

Furthermore, a fascinating avenue involves modifying the mean-field thermoacoustic model discussed in the thesis to incorporate the influence of turbulence. This modification aims to investigate how accurately the model can replicate the fractal nature of the heat release rate. If the adapted model successfully captures the observed loss of multifractality and scaling laws observed in the experiments, it could become a valuable tool for predicting

amplitudes, aligning with the findings of [Pavithran \*et al.\* \(2020\)](#).



## APPENDIX A

### VERIFYING LONGITUDINAL INSTABILITY IN THE ANNULAR COMBUSTOR

In the annular combustor, during the transition to thermoacoustic instability, we observe the dominant frequency remains at  $f_a = 220 \pm 10$  Hz (see figure A.1a). We identified a dominant mode with a frequency of approximately 218 Hz during low-amplitude thermoacoustic instability and 227 Hz during high-amplitude thermoacoustic instability. To confirm the nature of the mode, we compare the pressure fluctuations during low-amplitude and high-amplitude thermoacoustic instability obtained from three pressure transducers mounted at equidistant positions on the back-plane of the chamber, as shown in figure A.1(b,c).

The overlay of the time traces of pressure fluctuations from the three transducers on the top left and right panel of figure A.1(b,c) clearly indicates that there is a negligible difference

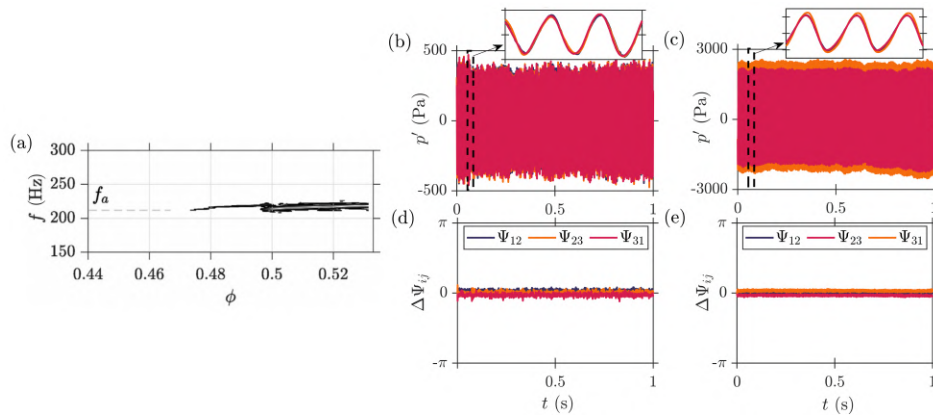


Figure A.1: Observed dominant frequency in the annular combustor as a function of the equivalence ratio and correspond to the condition reported in figure 4.4(b). Comparison of (b, c) time series, (d, e) phase difference obtained from three pressure transducers on the combustor backplane during low-amplitude and high-amplitude TAI.

in their phase, which is further confirmed by the plot of relative phase difference, which remains constant and near zero (see figure [A.1d,e](#)). From these observations, we conclude that the mode under consideration here is a longitudinal mode and not the azimuthal mode.

## APPENDIX B

### NUMERICAL PROCEDURE FOR SAMPLING OSCILLATOR FREQUENCY DISTRIBUTION FROM EXPERIMENTAL DATA

The density of oscillators in frequency domain  $g(\omega)$  is obtained from  $\hat{q}(\omega)$ , i.e., Fourier transform of the time series of  $\dot{q}'(t)$  during the occurrence of combustion noise. The  $\hat{q}(\omega)$  is available for discrete frequencies,  $\{\omega_1, \omega_2, \dots, \omega_{N_F}\}$ , where  $\omega_1 = 0$  and  $\omega_{N_F}$  is the maximum frequency. The  $\hat{q}(\omega)$  is normalized to obtain  $g(\omega) = |\hat{q}(\omega)| / \int_0^{\omega_{N_F}} |\hat{q}(\omega')| d\omega'$ . The normalization ensures  $\int_0^{\omega_{N_F}} g(\omega) d\omega = 1$ . The integration is performed numerically with the trapezoidal rule. This procedure gives  $g(\omega)$  at discrete frequencies, which is used for sampling the frequency for each of the  $N$  phase oscillators.

To obtain samples from arbitrary discrete distribution  $g(\omega)$ , we use the uniform distribution  $U(x)$  with support over  $x \in [0, C_{N_F}]$ , where  $C_k = \sum_{l=1}^k g(\omega_l)$ , i.e. for  $k = N_F$  we get  $C_{N_F}$  as cumulative sum over all the discrete  $g(\omega)$  values. The  $N$  data points  $\{x_1, x_2, \dots, x_N\}$  are sampled from  $U$ . The frequency of  $l^{\text{th}}$  oscillator is then obtained as

$$\omega_{s,l} = (1 - \alpha)\omega_k + \alpha\omega_{k+1}, \quad (\text{B.1})$$

where,

$$\alpha = (x_l - C_k) / (C_{k+1} - C_k),$$

and  $k$  satisfies  $C_k \leq x_i < C_{k+1}$ . This procedure samples the frequency of  $N$  phase oscillators according to the normalized distribution  $g(\omega)$  obtained from the experimental data.



## APPENDIX C

### CHOOSING OPTIMAL NUMBER OF PHASE OSCILLATORS

The optimal number of oscillators should be high enough so that it is able to reproduce the initial frequency distribution (figure 4.2) without requiring heavy computation cost. This is done by verifying the convergence of our results with respect to the number of phase oscillators. We plot the standard deviation ( $\nu$ ) of the acoustic pressure amplitude as a function of the number of oscillators (Fig. C.1). For each case, we performed 20 iterations using random initial conditions ( $\eta(0), \dot{\eta}(0), \theta_l(0)$ ) and examined the standard deviation of oscillations obtained from these iterations.

This procedure was repeated during the states of combustion noise (CN) and thermoacoustic instability (TAI) for the bluff-body stabilized dump combustor. Our analysis revealed that the results reached convergence beyond  $N = 2 \times 10^3$  phase

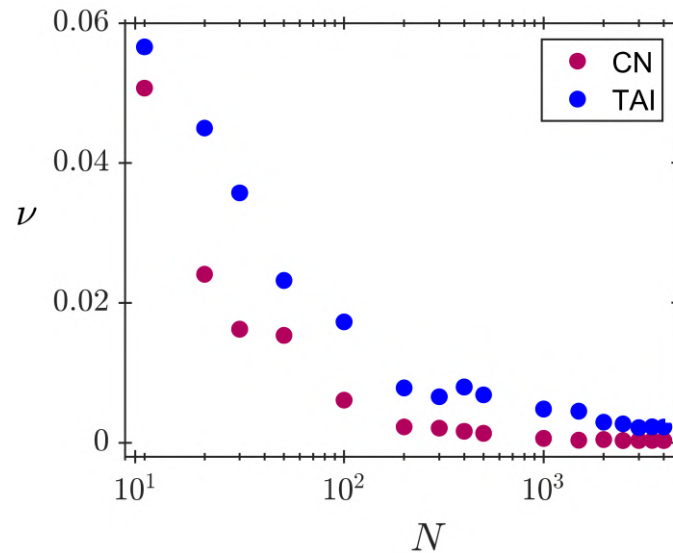


Figure C.1: Test for convergence of dynamics when the number of phase oscillators is varied. The standard deviation  $\nu$  is obtained from 20 simulations for each  $N$ .

oscillators. Consequently, we chose  $N = 2 \times 10^3$  for all simulations in our paper. It is crucial to note that our findings clearly demonstrate the dependence of results on the number of oscillators, as fewer oscillators would be insufficient to resolve the heat release rate spectrum  $[\hat{q}(f)]$  obtained from experiments.

## APPENDIX D

### PARAMETER OPTIMISATION WITH RANDOM INITIAL CONDITIONS

Parameter optimising is used to relate the control parameter in experiments with the model coupling strength. The initial conditions are included in the parameter optimisation to obtain a close match during the state of intermittency, which features periodic bursts randomly amidst aperiodic oscillations.

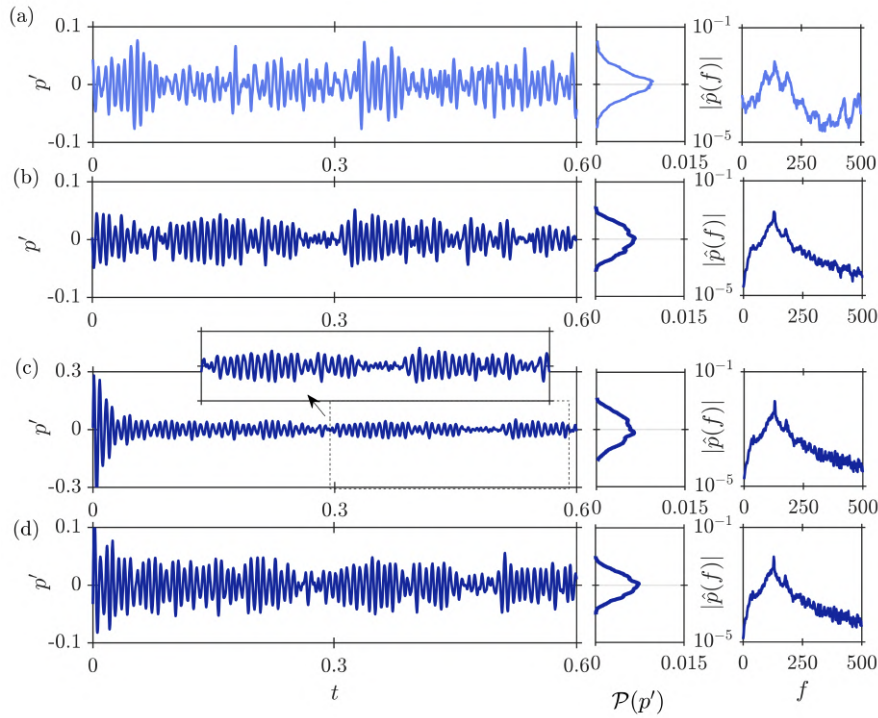


Figure D.1: Comparison of time series, probability density function, amplitude spectrum of  $p'$  obtained from model (b-d) with the experimental observations (a) during the state of intermittency in the bluff-body stabilized combustor. In the model, (b) is obtained by optimising the parameter vector ( $\mathbb{P}$ ), and (c-d) are obtained for randomly chosen initial conditions, with the optimised value of  $K$  and  $\zeta$  as 0.75 and 0.6, respectively. In (c), the initial conditions are  $\eta(0) = 0.22$ ,  $\dot{\eta}(0) = 0.09$  and  $\theta_l(0) = 0.5 + \mathcal{N}(0, 0.1)$  and in (d) the initial conditions are  $\eta(0) = 0.1$ ,  $\dot{\eta}(0) = 0.12$  and  $\theta_l(0) = 0.5 + \mathcal{N}(0, 0.1)$ .

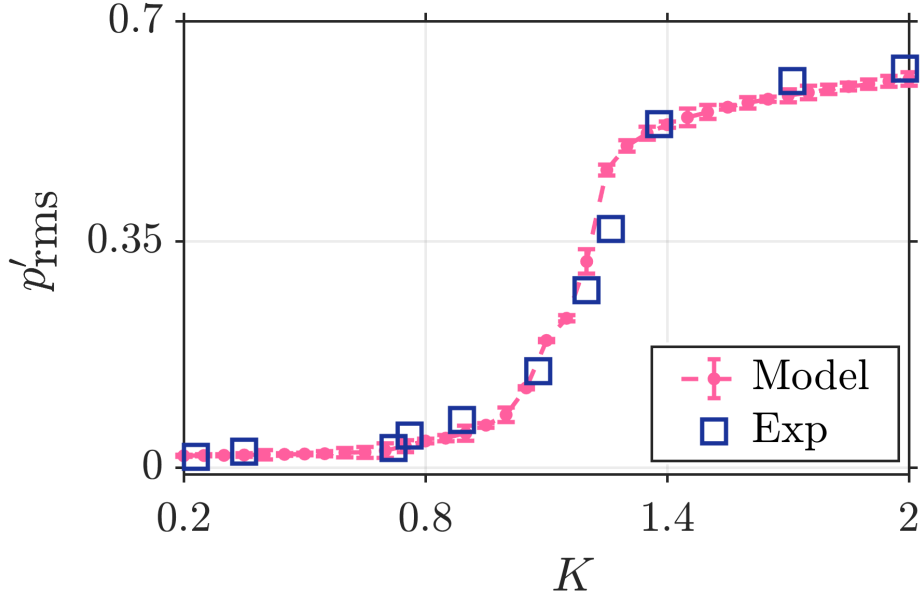


Figure D.2: The bifurcation plot illustrates the comparison of the amplitude of acoustic pressure obtained from the model and experiments as a function of the control parameter ( $K, \phi$ ). For each  $K$ , 10 iterations are performed with different sets of initial conditions. The evaluation indicates the initial conditions do not exert any influence on the dynamical states.

Consider the state of intermittency in the bluff-body stabilized combustor as shown in figure D.1(a). Figure D.1(b) shows the intermittency from the model when initial conditions are optimised. Figure D.1(c-d) shows the intermittency obtained from the model when random initial conditions are used. We notice that the probability density function (PDF) of the simulated states (b-d) matches with the PDF of the experimental state (a). However, the time series have noticeable differences in (c-d). While we notice the time series for the state where the initial conditions were optimised (b) matches much more closely to the experimentally observed state.

To investigate the impact of initial conditions on each state, we analyse the bifurcation plot obtained from the model without any optimisation and compare with the experimental results. To initiate the simulations, we randomly choose the initial conditions for  $\eta(0)$  and  $\dot{\eta}(0)$  from the uniform distribution. Similarly, the initial values of the phase oscillators ( $\theta_i(0)$ ) are chosen from a normal distribution with a standard deviation of 0.1. Figure

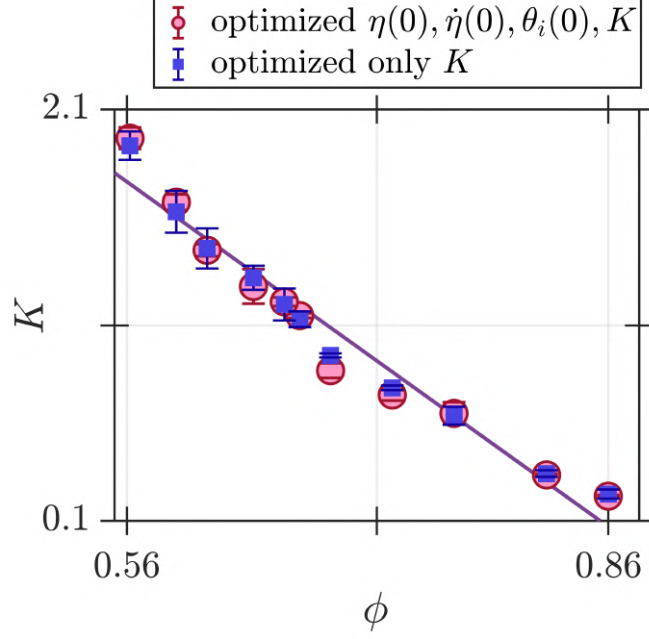


Figure D.3: Comparison of the  $K - \phi$  relationship obtained through the optimisation of only the coupling strength ( $K$ ) with the optimisation of both  $K$  and initial conditions ( $\eta(0), \dot{\eta}(0), \theta_i(0)$ ).

D.2 presents the relationship between the amplitude of acoustic pressure fluctuations and the coupling strength ( $K$ ). The coupling strength  $K$  is systematically varied from 0.2 to 2 in increments of 0.05, while  $\zeta$  is optimised during combustion noise and subsequently kept constant across all dynamical states. We perform 10 simulations with distinct sets of random initial conditions. The standard deviation of the amplitude of acoustic pressure at each  $K$  value is then employed to derive the error bar. Remarkably, the error bars observed are nearly negligible, indicating that the dynamics states remain largely unaffected by the initial conditions. Now, to map the bifurcation plot obtained from the experiments onto the bifurcation plot obtained from the model, we utilize the ( $K - \phi$ ) relationship depicted in Figure D.3. We notice a good match between the modeling and experimental results, without any estimation of parameters.

Further, to understand if the optimisation of the initial conditions affects the relationship between  $K$  and  $\phi$ , we consider random initial conditions ( $\eta(0), \dot{\eta}(0), \theta_i(0)$ ). The control parameter  $K$  is plotted as a function of  $\phi$  in figure D.3 and compared with the results

presented in figure 4.6(a) for the bluff-body stabilized combustor case. We notice that the relationship between  $K$  and  $\phi$  remains almost linear and does not differ from the case where the initial conditions are optimised. It is worth reiterating that the exact relationship between  $K$  and  $\phi$  is relatively unimportant, so long as the interpretation is consistent: A change in the control parameter (in this case  $\phi$ ) leading to thermoacoustic instability is always associated with an increase in the coupling strength and, hence, the synchronization of pressure and heat release rate oscillations. We have found the interpretation to be consistent across four different combustor configurations, three of which are presented in figure 4.6 and one case related to the control of instability is presented in figure 6.8.

## APPENDIX E

### SENSITIVITY ANALYSIS OF PARAMETER ESTIMATION

#### E.1 PARAMETER SENSITIVITY DURING THE TRANSITION TO THERMOACOUSTIC INSTABILITY

Estimating the parameter  $\mathbb{P}$  by minimizing the error in  $\mathbf{X}_m$  and  $\mathbf{X}_{exp}$  is numerically expensive. So, only a portion ( $t_w$ ) of the entire time series  $\mathbf{X}_{exp}$  is used for parameter optimisation. To ensure convergence in the estimate of the model parameter, we vary the length of the time series  $t_w$  used for optimisation. For each window size, the optimisation is performed for 1000 iterations to determine the value of  $K$ . Then the window is moved across the entire length of the time series to obtain a distribution of  $K$ . The standard deviation of this distribution is then used to obtain the error bar.

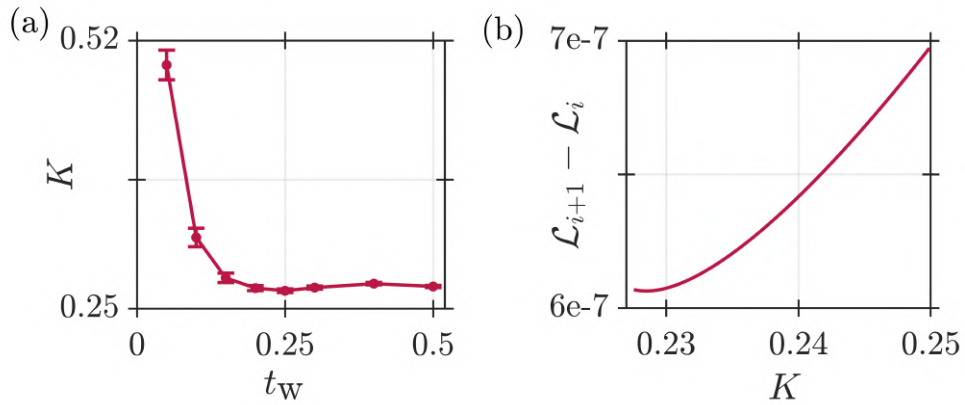


Figure E.1: Convergence of parameter optimisation algorithm. Panel (a) shows the variation in the estimated coupling strength ( $K$ ) as a function of the size of the time window ( $t_w$ ) used for optimising the loss function  $\mathcal{L}(\mathbb{P})$  for a fixed number of 1000 iterations. (b) Realisation of the minimisation scheme showing a change in the difference  $\mathcal{L}_{i+1} - \mathcal{L}_i$  when the optimisation is performed with an initial value of  $K = 0.25$  over 1000 iterations during the state of combustion noise in bluff-body stabilized combustor.

Figure E.1(a) shows the convergence of the model control parameter ( $K$ ) as a function of the time window ( $t_w$ ) used for performing optimisation according to Eq. (4.36). We find that the error in estimation  $K$  is quite low. We notice that the value of  $K$  reaches a constant value after a window of size  $t_w \approx 0.25$  s. Thus, we use  $t_w = 0.5$  s for optimising parameter across all data-sets.

Figure E.1(b) shows a typical realisation of an optimisation performed with the initial guess of  $K = 0.25$  and time window of size  $t_w = 0.4$  s. The minimisation is performed over 1000 iterations. The plot shows the manner in which  $\mathcal{L}_{i+1} - \mathcal{L}_i$  reduces with an increasing number of iterations. The difference in the value of the loss function is of the order of  $10^{-7}$ . The optimised value of  $K$  corresponds to a minima in  $\mathcal{L}_{i+1} - \mathcal{L}_i$ .

## E.2 PARAMETER SENSITIVITY DURING THE TRANSITION TO SUPPRESSION STATE

In order to estimate the model parameters and the initial condition, expressed as  $\mathcal{P}$ , we minimize the error between  $\mathbf{Y}_{\text{model}}$  and  $\mathbf{Y}_{\text{exp}}$ . We take the portion of the time series of

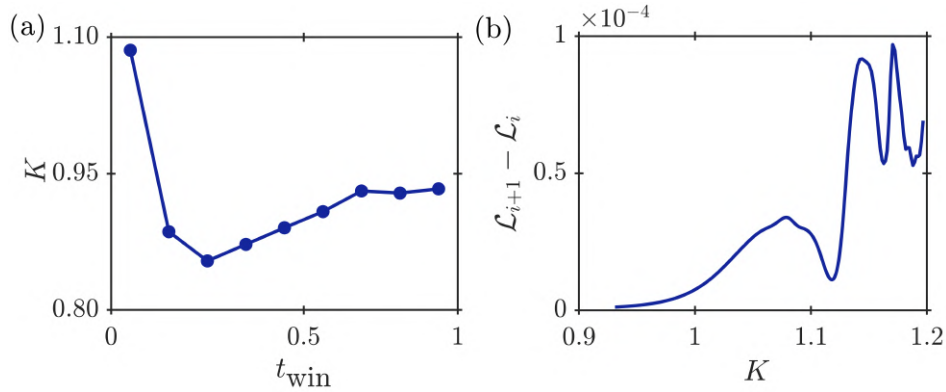


Figure E.2: Panel (a) depicts the convergence of the coupling strength ( $K$ ) as a function of the time window width ( $t_{\text{win}}$ ) of the time series of  $\mathbf{Y}_{\text{model}}$  and  $\mathbf{Y}_{\text{exp}}$  over 500 iterations using the parameter optimization algorithm. The initial value of  $K$  used is 1.2 and  $t_{\text{win}}$  is varied from 0.05 to 1 s. Panel (b) shows optimization of  $K$  by minimizing the loss function ( $\mathcal{L}_i$ ) over 500 iterations by taking difference between  $\mathcal{L}_{i+1}$  and  $\mathcal{L}_i$ . The sensitivity analysis on parameter estimation shown here is carried out during the state of suppression.

both  $\mathbf{Y}_{\text{model}}$  and  $\mathbf{Y}_{\text{exp}}$  for estimating  $\mathcal{P}$ . We first find out what portion of the time series of  $\mathbf{Y}_{\text{model}}$  and  $\mathbf{Y}_{\text{exp}}$  is enough for convergence of the model parameters. The window width of the time series  $t_{\text{win}}$  is varied from 0.05 to 1 s for obtaining  $\mathcal{P}$  over 500 iterations. In figure E.2(a), we show only the convergence of the coupling strength ( $K$ ) as a function of  $t_{\text{win}}$  during the suppression state. We observe that the value of  $K$  remains constant after  $t_{\text{win}} = 0.6$  s. Thus, we use  $t_{\text{win}} = 0.7$  s for estimating parameters across all the datasets.

The width of the time window is then fixed, and the window is moved across the entire time series of  $\mathbf{Y}_{\text{model}}$  and  $\mathbf{Y}_{\text{exp}}$  to determine the range of  $K$  variation at each dynamical state. Figure E.2(b) shows the realization of a minimization scheme used to obtain optimized  $K$ . The plot shows the reduction of the difference in  $\mathcal{L}_{i+1}$  and  $\mathcal{L}_i$  with change in iterations started with an initial guess of  $K = 1.2$ . Hence, the estimated parameter used in the model are properly optimized and verified using the above technique.



## APPENDIX F

### IDENTIFYING THE TYPE OF INTERMITTENCY IN OUR COMBUSTORS

In our investigation into the type of intermittency within our combustion systems, we adopted the methodology outlined by Pawar *et al.* (2016) for analysis of intermittency. Figure F.1 depicts regions of low-amplitude aperiodic behavior interspersed between consecutive periodic bursts, termed turbulent phases, alongside regions of high-amplitude periodic oscillations referred to as laminar phases. To characterize the type of intermittency observed, we ascertain the length of the turbulent phases ( $T$ ) in the acoustic pressure signal.

We employed a method proposed by Hammer *et al.* (1994) to calculate the length of the turbulent phase ( $T$ ). This method utilizes an amplitude threshold expressed as a fraction of the maximum pressure, where the threshold is defined as  $\max(P)/(2^n)$  and  $P$  represents the maximum amplitude of the acoustic pressure signal with  $n$  ranging between 1 and 6. Here, we present results corresponding to  $n = 2$ , equating to a normalized acoustic pressure amplitude threshold of 0.25.

The duration within the acoustic pressure signal, characterized by an amplitude below the selected threshold (i.e., the signal length between consecutive bursts), defines the length of the turbulent phase, as shown in figure F.1. The turbulent phase initiates when the last waveform of the periodic burst falls below the threshold and terminates when the first waveform of the subsequent burst surpasses the threshold. These turbulent lengths are aggregated into bins to calculate their probability distribution using a histogram during the state of intermittency. In figure F.2(a), we observe an exponential decrease in the probability distribution of the turbulent phase length, consistent with the findings

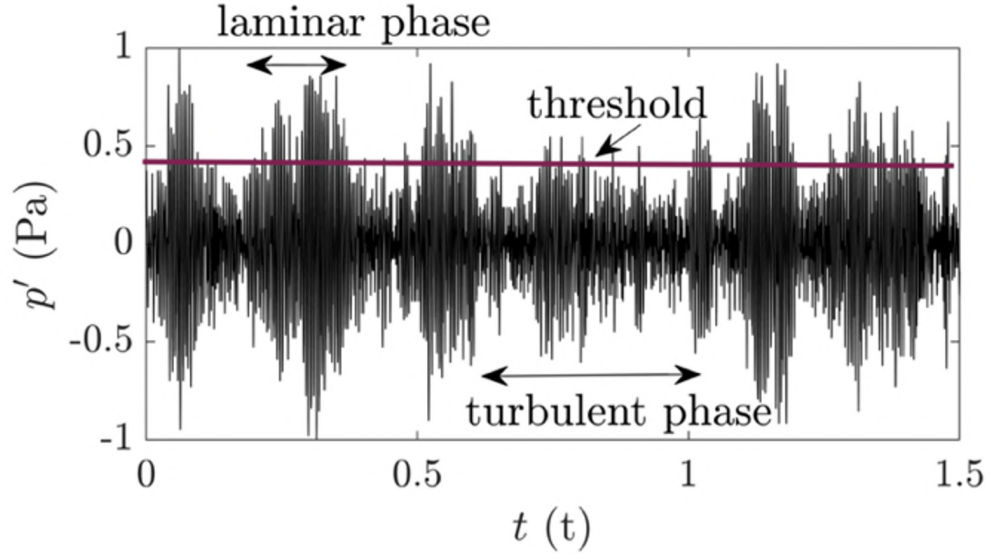


Figure F.1: Illustration of the acoustic pressure signal during the state of intermittency consisting of low-amplitude aperiodic fluctuations (turbulent phases) interspersed between high-amplitude periodic oscillations (laminar phases). A threshold marks the delineation between the two phases, distinguishing high-amplitude periodic oscillations from low-amplitude aperiodic fluctuations.

of Pawar *et al.* (2016). Figures F.2(b) and (c) depict a similar exponential decrease in the probability distribution of  $T$  observed in experiments and the mean-field model corresponding to bluff-body stabilized combustors and annular combustors, respectively. These distributions align with type-II intermittency behavior, where  $P \sim T^{-1}$  (Pawar *et al.*, 2016), thus confirming the presence of type-II intermittency in our combustion systems.

To further validate the efficacy of our model in capturing the specific type of intermittency, we examine the power-law scaling of the probability of turbulent time scales as a function of the control parameter. Figure F.3 illustrates the relationship between the average length of turbulent phases and the normalized control parameter. Precisely, figure F.3(a) corresponds to the findings discussed by Pawar *et al.* (2016), while figures F.3(b,c) depict the scaling law observed from experiments and the mean-field model corresponding to the bluff-body stabilized combustor, respectively. Given the apparently random appearance

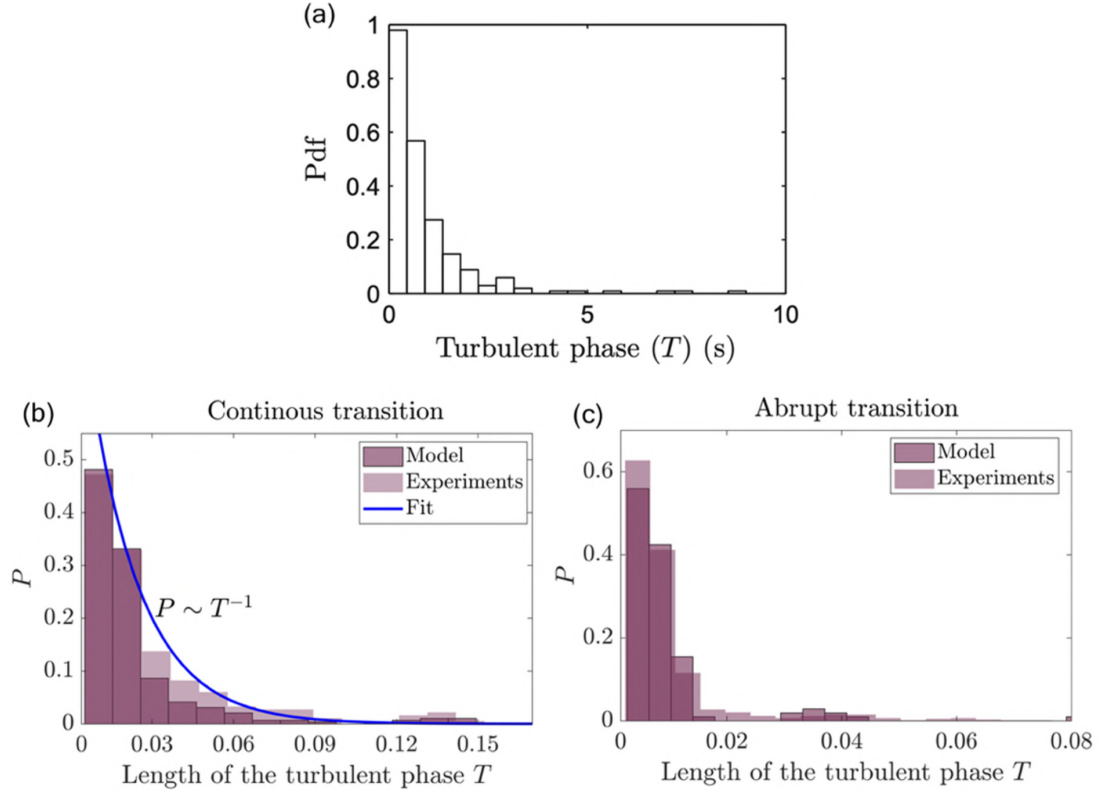


Figure F.2: Probability distribution of the length of turbulent phases observed in (a) Pawar *et al.* (2016), (b) experiments and mean-field model corresponding to the bluff-body stabilized combustor, and (c) experiments and mean-field model corresponding to the annular combustor. The distributions exhibit an exponential tail characteristic of type-II intermittency.

of bursts during intermittency, we utilize the average length of turbulent phases ( $\langle T \rangle$ ) as a representative measure of the total turbulent phase durations within the corresponding pressure signal. The plot of the mean duration of turbulent phases against the control parameter on a log-log scale reveals a power-law behavior. The variation of  $\langle T \rangle$  as a function of a control parameter in the experiments ( $\phi$ ) and model ( $K$ ) exhibits a linear relationship with slopes of -1.14 and -1.01, respectively. These values closely approximate the theoretical prediction for type-II intermittency, i.e.,  $\langle T \rangle \sim K \wedge (-1)$  (Pawar *et al.*, 2016; Pomeau and Manneville, 1980). Discrepancies between the theoretical slope (-1), and the experimental (-1.14) and model (-1.01) slopes may arise from factors such as the finite length of experimental signals, inherent noise in experiments and measurements, and challenges associated with accurately detecting the lengths of turbulent phases.

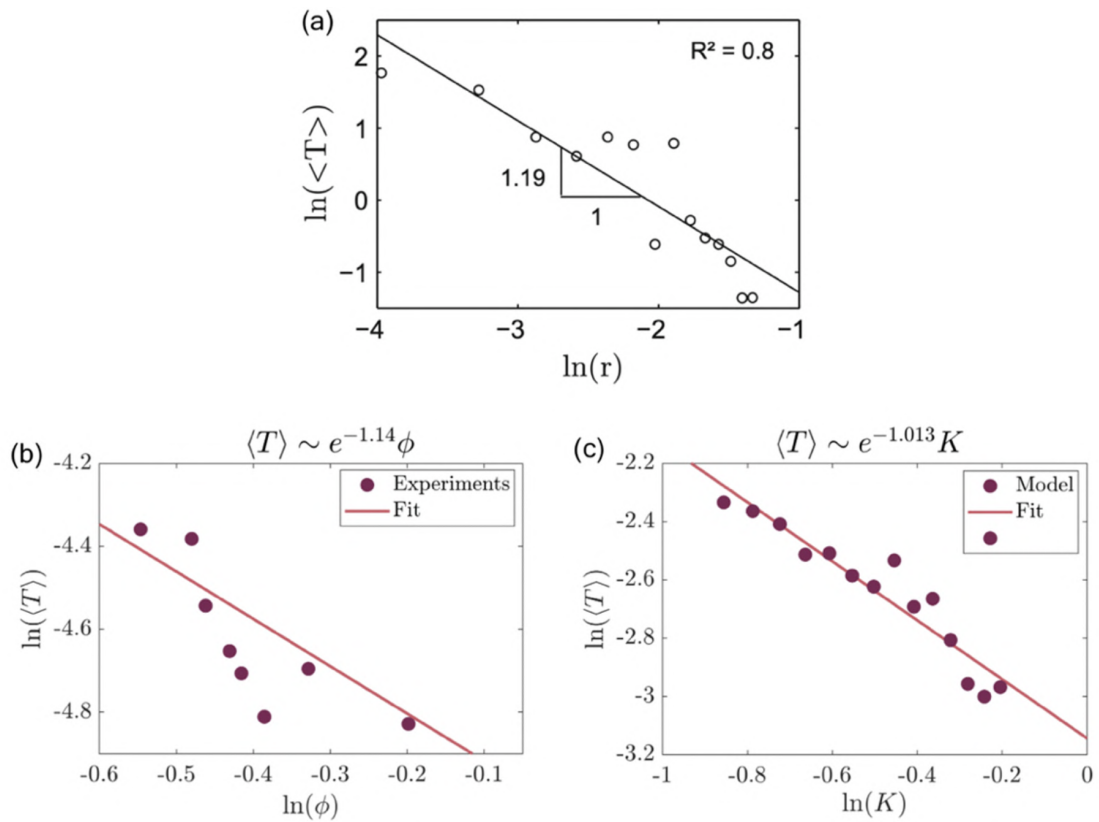


Figure F.3: A log–log plot of the average length of turbulent phases ( $\langle T \rangle$ ) plotted against the control parameter, demonstrating the scaling law behavior characteristic of type-II intermittency in (a) Pawar *et al.* (2016), and (b) experimental data (bluff-body stabilized combustor) and (c) model simulations.

## APPENDIX G

### MEAN-FIELD SYNCHRONIZATION MODEL WITH STOCHASTIC FORCING

The mean-field synchronization model, in its current form, does not explicitly account for the effects of turbulence. One way to do this would be to incorporate a stochastic term into the second order acoustic equation, which could simulate the effect of turbulent fluctuations on the acoustic pressure and heat release rate signal.

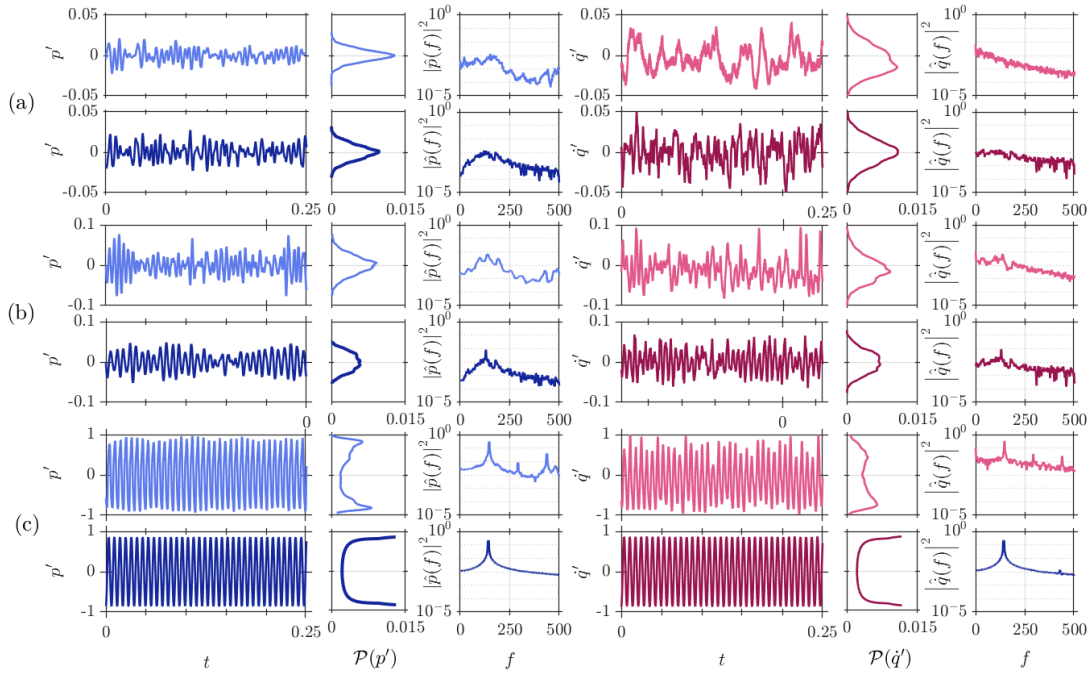


Figure G.1: Comparison of time series, probability distribution function and amplitude spectrum of  $p'$  and  $q'$  obtained from model with stochastic noise term with the experimental observations. The comparison is shown during the states of (a) combustion noise ( $K \approx 0.21$ ), (b) intermittency ( $K \approx 0.73$ ), and (c) thermoacoustic instability ( $K \approx 1.94$ ). The value of damping coefficient ( $\zeta$ ) is 0.6 obtained using parameter optimisation during combustion noise and the initial conditions ( $\eta(0)$ ,  $\dot{\eta}(0)$ ,  $\theta_i(0)$ ) are chosen randomly and noise intensity as 0.1.

Following Bonciolini *et al.* (Bonciolini *et al.*, 2021), we define a stochastically forced mean-field model as:

$$\ddot{\hat{\eta}}(t) + \zeta \dot{\hat{\eta}}(t) + \hat{\eta}(t) = \frac{\zeta}{N} \sum_{l=1}^N \sin[t + \theta_l(t)] + \xi(t), \quad (\text{G.1a})$$

$$\dot{\theta}(t) = \omega_l + K \hat{R}(t) \sin[\Phi(t) - \theta_l(t)]. \quad (\text{G.1b})$$

Here,  $\xi(t)$  is the Gaussian noise and is characterized by  $\langle \xi(t) \rangle = 0$  and  $\langle \xi(t) \xi(t') \rangle = 2D\delta(t - t')$  with  $D'$  being the noise strength. We run the simulation with modified Eq.(G.1) at  $D' = 0.1$  and present the results for three representative states observed in the bluff-body stabilized dump combustor. We notice asymmetry in the time series of the heat release rate fluctuations in figure G.1. As seen above, we can possibly improve the statistics of heat release rate fluctuations by including stochastic forcing. However, as a first-of-a-kind model, we would like to limit our present discussions to the aspects of bifurcation and the underlying synchronization. We aim to pursue this topic in the future more quantitatively by considering the effect of stochastic forcing on the results.

## APPENDIX H

### EXTRACTING ORDER PARAMETER FROM SPATIOTEMPORAL EXPERIMENTAL DATA

To reduce the noise and improve the quality of the signal, We first use a two-dimensional spatial median filter with a window of size  $3 \times 3$  pixels. The filtering operation sorts the pixels in the given window, determines the median value, and replaces the pixel in the middle of the given window with this median value (Khoukhi *et al.*, 2020). The median filter denoises the data and improves the signal quality. We then coarse-grain the chemiluminescence images over  $8 \times 8$  and  $6 \times 6$  pixels for the bluff-body stabilized combustor and annular combustor. This step helps reduce the noise further and significantly reduces the computation effort.

Now, to extract the order parameter from a spatiotemporal data, we normalize the time series of  $\dot{q}'(x, y, t)$  during various states of operation by the amplitude  $\dot{q}'$  during limit cycle oscillations. The resulting signal at each coarse-grained location depicts a transition from a low amplitude chaotic state to limit cycle oscillations of amplitude when the control parameter is varied.

Popovych *et al.* (2005) and Bick *et al.* (2011) showed that the collective behavior of oscillators with distributed frequencies yields chaotic behavior. Following the same approach, we assume that the heat release rate fluctuations measured at each coarse-grained location are a result of a set of limit-cycle oscillators. In other words, we assume that  $k^{\text{th}}$  pixel comprises  $n_k$  number of limit cycle oscillators. To simplify calculations, we assume that  $n_k = n$  for all the pixels. Let the phase for  $j^{\text{th}}$  oscillator at  $k^{\text{th}}$  pixel is  $\varphi_{kj}$ , where  $j = 1, \dots, n$ . Therefore, the complex order parameter for  $k^{\text{th}}$  pixel is expressed as:  $r_k e^{i\theta_k} = 1/n \sum_{j=1}^n e^{i\varphi_{kj}}$  (Strogatz, 2000), where  $r_k(t)$  and  $\psi_k(t)$  can be simply obtained

from the absolute value and argument of the Hilbert transform of  $\dot{q}'_k(t)$ . Here, we define  $\varphi_{kj}$  as the phase of  $j^{\text{th}}$  oscillator in the  $k^{\text{th}}$  pixel of the image and  $\psi_k$  is the mean-phase of the image. We obtained the  $\psi_k$  by considering each imaged has  $N_p$  number of pixels and each pixel is made of  $n$  oscillators. Consequently, the order parameter can be defined as:

$$\bar{r}e^{i\langle\theta\rangle} = \left\langle \frac{1}{N_p} \sum_{k=1}^{N_p} r_k e^{i\psi_k} \right\rangle_t, \quad (\text{H.1})$$

where successive averaging operations were taken over  $N_p$  in each image and the total number of chemiluminescence images in the time series. The value of  $\bar{r}$  so determined is then used in figures 4.8(a,b) and 6.9.

# APPENDIX I

## ESTIMATED MODEL PARAMETERS FROM EXPERIMENTS

### I.1 ESTIMATED PARAMETER VALUES DURING THERMOACOUSTIC TRANSITION

The estimated model parameters are shown in the tables I.1, I.2 and I.3 corresponding to the bluff-body stabilized, swirl-stabilized, and annular combustor, respectively. The damping coefficient ( $\zeta$ ) is obtained using parameter optimisation Eq. (4.36) and is subsequently fixed for determining other states during the transition. The value of  $\zeta$  during the state of combustion noise is obtained as 0.6, 0.4, and 0.3 for the bluff-body stabilized, swirl-stabilized, and annular combustor, respectively.

Table I.1: Parameter estimated for states observed in the bluff-body combustor and marked as b-d in figure 4.3.

States	$K$	$\eta(0)$	$\dot{\eta}(0)$	$\theta_m$	$\sigma$	$L$
Combustion noise	0.230	0.011	0.001	0.499	0.100	0.004
Intermittency	0.752	0.015	0.009	0.497	0.101	0.009
LCO	1.997	0.009	0.007	0.499	0.100	0.900

Table I.2: Parameter estimated for states observed in the swirl-stabilized combustor.

States	$K$	$\eta(0)$	$\dot{\eta}(0)$	$\theta_m$	$\sigma$	$L$
Combustion noise	0.506	0.108	-0.003	0.368	0.150	0.005
Intermittency	0.920	0.098	-0.009	0.366	0.130	0.055
Low-amplitude LCO	1.240	-0.040	-0.030	0.500	0.098	0.130
High-amplitude LCO	1.542	-0.116	0.180	1.390	0.094	1.100

Table I.3: Parameter estimated for different states observed in the annular combustor and marked as a-d in figure 4.5.

States	$K$	$\eta(0)$	$\dot{\eta}(0)$	$\theta_m$	$\sigma$	$L$
Combustion noise	1.091	0.085	-0.015	0.428	0.121	0.003
Intermittency	1.367	0.036	-0.001	0.494	0.101	0.005
Low-amplitude LCO	1.550	0.022	0.009	0.498	0.101	0.040
High-amplitude LCO	1.710	-0.258	0.689	0.199	0.102	0.319

## I.2 ESTIMATED PARAMETER VALUES DURING THE TRANSITION TO SUPPRESSION STATE

The estimated model parameters during thermoacoustic instability, intermittency and suppression state are shown in table I.4. The damping coefficient ( $\zeta$ ) is obtained by the gradient descent method during the state of suppression and has a value of 0.27.

Table I.4: Estimated parameter values in the rotating swirler combustor for different states marked as a-c in figure 6.5.

States	$K$	$\eta(0)$	$\dot{\eta}(0)$	$\theta_m$	$\sigma$	$L$
LCO	2.88	0.36	-0.18	0.54	0.11	1.15
Intermittency	1.14	0.05	-0.01	0.49	0.10	0.05
Suppression state	0.95	0.02	-0.03	0.49	0.10	0.01

## REFERENCES

1. **Abrams, D. M.** and **S. H. Strogatz** (2004). Chimera states for coupled oscillators. *Phys. Rev. Appl.*, **93**(17), 174102.
2. **Agharkar, P., P. Subramanian, N. Kaisare,** and **R. I. Sujith** (2013). Thermoacoustic instabilities in a ducted premixed flame: reduced-order models and control. *Combust. Sci. Technol.*, **185**(6), 920–942.
3. **Ahn, B., T. Indlekofer, J. R. Dawson,** and **N. A. Worth** (2022). Heat release rate response of azimuthal thermoacoustic instabilities in a pressurized annular combustor with methane/hydrogen flames. *Combust. Flame*, **244**, 112274.
4. **Altay, H. M., D. E. Hudgins, R. L. Speth, A. M. Annaswamy,** and **A. F. Ghoniem** (2010). Mitigation of thermoacoustic instability utilizing steady air injection near the flame anchoring zone. *Combust. Flame*, **157**(4), 686–700.
5. **Ananthkrishnan, N., S. Deo,** and **F. E. Culick** (2005). Reduced-order modeling and dynamics of nonlinear acoustic waves in a combustion chamber. *Combustion Science and Technology*, **177**(2), 221–248.
6. **Ananthkrishnan, N.** and **K. Sudhakar** (1996). Characterization of periodic motions in aircraft lateral dynamics. *J. Guid. Control Dyn.*, **19**(3), 680–685.
7. **Ananthkrishnan, N., K. Sudhakar, S. Sudershan,** and **A. Agarwal** (1998). Application of secondary bifurcations to large-amplitude limit cycles in mechanical systems. *J. Sound Vib.*, **215**(1), 183–188.
8. **Ariatabar, B., R. Koch, H.-J. Bauer,** and **D.-A. Negulescu** (2016). Short helical combustor: Concept study of an innovative gas turbine combustor with angular air supply. *J. Eng. Gas Turbines Power*, **138**(3), 031503.
9. **Baba, K., S. Kishiya, H. Gotoda, T. Shoji,** and **S. Yoshida** (2023). Early detection of thermoacoustic instability in a staged single-sector combustor for aircraft engines using symbolic dynamics-based approach. *Chaos*, **33**(7).
10. **Baillet, F., D. Durox,** and **R. Prud’Homme** (1992). Experimental and theoretical study of a premixed vibrating flame. *Combust. Flame*, **88**(2), 149–168.
11. **Balachandran, R., B. Ayoola, C. Kaminski, A. Dowling,** and **E. Mastorakos** (2005). Experimental investigation of the nonlinear response of turbulent premixed flames to imposed inlet velocity oscillations. *Combust. Flame*, **143**(1-2), 37–55.
12. **Balanov, A., N. Janson, D. Postnov,** and **O. Sosnovtseva**, *Synchronization: From Simple to Complex*. Springer Science & Business Media, 2008.

13. **Balasubramanian, K. and R. I. Sujith** (2008). Thermoacoustic instability in a Rijke tube: Non-normality and nonlinearity. *Physics of Fluids*, **20**(4), 044103.
14. **Balusamy, S., L. K. Li, Z. Han, M. P. Juniper, and S. Hochgreb** (2015). Nonlinear dynamics of a self-excited thermoacoustic system subjected to acoustic forcing. *Proc. Combust. Inst.*, **35**(3), 3229–3236.
15. **Bandt, C. and B. Pompe** (2002). Permutation entropy: a natural complexity measure for time series. *Phys. Rev. Lett.*, **88**(17), 174102.
16. **Basnarkov, L. and V. Urumov** (2007). Phase transitions in the Kuramoto model. *Phys. Rev. E*, **76**(5), 057201.
17. **Bauerheim, M., M. Cazalens, and T. Poinsot** (2015). A theoretical study of mean azimuthal flow and asymmetry effects on thermo-acoustic modes in annular combustors. *Proc. Combust. Inst.*, **35**(3), 3219–3227.
18. **Baydin, A. G., B. Pearlmutter, A. A. Radul, and J. M. Siskind** (2018). Automatic differentiation in machine learning: a survey. *J. Mach. Learn. Res.*, **18**.
19. **Bellows, B. D., A. Hreiz, and T. Liewen** (2008). Nonlinear interactions between forced and self-excited acoustic oscillations in premixed combustor. *J. Propuls. Power*, **24**(3), 628–631.
20. **Bellows, B. D., Y. Neumeier, and T. Liewen** (2006). Forced response of a swirling, premixed flame to flow disturbances. *J. Propuls. Power*, **22**(5), 1075–1084.
21. **Bhavi, R. S., I. Pavithran, A. Roy, and R. I. Sujith** (2023). Abrupt transitions in turbulent thermoacoustic systems. *J. Sound Vib.*, **547**, 117478.
22. **Bick, C., D. Timme, M. Paulikat, D. Rathlev, and P. Ashwin** (2011). Chaos in symmetric phase oscillator networks. *Phys. Rev. Lett.*, **107**(24), 244101.
23. **Bonciolini, G., E. Boujo, and N. Noiray** (2017). Output-only parameter identification of a colored-noise-driven Van-der-Pol oscillator: thermoacoustic instabilities as an example. *Phys. Rev. E*, **95**(6), 062217.
24. **Bonciolini, G., D. Ebi, U. Doll, M. Weilenmann, and N. Noiray** (2019). Effect of wall thermal inertia upon transient thermoacoustic dynamics of a swirl-stabilized flame. *Proc. Combust. Inst.*, **37**(4), 5351–5358.
25. **Bonciolini, G., A. Faure-Beaulieu, C. Bourquard, and N. Noiray** (2021). Low order modelling of thermoacoustic instabilities and intermittency: Flame response delay and nonlinearity. *Combust. Flame*, **226**, 396–411.
26. **Bourgouin, J.-F., D. Durox, J. Moeck, T. Schuller, and S. Candel** (2015). A new pattern of instability observed in an annular combustor: The slanted mode. *Proc. Combust. Inst.*,

- 35(3), 3237–3244.
27. **Bourgouin, J.-F., D. Durox, J. P. Moeck, T. Schuller, and S. Candel**, Self-sustained instabilities in an annular combustor coupled by azimuthal and longitudinal acoustic modes. *In Turbo Expo: Power for Land, Sea, and Air*, volume 55119. American Society of Mechanical Engineers, 2013.
  28. **Boyd, S., S. P. Boyd, and L. Vandenberghe**, *Convex optimization*. Cambridge university press, New York, 2004.
  29. **Cai, J., F. Ichihashi, B. Mohammad, S. Tambe, Y.-H. Kao, and S.-M. Jeng**, Gas turbine single annular combustor sector: Combustion dynamics. *In 48th AIAA Aerospace Sciences Meeting Including the New Horizons Forum and Aerospace Exposition*. 2010.
  30. **Călugăru, D., J. F. Tetz, E. A. Martens, and H. Engel** (2020). First-order synchronization transition in a large population of strongly coupled relaxation oscillators. *Sci. Adv.*, **6**(39), eabb2637.
  31. **Campa, G. and M. P. Juniper**, Obtaining bifurcation diagrams with a thermoacoustic network model. *In ASME Turbo Expo 2012*. ASME, 2012.
  32. **Candel, S.** (2002). Combustion dynamics and control: progress and challenges. *Proc. Combust. Inst.*, **29**(1), 1–28.
  33. **Candel, S., D. Durox, T. Schuller, J.-F. Bourgouin, and J. P. Moeck** (2014). Dynamics of swirling flames. *Annu. Rev. Fluid Mech.*, **46**, 147–173.
  34. **Candel, S. M., D. Durox, S. Ducruix, A. L. Birbaud, N. Noiray, and T. Schuller** (2009). Flame dynamics and combustion noise: progress and challenges. *Int. J. Aeroacoustics*, **8**(1), 1–56.
  35. **Chu, B. T.** (1965). On the energy transfer to small disturbances in fluid flow (Part I). *Acta Mech.*, **1**(3), 215–234.
  36. **Coats, C. M.** (1996). Coherent structures in combustion. *Prog. Energy Combust. Sci.*, **22**(5), 427–509.
  37. **Ćosić, B., B. C. Bobusch, J. P. Moeck, and C. O. Paschereit** (2012). Open-Loop Control of Combustion Instabilities and the Role of the Flame Response to Two-Frequency Forcing. *J. Eng. Gas Turbines Power*, **134**(6).
  38. **Crocco, L. and S.-I. Cheng** (1956). Theory of combustion instability in liquid propellant rocket motors. Technical report, Princeton University.
  39. **Culick, F.** (1994). Some recent results for nonlinear acoustics in combustion chambers. *AIAA journal*, **32**(1), 146–169.

40. **Culick, F.** and **P. Kuentzmann** (2006). Unsteady motions in combustion chambers for propulsion systems. Technical report, NATO Research and Technology Organization Neuilly-Sur-Seine (France).
41. **Culick, F. E.** (1988). Combustion instabilities in liquid-fuelled propulsion systems. *Tech. Rep.*, 430.
42. **Dawson, J. R.** and **N. A. Worth** (2014). Flame dynamics and unsteady heat release rate of self-excited azimuthal modes in an annular combustor. *Combust. Flame*, **161**(10), 2565–2578.
43. **de Oliveira, J. F.** and **C. V. Abud** (2020). Nonmonotonic critical threshold in the Kuramoto model. *Commun. Nonlinear Sci. Numer. Simul.*, **91**, 105428.
44. **Desroches, M., J. Guckenheimer, B. Krauskopf, C. Kuehn, H. M. Osinga,** and **M. Wechselberger** (2012). Mixed-mode oscillations with multiple time scales. *Siam Review*, **54**(2), 211–288.
45. **Docquier, N.** and **S. Candel** (2002). Combustion control and sensors: a review. *Prog. Energy Combust. Sci.*, **28**(2), 107–150.
46. **Dowling, A. P.** (1995). The calculation of thermoacoustic oscillations. *J. Sound Vib.*, **180**(4), 557–581.
47. **Dowling, A. P.** (1997). Nonlinear self-excited oscillations of a ducted flame. *J. Fluid Mech.*, **346**, 271–290.
48. **Dowling, A. P.** and **Y. Mahmoudi** (2015). Combustion noise. *Proceedings of the Combustion Institute*, **35**(1), 65–100.
49. **Dowling, A. P.** and **S. R. Stow** (2003). Acoustic analysis of gas turbine combustors. *J. Propuls. Power*, **19**(5), 751–764.
50. **Duperé, I. D.** and **A. P. Dowling** (2005). The Use of Helmholtz Resonators in a Practical Combustor. *J. Eng. Gas Turbines Power*, **127**(2), 268–275.
51. **Dutta, A. K., G. Ramachandran,** and **S. Chaudhuri** (2019). Investigating thermoacoustic instability mitigation dynamics with a kuramoto model for flamelet oscillators. *Physical Review E*, **99**(3), 032215.
52. **Eckstein, J., E. Freitag, C. Hirsch,** and **T. Sattelmayer** (2006). Experimental study on the role of entropy waves in low-frequency oscillations in a RQL combustor. *J. Eng. Gas Turbines Power*, **128**(2), 264–270.
53. **Emerson, B.** and **T. Lieuwen** (2015). Dynamics of harmonically excited, reacting bluff body wakes near the global hydrodynamic stability boundary. *Journal of Fluid Mechanics*, **779**, 716–750.

54. **Emerson, B., J. O'Connor, M. Juniper, and T. Lieuwen** (2012). Density ratio effects on reacting bluff-body flow field characteristics. *J. Fluid Mech.*, **706**, 219–250.
55. **Etikyala, S. and R. I. Sujith** (2017). Change of criticality in a prototypical thermoacoustic system. *Chaos*, **27**(2), 023106.
56. **Fang, Y., Y. Yang, K. Hu, G. Wang, J. Li, and Y. Zheng** (2021). Experimental study on self-excited thermoacoustic instabilities and intermittent switching of azimuthal and longitudinal modes in an annular combustor. *Phys. Fluids*, **33**(8), 084104.
57. **Faure-Beaulieu, A., T. Indlekofer, J. R. Dawson, and N. Noiray** (2021a). Experiments and low-order modelling of intermittent transitions between clockwise and anticlockwise spinning thermoacoustic modes in annular combustors. *Proc. Combust. Inst.*, **38**(4), 5943–5951.
58. **Faure-Beaulieu, A., T. Indlekofer, J. R. Dawson, and N. Noiray** (2021b). Imperfect symmetry of real annular combustors: beating thermoacoustic modes and heteroclinic orbits. *J. Fluid Mech.*, **925**, R1.
59. **Gabor, D.** (1946). Theory of communication. part 1: The analysis of information. *J. Inst. Electr. Eng.*, **93**(26), 429–441.
60. **Gang, W., L. Zhengli, P. Weichen, G. Yiheng, and J. CZ** (2018). Numerical and experimental demonstration of actively passive mitigating self-sustained thermoacoustic oscillations. *Appl. Energy*, **222**, 257–266.
61. **George, N. B., V. R. Unni, M. Raghunathan, and R. I. Sujith** (2018). Pattern formation during transition from combustion noise to thermoacoustic instability via intermittency. *J. Fluid Mech.*, **849**, 615–644.
62. **Ghirardo, G. and M. R. Bothien** (2018). Quaternion structure of azimuthal instabilities. *Phys. Rev. Fluids*, **3**(11), 113202.
63. **Ghirardo, G. and F. Gant** (2021). Averaging of thermoacoustic azimuthal instabilities. *J. Sound Vib.*, **490**, 115732.
64. **Ghirardo, G., M. Juniper, and J. P. Moeck** (2016). Weakly nonlinear analysis of thermoacoustic instabilities in annular combustors. *J. Fluid Mech.*, **805**, 52–87.
65. **Ghirardo, G. and M. P. Juniper** (2013). Azimuthal instabilities in annular combustors: standing and spinning modes. *Proceedings of the Royal Society A: Mathematical, Physical and Engineering Sciences*, **469**(2157), 20130232.
66. **Ghirardo, G., H. T. Nygård, A. Cuquel, and N. A. Worth** (2021). Symmetry breaking modelling for azimuthal combustion dynamics. *Proc. Combust. Inst.*, **38**(4), 5953–5962.
67. **Goh, C. S. and A. S. Morgans** (2013). The influence of entropy waves on the

- thermoacoustic stability of a model combustor. *Combust. Sci. Technol.*, **185**(2), 249–268.
68. **Gopakumar, R., S. Mondal, R. Paul, S. Mahesh, and S. Chaudhuri** (2016). Mitigating instability by actuating the swirler in a combustor. *Combust. Flame*, **165**, 361–363.
  69. **Gopalakrishnan, E. and R. I. Sujith** (2015). Effect of external noise on the hysteresis characteristics of a thermoacoustic system. *J. Fluid Mech.*, **776**, 334–353.
  70. **Gotoda, H., M. Amano, T. Miyano, T. Ikawa, K. Maki, and S. Tachibana** (2012). Characterization of complexities in combustion instability in a lean premixed gas-turbine model combustor. *Chaos*, **22**(4).
  71. **Gotoda, H., K. Michigami, K. Ikeda, and T. Miyano** (2010). Chaotic oscillation in diffusion flame induced by radiative heat loss. *Combust. Theory Model.*, **14**(4), 479–493.
  72. **Gotoda, H., Y. Shinoda, M. Kobayashi, Y. Okuno, and S. Tachibana** (2014). Detection and control of combustion instability based on the concept of dynamical system theory. *Physical Review E*, **89**(2), 022910.
  73. **Guan, Y., V. Gupta, K. Kashinath, and L. K. Li** (2019a). Open-loop control of periodic thermoacoustic oscillations: experiments and low-order modelling in a synchronization framework. *Proc. Combust. Inst.*, **37**(4), 5315–5323.
  74. **Guan, Y., V. Gupta, and L. K. Li** (2020). Intermittency route to self-excited chaotic thermoacoustic oscillations. *J. Fluid Mech.*, **894**, R3.
  75. **Guan, Y., L. K. Li, B. Ahn, and K. T. Kim** (2019b). Chaos, synchronization, and desynchronization in a liquid-fueled diffusion-flame combustor with an intrinsic hydrodynamic mode. *Chaos*, **29**(5), 053124.
  76. **Hammer, P. W., N. Platt, S. M. Hammel, J. F. Heagy, and B. D. Lee** (1994). Experimental observation of on-off intermittency. *Phys. Rev. Lett.*, **73**(8), 1095.
  77. **Han, X., D. Laera, D. Yang, C. Zhang, J. Wang, X. Hui, Y. Lin, A. S. Morgans, and C.-J. Sung** (2020). Flame interactions in a stratified swirl burner: Flame stabilization, combustion instabilities and beating oscillations. *Combust. Flame*, **212**, 500–509.
  78. **Hashimoto, T., H. Shibuya, H. Gotoda, Y. Ohmichi, and S. Matsuyama** (2019). Spatiotemporal dynamics and early detection of thermoacoustic combustion instability in a model rocket combustor. *Phys. Rev. E*, **99**(3), 032208.
  79. **Hernandez-Rivera, R., G. Troiani, T. Pagliaroli, and A. Hernandez-Guerrero** (2019). Detection of the thermoacoustic combustion instabilities of a slot burner based on a diagonal-wise recurrence quantification. *Phys. Fluids*, **31**(12), 124105.
  80. **Hummel, T., F. Berger, M. Hertweck, B. Schuermans, and T. Sattelmayer** (2017). High-frequency thermoacoustic modulation mechanisms in swirl-stabilized gas turbine

combustors—part ii: Modeling and analysis. *J. Eng. Gas Turbine. Power*, **139**(7), 071502.

81. **Hummel, T., F. Berger, B. Schuermans, and T. Sattelmayer** (2016). Theory and modeling of non-degenerate transversal thermoacoustic limit cycle oscillations. *GTRE-038*.
82. **Indlekofer, T., A. Faure-Beaulieu, J. R. Dawson, and N. Noiray** (2021a). Dynamics of azimuthal thermoacoustic modes in imperfectly symmetric annular geometries. *arXiv preprint arXiv:2104.07380*.
83. **Indlekofer, T., A. Faure-Beaulieu, N. Noiray, and J. Dawson** (2021b). The effect of dynamic operating conditions on the thermoacoustic response of hydrogen rich flames in an annular combustor. *Combust. Flame*, **223**, 284–294.
84. **Juniper, M. P. and R. I. Sujith** (2018). Sensitivity and nonlinearity of thermoacoustic oscillations. *Annual Review of Fluid Mechanics*, **50**, 661–689.
85. **Kabiraj, L. and R. I. Sujith** (2012). Nonlinear self-excited thermoacoustic oscillations: intermittency and flame blowout. *J. Fluid Mech.*, **713**, 376–397.
86. **Kasthuri, P., V. R. Unni, and R. I. Sujith** (2019). Bursting and mixed mode oscillations during the transition to limit cycle oscillations in a matrix burner. *Chaos*, **29**(4), 043117.
87. **Kelley, A. P. and C. K. Law** (2009). Nonlinear effects in the extraction of laminar flame speeds from expanding spherical flames. *Combust. Flame*, **156**(9), 1844–1851.
88. **Kheirkhah, S., J. D. M. Cirtwill, P. Saini, K. Venkatesan, and A. M. Steinberg** (2017). Dynamics and mechanisms of pressure, heat release rate, and fuel spray coupling during intermittent thermoacoustic oscillations in a model aeronautical combustor at elevated pressure. *Combust. Flame*, **185**, 319–334.
89. **Khoukhi, H. E., F. M. Idriss, A. Yahyaouy, and M. A. Sabri**, An efficiency study of adaptive median filtering for image denoising, based on a hardware implementation. *In Embedded Systems and Artificial Intelligence: Proceedings of ESAI 2019, Fez, Morocco*. Springer, 2020.
90. **Kim, J., W. Gillman, T. John, S. Adhikari, D. Wu, B. Emerson, V. Acharya, T. Lieuwen, M. Isono, and T. Saitoh**, Experimental investigation of fuel staging effect on modal dynamics of thermoacoustic azimuthal instabilities in a multi-nozzle can combustor. *In Turbo Expo: Power for Land, Sea, and Air*, volume 84942. American Society of Mechanical Engineers, 2021a.
91. **Kim, J., M. Jang, K. Lee, and A. Masri** (2019). Experimental study of the beating behavior of thermoacoustic self-excited instabilities in dual swirl combustors. *Experimental Thermal and Fluid Science*, **105**, 1–10.

92. **Kim, J.-w., W. Gillman, B. Emerson, D. Wu, T. John, V. Acharya, M. Isono, T. Saitoh, and T. Lieuwen** (2021*b*). Modal dynamics of high-frequency transverse combustion instabilities. *Proc. Combust. Inst.*, **38**(4), 6155–6163.
93. **Kim, K. T., J. G. Lee, B. Quay, and D. Santavicca** (2010). Response of partially premixed flames to acoustic velocity and equivalence ratio perturbations. *Combust. Flame*, **157**(9), 1731–1744.
94. **Kim, M., G. A. Mashour, S. B. Moraes, G. Vanini, V. Tarnal, E. Janke, A. G. Hudetz, and U. Lee** (2016). Functional and topological conditions for explosive synchronization develop in human brain networks with the onset of anesthetic-induced unconsciousness. *Front. Comput. Neurosci.*, **10**, 1.
95. **Kobayashi, H., H. Gotoda, S. Tachibana, and S. Yoshida** (2017). Detection of frequency-mode-shift during thermoacoustic combustion oscillations in a staged aircraft engine model combustor. *J. Appl. Phys.*, **122**(22), 224904.
96. **Komarek, T. and W. Polifke** (2010). Impact of Swirl Fluctuations on the Flame Response of a Perfectly Premixed Swirl Burner. *J. Eng. Gas Turbines Power*, **132**(6).
97. **Krebs, W., P. Flohr, B. Prade, and S. Hoffmann** (2002). Thermoacoustic stability chart for high-intensity gas turbine combustion systems. *Combust. Sci. Technol.*, **174**(7), 99–128.
98. **Krishnan, A., R. Manikandan, P. R. Midhun, K. V. Reeja, V. R. Unni, R. I. Sujith, N. Marwan, and J. Kurths** (2019). Mitigation of oscillatory instability in turbulent reactive flows: A novel approach using complex networks. *EPL (Europhysics Letters)*, **128**(1), 14003.
99. **Krylov, N. M. and N. N. Bogolyubov**, *Introduction to nonlinear mechanics*. Princeton University Press, 1947.
100. **Kuehn, C.** (2011). A mathematical framework for critical transitions: Bifurcations, fast–slow systems and stochastic dynamics. *Phys. D: Nonlin. Phenomena*, **240**(12), 1020–1035.
101. **Kuehn, C. and C. Bick** (2021). A universal route to explosive phenomena. *Science Advances*, **7**(16), eabe3824.
102. **Kumar, P., D. K. Verma, P. Parmananda, and S. Boccaletti** (2015). Experimental evidence of explosive synchronization in mercury beating-heart oscillators. *Phys. Rev. E*, **91**(6), 062909.
103. **Kuramoto, Y.**, Self-entrainment of a population of coupled non-linear oscillators. *In International symposium on mathematical problems in theoretical physics. Lecture Notes in Physics*. Springer, 1975.

104. **Kuramoto, Y.**, *Chemical oscillations, waves, and turbulence*. Courier Corporation, 2003.
105. **Kuramoto, Y.** and **D. Battogtokh** (2002). Coexistence of coherence and incoherence in nonlocally coupled phase oscillators. *arXiv preprint cond-mat/0210694*.
106. **Laera, D., G. Campa,** and **S. Camporeale** (2017a). A finite element method for a weakly nonlinear dynamic analysis and bifurcation tracking of thermo-acoustic instability in longitudinal and annular combustors. *Appl. Energy*, **187**, 216–227.
107. **Laera, D., T. Schuller, K. Prieur, D. Durox, S. M. Camporeale,** and **S. M. Candel** (2017b). Flame describing function analysis of spinning and standing modes in an annular combustor and comparison with experiments. *Combust. Flame*, **184**, 136–152.
108. **Lee, J. G., K. Kim,** and **D. Santavicca** (2000a). Measurement of equivalence ratio fluctuation and its effect on heat release during unstable combustion. *Proc. Combust. Inst.*, **28**(1), 415–421.
109. **Lee, J. G., K. Kim,** and **D. A. Santavicca** (2000b). Effect of injection location on the effectiveness of an active control system using secondary fuel injection. *Proc. Combust. Inst.*, **28**(1), 739–746.
110. **Lee, M., Y. Guan, V. Gupta,** and **L. K. B. Li** (2020). Input-output system identification of a thermoacoustic oscillator near a Hopf bifurcation using only fixed-point data. *Phys. Rev. E*, **101**(1), 013102.
111. **Lee, M., K. T. Kim, V. Gupta,** and **L. K. B. Li** (2021). System identification and early warning detection of thermoacoustic oscillations in a turbulent combustor using its noise-induced dynamics. *Proc. Combust. Inst.*, **38**(4), 6025–6033.
112. **Lefebvre, A. H.** and **D. R. Ballal**, *Gas turbine combustion: alternative fuels and emissions*. CRC press, 2010.
113. **Leyva, I., A. Navas, I. Sendiña-Nadal, J. A. Almendral, J. M. Buldú, M. Zanin, D. Papo,** and **S. Boccaletti** (2013). Explosive transitions to synchronization in networks of phase oscillators. *Sci. Rep.*, **3**(1), 1–5.
114. **Lieuwen, T., V. McDonell, E. Petersen,** and **D. Santavicca** (2008). Fuel flexibility influences on premixed combustor blowout, flashback, autoignition, and stability. *J. Eng. Gas Turbines Power*, **130**(1).
115. **Lieuwen, T., Y. Neumeier,** and **B. T. Zinn** (1998). The role of unmixedness and chemical kinetics in driving combustion instabilities in lean premixed combustors. *Combustion Science and Technology*, **135**(1-6), 193–211.
116. **Lieuwen, T.** and **B. T. Zinn**, The role of equivalence ratio oscillations in driving combustion instabilities in low Nox gas turbines. *In Symp. (Int.) Combust.*, volume 27.

Elsevier, 1998.

117. **Lieuwen, T. C.** (2002). Experimental investigation of limit-cycle oscillations in an unstable gas turbine combustor. *J. Propuls. Power*, **18**(1), 61–67.
118. **Lieuwen, T. C.** (2003). Modeling premixed combustion-acoustic wave interactions: A review. *J. Propuls. Power*, **19**(5), 765–781.
119. **Lieuwen, T. C.**, *Unsteady combustor physics*. Cambridge University Press, 2012.
120. **Lieuwen, T. C.**, *Unsteady Combustor Physics*. Cambridge University Press, New York, 2021.
121. **Lieuwen, T. C.** and **V. Yang**, *Combustion Instabilities in Gas Turbine Engines: Operational Experience, Fundamental Mechanisms, and Modeling*. American Institute of Aeronautics and Astronautics, 2005.
122. **Lieuwen, T. C.** and **V. Yang**, *Gas turbine emissions*, volume 38. Cambridge university press, 2013.
123. **Lores, M. E.** and **B. T. Zinn** (1973). Nonlinear Longitudinal Combustion Instability in Rocket Motors. *Combustion Science and Technology*, **7**(6), 245–256.
124. **Mahesh, S.**, **R. Gopakumar**, **B. Rahul**, **A. Dutta**, **S. Mondal**, and **S. Chaudhuri** (2018). Instability control by actuating the swirler in a lean premixed combustor. *J. Propuls. Power*, **34**(3), 708–719.
125. **March, M.**, **J. Renner**, and **T. Sattelmayer**, Acoustic and optical investigations of the flame dynamics of rich and lean kerosene flames in the primary zone of an air-staged combustion test-rig. *In Turbo Expo: Power for Land, Sea, and Air*, volume 86960. American Society of Mechanical Engineers, 2023.
126. **Marsden, J. E.** and **M. McCracken**, *The Hopf bifurcation and its applications*, volume 19. Springer Science & Business Media, 2012.
127. **Marwan, N.**, **M. C. Romano**, **M. Thiel**, and **J. Kurths** (2007). Recurrence plots for the analysis of complex systems. *Physics reports*, **438**(5-6), 237–329.
128. **Matveev, K. I.** and **F. Culick** (2003). A model for combustion instability involving vortex shedding. *Combustion Science and Technology*, **175**(6), 1059–1083.
129. **Mazur, M.**, **Y. H. Kwah**, **T. Indlekofer**, **J. R. Dawson**, and **N. A. Worth** (2021). Self-excited longitudinal and azimuthal modes in a pressurised annular combustor. *Proc. Combust. Inst.*, **38**(4), 5997–6004.
130. **McIntosh, A.** (1999). Deflagration fronts and compressibility. *Philosophical Transactions of the Royal Society of London. Series A: Mathematical, Physical and Engineering*

*Sciences*, **357**(1764), 3523–3538.

131. **McManus, K., T. Poinsot, and S. M. Candel** (1993). A review of active control of combustion instabilities. *Prog. Energy Combust. Sci.*, **19**(1), 1–29.
132. **Merk, H. J.** (1957). Analysis of heat-driven oscillations of gas flows. *Appl. Sci. Res.*, **6**(4), 317–336.
133. **Merk, H. J.** (1958). Analysis of heat-driven oscillations of gas flows. *Appl. Sci. Res.*, **7**(2), 175–191.
134. **Moeck, J. and C. Paschereit** (2012). Nonlinear interactions of multiple linearly unstable thermoacoustic modes. *Int. J. Spray Combust. Dyn.*, **4**(1), 1–27.
135. **Moeck, J. P., D. Durox, T. Schuller, and S. Candel** (2019). Nonlinear thermoacoustic mode synchronization in annular combustors. *Proceedings of the Combustion Institute*, **37**(4), 5343–5350.
136. **Mondal, S., S. A. Pawar, and R. I. Sujith** (2017a). Synchronous behaviour of two interacting oscillatory systems undergoing quasiperiodic route to chaos. *Chaos*, **27**(10).
137. **Mondal, S., V. R. Unni, and R. I. Sujith** (2017b). Onset of thermoacoustic instability in turbulent combustors: an emergence of synchronized periodicity through formation of chimera-like states. *J. Fluid Mech.*, **811**, 659–681.
138. **Morgans, A. S. and I. Duran** (2016). Entropy noise: A review of theory, progress and challenges. *Int. J. Spray Combust. Dyn.*, **8**(4), 285–298.
139. **Motter, A. E., S. A. Myers, M. Anghel, and T. Nishikawa** (2013). Spontaneous synchrony in power-grid networks. *Nature Phys.*, **9**(3), 191–197.
140. **Nair, V. and R. I. Sujith** (2014). Multifractality in combustion noise: predicting an impending combustion instability. *J. Fluid Mech.*, **747**, 635–655.
141. **Nair, V. and R. I. Sujith** (2015). A reduced-order model for the onset of combustion instability: physical mechanisms for intermittency and precursors. *Proc. Combust. Inst.*, **35**(3), 3193–3200.
142. **Nair, V., G. Thampi, S. Karuppusamy, S. Gopalan, and R. I. Sujith** (2013). Loss of chaos in combustion noise as a precursor of impending combustion instability. *International journal of spray and combustion dynamics*, **5**(4), 273–290.
143. **Nair, V., G. Thampi, and R. I. Sujith** (2014). Intermittency route to thermoacoustic instability in turbulent combustors. *J. Fluid Mech.*, **756**, 470–487.
144. **Nicoud, F., L. Benoit, C. Sensiau, and T. Poinsot** (2007). Acoustic modes in combustors with complex impedances and multidimensional active flames. *AIAA J.*, **45**(2), 426–441.

145. **Nicoud, F.** and **K. Wieczorek** (2009). About the zero Mach number assumption in the calculation of thermoacoustic instabilities. *International Journal of Spray and Combustion Dynamics*, **1**(1), 67–111.
146. **Noiray, N.** (2017). Linear growth rate estimation from dynamics and statistics of acoustic signal envelope in turbulent combustors. *Trans. ASME J. Engng Gas Turbines Power*, **139**(4), 041503.
147. **Noiray, N., M. Bothien,** and **B. Schuermans** (2011). Investigation of azimuthal staging concepts in annular gas turbines. *Combust. Theory Model.*, **15**(5), 585–606.
148. **Noiray, N., D. Durox, T. Schuller,** and **S. Candel** (2008). A unified framework for nonlinear combustion instability analysis based on the flame describing function. *J. Fluid Mech.*, **615**, 139–167.
149. **Noiray, N.** and **B. Schuermans** (2013). Deterministic quantities characterizing noise driven hopf bifurcations in gas turbine combustors. *International Journal of Non-Linear Mechanics*, **50**, 152–163.
150. **O’Connor, J., V. Acharya,** and **T. Lieuwen** (2015). Transverse combustion instabilities: Acoustic, fluid mechanic, and flame processes. *Prog. Energy Combust. Sci.*, **49**, 1–39.
151. **Palies, P., D. Durox, T. Schuller,** and **S. Candel** (2010). The combined dynamics of swirler and turbulent premixed swirling flames. *Combust. Flame*, **157**(9), 1698–1717.
152. **Paschereit, C., B. Schuermans,** and **P. Monkewitz**, Non-linear combustion instabilities in annular gas-turbine combustors. *In 44th AIAA aerospace sciences meeting and exhibit.* 2006.
153. **Pavithran, I., V. R. Unni, A. J. Varghese, D. Premraj, R. I. Sujith, C. Vijayan, A. Saha, N. Marwan,** and **J. Kurths** (2020). Universality in spectral condensation. *Scientific Reports*, **10**(1), 1–8.
154. **Pawar, S. A., S. Mondal, N. B. George,** and **R. I. Sujith** (2019). Temporal and Spatiotemporal Analyses of Synchronization Transition in a Swirl-Stabilized Combustor. *AIAA Journal*, **57**(2), 836–847.
155. **Pawar, S. A., A. Seshadri, V. R. Unni,** and **R. I. Sujith** (2017). Thermoacoustic instability as mutual synchronization between the acoustic field of the confinement and turbulent reactive flow. *J. Fluid Mech.*, **827**, 664–693.
156. **Pawar, S. A., V. R. Unni, M. Vadivukkarasan, M. V. Panchagnula,** and **R. I. Sujith** (2016). Intermittency route to combustion instability in a laboratory spray combustor. *J. Eng. Gas Turbines Power*, **138**(4).
157. **Pazó, D.** (2005). Thermodynamic limit of the first-order phase transition in the Kuramoto model. *Phys. Rev. E*, **72**(4), 046211.

158. **Peracchio, A. A. and W. M. Proscia** (1999). Nonlinear Heat-Release/Acoustic Model for Thermoacoustic Instability in Lean Premixed Combustors. *J. Eng. Gas Turbines Power*, **121**(3), 415–421. ISSN 0742-4795.
159. **Pietras, B., N. Deschle, and A. Daffertshofer** (2018). First-order phase transitions in the Kuramoto model with compact bimodal frequency distributions. *Phys. Rev. E*, **98**(6), 062219.
160. **Pikovsky, A., M. Rosenblum, and J. Kurths**, *Synchronization: A Universal Concept in Nonlinear Science*. Cambridge University Press, Cambridge, 2002.
161. **Pikovsky, A., M. Rosenblum, and J. Kurths**, *Synchronization: A Universal Concept in Nonlinear Sciences*. 12. Cambridge University Press, 2003.
162. **Poinsot, T.** (2017). Prediction and control of combustion instabilities in real engines. *Proc. Combust. Inst.*, **36**(1), 1–28.
163. **Poinsot, T. J., A. C. Trouve, D. P. Veynante, S. M. Candel, and E. J. Esposito** (1987). Vortex-driven acoustically coupled combustion instabilities. *J. Fluid Mech.*, **177**, 265–292.
164. **Polifke, W.** (2014). Black-box system identification for reduced order model construction. *Ann. Nucl. Energy*, **67**, 109–128.
165. **Polifke, W.** (2020). Modeling and analysis of premixed flame dynamics by means of distributed time delays. *Prog. Energy Combust. Sci.*, **79**, 100845.
166. **Polifke, W., C. O. Paschereit, and K. Döbbling** (2001). Constructive and destructive interference of acoustic and entropy waves in a premixed combustor with a choked exit. *Int. J. Acoust. Vib*, **6**(3), 135–146.
167. **Pomeau, Y. and P. Manneville** (1980). Intermittent transition to turbulence in dissipative dynamical systems. *Commun. Math. Phys.*, **74**, 189–197.
168. **Popovych, O. V., Y. L. Maistrenko, and P. A. Tass** (2005). Phase chaos in coupled oscillators. *Phys. Rev. E*, **71**(6), 065201.
169. **Premchand, C., M. Raghunathan, M. Raghunath, K. Reeja, R. I. Sujith, and V. Nair**, Smart Passive Control of Thermoacoustic Instability in a Bluff-Body Stabilized Combustor: A Lagrangian Analysis of Critical Structures. *In Turbo Expo: Power for Land, Sea, and Air*, volume 84133. American Society of Mechanical Engineers, 2020.
170. **Prieur, K., D. Durox, T. Schuller, and S. Candel** (2017). A hysteresis phenomenon leading to spinning or standing azimuthal instabilities in an annular combustor. *Combust. Flame*, **175**, 283–291.
171. **Prieur, K., D. Durox, T. Schuller, and S. Candel** (2018). Strong azimuthal combustion

instabilities in a spray annular chamber with intermittent partial blow-off. *J. Eng. Gas Turbines Power*, **140**(3).

172. **Putnam, A. A.**, *Combustion-driven oscillations in industry*. Elsevier Publishing Company, 1971.
173. **Rayleigh, J. W. S.**, *The Theory of Sound*, volume 2. Dover, 1945.
174. **Rayleigh, L.** (1878). The explanation of certain acoustical phenomena. *Nature*, **8**, 536–542.
175. **Renard, P.-H., D. Thevenin, J.-C. Rolon, and S. Candel** (2000). Dynamics of flame/vortex interactions. *Prog. Energy Combust. Sci.*, **26**(3), 225–282.
176. **Renner, J., M. March, C. Hirsch, and T. Sattelmayer** (2022). Flame dynamics in the lean burnout zone of an rql combustion chamber-response to primary zone velocity fluctuations. *Int. J. Spray Combust. Dyn.*, **14**(3-4), 238–250.
177. **Richards, G. A., D. L. Straub, and E. H. Robey** (2003). Passive control of combustion dynamics in stationary gas turbines. *J. Propuls. Power*, **19**(5), 795–810.
178. **Rogers, D. E. and F. E. Marble** (1956). A mechanism for high-frequency oscillation in ramjet combustors and afterburners. *Journal of Jet Propulsion*, **26**(6), 456–462.
179. **Romano, M. C., M. Thiel, J. Kurths, I. Z. Kiss, and J. L. Hudson** (2005). Detection of synchronization for non-phase-coherent and non-stationary data. *Europhys. Lett.*, **71**(3), 466.
180. **Roy, A., S. Mondal, S. A. Pawar, and R. I. Sujith** (2020). On the mechanism of open-loop control of thermoacoustic instability in a laminar premixed combustor. *J. Fluid Mech.*, **884**.
181. **Roy, A., C. P. Premchand, M. Raghunathan, A. Krishnan, V. Nair, and R. I. Sujith** (2021). Critical region in the spatiotemporal dynamics of a turbulent thermoacoustic system and smart passive control. *Combust. Flame*, **226**, 274–284.
182. **Samarasinghe, J., W. Culler, B. D. Quay, D. A. Santavicca, and J. O’connor** (2017). The Effect of Fuel Staging on the Structure and Instability Characteristics of Swirl-Stabilized Flames in a Lean Premixed Multinozzle Can Combustor. *J. Eng. Gas Turb. Power*, **139**(12), 121504.
183. **Samuelson, S.** (2006). Rich burn, quick-mix, lean burn (rql) combustor. *The Gas Turbine Handbook*, 227–233.
184. **Schadow, K. and E. Gutmark** (1992). Combustion instability related to vortex shedding in dump combustors and their passive control. *Prog. Energy Combust. Sci.*, **18**(2), 117–132.

185. **Schuller, T., T. Poinsot, and S. Candel** (2020). Dynamics and control of premixed combustion systems based on flame transfer and describing functions. *J. Fluid Mech.*, **894**.
186. **Schwing, J., T. Sattelmayer, and N. Noiray**, Interaction of vortex shedding and transverse high-frequency pressure oscillations in a tubular combustion chamber. *In Turbo Expo: Power for Land, Sea, and Air*, volume 54624. 2011.
187. **Seshadri, A., V. Nair, and R. I. Sujith** (2016). A reduced-order deterministic model describing an intermittency route to combustion instability. *Combust. Theory Model.*, **20**(3), 441–456.
188. **Seshadri, A., I. Pavithran, V. R. Unni, and R. I. Sujith** (2018). Predicting the amplitude of limit-cycle oscillations in thermoacoustic systems with vortex shedding. *AIAA Journal*, **56**(9), 3507–3514.
189. **Sethares, W. A.**, *Rhythm and transforms*. Springer Science & Business Media, 2007.
190. **Seume, J. R., N. Vortmeyer, W. Krause, J. Hermann, C.-C. Hantschk, P. Zangl, S. Gleis, D. Vortmeyer, and A. Orthmann** (1998). Application of Active Combustion Instability Control to a Heavy Duty Gas Turbine. *J. Eng. Gas Turbines Power*, **120**(4), 721–726. ISSN 0742-4795.
191. **Shanbhogue, S. J., S. Husain, and T. Lieuwen** (2009a). Lean blowoff of bluff body stabilized flames: Scaling and dynamics. *Prog. Energy Combust. Sci.*, **35**(1), 98–120.
192. **Shanbhogue, S. J., M. Seelhorst, and T. C. Lieuwen** (2009b). Vortex phase-jitter in acoustically excited bluff body flames. *Int. J. Spray Combust. Dyn.*, **1**(3), 365–387.
193. **Shin, D. and T. C. Lieuwen** (2013). Flame wrinkle destruction processes in harmonically forced, turbulent premixed flames. *J. Fluid Mech.*, **721**, 484–513.
194. **Shraiman, B. I.** (1986). Order, disorder, and phase turbulence. *Phys. Rev. Lett.*, **57**(3), 325.
195. **Shraiman, B. I., A. Pumir, W. van Saarloos, P. C. Hohenberg, H. Chaté, and M. Holen** (1992). Spatiotemporal chaos in the one-dimensional complex Ginzburg-Landau equation. *Phys. D: Nonlinear Phenom.*, **57**(3-4), 241–248.
196. **Shreekrishna, S. H. and T. Lieuwen** (2010). Premixed flame response to equivalence ratio perturbations. *Combust. Theory Model.*, **14**(5), 681–714.
197. **Smith, D. A.** (1985). *An experimental study of acoustically excited, vortex driven, combustion instability within a rearward facing step combustor*. Ph.D. thesis, California Institute of Technology.
198. **Steele, R. C., L. H. Cowell, S. M. Cannon, and C. E. Smith** (2000). Passive control

- of combustion instability in lean premixed combustors. *J. Eng. Gas Turbines Power*, **122**(3), 412–419.
199. **Strogatz, S. H.** (2000). From kuramoto to crawford: exploring the onset of synchronization in populations of coupled oscillators. *Phys. D: Nonlinear Phenom.*, **143**(1-4), 1–20.
  200. **Strogatz, S. H.**, *Nonlinear dynamics and chaos: with applications to physics, biology, chemistry, and engineering*. CRC press, 2018.
  201. **Subramanian, P., R. I. Sujith, and P. Wahi** (2013). Subcritical bifurcation and bistability in thermoacoustic systems. *J. Fluid Mech.*, **715**, 210–238.
  202. **Sujith, R. I. and S. A. Pawar**, *Thermoacoustic Instability - A Complex Systems Perspective*. Springer Nature, 2021.
  203. **Sujith, R. I. and V. R. Unni** (2020). Complex system approach to investigate and mitigate thermoacoustic instability in turbulent combustors. *Physics of Fluids*, **32**(6), 061401.
  204. **Tandon, S., S. A. Pawar, S. Banerjee, A. J. Varghese, P. Durairaj, and R. I. Sujith** (2020). Bursting during intermittency route to thermoacoustic instability: Effects of slow-fast dynamics. *Chaos*, **30**(10), 103112.
  205. **Terada, Y., K. Ito, T. Aoyagi, and Y. Y. Yamaguchi** (2017). Nonstandard transitions in the Kuramoto model: a role of asymmetry in natural frequency distributions. *J. Stat. Mech.*, **2017**(1), 013403.
  206. **Tony, J., E. Gopalakrishnan, E. Sreelekha, and R. I. Sujith** (2015). Detecting deterministic nature of pressure measurements from a turbulent combustor. *Physical Review E*, **92**(6), 062902.
  207. **Uhm, J. H. and S. Acharya** (2005). Low-bandwidth open-loop control of combustion instability. *Combust. Flame*, **142**(4), 348–363.
  208. **Vignat, G., D. Durox, A. Renaud, and S. Candel** (2020). High amplitude combustion instabilities in an annular combustor inducing pressure field deformation and flame blow off. *J. Eng. Gas Turbines Power*, **142**(1).
  209. **Wang, X., X. Han, H. Song, D. Yang, and C. J. Sung** (2021). Multi-bifurcation behaviors of stability regimes in a centrally staged swirl burner. *Phys. Fluids*, **33**(9), 095121.
  210. **Weng, F., S. Li, D. Zhong, and M. Zhu** (2016). Investigation of self-sustained beating oscillations in a rijke burner. *Combust. Flame*, **166**, 181–191.
  211. **Wilke, C.** (1950). A viscosity equation for gas mixtures. *The Journal of Chemical Physics*, **18**(4), 517–519.

212. **Worth, N. A. and J. R. Dawson** (2012). Cinematographic oh-plif measurements of two interacting turbulent premixed flames with and without acoustic forcing. *Combust. Flame*, **159**(3), 1109–1126.
213. **Worth, N. A. and J. R. Dawson** (2013a). Modal dynamics of self-excited azimuthal instabilities in an annular combustion chamber. *Combust. Flame*, **160**(11), 2476–2489.
214. **Worth, N. A. and J. R. Dawson** (2013b). Self-excited circumferential instabilities in a model annular gas turbine combustor: Global flame dynamics. *Proc. Combust. Inst.*, **34**(2), 3127–3134.
215. **Worth, N. A. and J. R. Dawson** (2017). Effect of equivalence ratio on the modal dynamics of azimuthal combustion instabilities. *Proc. Combust. Inst.*, **36**(3), 3743–3751.
216. **Yu, H., T. Jaravel, M. Ihme, M. P. Juniper, and L. Magri** (2019). Data assimilation and optimal calibration in nonlinear models of flame dynamics. *J. Eng. Gas Turb. Power*, **141**(12).
217. **Yu, H., M. P. Juniper, and L. Magri** (2021). A data-driven kinematic model of a ducted premixed flame. *Proc. Combust. Inst.*, **38**(4), 6231–6239.
218. **Zhang, J., S. Boccaletti, Z. Liu, and S. Guan** (2020). Synchronization of phase oscillators under asymmetric and bimodal distributions of natural frequencies. *Chaos Solit. Fractals*, **136**, 109777.
219. **Zhao, D.**, *Thermoacoustic Combustion Instability Control: Engineering Applications and Computer Codes*. Academic Press, 2023.
220. **Zhao, D. and X. Y. Li** (2015). A review of acoustic dampers applied to combustion chambers in aerospace industry. *Progress in Aerospace Sciences*, **74**, 114–130.
221. **Zhao, D., Z. Lu, H. Zhao, X. Li, B. Wang, and P. Liu** (2018). A review of active control approaches in stabilizing combustion systems in aerospace industry. *Progress in Aerospace Sciences*, **97**, 35–60.
222. **Zheng, L. and X. Zhang**, *Modeling and analysis of modern fluid problems*. Academic Press, 2017.
223. **Zhou, W., L. Chen, H. Bi, X. Hu, Z. Liu, and S. Guan** (2015). Explosive synchronization with asymmetric frequency distribution. *Phys. Rev. E*, **92**(1), 012812.
224. **Zinn, B. T. and T. C. Lieuwen** (2005). Combustion instabilities: basic concepts. *Progress in Astronautics and Aeronautics*, **210**, 3.



# CURRICULUM VITAE

**NAME** Samarjeet Singh

**DATE OF BIRTH** 05 November 1994

## EDUCATION QUALIFICATIONS

**2017** **Bachelor of Technology (B. Tech.)**

Institution Desh Bhagat University

Specialization Aeronautical Engineering

**2024** **M.S. and Ph.D. Dual Degree**

Institution Indian Institute of Technology, Madras

Specialization Aerospace Engineering

Registration Date 9<sup>th</sup> July 2018



# DOCTORAL COMMITTEE

## **Chairperson**

Prof. H. S. N. Murthy  
Professor and Head  
Department of Aerospace Engineering

## **Guide**

Prof. R. I. Sujith  
D. Srinivasan Institute Chair Professor  
Department of Aerospace Engineering

## **Members**

Prof. Sunetra Sarkar  
Professor  
Department of Aerospace Engineering

Prof. Nandan Kumar Sinha  
Professor  
Department of Aerospace Engineering

Prof. S. Lakshmi Bala  
Professor  
Department of Physics